

School of Chemistry

Synthesis protocols to porous carbons for energy storage applications

THRIA ALKHALDI

Thesis submitted to the University of Nottingham

for the degree of Doctor of Philosophy

[2023]

Abstract

In the context of limited availability of fossil fuel and the impact of fossil-based energy utilization to the environment, novel porous materials have been extensively investigated for applications in environmentally friendly energy storage. This Thesis describes work wherein porous carbons have been systematically studied to include development of existing methods, new synthesis strategies, and material characterization. Two main themes of this thesis are, firstly, to investigate how porosity affects the utilization of activated carbons in energy storage and gas adsorption, and secondly, to develop the synthesis protocols in order to ensure their sustainability.

Chapter 1 discusses activated carbon structures, classifications of pores, the fundamental properties of porous materials, and preparation and important applications of the materials.

Chapter 2 gives the basics of techniques used for characterization of the porous materials fabricated in this work. Gas sorption techniques applied for methane storage and carbon dioxide uptake are introduced.

Chapter 3 examines the effect of varying activation conditions (temperature and degree of activation) on the preparation of activated carbons derived from polypyrrole in terms of application to CO_2 uptake and methane storage. A compactivation approach, which incorporates a mechanical compression step before thermochemical activation, is explored. Series of samples were synthesised using the less toxic activating agent 'potassium oxalate'. Surface area of up to 3000 m^2/g and pores of size range 6-12 Å were achieved. The resulting carbons showed excellent CO_2 uptake and methane storage at moderate to high pressure and ambient temperature.

In Chapter 4, carbon nano-cages with hierarchical 3D structure were prepared via a template-assisted carbonisation method. Magnesium carbonate pentahydrates acted as a template and benzene as a carbon precursor. Carbons with pore volume of 1.5-4.6 cm^3/g and surface area of between 750- 1711 m^2/g were achieved. The effect of chemical activation for hCNCs in order to develop their SA and textural properties were studied.

Chapter 5 reports the synthesis of biomass-derived activated carbons with high microporosity and packing density that is suitable for CO_2 and methane storage at high pressure. Prickly pear peels were used as carbon precursor, and a range of carbonisation temperature (350- 600°C) were employed. Our findings present important insights on synthesis of activated carbons and represent a significant step in the development of cheap porous carbons for gas storage applications.

Chapter 6, the efficient storage of energy combined with a minimum carbon footprint is one of the major challenges facing the global pursuit of a transition toward progressive, sustainable, eco-friendly societies. For this reason, a sustainable and scalable method is presented in this study for the preparation of an ultra-microporous (average pore size ca. 0.6 nm) activated carbon cloth (ACC) with a large specific area (> 2000 m^2/g) and pore volume (~ 1.5 cm^3/g) by combining activation with chemical impregnation of low-cost cellulose-based polymeric fabric. The resultant ACC can store 2.0 mmol/g at 1 bar, 7.7 mmol/ g at 20 bar of CH_4 at 25°C, which is much higher than any value reported to date for activated carbon cloths. In addition, it can also store high amounts of CO_2 at 25°C; 2.0 mmol/g, 4.2 mmol/g and 13.4 mmol/g at 0.25 bar, 1 bar and 40 bar, respectively.

Finally, the conclusions for the Thesis including suggestions for future work are proposed in Chapter 7.

Conference presentations

Thria Alkhaldi, 14th International Conference on Materials Chemistry (MC14), Aston University, Birmingham, UK, 8 - 11 July 2019, 'The Synthesis of high packing density activated carbon from polypyrrole for CO_2 capture'.

Thria Alkhaldi, Second Joint NSFC-RSC Symposium on Sustainable Chemistry and Processes, University of York, York, UK, 19 - 20 September 2019, 'The synthesis of high packing density activated carbon from polypyrrole for CO_2 capture'.

Thria Alkhaldi, Women in chemistry conference, University of Nottingham, Nottingham, UK, 8 March 2020, 'Studying the effect of KOH activation on 3Dhierarchical carbon nanocages'.

Thria Alkhaldi, Chemistry of 2-dimensional materials: beyond graphene Faraday Discussion, online, 23 - 25 November 2020, 'The effect of N-dopping activated carbon in the CO_2 capture capability'.

Thria ALkhaldi, RSC Materials Chemistry Division poster symposium, online, 20 January 2021, 'Templated hierarchical carbon nanocages for efficient CO_2 capture and storage'.

Thria Alkhaldi, Women in chemistry conference, University of Nottingham, Online, 8 March 2021, 'N-activated carbon for efficient CO_2 capture as a technique of carbon circular economy CCE'.

Thria Alkhaldi, MSDE symposium 2021: frontiers in molecular engineering, United kinghdom, Online, 17-18 June 2021, 'A sustainable approach for high-pressure methane adsorption on biomass-based activated carbon'.

Thria Alkhaldi, 5th RSC Energy Sector Early Career Chemists Symposium, London, United Kingdom, 23 November 2021, 'Highly microporous activated carbon cloth as a versatile material for CH_4 adsorption and CO_2 storage at low pressure'.

Thria Alkhaldi, Next Generation Nano electrochemistry Faraday Discussion, United Kingdom, Online, 29 November 2021-01 December 2021, 'A sustainable approach of High-pressure methane adsorption and CO_2 storage on Biomass-based activated carbon'.

Thria Alkhaldi, Women in chemistry conference, University of Nottingham, Online, 8 March 2021, Nottingham, United Kingdom.

Thria Alkhaldi, 5th Annual UK Porous Materials Conference, University of Strathclyde, 13 June-14 June, Glasgow, United Kingdom.

Award

Thria Alkhaldi, 5th RSC Energy Sector Early Career Chemists Symposium, London, United Kingdom, 23 November 2021, 'Highly microporous activated carbon cloth as a versatile material for CH_4 adsorption and CO_2 storage at low pressure'.

List of the Abbreviations and acronyms

SA- surface area

CNTs- Carbon nanotube superstructures

CDCs- Carbide- derived carbons

CMPs- Conjugated microporous polymers

PAFs- Porous aromatic frameworks

POPs- Porous organic polymers.

IGA- Intelligent Gravimetric Analysis.

MOFs – Metal Organic Frameworks.

TGA- Thermal Gravimetric Analysis.

XRD–X-Ray Diffraction.

IGA– Intelligent Gravimetric Analysis.

DFT–Density Functional Theory.

BET– Brunauer, Emmett and Teller.

BJH- Barrett-Joyner-Halenda

PSD – Pore Size Distribution.

ACC- Activated carbon cloth.

ACs- Activated carbons.

CVD- Chemical vapour deposition.

LI- Liquid impregnation.

KOH –Potassium hydroxide.

PO- Potassium oxalate.

CO_2– Carbon dioxide.

CO– Carbon monoxide.

HCl– Hydrochloric acid.

$ZnCl_2$- Zinc chloride.

NH_4Cl- Ammonium chloride.

IUPAC Classification:

Micro-pores – pores of < 20 Å

Meso-pores– pores of 20 – 500 Å

Macro-pores- pores of >500 Å

Acknowledgements

In the name of Allah, the most merciful and gracious. First and foremost, I am grateful to ALLAH for granting me the strength, knowledge, ability, and opportunity to undertake and successfully complete this study.

Secondly, I would like to thank my supervisor, Professor Robert Mokaya, for his invaluable assistance during my study. I am grateful for the encouragement and motivation I received from my friend Afaf Al Husayni and my lab colleagues, particularly Asma Madkhali, Abdulsalam al jumaily, Alison Taylor, and Leo Blankenship. Also, I need to express my deep gratitude to Neil Barnes and Mark Guyler for their technical support.

I am deeply grateful to my mom for her support, appreciation, encouragement, and keen interest in my academic achievements. I thankfully acknowledge the moral support that I have from my brothers and sisters: Dalal, Abdulaziz, Sara, Sahar, Samar, Futun, and Helal. I would also like to give special thanks for my supportive husband, Dr Rabi and my little angels Rose and Abdulaziz.

Table of Contents

1. Introduction 1

1.1. Activated carbon. 2

1.2. Activated carbon feedstock. 2

1.2.1. Non-carbonised feedstock. 3

1.2.2. Carbonised feedstock. 4

1.3. The carbonisation of carbon precursors. 5

1.3.1. Pyrolysis. 5

1.3.2. Hydrolysis 5

1.3.3. Flash carbonisation 7

1.3.4. Template-assisted carbonisation. 8

1.4. Mesoporous carbons. 10

1.4.1. Hard template synthesis strategy. 11

1.4.2. Soft template synthesis strategy. 12

1.5. Activated carbon cloth. 12

1.6. Activation processes 13

1.6.1. Chemical activation. 14

1.6.2. Physical activation. 18

1.6.3. Microwave-assisted activation. 20

1.6.4. Mixed activation. 21

1.7. Activated carbon Gas capture and storage applications. 21

1.7.1. Hydrogen storage 22

1.7.2. CO_2 capture. 25

1.7.3. Methane storage 26

1.8. References 31

2. Porous material characterization and analytical techniques. 36

2.1. Thermogravimetric Analysis (TGA). 36

2.2. Elemental Analysis (CHN). 38

2.3. Scanning Electron Microscopy (SEM). 39

2.4. Powder X-ray Diffraction (P-XRD). 41

2.5. Physisorption of gas by porous material. 43

2.5.1. Types of adsorption/ desorption isotherm 44

2.5.2. Capillary Condensation 45

2.5.3. Hysteresis loop 46

2.5.4. Pore size classification 46

2.5.5. Surface area determination 47

2.6. Gas adsorption measurement. 52

2.7. Packing density determination. 53

2.8. References. 54

3. Highly microporous polypyrrole-derived activated carbons for high CO_2 and CH_4 storage 55

3.1. Introduction 55

3.2. Experimental section 58

3.2.1. Materials synthesis 58

3.2.2. Material Characterisation. 59

3.3. Result and discussion 60

3.3.1. PPY-derived activated carbons: Yields, structure, nature, and morphology 61

3.3.2. Porosity and textural properties analysis 68

3.3.3. CO_2 uptake measurements 76

3.3.4. Methane uptake 80

3.4. Conclusion 87

3.5. References 88

4. Mesoporous hierarchical carbon nanocages with high CH4 and CO2 adsorption under high pressure 90

4.1. Introduction 90

4.2. Experimental Section 94

4.2.1. The formation of hierarchical carbon nanocages (hCNCs) 94

4.2.2. The activation of hCNCs 95

4.2.3. Structural analysis 96

4.2.4. CH_4 and CO_2 uptake measurements 96

4.3. Results and Discussion 96

4.3.1. Nature and structure of MgO 96

4.3.2. Structure of hCNCs carbons 99

4.3.3. Vap-hCNCs carbons prepared via chemical vapour deposition. 100

4.3.4. LI-hCNCs-120 templated carbon prepared via liquid impregnation. 115

4.3.5. The chemical activation of LI-hCNCs-120 119

4.4. Conclusion 129

4.5. References 130

5. Highly porous biomass-derived activated carbon with enhanced CO2 and methane uptake 133

5.1. Introduction 133

5.2. Experimental section 135

5.2.1. Material synthesis 135

5.2.2. Characterization methods 136

5.2.3. CO_2 and CH_4 uptake measurements 137

5.3. Results and Discussion 137

5.3.1. Study of the nature of Char 137

5.3.2. Study of the PPPS-derived activated carbons 141

5.3.3. Methane uptake 154

5.3.4. CO_2 uptake 161

5.4. Conclusion 165

5.5. References 167

6. Highly microporous activated carbon cloth as a versatile material for CH_4 170

and CO_2 storage at low pressure 170

6.1. Introduction 170

Comparison to benchmark materials 172

6.2. Experimental Section 175

6.2.1. Material synthesis 175

6.2.2. Material Characterisation 176

6.2.3. Methane and CO_2 uptake measurements 177

6.3. Results and Discussion 177

6.3.1. Direct Activation of Viscose Rayon 178

6.3.2. ACC prepared via KOH activation following stabilisation with NH_4Cl and 180

$ZnCl_2$ 180

6.3.3. ACC via simultaneous stabilisation and activation with NH_4Cl and $ZnCl_2$ 183

6.3.4. ACC prepared via stabilisation with NH_4Cl and PO activation. 190

6.3.5. ACC via carbonisation and PO activation 195

6.4. Methane storage and CO_2 uptake 204

6.5. Conclusion 209

6.6. References 210

7. Conclusion and Future work 213

7.1. Conclusion 213

7.2. Future work 215

Chapter 1: Porous carbon material: background, preparation methods, and applications.

1. Introduction

Meeting society's growing energy demands while avoiding resource depletion and environmental pollution requires the development of energy storage and production systems that are high-performance, low-cost, and environmentally friendly. Recent research has sought to develop and improve energy-storage devices, such as batteries and super-capacitors, and energy-production systems such as fuel cells. Key factors to accomplish this include the design of novel materials, the development of synthesis processes that allow precise control over the structural and chemical characteristics of the material, and the seeking of greener and more cost-effective material synthesis processes for the widespread utilization of such devices.

Porous carbon is one of many solid materials that has been intensively studied for applications that require controlled spaces, such as energy applications. Carbon has many advantages over other solid-state materials; it is widely available, chemically and physically stable, easy to prepare, and amenable to property tuning to meet specific applications requirements. Activated carbon is one of the most porous carbons that has been explored. It has traditionally been used as a catalyst to support chemical reactions, but it also has the ability to adsorb undesirable particles. For example, activated carbon was used in protective gas masks in World War I. The ability to control its surface area (porosity structure) and the character of its pores (pore volume and pore size distribution (PSD)) further make it an excellent candidate for gas storage devices in energy applications. Because it is cheap and readily abundant, it can be effectively employed in large-scale applications.

This chapter provides an overview and historical background for the major themes explored in this thesis, in addition to a classification of activated-carbon materials. Different types of activated carbon materials, based on porosity, are discussed. An emphasis is placed on their fundamental properties and preparation methods and potential uses of porous carbon materials for hydrogen storage, with an emphasis on methane storage and carbon (CO_2) capture.

1.1. Activated carbon.

Activated carbons are amorphous materials composed of carbon atoms arranged in a short-range lamellar structure. They are among the most well-known porous solids, and due to their potential for large surface areas and plethora of possible functional groups, they possess excellent adsorption properties.[1–7] Activated carbons obtain their surface areas from the development of large internal surfaces during the thermal treatment of carbonaceous precursors during the preparation process. Consequently, they are effective adsorbents in a wide variety of applications and are commonly used in gas- and liquid-phase adsorption processes. Several processes and techniques have been proposed to regulate the textural properties and physical forms of activated carbons. Activated carbons are currently available in a variety of forms, including powder,[2,5,7–12] fibres,[13,14] cloth,[1,15–19] and granular,[20,21] to meet the ever-expanding range of industrial technological requirements.

Because the performance of porous materials is heavily dependent on their internal pore structure, it is one of the most essential features of practical applications. Several kinds of pore size are described. According to the widely accepted IUPAC classification, pore width (w) can be classified into three groups: macropores, mesopores, and micropores.

(i) Micropores: Pore diameter less than 2 nm.

(ii) Mesopores: Pore diameter between 2 and 50 nm.

(iii) Macropores: Pore diameter greater than 50 nm.

The micropores can be further subdivided into ultra-micropores (diameter < 0.7 nm) and supermicropores (0.7–2.0 nm).

1.2. Activated carbon feedstock.

It is possible to prepare activated carbon from two major feedstocks: carbonised material, such as coal, low temperature lignite coke, charcoal or biochar,[22,23] and non-carbonised material, such as agricultural or forest biomass (wood, sawdust, peat, coconut shells, fruit bones, and rice husk). The production of activated carbon from biomass-based materials has recently become attractive due

to their high abundance and low cost. Further, it provides the possibility of converting low-value starting materials into high-value commercial products. However, the characteristics and structure of the resulting activated carbon depend on the source, so it is important to study the different carbons to determine which is most suitable for any given application.[24–28]

1.2.1. Non-carbonised feedstock.

Biomass-based material, whether from agricultural sources, food production processes, or forest waste, is attractive. It converts materials with less value into valuable commercial products. This readily available and cheap precursor may result in high-surface-area activated carbons. The pore characteristics (structure and heteroatom content) can be controlled via the activation methodology (chemical, physical or mixed) and the type of biomass source (starting material).[24]

For instance, Bagheri and Abedi prepared activated carbon with a high surface area using corncobs as the carbon precursor. The carbon was chemically activated using KOH. They observed that this activated carbon from corncobs has a greater surface area compared to commercial activated carbons from a carbonised source: coal.[29] Ramesh *et al.,* prepared activated carbon for hydrogen storage applications from a tamarind seed precursor. Both microwave and thermal treatments were used for carbonisation. This was then mixed with KOH to create a porous structure. Increasing the duration of microwave pyrolysis led to increased porosity, which further increased the hydrogen-adsorbing capacity. In this case, the hydrogen storage capacity of the produced activated carbon increased to 4.73 wt%, which is 80% of the hydrogen storage capacity set by the U.S. Department of Energy (DOE). It should be noted that using microwave irradiation in the carbonisation step can decrease the time taken to obtain highly porous activated carbon as compared to direct thermal treatments. Moreover, in the case of tamarind seed precursors, microwave-energy-generated microporous structures are ideal for hydrogen storage application, while thermal treatments generate inferior mesoporous structures.[30]

Increasing reagent efficiency is important for sustainability. Many studies show that the quantity of activating agent required for the chemical activation of some biomass feedback precursors can be decreased. In 2015, Heo and Park prepared activated carbon from rice husks. The obtained carbon was found to be the most effective at storing up to 2.85 wt.% hydrogen at 77 K and 1 bar. Activation

with KOH occurred at 600 °C or higher, and the carbonisation of the precursor was performed at 500 °C.[31] It is important to mention that the carbon structure can benefit from increased KOH loadings. Another study showed that increasing the quantity of activating agent (KOH) could develop the carbon's porosity structure and surface area. When using a 1:1 ratio of carbon precursor to KOH, the maximum pore volume was 0.79 $cm^3\ g^{-1}$ and the hydrogen storage capacity was also at its highest; 2.85 wt.%, at 77 K, 1 bar.[32] Akasaka *et al.* studied the efficiency of activated carbon produced from coffee bean waste using KOH as an activating agent for hydrogen storage at temperatures of 298 and 77 K. They reported that the hydrogen storage capacity at 298 K was linearly dependent on the surface area. It was 0.6 wt.% with a surface area of 2070 $m^2\ g^{-1}$ under 12 MPa. On the other hand, the hydrogen storage capacity at 77 K reached a higher value, up to 4.0 wt.%, and was dependent of the micro-pore volume size.[33]

1.2.2. Carbonised feedstock.

Oil derivatives have been used for several energy applications and have historically been sufficient to cover demand. However, the world's accessible oil reserves are gradually depleting. Many countries have thus sought to upgrade their energy production methods to those that incorporate sustainable resources. Pollution released from oil derivatives is also a significant reason to substitute oil with greener, more sustainable sources.[24] Carbonised feedstock such as coal, low temperature lignite coke, charcoal, or bio-char[1,2] may also be used as carbon precursors to prepare activated carbon. However, using non-sustainable resources as materials in sustainable energy applications is clearly not ideal. Although many studies have provided examples of preparing activated carbon from coal, low temperature lignite coke, charcoal or biochar,[22,23] activated carbon sourced from biomass feedstock tends to have a higher surface area and better structured porosity.[29]

It is important to mention that organic compounds can be used as a starting material to prepare carbon precursors. Porous organic polymers (POPs) such as polypyrrole have potential adsorbents for CO_2 capture due to their high surface areas, tuneable pore sizes, and tailored functionality. Hence, they have been attracting increasing attention in recent years. However, many polymers involve costly and toxic starting materials such as conjugated microporous polymers (CMPs),

expensive catalysts such as porous aromatic frameworks (PAFs), and harsh synthetic conditions such as PAFs, all of which make their large-scale preparation a challenge.

1.3. The carbonisation of carbon precursors.

Generally, carbonisation is the conversion of a precursor into a carbon-rich carbonaceous matter known as char[7,8,11,27,34] or hydrochar[2,35,36,37]. Pyrolysis or hydrolysis occurs either in air or in the flow of an inert atmosphere with the simultaneous removal of volatile products.

1.3.1. Pyrolysis.

Pyrolysis is the thermal decomposition of materials at elevated temperatures (300–700 °C) in an inert atmosphere. This process involves a change in chemical composition and is irreversible. In the case of preparing porous carbon materials, the pyrolysis of biomass has been intensively studied.[8, 35] Biomass carbonisation is a slow pyrolysis process where biomass is converted into a highly carbonaceous, charcoal-like material (biochar).

1.3.2. Hydrolysis.

Hydrolysis is a chemical reaction where water is used to break down the bonds of a particular substance. The hydrothermal approach is popular methodology for carbonisation. 'Hydrothermal' refers to aqueous carbonisation at an elevated temperature and pressure. An autoclave is typically used for this purpose. Many studies have used the hydrothermal approach for biomass, where a biomass precursor is placed in a closed reactor (i.e., autoclave) and treated at approximately <300 °C under self-generated pressure.

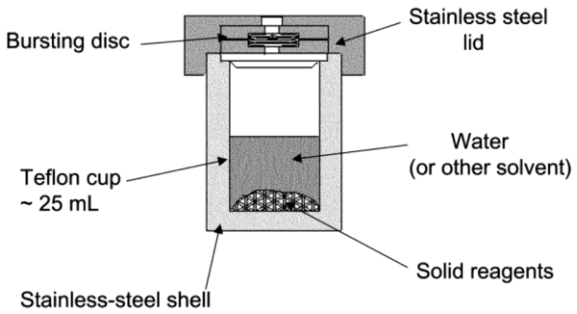


Figure 1. A schematic of the autoclave method used for hydrothermal carbonisation.

Complex chemical reactions occur during this process. The hydrothermal carbonisation or wet pyrolysis methodologies, however, can lead to a reduction in the carbonisation step's temperature in physical activation. The starting material and water mixture are exposed to the thermal treatment at temperatures of 150–350 °C. Many studies have demonstrated that hydrothermal carbonisation is effective in maximising yields. Wang *et al.* prepared novel anode materials for Li-ion batteries using the hydrothermal activation process. They obtained a product with an ideal morphology: controlled pore size and a smooth texture.[38] Antonietti *et al.,* hydrothermally prepared carbonaceous material from complex biomass waste that was treated at only 200 °C.[39]

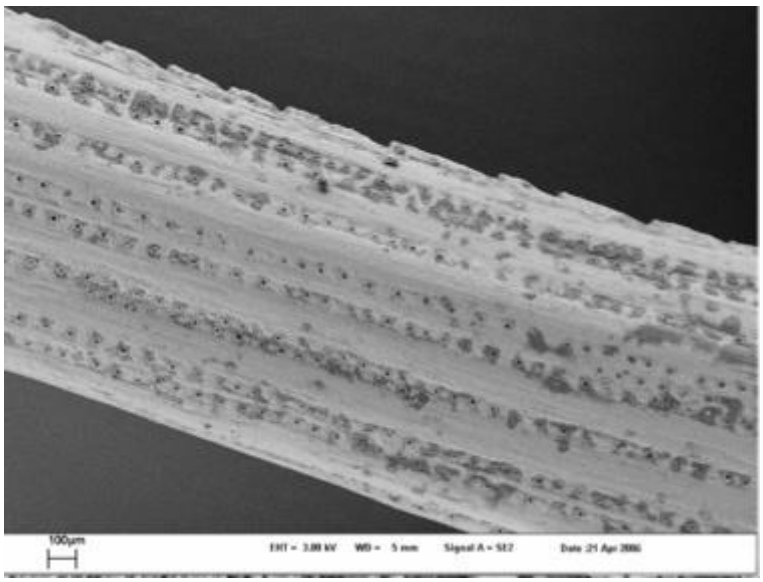


Figure 2. Antonietti's biomass before being carbonised hydrothermally at 200 °C for 12 h.[39]

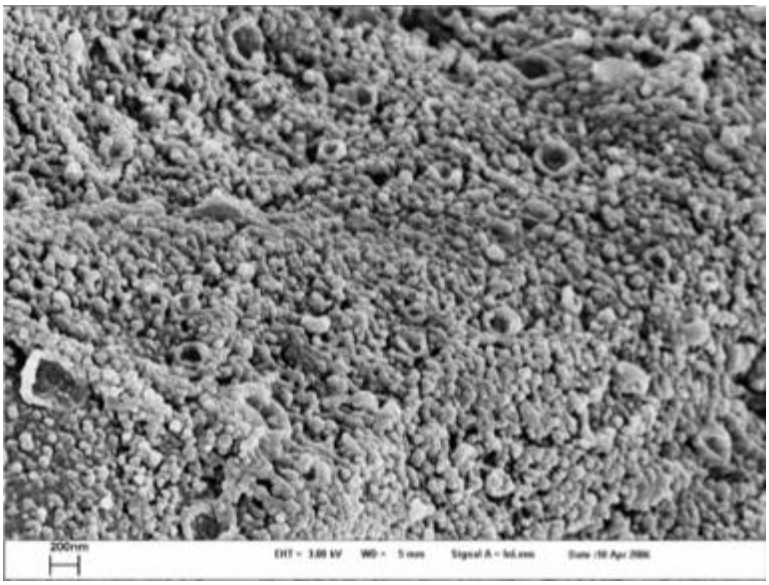


Figure 3. Antonietti's biomass after being carbonised hydrothermally at 200 °C for 12 h.[39]

The final product is a solid residue known as hydrochar.[2,35,36,40,41] If hydrochar is prepared at a low degree of carbonisation, its potentially weak chemical stability remains an issue. Notably, Liu *et al.* proposed a feasible solution that provides high-stability hydrochar via the sequential carbonisation of biomass.[42] Hydrochar was derived from corn straw and corncobs using consecutive hydrothermal carbonisation at 200 °C followed by pyrolysis at temperatures of 350–650 °C. The resulting pyro-hydrochar is a carbon-rich material with a large specific surface area (SSA), rich functional groups, and strong chemical oxidation stability.

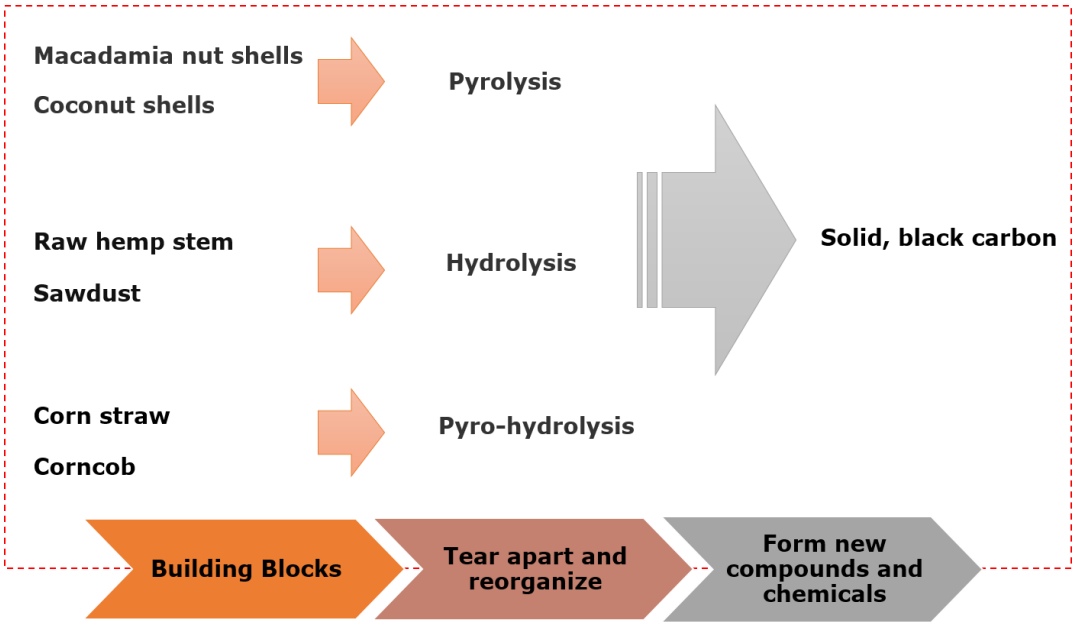


Figure 4. Carbonisation routes of biomass to form carbonaceous matter.

1.3.3. Flash carbonisation

The evolution of volatiles (i.e., H_2O, CO_x, CH_4, and light hydrocarbons) during high-temperature pyrolysis occurs at temperatures between 200 and 350°C, with only negligible mass loss above 400°C. This fact should be considered when weighing the possibility of using lower temperatures for biomass carbonisation processes. It indicates that the transformation of biomass to carbonaceous matter is essentially complete at approximately 400°C. With this in mind, and in an effort to simplify the carbonisation step, it would be desirable to investigate pathways that achieve comparable results using less time (5–10 minutes) and lower temperatures (>400°C) with the

presence of oxygen. These processes, which occur at low temperatures in the presence of air, are known as flash carbonisation.

Taylor *et al.,* successfully converted biomass precursor (eucalyptus sawdust) into carbonaceous matter by flash heating for 5–10 minutes in the presence of air flow. As a first work, the flash carbonisation of biomass efficiency was reported.[34] It important to mention that the mode of carbonisation can play a significant role in the chemical composition of the resulting activated carbon. Flash carbonisation increases the C-content more than hydrothermal carbonisation. For instance, hydrothermal carbonisation (HTC) of date seeds (at 250°C) resulted in a hydrochar with elemental composition (wt%) of C (68.7), H (6.0), N (1.5), and O (23.8), giving a O/C ratio of 0.25. On the other hand, the carbon content (78.5 wt%) of the air carbonised date seeds (with O/C ratio of 0.156) is significantly higher than that of the hydrochar.[43]

1.3.4. Template-assisted carbonisation.

The template method involves replicating the structure and texture of a template into carbon, a process that has been successfully applied to prepare carbon flakes, carbon nanotubes, nanofibers, and nanoporous carbons. It was first proposed to control the morphology of carbon materials and later used to prepare nanoporous carbons with controlled pore size, volume, and alignment by employing various templates.

Morphology is an important parameter for the characterisation of material properties, especially in porous materials. Along with particle size, surface area, and pore structure, morphology can determine the properties of porous materials and thus pinpoint their application.[44,45] Templating primarily changes the morphology of products by controlling the carbon precursor deposition during the templating process. The route of template carbon synthesis is generally divided into three steps. Firstly, the template is prepared. Secondly, common synthetic approaches such as chemical vapour deposition (CVD) and liquid impregnation (LI) are used to fabricate target materials under the direction of the template. Thirdly, the template is removed.

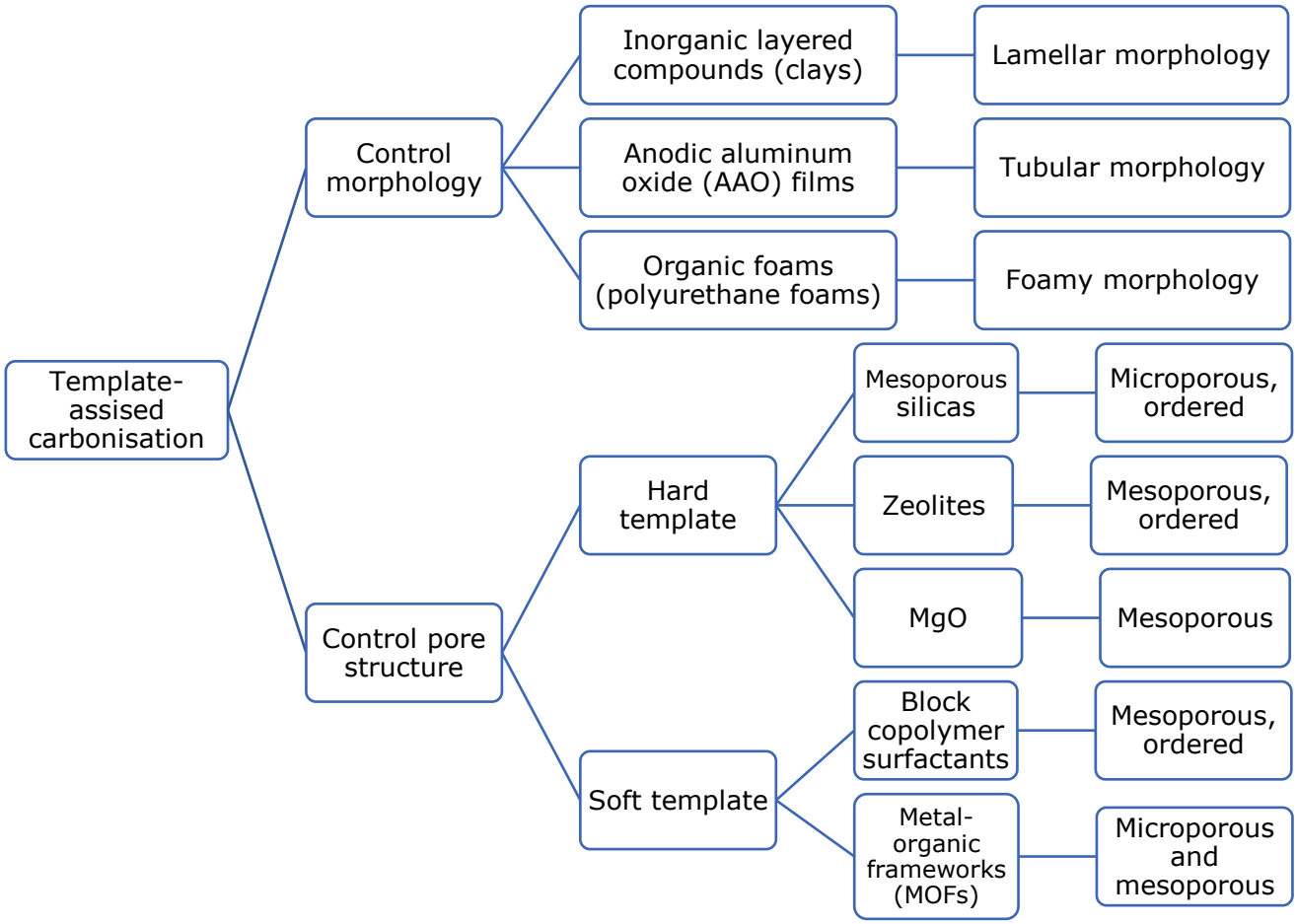


Figure *5.* A schematic of commonly used templates in the literature, with the characteristics of *their resultant carbons*[46].

The choice of template for micro- or meso-material preparation is critical. Templates can usually be grouped into two major categories: natural substances (nano-mineral, biological molecules, cells and tissues, etc.) and synthetic materials (surface-active agents, porous materials and nanoparticles, etc.).[47,48] Templates are additionally often divided into two groups, hard and soft, based on stiffness and structural differences.[46]

A recent study notably proposed template-assisted hydrothermal carbonisation.[49] However, the structural properties of hydrothermal carbon are not very good due to factors such as low specific surface and pore size.[50] Zhao *et al.* prepared a novel mesoporous carbon via the hydrothermal template method using sodium lignosulfonate (LS) as a raw material and cetyltrimethylammonium bromide (CTAB) as a template agent.[49]

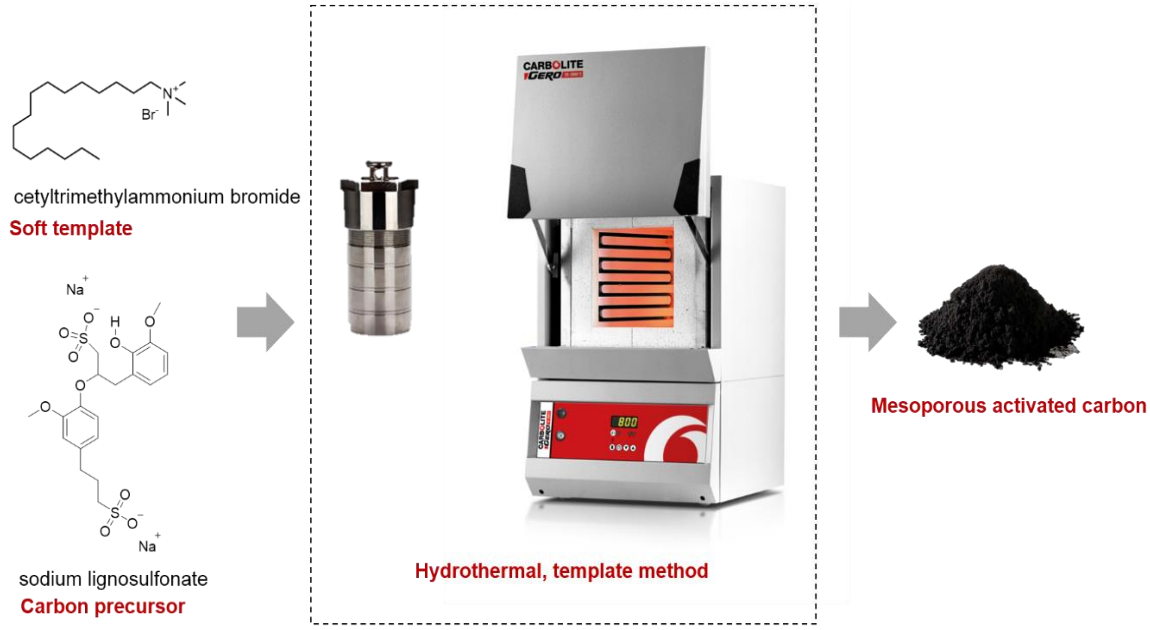


Figure 6. Hydrothermal template carbonisation preparation scheme.

As shown in Table 1, the surface area of carbon-LSs+ CTAB, where the template agent is added in the hydrothermal carbonisation process, is nine times greater than that of carbon-LSs without the addition of the template agent in the hydrothermal carbonisation process.

Table 1. Textural properties of resulting meso-carbons from the hydrothermal carbonisation of lignosulfonate carbon-LSs and hydrothermal-templated meso-carbons carbon-LSs+CTAB.

Sample	*BET SA* ($m^2\ g^{-1}$)	V_t ($cm^3\ g^{-1}$)	*Pore size (nm)*
Carbon-LSs+CTAB	633	0.41	5
Carbon-LSs	67	0.41	5

1.4. Mesoporous carbons.

Mesopores are generally defined as pores with widths between 20Å and 500 Å (2 and 50 nm). Most Activated carbons are microporous and are well studied in several applications involving small molecules, such as gas storage and in catalysis applications.[2,51,4] However, there are certain uses where the presence of mesoporous or even macroporous would be favourable; for instance, in the adsorption of large hydrophobic molecules such as vitamins, dyes, and polymers, chromatographic

separations, or electrochemical double-layer capacitor applications. Porous carbon is typically prepared via carbonisation followed by either physical or chemical activation that develops its porosity and textural properties. Porous carbon usually has disordered structures and a wide PSD. This is because the pores in disordered porous carbons are generated using etching processes, which are difficult to control, or by the escape of gases during the carbonisation of carbon precursors. Mesoporous carbons can be prepared via catalytic activation using cobalt,[52] the carbonisation of polymer blends,[53] the carbonisation of organic gels,[54] and colloidal imprinting.[55] However, these synthesis routes are not efficient enough to provide such ordered material and are often unsustainable in terms of catalysis usage. To improve the level of structural ordering, the template method can be used to guide pore formation during carbonisation.[56]

Templated mesoporous carbon material can be manufactured using two types of templates, soft templates and hard templates, which are used as moulds to form porous materials. The hard template carbonisation method, which usually entails several processes. It offers stiff nanocast moulds as real templates for replicating other materials. To build a pure carbon framework, the hard templates must be thermally stable, chemically inert to carbon precursors, and removable. The soft template approach, on the other hand, involves collaborative assembly in solution of structure-directing agents (typically surfactants or copolymers) and organic precursor species. As a result, carbon structures formed using soft templates are more flexible, and their creation is temperature, solvent type, and ionic strength dependant.

1.4.1. Hard template synthesis strategy.

A hard template is a rigid material whose stable structure directly determines the sample particle's size and morphology. A wide variety of hard templates are available, such as the nano-zeolite molecular sieve and mesoporous metal oxides. It is a commonly used method for the synthesis of meso- or macro-structured materials due to its ability to prepare templates with different 'hole' sizes and structures under various requirements using physical or chemical growth or the deposition of precursors for porous material fabrication, while the dimensions and specifications of the target production can be precisely controlled. Following the deposition of the carbon precursor, the removal

of the template is required. Many solvents can be used for this, such as HF to remove zeolite[57] and aqueous HCl solution to remove MgO.[58,59]

1.4.2. Soft template synthesis strategy.

The soft template does not have a fixed, rigid structure. In nanoparticle synthesis, an aggregate with certain structural features is formed using intermolecular or intramolecular interaction forces (hydrogen bonding, chemical bonding, and static electricity). Inorganic species are deposited on the surface or interior of these templates through the electrochemical method, precipitation, and other synthetic methods, thus creating particles of certain shapes and sizes. Common soft templates include surfactants, polymers, and biopolymer. They are easy to build and remove and do not require complex equipment or strict production conditions to achieve good reaction controllability.[60,61,62]

1.5. Activated carbon cloth.

Activated carbons are widely employed as effective adsorbent materials for the storage of adsorbates such as H_2, CH_4, and CO_2 due to their large specific surface areas (SSA), good chemical stability and low cost. When nanoporous activated carbon is used for these applications, it must still be treated to generate a functional material (e.g., membranes, thin films) from carbon powder. This results in a lowering of the specific surface area and pore volume, due to the effects of aggregation and pore blockage.[63] Since these textural properties play a key role in energy related gas storage and other energy storage applications, it would be highly desirable to develop a cost-effective and simple processing procedure for a lightweight, mechanically and chemically stable, flexible, non-fragile material without losing porosity. This may exist in the form of activated carbon cloth (ACC),[64,65] whose conformability and flexibility make it much more versatile and robust as a potential liner in gas storage tanks.

Furthermore, the large surface areas of activated carbon cloth enable faster adsorption kinetics and mass transfer as compared to the powder and granular forms of activated carbon. This is in addition to the safe handling benefits, with regard to health, and the convenient commercialisation opportunities that tank processes offer. Dehydrating agents are used during activation to create

pathways of pores and prevent tar production. Upon activation, the salts left in the pores are eliminated with an acid wash.[1,15,17–19,63,64]

The preparation of activated carbon cloth (ACC) involves a number of steps, which include polymerisation, stabilisation, and physical or chemical activation.[1,15–19,63,65,66] Huidobro *et al.,* investigated the chemical activation of viscous rayon fabric through impregnation with solutions of different chemicals (NH_4Cl, $AlCl_3$, $ZnCl_2$, $CuCl_2$, $FeCl_3$, H_3PO_4, or Na_2HPO_4), followed by carbonisation in an inert atmosphere. The authors argued that the impregnation modifies the precursor's pyrolysis, favouring dehydration over depolymerisation and resulting in a larger ACC yield.[63] Kostoglou *et al.,* presented a simple, reproducible, and scalable method for the preparation of ultra-microporous ACC with large SSA (> 1200 m^2/g) and pore volume (0.5 cm^3/g) by combining chemical impregnation, carbonization, and CO_2 activation of a low-cost, cellulose-based polymeric fabric.[19] Attia *et al.* recently proposed the development of a nanoporous activated carbon fabric via the polarisation of polypyrrole in a dispersed state on the fibre surfaces of commercial viscose rayon fabric. The material was then carbonised and activated using separate physical and chemical activation techniques. This produced a nanoporous carbon textile with a high nitrogen content, a surface area of ~2000 m^2/g, and a total pore volume of 0.85 cm^3/g[1].

1.6. Activation processes

Precursor characteristics and the employed activation method have significant impact on the nature of the produced activated carbon. This holds especially true for its chemical and physical properties. Thus, by controlling the activation method, a wide range of activated carbons can be obtained to meet the varied requirements of diverse applications. The chemical activation process involves a single step: carbon precursor is mixed with the activating agent, such as KOH, and exposed to thermal treatment in an inert atmosphere that is between 450–900 °C.[67,68] Physical activation, on the other hand, involves two steps: carbonisation of the carbon precursor and gasification using an oxidising gas (CO, CO_2, air). Both steps are conducted at temperatures of 350–1000 °C.[68,69] These different methodologies produce different carbonaceous materials in which structures, surface area, pores size, and, therefore, applications vary.

Considering the 12 principles of green chemistry, it is necessary to mention the large amount of energy that is consumed by these high-temperature processes. The need to decrease energy consumption is both a commercial and sustainability goal; continued growth of the human population requires more efficient energy usage. Hydrothermal carbonisation and microwave radiation can decrease the energy required for the processes. Effective hydrothermal carbonisation can reduce the carbonisation temperature and lead to a higher yield. Microwave radiation can also reduce the activation energy, time, inert gas consumption, and production costs. On the other hand, the recovery of the activating agent in the chemical activation method leads to a reduction in the required amount of chemical agent, and therefore leads to reduced disposal related costs.

1.6.1. Chemical activation.

Chemical activation is a single-step method where carbon precursors are mixed with an activating agent (such as $ZnCl_2$, H_3PO_4, $AlCl_3$, $MgCl_2$, KOH, NaOH, or $K_2C_2O_4$) at a high temperature (450–900 °C). This process allows surface area and pore development within the carbon structures. KOH and NaOH are very similar in their reactivity, yet their activation results are not necessarily the same. KOH, H_3PO_4, and $ZnCl_2$ are the most commonly used. These reagents react with carbon precursors in different ways. For instance, KOH oxidises carbon, whereas $ZnCl_2$ and H_3PO_4 are dehydrating agents.[70,71]

Jagtoyen and Derbyshire studied the role of H_3PO_4 as an activating agent to produce activated carbon. They observed that at low temperatures, H_3PO_4-promoted dehydration leads to the evolution of CO and CO_2. Then, during thermal treatment, the carbon precursor is dehydrated. The authors assumed that cross-linking reactions (cyclization and condensation processes) were predominant in the dehydration step. Thus, particle dimensions were reduced.[72] Molina *et al.* concluded that uniform micro-pore sizes can be obtained by using small amounts of $ZnCl_2$ and its hydrates.[70]

Regarding KOH activation, there is widespread agreement that pore formation occurs through three primary processes: (i) chemical activation, in which redox reactions between K compounds and the carbon framework occur; (ii) formation of the physical activating agents CO_2 and H_2O, which induce gasification of carbon to further develop porosity; and (iii) metallic K intercalation between graphitic

sheets. Washing the sample eliminates both intercalated K and K oxides and carbonates, resulting in permanently porous carbon. [73,74]

For activation temperatures below 700 °C, the possible mechanism of chemical reactions with KOH have been suggested as follows:

$$6KOH + 2C \rightarrow 2K + 3H_2 + 2K_2CO_3 \qquad \textit{Equation 1}$$

The reaction of KOH with carbon produces salts on the carbon surface and layers, which act as active sites in the gasification process for developing pore structure. For temperatures above 700 °C, the evolution of CO_2 due to the decomposition of K_2CO_3 according to equation below leads to larger pore size development.

$$K_2CO_3 \rightarrow K_2O + CO_2 \qquad \textit{Equation 2}$$

The development of surface area and evolution of pore size distribution can be explained by the formation of various K compounds during the thermal treatment in the carbon matrix which leads to the widening of carbon layers or destruction of the original structure due to the removing of these compounds. [73,74]

Chemical activation is preferred to physical activation as it involves only one step and results in higher yields. This is because pyrolysis is conducted at relatively low temperatures compared to physical activation. In addition, it produces high-surface-area materials (up to 3600 $m^2\ g^{-1}$), and porosity and pore sizes may be controlled. These properties are significant in many important applications, such as gas storage (H_2, CO_2, CH_4), that require pore sizes to be 0.7–1 nm. The high surface area of the produced carbons also means that they are efficient electrode materials for super-capacitor applications; the pore size control is useful in allowing electrolyte ions to move smoothly.[76,77] It should be noted that up to recently the highest yield of activated carbon reported so far is 40%. However, Mokaya *et al.,* more recently achieved a much higher yield: up to 80% under mild conditions (KOH/carbon precursor ratio of 2 at 600 °C) and 32% under harsher conditions (KOH/carbon precursor ratio of 4 at 800 °C). They prepared activated carbon using burnt wood from the CNL building (Carbon Neutral Laboratory) at Nottingham University. Table 2 shows

surface area, yield, and pore volume values at various activation temperatures and activating agent–carbon precursor ratios.[4]

Table 2. Activated carbon properties at various temperatures and activating agent/precursor ratios[4].

KOH: precursor ratio	*Activation temp., °C*	*Surface area* $m^2 g^{-1}$	*Pore volume* $cm^3 g^{-1}$	*Yield* *wt.%*
1:2	600	1190	0.55	80
	700	1399	0.63	65
	800	1326	0.60	52
1:4	600	1121	0.53	68
	700	1280	0.65	53
	800	2183	1.05	32

What is apparent is the wide range of yields, pore volumes, and surface areas seen depending on the conditions used. The harshest conditions, a 1:4 KOH–precursor ratio at 800 °C, gave the lowest yield of activated carbon but show a remarkable increase in surface area compared to the least harsh conditions, a 1:2 KOH–precursor ratio at 600 °C. This increase is associated with pore widening (pore volume 1.05 $cm^3 g^{-1}$) and carbon precursor weight loss (yield is only 32%). The highest yield (80%) was obtained at 600 °C and demonstrated one of the lowest surface areas (1190 $m^2 g^{-1}$), about half that of the highest value. Thus, in this instance, there is a compromise between yield and surface area.

Activating agent recovery.

The environmental implications of using chemical activation agents are an important consideration where industrial-scale processes are concerned. Most activated carbon research fails to consider using a sustainable approach to the activating agents themselves. Reusing activating agents reduces production costs as well as costs related to disposal. If a sufficient recovery process for the activating agent is applied, it can be considered a catalyst. The chemical recovery of activation

agents has been found to be inversely proportional to the activation temperature; a high percentage of chemical recovery is possible at low activation temperatures. Table 3 shows the effect of the activation temperature and the type of activating agent on the percentage of chemical recovery when macadamia nut shells were used as the carbon source (1:1 ratio of carbon–activating agent) for 60 minutes.[78]

Table 3. The effect of activation temperature and type of activating agent on the chemical recovery of the activating agent when preparing activating carbon from a macadamia nutshell carbon source (1:1 ratio) after 60 minutes.[78]

Precursor	*Activating agent*	*Activation temperature (˚C)*	*Chemical recovery (%)*
Macadamia nut shells	$ZnCl_2$	500	64
		600	5
		700	3
	KOH	600	93
		700	86
		800	77

The highest recovery was for potassium hydroxide, with recovery at 93% after activation at 600 °C. $ZnCl_2$ recovery was much more sensitive to the activation temperature. In a different study, the recovery of phosphoric acid was found to be much lower, even at lower temperatures, when reclaimed from activated carbon generated from agave bagasse (Table 4). Table 4 also shows that $ZnCl_2$ was much more satisfactorily recovered at lower temperatures, the effect of the differing carbon precursor uncertain in this case.

Table 4. Chemical recovery as a function of production conditions using agave bagasse as a carbon source in activated carbon generation.[79]

Activating agent	T (°C)	R (g\g)	CR (%)
H_3PO_4	250	0.40	28
	250	1.00	46
	350	0.40	25
	350	1.00	34
$ZnCl_2$	250	0.40	89
	250	1.00	87
	350	0.40	88
	350	1.00	86

T: Activation temperature, R: Activation agent\ precursor ratio, CR: percentage of chemical recovery.

It has been argued that a major reason for the low percentage of recovery of phosphoric acid is its ability to form stable links with carbon. This may also have implications for the quality/properties of the activated carbon.[79]

1.6.2. Physical activation.

As mentioned above, the physical activation of carbon precursors requires two steps. First, carbon precursors are exposed to high temperatures of up to 900 °C in an inert medium (e.g., N_2, Ar, or He). This pyrolysis step aims to eliminate the bulk of volatile matter. Second, the product is exposed to a partial gasification process at 350–1000 °C with an oxidising agent, such as air, CO_2, or O_2. The active part of the oxidising agent (oxygen) then reacts to remove the carbon atoms, opening

pores and changing the usually broad PSD. The reactivity of the oxidising agent is the most significant factor in determining the micro-porous structure. In addition, the obtained activated carbon is dependent on the nature of the starting material as well as the temperature and duration of activation. For instance, high pyrolysis temperatures and activating times often lead to high porosity. Moderate-to-high porous carbon has been achieved using the physical activation method.[68,69]

Using the 12 principles of green chemistry as a guide, different parts of the physical activation process can be considered in turn. When considering the oxidising agent, 'substances and the form of a substance used in a chemical process should be chosen so as to minimize the potential for chemical accidents, including releases, explosions, and fires.[80] CO and CO_2 are thus preferred to air as oxidising agents as they react in a controlled manner. Air (oxygen) reacts exothermically with carbon in a high-speed reaction, which leads to lower activated carbon yields and greater difficulty controlling temperatures. Porosity is also negatively affected. On the other hand, considering the energy used for the activation, 'energy requirements should be recognized for their environmental and economic impacts and should be minimized. Synthetic methods should be conducted at ambient temperature and pressure'. Using air as the activating agent requires less energy and minimises production costs compared with CO_2 and steam. Many researchers have considered these trade-offs. Feng and Bathia studied the properties of activated carbon that is obtained from physical activation of coal char precursors using air and CO_2. They pointed out that the gasification temperature of air (380 °C) is much lower than for CO_2 (800 °C). In addition, air gasification produces activated carbon with higher surface areas and pore volumes (~700 $cm^2\,g^{-1}$ and ~0.55 $cm^3\,g^{-1}$) than CO_2 (~500 $cm^2\,g^{-1}$ and ~0.22 $cm^3\,g^{-1}$).[81]

Ganan *et al.,* obtained activated carbon with higher surface areas (up to ~560 $cm^2\,g^{-1}$) and pore volumes (1.31 $cm^3\,g^{-1}$) using air gasification at 190–260 °C. They used almond tree feedstock and concluded that the micro-porous structure of activated carbon could be developed by increasing the time and energy of activation.[82] More recently, Osswald *et al.,* studied the performance of air and CO_2 in activating TiC-derived, carbide-derived carbons (TiC–CDCs). They observed that when using air activation, the surface area and pore size increased by about 10% along with large weight loss.

The activation depended on activation time and temperature. For CO_2 activation, however, a remarkable increase in surface area (up to 77%) was observed and the pore size doubled. In fact, CO_2 activation at 950 °C for 2 h generated a surface area of 3100 $m^2 g^{-1}$ and a pore volume of 1.3–1.4 $cm^3 g^{-1}$[83].

1.6.3. Microwave-assisted activation.

Using microwave energy for the activation of biomass-based materials has been recently explored and good yields have been obtained. In addition, microwave heating technique has numerous advantages over conventional heating technologies, including faster volumetric heating, higher chemical reaction rate and selectivity, and shorter reaction time. Figure 7 shows how heating is distributed in conventional and microwave heating.[14,84–86]

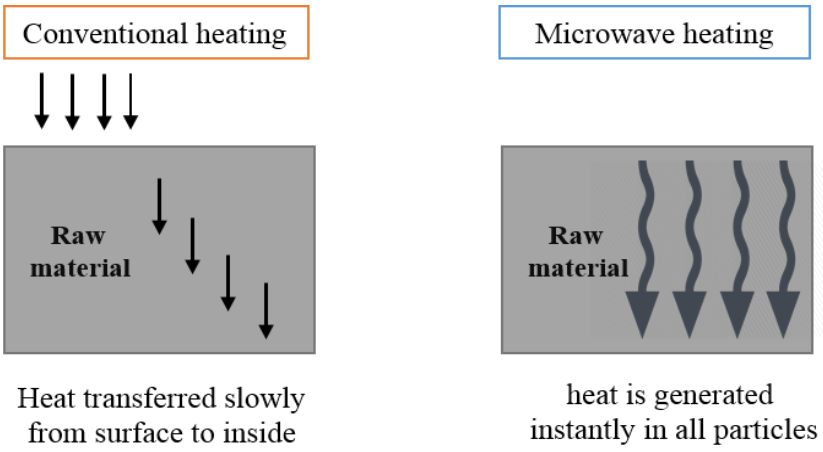


Figure 7. Comparison between conventional heating and microwave heating techniques.

Because microwave heating uses electromagnetic radiation to heat the matter, it is more uniform than conventional heating, which relies on conduction, convection, and radiation to transfer heat to the matter.

Heat is transmitted to the matter from the outside to the inside in conventional heating, which can result in uneven heating. The matter's outside layers may become overheated or charred, while the inside layers may stay cold. This is due to the fact that heat takes time to pass through matter and that the exterior layers of matter may absorb more heat than the inner layers.

Microwave heating, on the other hand, immediately heats the matter using electromagnetic radiation. This radiation is absorbed by the matter and transformed into heat, which is then disseminated throughout. As a result, the matter is heated more uniformly from the inside out. Furthermore, microwaves can penetrate deeper into matter than traditional heating methods, allowing for more even heating of thicker matters. Overall, microwave heating is more uniform and effective than traditional methods of heating.[14,84–86]

1.6.4. Mixed activation.

In mixed activation, activated carbon is obtained through a combination of chemical and physical activation. It involves two stages: First, chemical activation is performed, which normally involves the use of phosphoric acid (H_3PO_4) or zinc chloride ($ZnCl_2$) as the activating agent. This is then followed by thermal activation that uses carbon dioxide in a gasification step. The combination of these methods allows porosity development and tuneable PSD. A small amount of the chemical reagent (KOH, $ZnCl_2$, H_3PO_4) generates narrow micropores, and gasification by the oxidant gas (CO_2) then develops the micro-porosity structure and tunes the PSD. It necessary to clarify that this method allows high yields to be obtained, as the density of the starting material is maintained in the chemical activation step. Activated carbon with a surface area of 2400 $m^2\,g^{-1}$ and yields of 14–94% may be obtained.[87] Using the same approach, Arami-Niya *et al.,* prepared activated carbon and modified their textural properties to meet methane storage application demands.[88]

1.7. Activated carbon Gas capture and storage applications.

Due to their ability to tailor porosity/structure characteristics, activated carbons can be used in many applications where surface area is important. For example, they may be used for energy storage in devices such as batteries and fuel cells, which are important applications for the development of renewable energy technologies. But it is hydrogen, methane storage, and CO_2 capture that are the most promising applications of activated carbon in the energy sector. Many papers discuss the activated carbon's ability to store H_2 at ambient and cryogenic temperatures. Additionally, the ability to capture CO_2 in activated carbons from various feedstocks has attracted much attention, with the eventual goal of tackling the problem of high CO_2 atmospheric concentrations. Finally, activated carbon show promising potential for CH_4 storage.

1.7.1. Hydrogen storage

One of the promising energy sources uses in the present decade is hydrogen. Both green hydrogen (produced by electrolysis of water molecules using renewable energy sources) and blue hydrogen (produced from a natural gas feedstock with carbon dioxide captured as a by-product) are regarded as clean and environmentally friendly energy sources for a variety of reasons: 1. No greenhouse gas emissions: When hydrogen is used as a fuel, the sole waste is water, implying that no greenhouse gas emissions are produced. In comparison, traditional fossil fuels release carbon dioxide and other pollutants that contribute to climate change. 2. plentiful and renewable: Hydrogen is the most plentiful element in the universe and can be created using a number of renewable energy sources such as solar, wind, and hydro power. As a result, hydrogen has the potential to be a genuinely renewable energy source. 3. Versatile: Hydrogen may be used for transportation, heating, and power generation, among other things. It can either be used directly in fuel cells to generate power or burned in internal combustion engines. 4. Efficient: Because hydrogen has a high energy density, it carries a lot of energy per unit of weight. As a result, it is a more efficient fuel source, requiring less fuel to create the same amount of energy as other fuels. 5. Safe: In its pure state, hydrogen is non-toxic and non-flammable, and it may be securely stored and transported if necessary precautions are taken. Overall, hydrogen has the potential to play an important role in the transition to a cleaner, more sustainable energy system that reduces our reliance on fossil fuels and aids in the mitigation of climate change.

The fundamental challenge with hydrogen energy storage and release is that it cannot be use the existing transportation and storage infrastructure owing to:

1. Storage: Because hydrogen has a lower energy density than conventional fuels like petrol or diesel, it takes up more room to store the same amount of energy. This makes hydrogen storage difficult since it necessitates specialised containers and equipment that are not yet commonly available.

2. Transportation: Because hydrogen is a gas at room temperature and pressure, it must be compressed or liquified before it can be transported efficiently. This necessitates the use of

specialised transportation infrastructure, like as pipelines or tanker trucks, which are currently in short supply.

3. Infrastructure: The existing infrastructure for producing, distributing, and storing hydrogen is limited, and major investment would be required to build out the infrastructure required to allow broad use of hydrogen as a fuel.

4. Cost: at the moment, the cost of manufacturing hydrogen is considerable, and it is not yet cost-competitive with alternative fuels. This is due in part to the high energy required for creating hydrogen, as well as the small scale of production.

5. Safety: Hydrogen is highly combustible and must be handled with caution to avoid accidents. Specialised safety procedures for storage, transit, and usage are required, which may increase the expense and complexity of using hydrogen as a fuel.

Besides compression and storage as a liquid, metal organic frameworks (MOFs) and carbon surfaces have been explored for hydrogen storage. However, these methods face large barriers and difficulties, such as high costs. Studies are therefore concerned with increasing the performance of hydrogen fuel storage while decreasing the cost. For example, efforts towards developing hydrogen cerium fuel cells and the use of formic acid have been made.[33,89–91]

Porous carbon, especially activated carbon, is considered as one of the most important solid materials for energy applications. One of these applications is hydrogen storage; efforts towards this goal are now about thirty years old. Activated carbon has many suitable properties: a high surface area, large pore size volume, chemical and physical stability, and the possibility of tailoring its porosity. Further investigations have been driven by the need to meet the requirements of hydrogen energy applications. As expected, there is a correlation between hydrogen adsorption under different conditions (temperature and pressure) and the properties of activated carbon (surface area, pore size, PSD of porosity structure, and packing density).[33,89–91] These correlations will be considered in the following section.

Room-temperature hydrogen storage.

The hydrogen uptake capacity of different types of activated carbon has been studied. Although most research has focused on hydrogen storage in activated carbon at cryogenic temperatures, many studies have been conducted at ambient temperature. Uptake values are typically reported at 25 °C. Cryogenic temperatures are used because hydrogen uptake levels at ambient temperatures are usually low. For instance, the maximum uptake capacity of activated carbon from anthracite is only 1 wt.% at 100 bar.[92] Higher hydrogen uptake can be achieved at very high pressures.

Linares-Solano *et al.,* and Vix-Guterl *et al.* report that the ideal pore size for storing hydrogen is about 0.6 nm.[92,93,42,43] Moreover, the porosity structure of the activated carbon plays a significant role in determining hydrogen uptake capacity. Jorda-Beneyto measured hydrogen adsorption capacity at room temperature and −196 °C at a range of high pressures for different types of chemically activated carbon. They discovered that hydrogen uptake capacity at room temperature was 1.2 wt.% at 200 bar and 2.7 wt.% at 500 bar. The author concluded that the hydrogen storage capacity relied on micro-pore characteristics (pore volume and PSD).[91] Jin *et al.* studied the hydrogen storage capacity of activated carbon from coconut shells, concluding that the maximum H_2 uptake at ambient temperature and 100 bar was just 0.85 wt.% with a surface area of 2800 m^2 g^{-1}.[90]

Cryogenic hydrogen storage.

Storing hydrogen in porous carbon materials at cryogenic temperatures is a promising technique. At room temperature, hydrogen uptake depends on micro-pore characteristics: pore size and PSD. Jorda-Beneyto *et al.* measured activated carbon adsorption capacities. At 20 MPa and 298 K, it was 1.2 wt.%, whereas at 50 MPa, it was 2.7 wt.%. On the other hand, the adsorption capacity at cryogenic temperatures was much higher: up to 5.6 wt.% at only 4 MPa. At high pressures (greater than 500 bar), the hydrogen uptake capacity decreases due to the interaction between the activated carbon surface and hydrogen molecules.[91]

Akasaka has also measured hydrogen uptakes at low temperatures. Activated carbon derived from coffee bean waste was investigated for hydrogen storage at cryogenic temperatures, and it was

found to give 4.0 wt.% at 40 bar. The hydrogen storage capacity of the coffee bean-derived activated carbons at 77 K was 69.6 mg cm^{-3}, whereas it was only 5.7 mg cm^{-3} at 298 K. There was a linear relationship between hydrogen storage and micropore volume.[33]

Mokaya *et al.,* report that the hydrogen uptake capacity of activated carbons at cryogenic temperatures follows a simple relationship: a higher surface area of activated carbon leads to higher hydrogen uptake. The hydrogen uptake capacity at cryogenic temperatures and 1 bar was between 1 and 3 wt.%, while at moderate pressures (10–100 bar) the H_2 uptake was between 2–7 wt.%.[94] Recently, Chilev and Lamari studied hydrogen uptake capacities at cryogenic temperatures and different pressures for automobile manufacturing applications. They observed the highest hydrogen adsorption at 293 K and 60 MPa (7.8 mmol g^{-1}), whereas at 77 K, the highest adsorption was at 3 MPa (25.95 mmol g^{-1}).[89]

1.7.2. CO_2 capture.

Greenhouse gas emission, especially carbon dioxide, has a significant negative impact on the atmosphere. Fossil fuel, synthetic fuel plants, fossil fuel-based hydrogen production plants, and natural gas (NG) production plants have contributed to the increasing CO_2 levels in the atmosphere. Carbon dioxide release is considered to be the main cause of global warming. The need to remove CO_2 from the atmosphere to a long-term storage location has become a key target. There has thus been extensive research into the design and manufacture of CO_2 capture and storage methods (CCS). The captured carbon dioxide can be stored in different ways, such as compression, transportation to the ocean, in geological formations, mineral carbonates, or for use in industrial processes. This section will present some examples of approaches to CO_2 capture using activated carbons.

Sevilla and Fuertes prepared activated carbon from polysaccharides (starch and cellulose) and biomass (sawdust) using KOH as activating agent. The preparation process was conducted using various activation conditions (4:1 KOH–precursor, or the milder 2:1 KOH–precursor) at temperatures of 600–800 °C. They observed that samples prepared using harsher conditions have a larger surface areas and wider pores compared to those prepared using milder activation conditions.[95] Plaza *et al.* prepared activated carbon from coffee grounds. Coffee grounds (from

single-use capsules) were chemically activated with KOH and physically with CO_2 in order to produce activated carbon for CO_2 capture. They observed that the obtained product from chemical activations demonstrate higher CO_2 uptakes than those obtained by physical activation. On the other hand, the physical activation process generated less pollution than the chemical process. The adsorption of CO_2 at 0 °C and 25 °C were as high as 4.8 mmol g^{-1} and 3.0 mmol g^{-1}, respectively. In addition, carbon dioxide uptake levels of up to 3.9 mmol g^{-1} were reported for activated carbon by Plaza *et al.* in 2013.[96] They prepared activated carbon from coconut shells, which were physically activated by pre-carbonization in nitrogen followed by CO_2 activation at 800 °C. At 760 mmHg and 25 °C, the highest carbon dioxide uptake was 3.9 mmol g^{-1}, while material with the same surface area gave values of 5.6 mmol g^{-1} at 0 °C.[6]

Wang *et al.*[97] studied the extent to which activated carbon fibres (ACFs) from natural silk fibres (SFs) as a starting material could be used for CO_2 capture. ACFs are a form of activated carbon that are considered to be one of the most promising technologies for hydrogen storage, CO_2 capture, and water treatment. The porous structure (N–SFs) was generated at a high temperature with chemical activation using KOH. Products with high surface areas (up to 3000 m^2 g^{-1}) and pore volumes (up to 1.38 cm^3 g^{-1}) were obtained. The authors observed that at 0 °C, N–ACFs demonstrated high CO_2 capture capacities (up to 7.0 mmol g^{-1}) whereas at 25 °C, the CO_2 capture capacity was only 4.8 mmol g^{-1}[97]. Recently, Al Abadi *et al.* prepared activated carbon with a high carbon dioxide adsorption capacity (up to 7.49 mmol g^{-1}). The starting materials were mixed gelatine and starch, and the carbon was chemically activated with KOH. At 25 °C, the adsorption capacity of CO_2 was 3.28–3.80 mmol g^{-1} while at 0 °C, it was 4.74–7.49 mmol g^{-1}. In addition, they observed that under similar experimental conditions, when gelatine and starch were activated individually, there were limitations on the improvements of surface areas and CO_2 capture capacity. This is in contrast to the case of the gelatine and starch mixture, which suggests that more interesting activated carbons might be obtainable with other mixtures.[12]

1.7.3. Methane storage

In 2007, it was stated that a quarter of global greenhouse gas emissions were generated by transportation activities. This source of U.S. greenhouse gas emissions demonstrates the highest

rate of growth.[98] The demand for alternative fuels is higher than it has ever been before. With abundant supplies and a low emission factor, methane is an obvious option as a petroleum substitute in automobiles and other mobile applications. Natural gas (NG) largely consists of methane (>95 percent),[99] with ethane and heavier hydrocarbons, nitrogen, and carbon dioxide making up the remaining components. Due to its critical temperature of 191 K, methane must be compressed and chilled in order to become a liquid (-82°C). Methane is abundant in nature; nevertheless, the absence of effective storage systems has hindered its widespread use in automobiles. The two major techniques of NG storage are the following: (1) liquefaction at low temperature and (2) compression to 200–300 bar at ambient temperatures.[99–102]

Porous adsorbents have been proposed as a safer, simpler, and possibly more cost-effective way to store NG at ambient temperatures and moderate pressures (about 35 bar) in the form of adsorbed NG (ANG).[43] Numerous porous materials, including aluminosilicate, zeolites,[103–105] carbon,[106], activated carbon,[20,107–109] carbon nanotubes,[110] and MOFs[102,111–113] have been investigated as adsorbents, and some are now used in the industry.

There are currently no effective storage techniques available to accomplish widespread methane use in the automobile sector. Advanced porous materials, metal–organic frameworks, and POPs have garnered substantial attention because of their extraordinarily large surface areas and chemically-tuneable architectures. Recent improvements in NG-adsorbing, high-surface-area materials have showed promise in improving the density of NG under mild circumstances in the form of ANG. This represents a substantial possibility for the development of tiny, lightweight, and high-capacity tanks for vehicular applications. Activated carbons are among these materials. Due to methane's non-polar molecular structure, its adsorption is predominantly governed by physical adsorption. Methane adsorption is non-specific, and there was no chemical reaction. As methane gas passes through a porous space, the gas's energy is progressively lost and retained within the AC pore networks. The physical bond of the van der Waals force, which exists between the molecules of methane gas and the ACs surface defect, holds the methane molecules together. As methane gas passes through the surface defects of ACs, it is rapidly adsorbed into the carbon network to form a monolayer or multilayer structure on the adsorbate surface (ACs).

For better understanding and prediction of methane storage, it is necessary consider three factor that affect the efficiency of methane storage which are: the ACs surface area, pore volume, pore size, and backing density.

1- Surface area:

In general, increased surface area is associated with enhanced gravimetric absorption. In addition, the lack of a strong correlation between gravimetric surface area and volumetric capacity diminishes its utility as a variable for CH_4 storage. Consequently, metrics such as packaging density and volumetric surface area are frequently cited in lieu of or in addition to the conventional gravimetric value.

2- Pore capacity:

Considering that pore volume is generally proportional to surface area, an increase in pore volume is typically accompanied by an increase in gas adsorption capacity. Obviously, the intensity of the relationship between pore volume and surface area is affected by the size of the pores in question; an ultramicropore with the same surface area will contribute significantly less pore volume. If a sample is predominantly microporous and has a high total pore volume, this indicates that the sample contains a large number of or very deep micropores. This sample is advantageous for the adsorption of small molecules, particularly at reduced pressures. Therefore, (percentage) micropore volume rather than total pore volume is likely a more accurate indicator of CH_4 uptake. For effective methane storage at moderate-to-high pressures (35–100 bar), a porous material must be predominately microporous with a high surface area and low mesoporosity. A high microporous volume is required to achieve strong adsorption of methane molecules, yet a certain amount of mesoporosity is necessary for effective sorption kinetics. In addition, pore channels ranging in size from 0.8–1.5 nm are optimally suited for the adsorption of two or three methane molecules by optimising the packing of the adsorbed phase within the pores. Additionally, it has been hypothesised that pore channels of 1.1 nm are optimal for methane storage.[92,98,114–117]

3- Packing density:

While gravimetric measures of porosity have traditionally been associated with gas absorption, applications such as methane storage require a high volumetric capacity. Numerous studies have demonstrated that particle density is a good predictor of H_2, CH_4 and CO_2 capacity, so long as it is balanced with an adequate pore size, a high surface area, and a high pore volume.

Some of the best-performing porous carbons for volumetric methane storage at 25°C and 35 bar include mesophase-pitch-derived activated carbons, LMA738 and DO00-3:1_700, that store 142 and 160 cm^3 (STP) cm^{-3} methane[118] respectively; zeolite templated carbons, ZTC (BEA-ZTC) and thermally treated BEA-ZTC (BEA-ZTC-873), that store 125 and 145 cm^3 (STP) cm^{-3} methane[119] respectively; and biomass-derived activated carbon, ACDS4700, that store 196 cm^3 (STP) cm^{-3} of excess methane.[43]

This thesis aims to investigate activated carbon synthesis protocols in order to tailor the porosity of the resulting carbons to meet gas capture and energy storage applications, such as for CO_2 capture and CH_4 storage. Many carbon precursors were utilised to create activated carbons with various chemical compositions, forms, and porosities. In addition, it discusses the possibility of minimising preparation steps, costs, energy consumption, and the replacement of corrosive chemicals with mild ones.

The main points of this work are as follows:

1. Study the preparation of chemically activated carbon using mild activating agent potassium oxalate (PO) and polypyrrole (PPY) as the carbon precursor. It explores the effect of compaction on the carbon-activation process and the resulting carbon's porosity and textural properties. It demonstrates how porosity can be adjusted to achieve extraordinary levels of moderate-to-high pressure methane and CO_2 adsorption (both in terms of gravimetric and volumetric capacity).
2. Construct 3D hierarchical carbon nanocages (hCNCs) with a large surface area, network geometry, and coexisting micro-, meso-, and macro-pores. Methods are developed to attain the target of having pore volume > 4.0 cm^3/g, to provide a high storage capacity for CO_2 and methane at high pressure. The impact of chemical activation of the resulting templated carbons is also investigated. Furthermore, purity,

thermal stability, textural characteristics, structural shape, and CO_2/CH_4 uptake capabilities areall measured using a variety of analytical techniques.

3. prepare activated carbon Using biomass (prickly pears peel PPPS), the porosity created in carbonised biomass as a function of the activation parameters is presented, specifically the KOH/carbon ratio and temperature. The porosity of the resultant carbons prompted the researchers to investigate their use as CO_2 and CH_4 storage materials. Comparisons of the carbonisation of char at different temperatures from 350°C-600°C are also presented for context.
4. Develop the preparation of ACC, this development involves minimisation of energy consumption, chemicals, and a few preparatory steps. In addition, it proposes a novel method that eliminates the process of stabilising; a crucial step that has been conducted in prior work to preserve the flexibility of activated carbon fabric.

1.8. References

1 N. F. Attia, M. Jung, J. Park, H. Jang, K. Lee and H. Oh, *Chemical Engineering Journal*, 2020, **379**, 122367.

2 N. Balahmar, A. S. Al-Jumialy and R. Mokaya, *J Mater Chem A Mater*, 2017, **5**, 12330–12339.

3 A. M. Aljumialy and R. Mokaya, *Mater Adv*, 2020, **1**, 3267–3280.

4 E. Haffner-Staton, N. Balahmar and R. Mokaya, *J Mater Chem A Mater*, 2016, **4**, 13324–13335.

5 M. Sevilla, A. S. M. Al-Jumialy, A. B. Fuertes and R. Mokaya, *ACS Appl Mater Interfaces*, 2018, **10**, 1623–1633.

6 A. S. Ello, L. K. C. de Souza, A. Trokourey and M. Jaroniec, *Microporous and Mesoporous Materials*, 2013, **180**, 280–283.

7 M. Sevilla, P. Valle-Vigõn and A. B. Fuertes, *Adv Funct Mater*, 2011, **21**, 2781–2787.

8 B. Adeniran and R. Mokaya, *Chemistry of Materials*, 2016, **28**, 994–1001.

9 M. Sevilla, J. B. Parra and A. B. Fuertes, *ACS Appl Mater Interfaces*, 2013, **5**, 6360–6368.

10 H. M. Coromina, D. A. Walsh and R. Mokaya, *J Mater Chem A Mater*, 2015, **4**, 280–289.

11 J. Wang, P. Nie, B. Ding, S. Dong, X. Hao, H. Dou and X. Zhang, *J Mater Chem A Mater*, 2017, **5**, 2411–2428.

12 A. Alabadi, S. Razzaque, Y. Yang, S. Chen and B. Tan, *Chemical Engineering Journal*, 2015, **281**, 606–612.

13 A. G. Dumanlı and A. H. Windle, *J Mater Sci*, 2012, **47**, 4236–4250.

14 J. M. V. Nabais, P. J. M. Carrott, M. M. L. R. Carrott and J. A. Menéndez, in *Carbon*, 2004, **42**, 1315–1320.

15 A. C. Pastor, F. Rodrıguez-Reinoso, H. Marsh and M. A. Martınez, *Carbon*, 1999, **37**, 1275-1283.

16 G. Rodríguez-Blanco, L. Giraldo and J. C. Moreno-Piraján, *Appl Surf Sci*, 2010, **256**, 5221–5225.

17 B. Babic, S. Milonjic, M. Polovina and B. v Kaludierovič Kaludierovič, *Carbon*, 1999, **37**, 477–481.

18 ´ A Huidobro, A. C. Pastor, F. Rodrıguez- and R. Reinosó, *Carbon*, 2001, **39**, 389-398.

19 N. Kostoglou, C. Koczwara, C. Prehal, V. Terziyska, B. Babic, B. Matovic, G. Constantinides, C. Tampaxis, G. Charalambopoulou, T. Steriotis, S. Hinder, M. Baker, K. Polychronopoulou, C. Doumanidis, O. Paris, C. Mitterer and C. Rebholz, *Nano Energy*, 2017, **40**, 49–64.

20 Y. Wang, C. Ercan, A. Khawajah and R. Othman, *AIChE Journal*, 2012, **58**, 782–788.

21 H. Wei, S. Deng, B. Hu, Z. Chen, B. Wang, J. Huang and G. Yu, *ChemSusChem*, 2012, **5**, 2354–2360.

22 J. M. Andrésen, Y. Zhang, C. E. Burgess and H. H. Schobert, *Fuel Processing Technology*, 2004, **85**, 1361–1372.

23 R. Azargohar and A. K. Dalai, *Appl Biochem Biotechnol*, 2006, **131**, 762-73.

24 K. Y. Foo and B. H. Hameed, *Adv Colloid Interface Sci*, 2009, **152**, 39–47.

25 P. A. Brown, S. A. Gill and S. J. Allen, *Water research, 2000*, **34**, 3907-3916.

26 J. M. Dias, M. C. M. Alvim-Ferraz, M. F. Almeida, J. Rivera-Utrilla and M. Sánchez-Polo, *J Environ Manage*, 2007, **85**, 833–846.

27 A. R. Mohamed, M. Mohammadi and G. N. Darzi, *Renewable and Sustainable Energy Reviews*, 2010, **14**, 1591–1599.

28 O. Ioannidou and A. Zabaniotou, *Renewable and Sustainable Energy Reviews*, 2007, **11**, 1966–2005.

29 N. Bagheri and J. Abedi, *Chemical Engineering Research and Design*, 2009, **87**, 1059–1064.

30 T. Ramesh, N. Rajalakshmi and K. S. Dhathathreyan, *J Energy Storage*, 2015, **4**, 89–95.

31 Y. J. Heo and S. J. Park, *Journal of Industrial and Engineering Chemistry*, 2015, **31**, 330–334.

32 A. Gałuszka, Z. Migaszewski and J. Namieśnik, *TrAC - Trends in Analytical Chemistry*, 2013, **50**, 78–84.

33 H. Akasaka, T. Takahata, I. Toda, H. Ono, S. Ohshio, S. Himeno, T. Kokubu and H. Saitoh, *Int J Hydrogen Energy*, 2011, **36**, 580–585.

34 E. A. Hirst, A. Taylor and R. Mokaya, *J Mater Chem A Mater*, 2018, **6**, 12393–12403.

35 M. M. Titirici and M. Antonietti, *Chem Soc Rev*, 2010, **39**, 103–116.

36 S. Sahu, B. Behera, T. K. Maiti and S. Mohapatra, *Chemical Communications*, 2012, **48**, 8835–8837.

37 H. Wang, J. Deng, Y. Chen, F. Xu, Z. Wei and Y. Wang, *Nano Res*, 2016, **9**, 2672–2680.

38 Q. Wang, H. Li, L. Chen and X. Huang, *Solid State Ionics*, 2002, **152**, 43-50.

39 M. M. Titirici, A. Thomas, S. H. Yu, J. O. Müller and M. Antonietti, *Chemistry of Materials*, 2007, **19**, 4205–4212.

40 T. Rogalinski, T. Ingram and G. Brunner, *Journal of Supercritical Fluids*, 2008, **47**, 54–63.

41 H. Pińkowska, P. Wolak and A. Złocińska, *Biomass Bioenergy*, 2011, **35**, 3902–3912.

42 Y. Liu, S. Ma and J. Chen, *J Clean Prod*, 2018, **176**, 187–195.

43 A. Altwala and R. Mokaya, *Energy Environ Sci*, 2020, **13**, 2967–2978.

44 Z. Wei, M. Zhou, H. Qiao, L. Zhu, H. Yang and T. Xia, *J Nanomaterial*, 2009, DOI:10.1155/2009/968058.

45 E. M. Johansson, J. M. Córdoba and M. Odén, *Microporous and Mesoporous Materials*, 2010, **133**, 66–74.

46 M. Inagaki, M. Toyoda, Y. Soneda, S. Tsujimura and T. Morishita, *Carbon N Y*, 2016, **107**, 448–473.

47 K. Nielsch, J. Choi, K. Schwirn, R. B. Wehrspohn and U. Gösele, *Nano Lett*, 2002, **2**, 1–4.

48 H. Tamon, H. Ishizaka, T. Yamamoto and T. Suzuki, *Carbon N Y*, 1999, **37**, 2049–2055.

49 W. Zhao, X. Lin, H. Cai, T. Mu and X. Luo, 2017, **56**, 12745–12754.

50 B. Huang, L. Peng, F. Yang, Y. Liu and Z. Xie, *Journal of Energy Chemistry*, 2017, **26**, 712–718.

51 B. Adeniran and R. Mokaya, *Nano Energy*, 2015, **16**, 173–185.

52 A. Oya, S. Yoshida, J. Alcaniz-Monge and A. Linares-Solano, *Carbon N Y*, 1995, **33**, 1085–1090.

53 J. Ozaki, N. Endo, W. Ohizumi, K. Igarashi, M. Nakahara, A. Oya, S. Yoshida and T. Iizuka, *Carbon N Y*, 1997, **35**, 1031–1033.

54 H. Tamon, H. Ishizaka, T. Araki and M. Okazaki, *Carbon N Y*, 1998, **36**, 1257–1262.

55 Z. Li and M. Jaroniec, *J Am Chem Soc*, 2001, **123**, 9208–9209.

56 A. B. Fuertes, *J Mater Chem*, 2003, **13**, 3085–3088.

57 V. Malgras, Q. Ji, Y. Kamachi, T. Mori, F. K. Shieh, K. C. W. Wu, K. Ariga and Y. Yamauchi, *Bull Chem Soc Jpn*, 2015, **88**, 1171–1200.

58 T. Morishita, K. Ishihara, M. Kato and M. Inagaki, *Carbon N Y*, 2007, **45**, 209–211.

59 Z. Lyu, D. Xu, L. Yang, R. Che, R. Feng, J. Zhao, Y. Li, Q. Wu, X. Wang and Z. Hu, *Nano Energy*, 2015, **12**, 657–665.

60 J. Lee, J. Kim and T. Hyeon, *Advanced Materials*, 2006, **18**, 2073–2094.

61 Y. Wan, Y. Shi and D. Zhao, *Chem. Commun., 2007, **9**, 897-926.*

62 Y. Wan, H. Yang and D. Zhao, *Acc Chem Res*, 2006, **39**, 423–432.

63 ´ A Huidobro, A. C. Pastor, F. Rodrıguez- and R. Reinosó, *Carbon*, 2001, **39**, 389-398.

64 P. T. Williams and A. R. Reed, *J Anal Appl Pyrolysis*, 2004, **71**, 971–986.

65 F. Suárez-García, A. Martínez-Alonso and J. M. D. Tascón, *Carbon N Y*, 2004, **42**, 1419–1426.

66 X. Huang, *Materials*, 2009, **2**, 2369–2403.

67 Y. Gogotsi, C. Portet, S. Osswald, J. M. Simmons, T. Yildirim, G. Laudisio and J. E. Fischer, *Int J Hydrogen Energy*, 2009, **34**, 6314–6319.

68 M. Sevilla, N. Alam and R. Mokaya, *Journal of Physical Chemistry C*, 2010, **114**, 11314–11319.

69 E. A. Dawson, G. M. B. Parkes, P. A. Barnes and M. J. Chinn, *Carbon*, 2003, **41,** 571-578.

70 M. Molina-Sabio and F. Rodríguez-Reinoso, in *Colloids and Surfaces A: Physicochemical and Engineering Aspects*, 2004, **241**, 15–25.

71 Y. Nakagawa, M. Molina-Sabio and F. Rodríguez-Reinoso, *Microporous and Mesoporous Materials*, 2007, **103**, 29–34.

72 M. Jagtoyen and F. Derbyshire, *Carbon, 1998, **36**, 1085-1097.*

73 M. A. Lillo-Ródenas, J. Juan-Juan, D. Cazorla-Amorós and A. Linares-Solano, *Carbon*, Elsevier Ltd, 2004, **42**, 1371–1375.

74 M. Lillo-Rodenas, D. Cazorla-Amoros and A. Linares-Solanó, *Carbon*, 2003, **41,** 267-275.

75 H. Teng and L.-Y. Hsu, *Ind. Eng. Chem. Res*. 1999, **38**, 2947–2953

76 M. G. Nijkamp, J. E. M. J. Raaymakers, A. J. van Dillen and K. P. de Jong, *Appl Phys A Mater Sci Process*, 2001, **72**, 619–623.

77 M. Sevilla and A. B. Fuertes, *J Mater Chem A Mater*, 2013, **1**, 13738–13741.

78 C. Nieto-Delgado, M. Terrones and J. R. Rangel-Mendez, *Biomass Bioenergy*, 2011, **35**, 103–112.

79 A. Ahmadpour and D. D. Do, *Carbon N Y*, 1997, **35**, 1723–1732.

80 P. T. Anastas, L. B. Bartlett, M. M. Kirchhoff and T. C. Williamson, *Catal Today*, 2000, **55,** 11-22.

81 B. Feng and S. K. Bhatia, *Carbon*, 2003, **41,** 507-523.

82 J. Gañán, J. F. González, C. M. González-García, A. Ramiro, E. Sabio and S. Román, *Appl Surf Sci*, 2006, **252**, 5988–5992.

83 S. Osswald, C. Portet, Y. Gogotsi, G. Laudisio, J. P. Singer, J. E. Fischer, V. v. Sokolov, J. A. Kukushkina and A. E. Kravchik, *J Solid State Chem*, 2009, **182**, 1733–1741.

84 J. A. Menendez, E. M. Menendez, M. J. Iglesias, A. Garcıa and J. J. Pis´instituto, *Carbon*, 1999, **37,** 115-1121.

85 E. Yagmur, M. Ozmak and Z. Aktas, *Fuel*, 2008, **87**, 3278–3285.

86 J. Guo and A. C. Lua, *Carbon*, 2000, **38,** 1985-1993.

87 Z. Hu, H. Guo, M. P. Srinivasan and N. Yaming, *Separation and Purification Technology*, 2003, **31**, 47-52.

88 A. Arami-Niya, W. M. A. W. Daud and F. S. Mjalli, *Chemical Engineering Research and Design*, 2011, **89**, 657–664.

89 C. Chilev and F. D. Lamari, *Int J Hydrogen Energy*, 2016, **41**, 1744–1758.

90 H. Jin, Y. S. Lee and I. Hong, *Catal Today*, 2007, **120**, 399–406.

91 M. Jordá-Beneyto, F. Suárez-García, D. Lozano-Castelló, D. Cazorla-Amorós and A. Linares-Solano, *Carbon N Y*, 2007, **45**, 293–303.

92 D. Lozano-Castelló, J. Alcañiz-Monge, M. A. de La CasaLillo, D. Cazorla-Amorós and A. Linares-Solano, *Fuel*, 2002, **81**, 1777-1803.

93 R. Gadiou, S. E. Saadallah, T. Piquero, P. David, J. Parmentier and C. Vix-Guterl, *Microporous and Mesoporous Materials*, 2005, **79**, 121–128.

94 M. Sevilla and R. Mokaya, *Energy Environ Sci*, 2014, **7**, 1250–1280.

95 M. Sevilla, A. B. Fuertes and R. Mokaya, *Energy Environ Sci*, 2011, **4**, 1400–1410.

96 M. G. Plaza, A. S. González, C. Pevida, J. J. Pis and F. Rubiera, *Appl Energy*, 2012, **99**, 272–279.

97 P. Wang, J. Lang, S. Xu and X. Wang, *Mater Lett*, 2015, **152**, 145–147.

98 T. A. Makal, J. R. Li, W. Lu and H. C. Zhou, *Chem Soc Rev*, 2012, **41**, 7761–7779.

99 V. C. Menon and S. Komarneni, *Journal of Porous Materials,* 1997, **5**, 43–58.

100 H. Furukawa and O. M. Yaghi, *J Am Chem Soc*, 2009, **131**, 8875–8883.

101 T. Düren, L. Sarkisov, O. M. Yaghi and R. Q. Snurr, *Langmuir*, 2004, **20**, 2683–2689.

102 S. Ma, D. Sun, J. M. Simmons, C. D. Collier, D. Yuan and H. C. Zhou, *J Am Chem Soc*, 2008, **130**, 1012–1016.

103 K. Berlier, M.-G. Olivier and R. Jadot, *J. Chem. Eng. Data*, 1995, **40,** 1206–1208.

104 R. Babarao and J. Jiang, *J Am Chem Soc*, 2009, **131**, 11417–11425.

105 M. Kishima, H. Mizuhata and T. Okubo, *Journal of Physical Chemistry B*, 2006, **110**, 13889–13896.

106 C. Guan, L. S. Loo, K. Wang and C. Yang, *Energy Convers Manag*, 2011, **52**, 1258–1262.

107 X. D. Dai, X. M. Liu, G. Zhao, L. Qian, K. Qiao and Z. F. Yan, *Asia-Pacific Journal of Chemical Engineering*, 2008, **3**, 292–297.

108 L. Giraldo and J. C. Moreno-Piraján, *Adsorption Science & Technology*, 2009, **27,** 255-265.

109 J. A. F. Macdonald and D. F. Quinn, *Carbon*, 1996, **34**, 1103-1108.

110 J. W. Lee, H. C. Kang, W. G. Shim, C. Kim and H. Moon, *J Chem Eng Data*, 2006, **51**, 963–967.

111 Y. He, W. Zhou, G. Qian and B. Chen, *Chem Soc Rev*, 2014, **43**, 5657–5678.

112 B. Li, H. M. Wen, W. Zhou, J. Q. Xu and B. Chen, *Chem*, 2016, **1**, 557–580.

113 Y. Peng, V. Krungleviciute, I. Eryazici, J. T. Hupp, O. K. Farha and T. Yildirim, *J Am Chem Soc*, 2013, **135**, 11887–11894.

114 L. S. Blankenship and R. Mokaya, *Mater Adv*, 2022, **3**, 1905–1930.

115 J. Romanos, S. Sweany, T. Rash, L. Firlej, B. Kuchta, J. C. Idrobo and P. Pfeifer, *Adsorption Science & Technology*, 2014, **32**, 681-691.

116 C. Guan, L. S. Loo, K. Wang and C. Yang, *Energy Convers Manag*, 2011, **52**, 1258–1262.

117 D. A. Gómez-Gualdrón, C. E. Wilmer, O. K. Farha, J. T. Hupp and R. Q. Snurr, *Journal of Physical Chemistry C*, 2014, **118**, 6941–6951.

118 M. E. Casco, M. Martínez-Escandell, K. Kaneko, J. Silvestre-Albero and F. Rodríguez-Reinoso, *Carbon N Y*, 2015, **93**, 11–21.

119 S. Choi, M. A. Alkhabbaz, Y. Wang, R. M. Othman and M. Choi, *Carbon N Y*, 2019, **141**, 143–153.

2. Porous material characterization and analytical techniques.

Due to their ability to adsorb substances, porous materials have been extensively used in adsorption, phase separation techniques, and catalysis. Pore structure and the management of solids' porosity are crucial considerations in the design of an adsorbent application since the characteristics of porous materials are directly related to their pores. Numerous experimental techniques for characterising porous materials have been developed as a result of the complexity and variety of these materials. Gas adsorption measurements are frequently employed to determine textural parameters such as surface area, pore volume, and pore size distribution of various porous solids, even though several experimental approaches have been presented for the characterisation of porous materials. Other characterisation techniques, like as powder X-ray diffraction, elemental analysis, and thermalgravimetric analysis, are frequently needed to obtain the data needed to pinpoint the precise nature of porous materials.

2.1. Thermogravimetric Analysis (TGA).

Thermogravimetric analysis TGA is used to monitor how the mass of a substance changes with temperature fluctuations as a function of time. The operating principle works as follows: the sample is heated to very high temperatures ≥ 1000°C under air flow. During the heat treatment, several reactions can occur such as dehydration, desorption and oxidation. The TGA curve is plotted as weight change versus either temperature or time as shown in Fig.1.

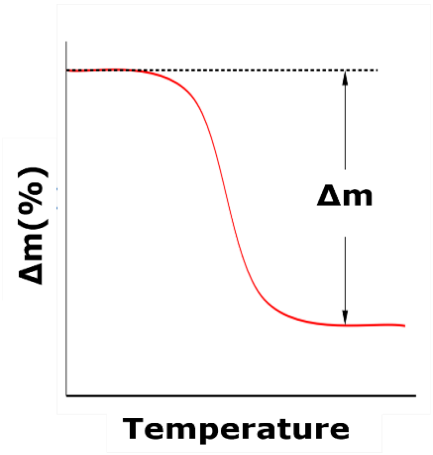


Figure 1: The typical thermogravimetric measurement (relative weight change vs. temperature).

It important to mention that TGA run consistency is affected by several factors, including the instrument, sample preparation, and experimental conditions. Firstly, The TGA instrument's quality and calibration can have a considerable impact on the reproducibility of TGA operations. To achieve accurate and consistent measurements, the equipment must be calibrated properly and maintained on a regular basis. Secondly, the quality and uniformity of sample preparation affects the reproducibility of TGA runs. To produce consistent findings, careful sample preparation is required, including uniform particle size and sample mass. And finally, the repeatability of TGA runs can be influenced by experimental settings such as heating rate, atmosphere, and experiment duration. To guarantee that the results are reproducible, these parameters should be properly controlled and documented. To increase the repeatability of TGA runs, it is advised that standard operating procedures (SOPs) be followed and that many runs be performed for each sample to verify uniformity. The comparison of results from numerous runs can assist uncover causes of variability and enhance data reliability. Furthermore, appropriate statistical methods must be used to analyse the data and report the uncertainty associated with the measurements. In conclusion, repeatability is a key factor to consider in TGA analysis, and it can be increased by paying close attention to instrument calibration, sample preparation, experimental conditions, and data processing.

The main aim of it in this thesis, to evaluate purity by comparing the initial and final masses of a carbon sample after burning it off in air. In addition, TGA provide other information such as thermal stability of a sample, the percentage of inorganic and organic material in the sample, temperature of degradation and adsorbed moisture content. The weight of the sample is calculated from the change in the mass as it is heated or cooled in the furnace. In case of this project when the temperature inside the furnace reaches 1000 °C, the remaining carbon weight should be 0%, however, if the remaining carbon weight is above 0%, it is inferred that there are other materials that burn off at temperatures higher than 1000°C, such as alkaline activating agents or metal catalysts.

Usually, the TGA instrument consists of four major components: the sample and either the container or holder that carries the sample, the sensors that either measure the temperature or detect a particular property of the sample, an enclosure, in which the parameters of the experiment are controlled (e.g., pressure and gas atmosphere) and the computer programme, which controls the parameters of the experiment (temperature programme) and collects data from the sensors.[1]

In this work, Thermal Gravimetric Analysis (TGA) was performed for the majority of samples using an SDT Q600 TGA analyser (from room temperature to up to 1000 °C at a heating ramp rate of 10°C min^{-1} in an air environment). The acquired data was converted with TA Instruments' Universal Analysis software. Approximately 5 mg of the sample were placed in an alumina pan, which was sitting on a vibrating balance with a sensitivity of 0.1 mg that was contained within a furnace.

2.2. Elemental Analysis (CHN).

There are various approaches for determining CHNS. It provides a new degree of precision, accuracy, analytical speed, and ease of use. The built-in chromatographic column transforms and elutes the chemical into NO_2, CO_2, SO_2, H_2O, which is subsequently detected by the Thermal Conductivity Detector.

The elemental analyser has fundamental components are autosampler, combustion reactors, chromatography column, and the thermal conductivity detector TCD. The TCD, also known as a katharometer, is a chemical specific detector and a bulk property detector that is extensively used in gas chromatography. This detector detects changes in the thermal conductivity of the column eluent and compares it to a carrier gas reference flow. Because most compounds have much lower thermal conductivities than the common carrier gases helium or hydrogen, when an analyte elutes from the column, the effluent thermal conductivity is reduced, and a detectable signal is produced.

A model CE-440 elemental analyser was used for elemental microanalysis for C, H, N content. The method uses thermal conductivity detection to measure carbon, hydrogen and nitrogen after combustion and reduction. Combustion of the weighed sample occurs in a high temperature

furnace (975°C) under pure oxygen gas, and then the combustion gas is released to each pair of thermal conductivity detection cells (sample and trap cell) to measure C, H and N content. The differential signal read of samples before and after the traps reflects the C, H and N content (%). However, the O% can be calculated as O%= 100%- (C%+ H%+ N%). And the atomic ratio of any elements (i.e., O/C) can be calculated by divide the average atomic mass by the reference standard.

The schematic of elemental analyser is shown below.

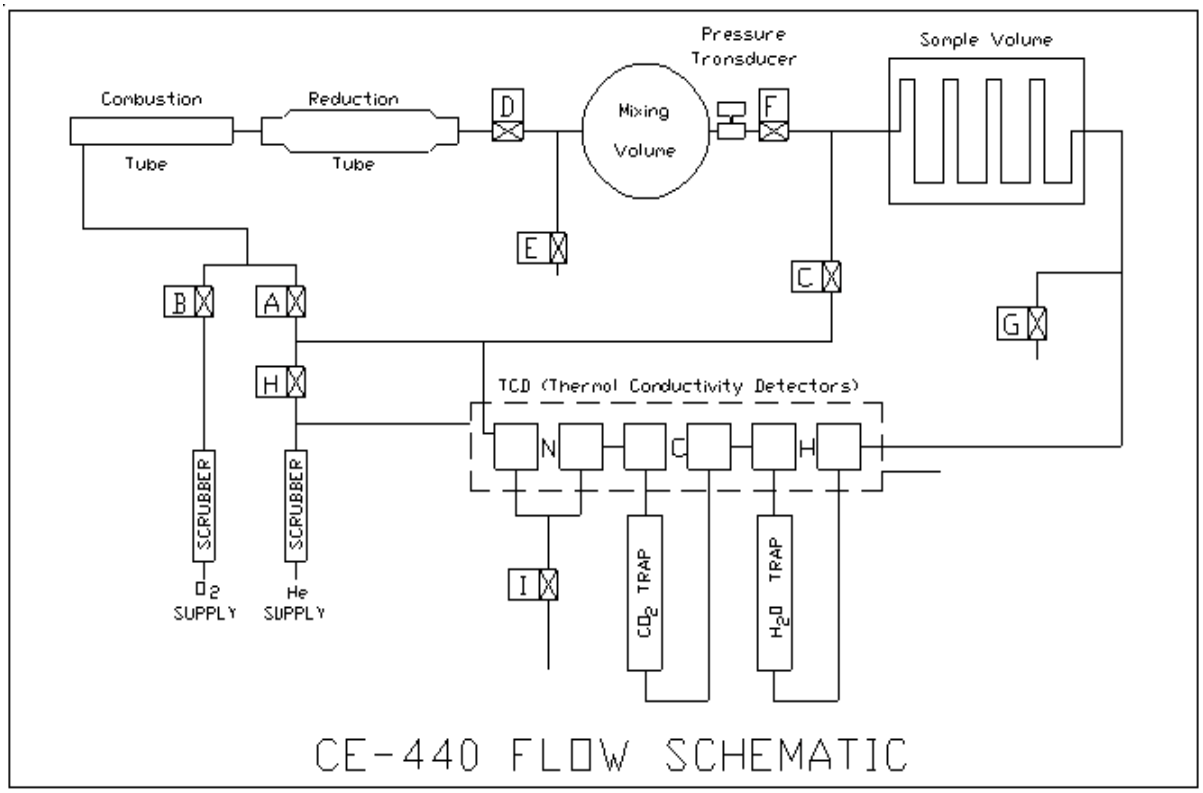


Figure 2: Schematic of elemental analyser for C, H and N measurement.

2.3. Scanning Electron Microscopy (SEM).

An SEM can provide three-dimensional images with a resolution down to 5 nm, which give information on particle morphology (particle size and surface texture), ordering at the nanoscale, by accelerating a fine electron beam onto the material within a vacuum, specifically by scanning

across the sample using scan coils (Fig. 5). As a result, the sample atoms are interacting with the incident beam and producing detectable signals. The magnitude of these reflected signals is used to build an image of the sample. In a non-conducting sample, the surface is coated with conducting material (usually gold) to prevent the build-up of surface charge.

SEM is different from other microscopes because it can use a thick specimen and produce its image. The generated secondary electrons (SE), backscattered electrons (BSE) and Xray photons (as shown in Fig. 3 below) are collected by dedicated detectors. By utilising their signals, an intensity map is constructed on the screen, which is the microscopic image.

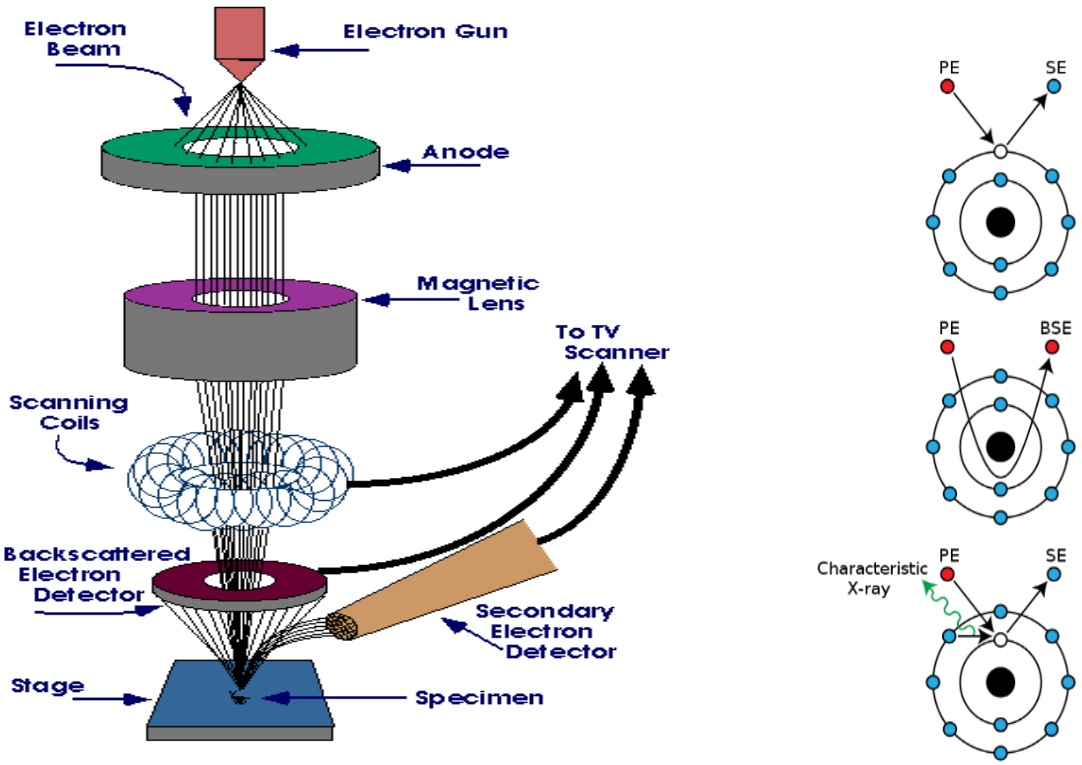


Figure 3: Mechanisms of emission of secondary electrons (SE), backscattered electrons (BSE), and characteristic X-rays from atoms of the sample.

Secondary electrons signal (10 eV- 50 eV) is widely used in scanning electron microscopy. Due to their low energy, only the secondary electrons near the surface «10 nm) can exit from the

specimen making it possible to investigate the topography of the surface features of the sample. In this project, the images were recorded using a Scanning Electron Microscopy JEOL 7100F FEG-SEM, which was operating with a 5 kV accelerating voltage.

2.4. Powder X-ray Diffraction (P-XRD).

Powder XRD is considered an effective analytical technique for determining crystalline structures. It can also provide information on the conformation of known structures and identify and characterise unknown crystalline materials. The X-ray radiation is characterised by its wavelength (λ), which is related to energy according to equation 1.

$$E = h\nu = \frac{c}{\lambda} \qquad \textit{Equation 1}$$

In an X-ray diffraction experiment, two light beams (beam 1 and beam 2) with the same wavelength travelling in the same direction can either boost or eliminate each other, depending on their phase difference (nλ, where n is an integer). X-ray beams incident will be directed into a material and diffracted by the crystal planes (A and B) as shown in Fig.4.

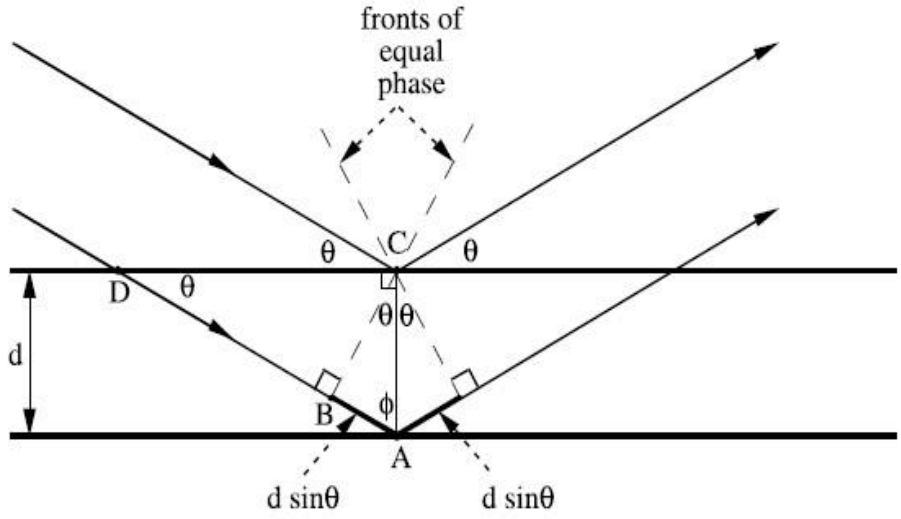


Figure 4. Geometry for interference of a wave scattered from two planes separated by interplanar spacing, d.[2]

The diffracted beams can be in phase as described by Bragg's law, which combines a measurement of the lattice of the crystal structure; the distance d between lattice planes, the wavelength λ of the X-rays radiation and the diffraction angle θ.[2]

$$n\lambda = 2d\,sin\,\theta \qquad \textit{Equation 2}$$

Where n = 1, 2, 3 … is a positive integer, θ is the diffraction angle (Bragg's angle), d is the interlayer spacing distance (lattice distance) and λ is the X-ray's wavelength. Two possible processes can occur: absorbing and scattering. Some of the X-rays will diffract and so contribute to diffraction beams, whereas others will be absorbed. The diffracted beams are used to provide a three-dimensional picture that allows the crystalline structure to be inferred.[3]

By measuring the geometry of the diffraction, information can be gained on crystalline plane orientation of the materials and by further investigating the intensity distribution of the reflection, information on positions of the atoms can be obtained.

Two X-ray beams with the same wavelength and traveling in the same direction can either reinforce or cancel each other, depending on their phase difference. Constructive interference happens when they are in phase whereas destructive interference occurs when they are out of phase, as shown in Fig. 5 below.

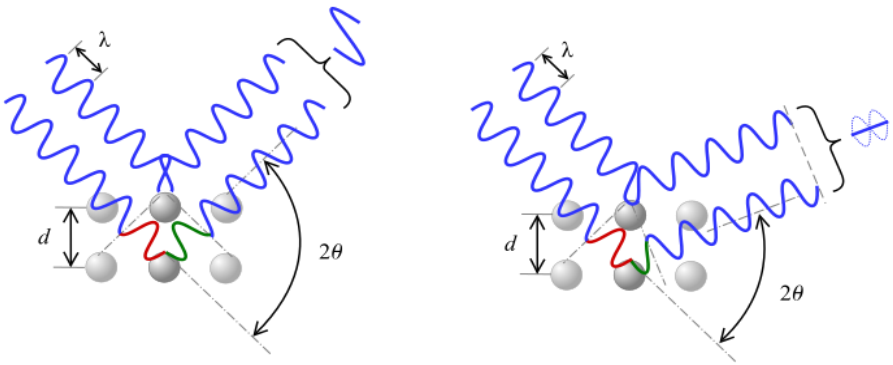


Figure 5. The 2θ deviation, the phase shift causes constructive (left figure) or destructive (right figure) interferences.

There is a strong relationship between the incident beams and atomic arrangements that give rise to diffraction patterns due to the ordered arrangement of the materials. Crystalline structures with long repeat distances show diffraction at small angles, whereas short repeat distances lead to the diffraction at high angles. Materials that comprise of precise atomic arrangement have sharp and clear diffraction peaks, whereas imperfect crystals cause broad and weak peaks. A diffraction pattern corresponds to a different interplanar spacing, d. For cubic crystal with lattice parameter α_o, interplanar spacing is denoted as d_{hkl}:

$$d_{hkl} = \frac{a_o}{\sqrt{h^2+K^2+l^2}} \quad \textit{Equation3}$$

From Bragg's law, the (hkl) diffraction presents at the angle $2\theta_h kl$:

$$2\theta_{hkl} = 2\,arcsin\left(\frac{\lambda\sqrt{h^2+k^2+l^2}}{2a_o}\right) \quad \textit{Equation4}$$

Recently, XRD became very important analytical technique which takes place on both qualitative and quantitative analyses because of significant improvement in instrumentation itself which allows solving and identifying complex structures and identifying components within the materials as specific compounds.[4]

In this work, Powder X-Ray diffraction (P-XRD) was performed to determine whether amorphous materials had been made and their level of graphitisation, if any. This was performed using a PAN analytical X'Pet Pro diffractometer utilising CuKα radiation (λ=1.5418 Å). Data was collected between 2θ = 2 - 80°.

2.5. Physisorption of gas by porous material.

Adsorption is typically defined as a rise in one or more components on surfaces, or an excess of molecules at the solid surface relative to a bulk gas or vapour phase. Adsorption, which distinguishes itself from absorption, in which gas molecules enter the material, was proposed as a name to describe both processes. Adsorbate is the term used to describe a substance, such as

gases or vapours, that has been adsorbed. Desorption, which is the opposite of adsorption in direction, is the process by which the amount adsorbed is reduced. Condensation of a gas or vapour without the formation of a chemical bond is caused by the physisorption process. It typically happens when temperature and pressure are rising.[5]

The porosity of materials has been extensively studied by adsorbing gases onto their surfaces. Typical experiments study N_2 adsorption at 77K, and 1 atm is the optimal adsorbate pressure for calculating the surface area and pore size distribution. Adsorption isotherms should be plotted as the amount of material adsorbed vs the relative pressure p/p_0 at constant temperature. This process is very dependent on the nature of the pore width, as this impacts the pores' accessibility. The analysis of an adsorption isotherm can offer information regarding the surface area, pore size distribution, and pore volume of the measured materials. The following definitions are indispensable. These phrases are utilised in the adsorption process and deserve further examination. Monolayer adsorption refers to all adsorbed molecules in contact with a solid's surface. Multilayer adsorption involves the adsorption space accommodating many layers of adsorbed molecules, so that not all molecules are in direct contact with the surface materials. The monolayer capacity of an adsorbent is defined as the number of molecules required to create a full monolayer. Capillary condensation refers to the pores that are filled with condensate of gas when multilayer adsorption occurs. The menisci separate the pore space from the gas phase. Hysteresis accompanies capillary condensation frequently. Filling micropores refers to the adsorption of molecules inside micropores. The definition of surface coverage for monolayer and multilayer adsorption is the number of molecules adsorbed divided by the monolayer capacity.

2.5.1. Types of adsorption/ desorption isotherm

The shape of the adsorption isotherm will reveal information about both the type and degree of a material’s porosity. According to International Union of Pure and Applied Chemistry (IUPAC), adsorption isotherms are classified from I to VI, with type VI being rare.

Type I isotherms denote a microporous solid adsorbent with a small percentage of external surface. The adsorption gas is limited by the accessibility of the micropore volume rather than by the internal surface area.

Type II isotherms denote a macroporous or non-porous material with full monolayer adsorption; multilayer adsorption only occurs at a high relative pressure.

Type III isotherms show a weak interaction between adsorbate/adsorbent and that leads to low absorption at low relative pressure: not a very common isotherm.

Type IV isotherms denote a mesoporous material featuring capillary condensation.

Type V isotherms (also rare) show weak interactions between the adsorbate/adsorbent and low uptake at low relative pressure.

Type VI isotherms denote a non-porous material with stepwise multilayer adsorption.

The sharpness in these isotherms depends on the temperature and type of system.

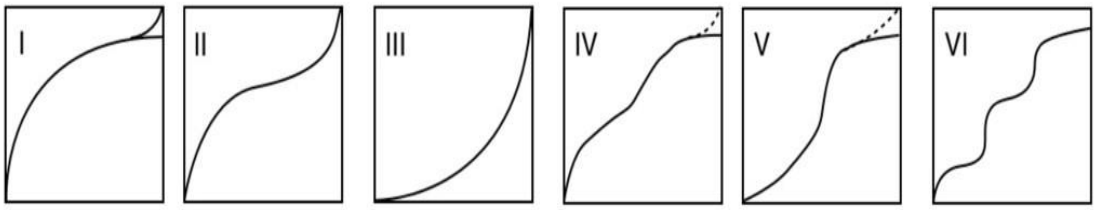


Figure 6. The 6 types of Adsorption Isotherm.

Where adsorption and desorption curves do not overlap, hysteresis loops exist. In mesoporous materials, the occurrence of adsorption hysteresis in the multilayer range of the physical sorption isotherm is typically correlated with capillary condensation.

2.5.2. Capillary Condensation

Capillary condensation is the process by which a liquid adsorbate phase is drawn into a pore, and most commonly applies to mesoporous materials. This process exhibits irreversibility between adsorption and desorption generally assumed to be due to the difference in contact angle of the liquid phase with the pore wall. The Kelvin equation, which associates the vapour relative pressure with pore radius, is used to calculate pore size distribution from isothermal measurements of the desorption process.

2.5.3. Hysteresis loop

In the case of capillary condensation occurring in mesopores, the desorption path will be different from that of adsorption, resulting in the formation of a hysteresis loop as shown in Figure 7. The type of loop is mostly associated with the pore shape.[6] Materials with uniform distribution of spherical and cylindrical narrow mesopores exhibit H1 type of hysteresis loop. Type H2 hysteresis is common for inorganic oxides with a complex network of interconnected narrow pores. An oversimplified theory attributes it to difference in condensation and adsorption rates in narrow necks versus the wider bodies—ink bottle pores. Loops of type H3 are found in solids consisting of aggregated non-rigid plate-like particles, e.g., some clays. Type H4, on the other hand, is characteristic of microporous substances with type I isotherms, with narrow slit-like pores.

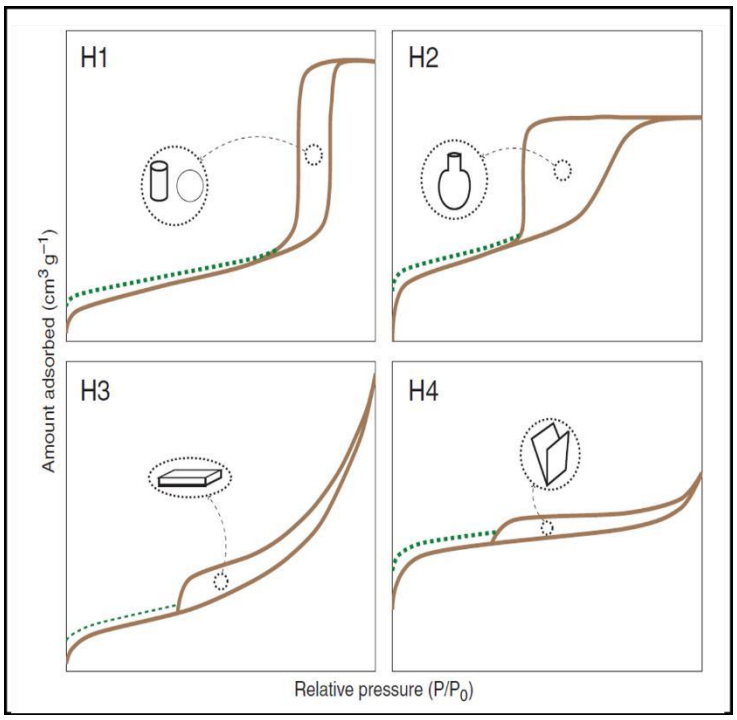


Figure 7. Types of hysteresis loops and cross bonding pore shape obtained by nitrogen physisorption.[6]

2.5.4. Pore size classification

Because the performance of porous materials is heavily dependent on the internal pore structure, pore size is one of the most essential features in practical applications. Several kinds of pore size are described. According to the widely accepted IUPAC classification, Kelvin's equation classifies

pore width (w) into three groups. macropores, mesopores and micropores. These sizes were determined during N_2 adsorption isothermal at 77 K and 1 atm. The many mechanisms; microporous macropores undergo filling, capillary condensation, and multilayer adsorption. Mesopores and micropores, in that order.

The critical pore widths of 50 and 2 nm relate to the capillary condensation of the pore, which occurs at distinct pressure-to-porosity ratios (p/p_0). At a relative pressure of 0.96, a pore width of 50 nm is related with capillary condensation, as shown on the N_2 sorption isotherm. Experiments for N_2 adsorption above a relative pressure of 0.96 are difficult, and the applicability of the capillary condensation theory has not been adequately investigated. At a relative pressure of 0.39, unstable behaviour of the N_2-adsorbed layer is seen according to the tensile strength effect, and capillary condensation cannot be performed using the Kelvin equation for pores with a width of less than 2 nm. Even when pores range from 2 to 50 nm (mesopores), capillary condensation occurs. Ultra-micropores (w 0.7 nm) are associated to the bilayer thickness of nitrogen molecules adsorbed (the statistical monolayer thickness of N_2 molecule is 0.354 nm), and supermicropores (0.7 nm w 2 nm) are specified for the pore width between ultra-micropores and micropores.

2.5.5. Surface area determination

There are several experimental models used for evaluating the surface area of porous materials. The measured surface area of a porous material is the surface area which is interacting with the chosen adsorbate.

BET equation.

BET theory is an analytical tool that is used to characterise the porosity of materials. It does so via the gas adsorption principle for solid surfaces, which provides information about specific surface area, the volume of the pores, pore size and pore size distribution. It relies on the ability of porous solids to adsorb large quantities of matter (gaseous or liquid) into their bulk where adsorption may be accompanied by swelling. BET method was developed by Stephen Brunauer, P.H. Emmett and Edward Teller in 1938. It is an extension to the theoretical basis established by Langmuir who assumed that gas molecules adsorb on a surface to cover it with a single molecular

layer, i.e., the monolayer capacity. The BET model assumes that adsorption can occur beyond monolayer coverage to result in multilayer adsorption. It measures the adsorption of gas at low temperature because physisorption is otherwise hard to detect.[7] Notably, there are assumptions that should be considered regarding the extension of the BET theory to multilayer adsorption (from monolayer adsorption). Firstly, the gas molecules adsorb on a flat and homogenous surface. Secondly, the assumption is that there is no interaction between each layer. Finally, the uppermost layer is in equilibrium with the vapour phase, and the number of layers becomes infinite when the pressure is at saturation.

The way in which the BET analyser unit (Fig.8) works is summarised as follows: evacuate the sample at a high temperature, typically up to 400°C, under vacuum conditions; cool the sample to the liquid temperature of adsorbate (for example, 77K for N_2); after obtaining the adsorption isotherm by varying partial pressure up to the saturation pressure, reduce the pressure to obtain the desorption isotherm; finally, bring the sample to atmospheric pressure.

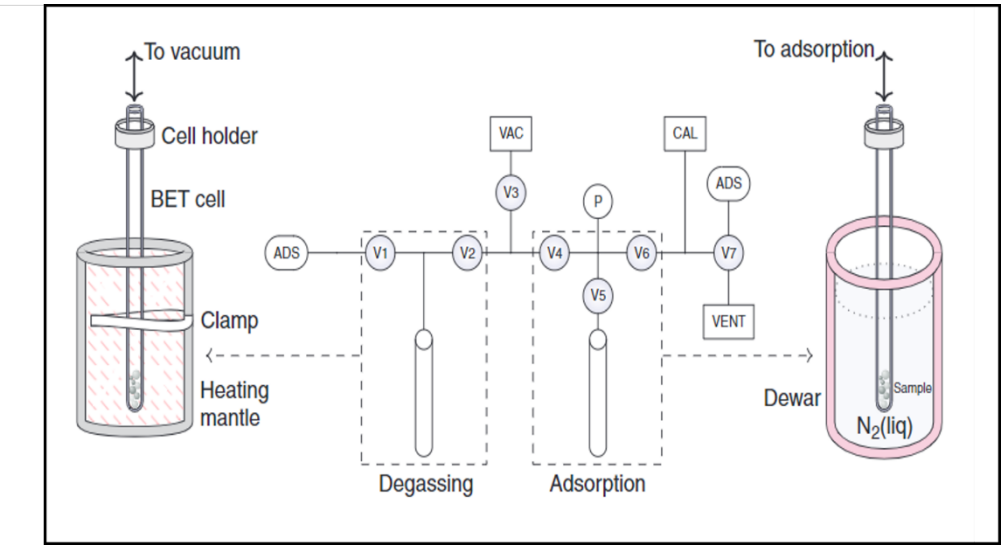


Figure 8. Gas physisorption apparatus to obtain adsorption-desorption isotherm (vacuum (VAC), calibration (CAL), adsorbate (ADS), pressure gauge(P), V1-V7 valves).[8]

The main reason for the degassing step prior to porosity analysis is to remove any gas that may be present on the surface of the sample. Nitrogen and argon are the most popular adsorbent gases that are used for porosity analysis; because they have a relatively small diameter, all micropore and mesopore surfaces can be filled. The mode of adsorption of adsorbate on the

porous solid (adsorbent) can be followed by obtaining an adsorption isotherm, which plots the amount adsorbed vs. the relative pressure *p/p°* of the adsorbate that can be used to characterise the adsorbent. The shape of the adsorption isotherm will reveal information about both the type and degree of a material's porosity. According to International Union of Pure and Applied Chemistry (IUPAC), adsorption isotherms are classified from I to VI, with type VI being rare.

The BET equation, is used to model multilayer adsorption:

$$\frac{p}{v_a(p_0-p)} = \frac{1}{v_m c} + \frac{[c-1]}{v_m c}\frac{p}{p_0} \quad \textit{Equation 5}$$

Where: v_m = monolayer volume, v_a = volume adsorbed, p_0 = saturation pressure, and *c* = constant related to the enthalpy of adsorption.

In the pressure range p/v_0= 0.02-0.25, BET data of the isotherm is used to calculate the BET surface area.

$$S_{BET} = (V_m\, N_A\, A_M)/mM_V \quad \textit{Equation 6}$$

Where: S_{BET} = BET surface area, N_A = Avogadro's number (6.022 × 10^{23}), A_M = cross-sectional area occupied by each adsorbed nitrogen molecule (0.162 nm^2), m is mass of test powder in gram, and M_V = the molecular volume (22414 ml).

Pore Volume

The total pore volume is often derived from the amount of gas adsorbed at a relative pressure P/Po of 0.95-0.99, i.e., close to the saturation vapour pressure, by converting the mass of the adsorbed material to the corresponding volume of the liquid adsorbate at the temperature of the adsorption measurement. For N_2 at 77 K, the conversion factor from the amount adsorbed to the volume of liquids adsorbed is 0.0015468 cm^3/g at STP (standard temperature and pressure).

The t-plot

The t (thickness-plot) method is a comparison of an isotherm of microporous material with a standard Type II isotherm proposed by Lippens and de Boer.[9,10] This method gives information about micropore volume, surface area and average pore size. In the t method analysis, the mass of adsorbed material obtained from the experimental data on a nonporous adsorbent is converted

to the average thickness, t (Å). The experiment isotherm is expressed as t-plot, which is a plot of the amount of gas adsorbed as a function of t. A popular thickness equation was proposed by de Boer which describes as follows:

$$t = \left[\frac{13.99}{log\left(\frac{p^s}{p}\right)+0.034}\right]^{1/2} \quad \textit{Equation 7}$$

A similar thickness equation was obtained by Harkins-Jura shown as;

$$t = 3.54\left[\frac{5}{ln\frac{p^s}{p}}\right]^{\frac{1}{3}} \quad \textit{Equation 8}$$

If the experimental isotherm exhibits multilayer adsorption characteristics, and the t- plot is a straight line that passes through the origin, then equation 9 is valid. In this instance the slop (s) is proportional to the surface area (S_t, m^2/g) according to equation 9.

$$S_t = s * 15.47. \qquad \textit{Equation 9}$$

In the case of partial presence of micropores, the surface area is evaluated by the BET method. The adsorption isotherm exhibits an increased volume adsorbed at low relative pressure. The intercept (i) on the adsorption axis is equivalent to the micropore volume (V_{MP}, cm^3):

$$V_{MP} = i * 0.0015. \qquad \textit{Equation 10}$$

In this case, the external surface area (S_{ext}) of micropore can be obtained from the slope of the t-plot, and the micropore surface area can be determined according to the relation:

$$S_{micro} = S_{BET} - S_{ext} \qquad \textit{Equation 11}$$

Pore size distribution

The measurement of the mesopore size distribution can be obtained by the Kelvin equation which is based on the concept of capillary condensation in mesopores. Considering the cylindrical narrow pore where the adsorbed gas molecules condense to form liquid layers with a curved meniscus at vapor pressure that are lower than the saturated vapour pressure of the bulk liquid, the Kelvin equation describes the saturated vapour depression of the curved liquid layer in a capillary with radius (r) as follows:[10]

$$ln\frac{p}{p^{\circ}} = \frac{2\gamma Vm}{rRT} \qquad \textit{Equation 12}$$

where the *Po* is saturated pressure of bulk liquid, *P* is lower vapor pressure of sample, γ is surface tension, V_M is molar volume, R is the universal gas constant (8.3145 J/K mol), T is temperature and r is radius of meniscus.

For nitrogen adsorption at 77 K, the following value can be applied: γ = 8.85 m/Nm; M = 28.01 g/mol; density = 0.807 g/cm^3 and V_M = 34.71 cm^3/mol. Therefore:

$$\frac{r_k}{nm} = \frac{0.415}{log\left(\frac{p_{\circ}}{p}\right)} \qquad \textit{Equation 13}$$

where r_k is Kevin radius, P and Po are sample and saturated vapor pressure, respectively.

Barrett, Joyner, and Helenda (BJH)

It important to mention that, if multilayer adsorption takes place in a mesoporous solid followed by capillary condensation, the Kelvin equation is limited in such case. Many methods have been developed for the calculation of pore size distribution based on the Kelvin equation with a correction term for the thickness of the multilayer adsorbed film. The BJH (Barrett, Joyner and Helenda) model is commonly used to determine pore size distribution. The BJH model evaluates the relationship between nitrogen desorption isotherm at 77 K and the pore size distribution.[8,11,12]

The BJH model makes two fundamental assumptions; first, the shape of pore is cylindrical, and the second that the level of absorption (amount of adsorbed gas on adsorbent surface) results from both the physical adsorption on the walls of the pore and capillary condensation in the mesopores.[11] Thus all pores are filled with liquid. The largest pore has a radius; r_{p1}, with the thickness; t_1. When the pressure decreases to lower $(P/Po)_2$, evaporation occurs, thus the inner capillary is thinner (t_2), with radius r_{p2}. The reduction of relative pressure will result in emptying of the largest pore of its capillary condensate as well as the reduction in thickness of the adsorbed layer by the amount of Δt_1. As a consequence, the BJH equation is expressed as follows:

$$V_{pn} = \frac{r_{pn}^2}{(r_{kn}+\Delta t_n)^2} \cdot \Delta Vn - \frac{r_{pn}^2}{(r_{kn}+\Delta t_n)^2} \cdot \Delta t_n \cdot \sum_{j=1}^{n-1} \frac{r_{pj}-t_j}{r_{pj}} A_{pj} \qquad \textit{Equation 14}$$

where V_{pn} is pore volume corresponding to the nth desorption step, r_{pn} is pore radius corresponding to nth desorption step, r_{kn} is inner capillary radius corresponding to nth desorption step, Δtn is reduction in thickness of adsorbed layer corresponding to nth desorption step, t is thickness of adsorbed layer on the pore surface and A_p is area of each pore ($A_p = 2Vp/rp$).

For each desorption step, the average diameter of the pore, which undergoes capillary condensation is calculated from the Kelvin equation and t-plot equation:

$$r_p = r_k + t \quad \textit{Equation 15}$$

where r_p is average pore radius, r_k is Kevin radius and t is film thickness of the adsorbed layer.

$$log\,\frac{p}{p^\circ} = 0.034 - \frac{13.99}{r^2} \quad \textit{Equation 16}$$

$$log\,\frac{p}{p^\circ} = \frac{-4.14}{rk} \quad \textit{Equation 17}$$

In recent years, a particular approach based on statistical mechanisms; the non-local density functional theory (NLDFT) has been developed to provide the density profile of the fluid as it is subjected to adsorption forces close to the pore walls. The NLDFT appears to give a satisfactory desorption of adsorption and phase transition in slit-shaped and cylindrical mesopores. The pore size distribution is calculated from experimental adsorption isotherm, which is expressed in the form.

$$N_{exp} = \int_{D_{min}}^{D_{max}} N_s\left(\frac{p}{p^\circ}, D\right) f(D)\, dD \qquad \textit{Equation 18}$$

where N_{exp} is the experimental isotherm, $Dmin$ and $Dmax$ are minimum and maximum pore sizes, N_s $(P/Po,\ D)$ represents individual theoretical isotherms in pores of diameter D, and $f(D)$ is PSD over a finite range of pore size.

2.6. Gas adsorption measurement.

Since the physisorption mechanism is responsible for the adsorption of gases on porous material, molecules of gases are exclusively adsorbed on the surface of porous materials. Consequently, porous solids with a large specific surface area are suited for a high absorption capacity. The adsorption isotherm of porous material describes its adsorption capability. Gravimetric approach for determining gas adsorption isotherms has gained popularity as a result of recent

developments in microbalance. During an experimental test, the change in weight of the adsorbent is determined with the use of an adsorption balance.

To describe porous materials for use in gas storage, the excess CO_2 and CH_4 uptake is measured. This is the quantity of CO_2 or CH_4 adsorbed in the porous material in excess of the amount that would have been stored in the pores under similar conditions (temperature and pressure) if there was no contact between the gas molecules and the pore walls. The overall adsorption is derived from the surplus storage by calculating the number of gas molecules compressed into the carbon pore volume space. Our gravimetric techniques measured the excess uptake (Exc), from which we computed the total storage (Tol) using the following equation:

$$\theta_{Tol} = \theta_{Exc} + \rho_{CH4 \text{ or } CO2} * \nu\tau \qquad \textit{Equation 19}$$

where, θ_{Tol} is total methane uptake, θ_{Exc} is excess methane uptake, ρ_{CH4} is density (g/cm^3) of methane gas under the prevailing temperature and pressure, and ν_τ is total pore volume (cm^3/g) of the activated carbon. The methane density was obtained from the National Institute of Standards and Technology (NIST) website (https://www.nist.gov/).

2.7. Packing density determination.

The amount of mass that may be contained within a given volume of material is referred to as packing density. It is a measure of how tightly packed a material's particles or molecules are within a specific volume. A material's packing density is often represented in mass per unit volume measures such as grammes per cubic centimetre (g/cm^3) or kilogrammes per cubic metre (kg/m^3).

The packing density of a material can be affected by a number of factors, including particle size and shape, particle arrangement within the material, and external conditions such as temperature and pressure. larger packing density materials have a larger mass per unit volume, which means they are more compact and take up less space.

Packing density can be measured practically from the pellets compacted in a 1.3 cm die for 5-10 minutes at 7 MPa. However, similar values are typically obtained from the Grain Density Equation:

$$d_{carbon} = (\frac{1}{\rho_s} + \nu_t)^{-1} \qquad \textit{Equation 20}$$

where *ρs* is the skeletal density determined via helium pycnometry and ν_t is the total pore volume

2.8. References.

1 A. W. Coats and J. P. Redfern, *Analyst,* 1963, **88**, 906-924

2 *Y. Leng, Materials Characterization: Introduction to Microscopic and Spectroscopic Methods*, Wiley, Singapore, 2008.

3 M. J. Wilson, *A handbook of determinative methods in clay mineralogy*, The University of California, Blackie, 1987.

4 B. E. Warren, *X-Ray Diffraction*, Dover publications, New York, 1990.

5 R. Bardestani and G. S. Patience, *Can J Chem Eng*, 2019, **97**, 2781–2791.

6 K. S. W. Sing and R. T. Williams, *Adsorption Science and Technology*, 2004, **22**, 773– 782.

7 S. Brunauer, P. H. Emmett and E. Teller, *Adsorption of Gases in Multimolecular Layers*, 1938.

8 M. L. Ojeda, J. M. Esparza, A. Campero, S. Cordero, I. Kornhauser and F. Rojas, *Physical Chemistry Chemical Physics*, 2003, **5**, 1859–1866.

9 J. E. S. M. A. T. and M. T. S. Lowell, *Characterization of porous solids and powders: surface area, pore size and density, Springer Science + Business Media*, New York, 2004.

10 Katsumi Kaneko, *J Memb Sci*, 1994, **96**, 59–89.

11 E. P. Barrett, L. G. Joyner and P. P. Halenda, *J Am Chem Soc*, 1951, **73**, 373–380.

12 J. C. Groen, L. A. A. Peffer and J. Pérez-Ramírez, *Microporous and Mesoporous Materials*, 2003, **60**, 1–17.

3. Highly microporous polypyrrole-derived activated carbons for high CO_2 and CH_4 storage.

3.1. Introduction

Carbon dioxide emissions mitigation has received an extensive amount of attention because it is the primary anthropogenic contributor to climate change. Among the various CO_2 abatement strategies, much emphasis has been placed on CO_2 capture and storage. CO_2 capture via chemical absorption processes employing various forms of amine-containing molecules is an established method. [1–9] However, this technology has several drawbacks (such as energy consumption, apparatus corrosion, toxicity, etc.) and, as a result, there is significant interest in developing alternative capture methods. Using sorbents to capture CO_2 via pressure, temperature, or vacuum swing adsorption systems and their combinations is a viable alternative.

Current research topics include a number of potential solutions for the conservation and restoration of the environment in response to the effects of CO_2 release. These include not only the capture and storage of carbon dioxide (CO_2), but also the use of cleaner fuels such as natural gas (NG) and hydrogen (H_2). [10] Although natural gas still produces CO_2, it is significantly greener than petroleum-based fuels. Discovering efficient methods to separate, capture, and reversibly store these energy-related gases is the primary factor preventing the commercialisation of these fuels in the automobile industry. The two common methods of NG storage currently used are: (i) liquefaction at low temperature and, (ii) compression to 200–300 bar at room temperature. Despite efforts to enhance cylinders and compressors, the amount of NG stored in a tank only allows for a limited driving range on light-duty automobiles, and high-pressure storage on vehicles raises safety problems.

As prospective candidates for CO_2 capture, porous solids such as zeolites, metal-organic frameworks (MOFs), porous carbons, and organic–inorganic hybrid sorbents have been investigated. Hybrid sorbents necessitate expensive, multistep fabrication processes involving the impregnation or grafting of porous solids (e.g., silica or carbon) with various amines. In addition, these materials require high temperatures for regeneration and experience a significant reduction in adsorption capacity after multiple cycles.

Due to their low cost, wide availability, large surface area, easily designed pore structure, surface functionalization, and low energy requirements for regeneration, carbon-based materials such activated carbons are regarded as one of the most promising adsorbents for capturing carbon dioxide. In addition, activated carbon demonstrates promising potential as CH_4 storage material[10] compared to other material, such as MOFs.[11,12] Methane as a fuel has the potential to substantially lower polluting emissions when compared to current gasoline and diesel fuel options, as the combustion of CH_4 releases lower amounts of CO_2.

It is important to mention that porous carbons-capturing properties can be improved by (a) treating porous carbons with ammonia at high temperatures,[1–3] and (b) using chemical compounds containing nitrogen as carbon precursors[4,5] such as polypyrrole (PPY)[6]. PPY is a widely studied conductive polymer with a high nitrogen content (up to ~16 %) and a high carbonaceous residue yield (~54 %) after pyrolysis.[6–8] It has previously been utilised as a precursor for the nanocasting fabrication of mesoporous carbons.[8,9]

Capturing properties can be enhanced also by enhancing the activation process efficiency e.g., employing a new activating agent or compressing the precursor and activating agent into pellets prior to activation. Some studies reported that the process of compactivation, also known as mechanochemical activation, in which mixtures of the precursor and KOH are compacted into pellets prior to activation, permits initial solid–solid interaction between the activating agent and the precursor; this evolved with the goal of increasing proximity (solid–solid contacts) between the precursor and KOH in order to increase the activating agent's efficiency with respect to the porosity generated, and reduce interparticle voids This approach has been studied previously using KOH as

an activating agent. It was demonstrated that compactivation (a mechanical compression step prior to thermochemical activation) can greatly improve the level of activation and created porosity, particularly at lower KOH–carbon ratios, without having any negative impact on pore size or pore size distribution.[13] In the same manner, the compactivation were investigated using a mild activation agent, potassium oxalate (PO). Several studies have demonstrated the use of PO ($K_2C_2O_4$) as an activating agent for carbons with low-to-medium surface area (usually <1500 m^2/ g) for activation at 800 °C or below.[14–18]

This report will study the preparation of chemically activated carbon using PO as activating agent and PPY as the carbon precursor. It will explore the effect of compaction on the carbon-activation process and the resulting carbon's porosity and textural properties. It will demonstrate how porosity can be adjusted to achieve extraordinary levels of moderate-to-high pressure methane and CO_2 adsorption (both in terms of gravimetric and volumetric capacity).

3.2. Experimental section

3.2.1. Materials synthesis

Carbon precursors

Polypyrrole (PPY) was prepared using $FeCl_3$ as oxidant. In a typical synthesis, pyrrole (3 g) was added to a solution of $FeCl_3$ (0.5 M, 200 ml) and the mixture was magnetically stirred at room temperature for 2 h. The resulting PPY was separated by filtration, washed with distilled water, and dried according to Scheme 1 below. The PPY yield was close to 100%.

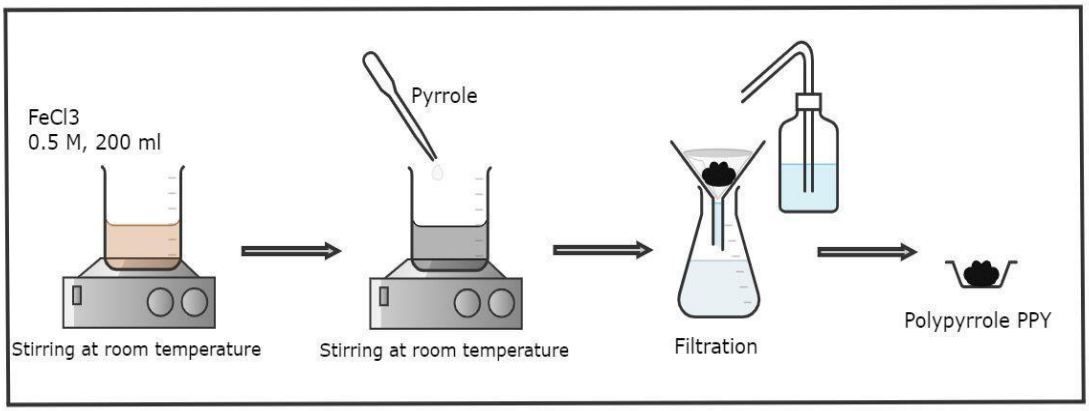


Figure 1 Polypyrrole preparation diagram.

Conventional activation and compactivation.

For both the conventional activation and compactivation process, the carbon-precursor (PPY) and activating agent (PO) were ground to a fine powder. However, in the compactivation processes, the resulting powdered mixture was compacted for 5 min at a load of 10 tonnes in a 1.3 cm die (equivalent to 740 Mpa). The powder mixture (conventional activation) or compacted pellets (compactivation) were placed in an alumina boat and heated to the target temperature in a horizontal furnace tube under nitrogen flow a ramp rate of 3 ºC/min and held at the final temperature for 1 h before being allowed to cool under a flow of nitrogen. The resulting activated carbons were thoroughly washed with 10% HCl to remove any inorganic salts, followed by washing

with deionised water until the water was at pH ~7. The obtained activated carbons were dried at 100 ºC. The prepared samples were designated as **PPY-XT** or **PPY-XTP**, where **X** is the PO/PPY ratio, **T** is the activation temperature, and **P** indicates activation in pellet form (i.e., compactivation)

3.2.2. Material Characterisation.

Thermogravimetric analysis (TGA) was performed using a TA Instruments Discovery analyser or TA Instruments SDT Q600 analyser under flowing air conditions (100 mL/min). A PANalytical X'Pert PRO diffractometer was used to perform powder XRD analysis using CuKα light source (40 kV, 40 mA) with step size of 0.02° and 50 s time step. Elemental, CHN, analysis was performed on an Exeter Analytical CE-440 Elemental Analyser. Nitrogen sorption (at -196°C) with a Micromeritics 3FLEX sorptometer was used for porosity analysis and to determination textural properties. Prior to analysis the carbon samples were degassed under vacuum at 200°C for 12 h. Surface area was calculated using the Brunauer-Emmett-Teller (BET) method applied to adsorption data in the relative pressure (*P/Po*) range of 0.02 – 0.22, and pore volume was estimated from the total nitrogen uptake at close to saturation pressure (P/Po ≈ 0.99). The micropore surface area and micropore volume were determined via t-plot analysis. The pore size distribution was determined using non-local density functional theory (NL-DFT) applied to nitrogen adsorption data. Scanning electron microscopy (SEM) images were recorded using a Microscopy JEOL 7100F FEG-SEM, operating at a 5 kV accelerating voltage.

3.2.3. Methane and CO_2 uptake measurements.

Methane and CO_2 uptake were determined using a Hiden Isochema XEMIS Analyser. Before the uptake measurements, the carbon samples were degassed at 240°C under vacuum for several hours. Adsorption-desorption isotherms were obtained at 25 °C, over methane (CH_4) pressure range of 0 – 100 bar, and (CO_2) pressure range 0-40 bar.

3.3. Result and discussion

Polypyrrole as precursor

PPY is employed as a carbon precursor as it generates high-surface-area activated carbons that retain high packing density.[13,19] It has a sponge-like structure composed of linked microparticles, as is demonstrated in PPY SEM images in Fig.2 (1 and 2 a). This morphology provides a broad interfacial area for the polymer to react with PO and ensures that the activation process proceeds uniformly, which is crucial for optimal pore development. Compactivation and direct activation were performed at various PO/PPY ratios (2, 3, 4, and 5) over the temperature range of 600–900 °C.

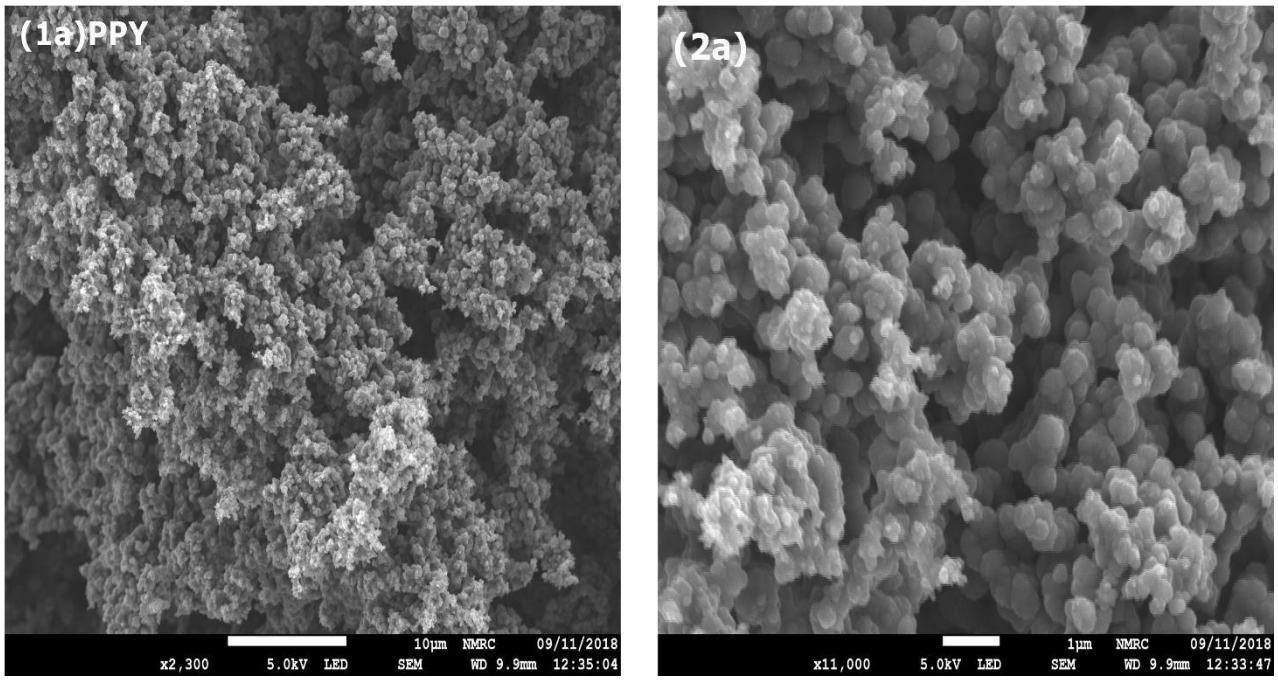


Figure 2: PPY morphology.

The activation process can be described by the following reactions:[20]

(1) Decomposition of PO to the carbonate in the range ~350−580°C:

$$C_2O_4K_2 \rightarrow K_2CO_3 + CO \qquad \textit{Equation 1}$$

(2) The redox reaction between carbon and the potassium carbonate produced from PO at T>700 °C, which causes partial carbon etching (generating porosity) under controlled activation conditions:

$$K_2CO_3 + 2C \rightarrow 2K + 3CO \qquad \textit{Equation 2}$$

(3) Slow partial decomposition of potassium carbonate at 850 °C:

$$K_2CO_3 \rightarrow K_2O + CO_2 \qquad \textit{Equation 3}$$

(4) Partial carbon gasification at 850 °C:

$$C + CO_2 \rightarrow 2CO \qquad \textit{Equation 4}$$

3.3.1. PPY-derived activated carbons: Yields, structure, nature, and morphology

The yield of activated carbons with respect to the PPY are summarised in Table 1. The yields vary from 8 to 64% depending on the activation conditions and in particular the temperature. The yield for samples activated at 600 °C is 60 – 64% and does not appear to be affected by the amount of PO used as PO/PPY changes from 2 to 5. The same trend is observed for activation at 700 °C (34 – 43%), 800 °C (24 – 32%). These observations are consistent with previous findings that due to the relatively mild nature of PO as activating agent, the activation temperature is the main determinant of the level of activation. [13,21] It is only at 900 °C that the amount of PO appears to have an effect, wherein the yield of samples activated at PO/PPY ratio of 2 is 18 – 24%, which then significantly drops to 8 – 11% at PO/PPY ratio of 4. It is likely that at 900 °C, reactions of equation 10 and 11 proceed at a much faster rate meaning that the mechanism of activation is different from that of lower temperatures. A faster reaction 10 would form K_2O more quickly meaning that the activation mechanism becomes akin to that of activation with KOH and therefore that the amount of PO becomes important. In such a scenario, the yield at PO/PPY ratio 4 should be much lower that at PO/PPY ratio 2, as confirmed by the data in Table 1.

Table 1 shows the elemental composition of the PPY and activated carbons. The carbon content of the PPY was 53.9 %. The carbon content in the activated carbons increased as a function of the activation temperature with a maximum of 92 % for PPY-4900. The carbon content of pellet samples is in general higher than that of powder samples due to the enhanced nature of the solid–solid interaction during compactivation, which means that the PO is more efficiently used. In a sense, compactivation achieves greater levels of activation compared to equivalent conventional activation conditions with respect to amount of PO and activation temperature. The nitrogen content decreased

significantly with increasing activation temperatures; samples prepared at 600 °C have a nitrogen content of ~12 %, which falls to ~0.3 % at 900 °C. The N content may have implications on gas uptake as nitrogen functional groups are thought to affect the selectivity of gas capture in carbons.[13,21]

Table 1. Yield and elemental composition of PPY-derived activated carbons.

Sample	Yield %	C %	H %	N %	O %
PPY	100	53.9	3.1	15.7	27.3
PPY-2600	60	60.2	2.8	11.1	25.9
PPY-2600P	62	60.2	2.3	10.4	27.1
PPY-2700	38	73.6	2.1	3.3	21.0
PPY-2700P	41	76.4	1.6	3.2	18.8
PPY-2800	25	79.8	1.0	3.5	15.7
PPY-2800P	24	87.3	0.2	1.0	11.5
PPY-2900	24	87.9	0.0	1.0	11.1
PPY-2900P	18	90.5	0.0	1.2	8.3
PPY-3700	38	79.0	0.5	3.7	16.8
PPY-3700P	43	68.6	0.6	3.0	27.8
PPY-3800	26	85.0	0.1	1.0	13.9
PPY-3800P	30	87.8	0.0	0.9	11.3
PPY-4600	64	61.0	2.3	11.3	25.4
PPY-4600P	63	63.1	1.9	10.1	24.9

PPY-4700	42	72.7	1.0	3.0	23.3
PPY-4700P	34	88.4	0.0	0.7	10.9
PPY-4800	31	87.4	0.1	0.9	11.6
PPY-4800P	32	88.0	0.0	0.9	11.1
PPY-4900	8	92.0	0.1	0.3	7.6
PPY-4900P	11	87.1	0.1	1.1	11.7
PPY-5600	60	68.1	1.3	12.3	18.3
PPY-5600P	62	58.0	1.2	9.4	31.4
PPY-5700	41	68.5	1.4	3.0	27.2
PPY-5800	31	84.6	0.0	0.7	14.7
PPY-5800P	31	88.5	0.07	0.8	10.7

As demonstrated in Table 1, the yield of activated carbons decreased by approximately 40% as the activation temperature increased. The yield of samples prepared at 600 °C is up to 60% greater than those activated at 700 °C, 800 °C, and 900 °C. However, samples activated at 900C had the lowest yields, as PPY-4900 lost up to 92% of the polypyrrole's initial weight. In addition, sample yield is affected by the activating agent ratio; samples activated at different ratios (2,3,4, and 5) and activated at the same temperature generate yields that are slightly different, e.g., PPY-2800 (25%), PPY-3800 (26%), PPY-4800 (31%), and PPY-5800 (31%).

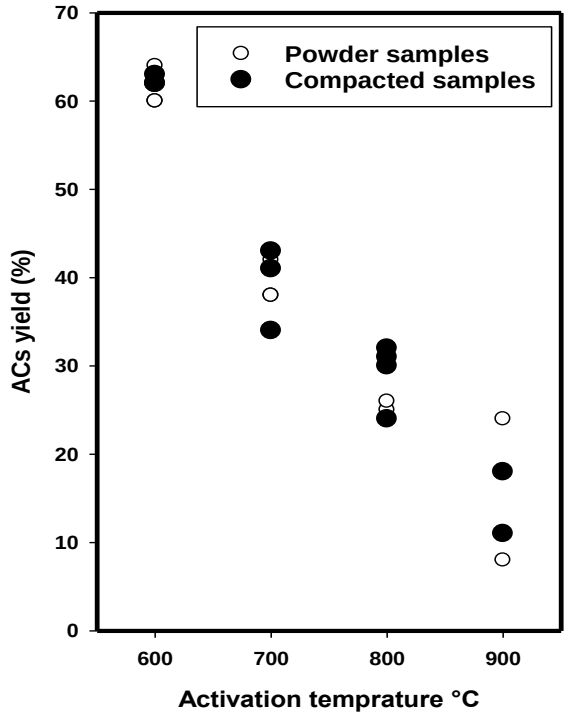


Figure 3: The effect of activation temperature on powder and compact samples yields.

Thermal Gravimetric Analysis (TGA) was performed for the majority of samples using an SDT Q600 TGA analyser (from room temperature to up to 1000 °C at a heating ramp rate of 10 °C min^{-1} in an air environment). TGA was performed to assess the purity and thermal stability of the prepared activated carbons. Fig.4 below shows a large decrease in mass between 400–580 °C, which is due to carbon burn off. This indicates that all ACs samples are made up entirely of carbonaceous matter.

The thermal stability of samples produced at a low activation temperature (600°C) was up to 400 °C. Nevertheless, samples produced at higher activation temperatures of 800°C and 900°C exhibited greater thermal stability up to 600°C. One of the causes for PPY-X600's low thermal stability is the presence of a high oxygen content of up to 30%. During the activation process, hydroxyl and carboxylic acid groups are formed on the surface of activated carbon. These groups are more reactive than the carbon backbone and are susceptible to thermal decomposition at lower temperatures than carbon. At ~650 °C, the carbon content was burned off in all samples; no carbon or residual weight remained, which confirmed the purely carbonaceous nature of the PPY-derived carbons.

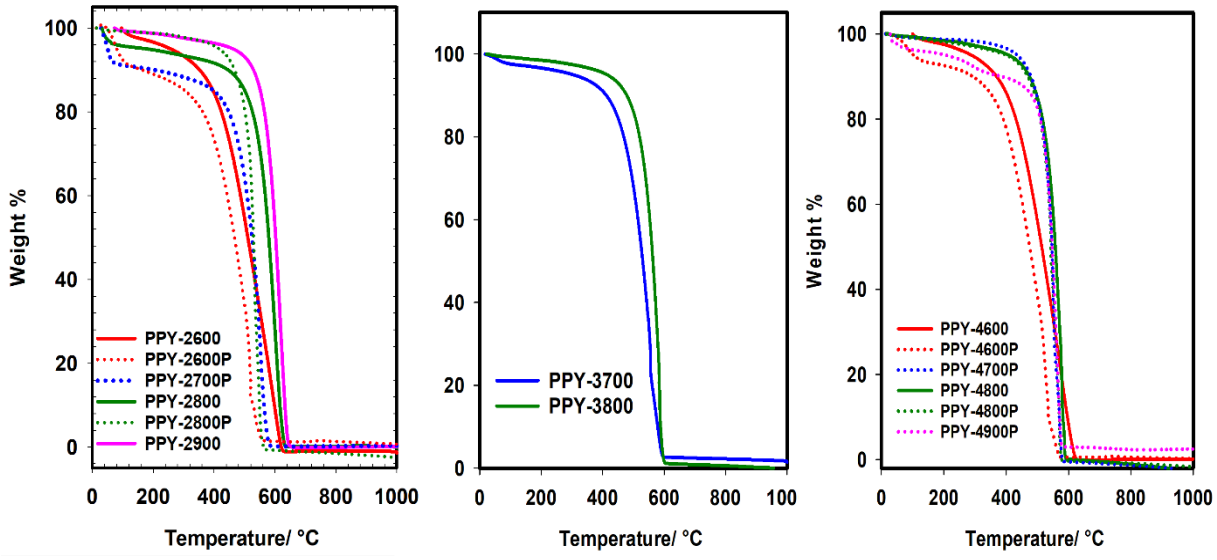


Figure 4. TGAs curves of PPY-derived activated carbons. The heating regime was a ramp rate of 10 °C min^{-1} in an air environment.

Powder X-ray diffraction (P-XRD) was performed to determine the graphitic (or not) nature of the activated carbons. All activated carbons (Fig. 5, 6, 7, and 8 below) show peaks centred at 2 θ = 26° and 44°, which arise the graphitic/turbostratic nature of the carbons. The peak at 2θ = 26° corresponds to the (002) plan of graphite and shifts slightly between samples. The low intensity of this peak indicates that any graphitic ordering in the activated carbons is very limited and points to the presence of small graphitic domains rather than wholesome graphitic ordering. The majority of the carbons show a weak peak at 2θ= 23–26°, which indicates a very low level of graphitisation. However, the XRD patterns of samples prepared at low temperature of 600 °C exhibit a higher intensity peak at 2θ = 26°, which suggests higher levels of graphitisation, which may in part explain the lower porosity of these samples (discussed below). Harsher activation conditions (higher activation temperature or higher amounts of PO) result in less graphitic carbons. This effect is seen more strongly for samples PPY-4900 and PPY-4900P, which have the weakest peak at 2θ = 23–26°. It is important to mention that sharp peaks in the P-XRD spectra may indicate presence of crystalline inorganic residues (K salts), which can be retained from the activation and washing steps. The XRD patterns of the activated carbons do not show such peaks, which is consistent with the TGA curves above in confirming that they are essentially purely carbonaceous.

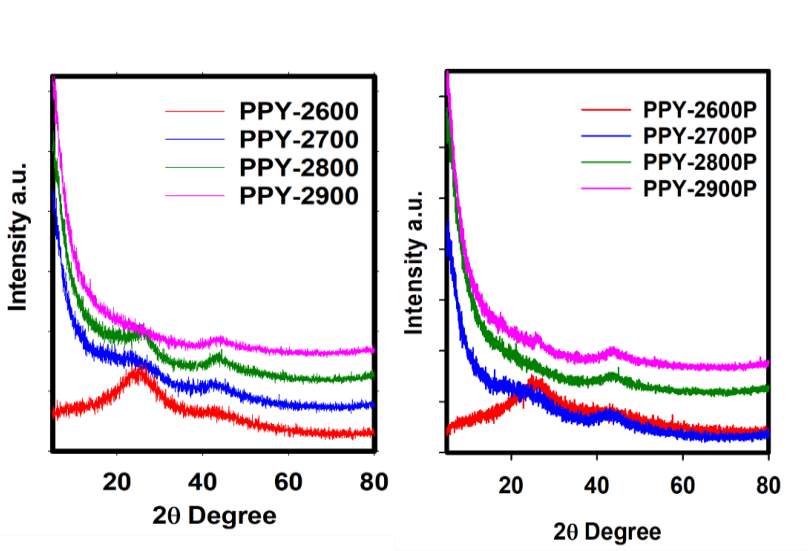


Figure 5. XRD patterns of PPY-derived activated carbons prepared at a PO/PPY ratio of 2 at activation temperatures ranging between 600 and 900°C.

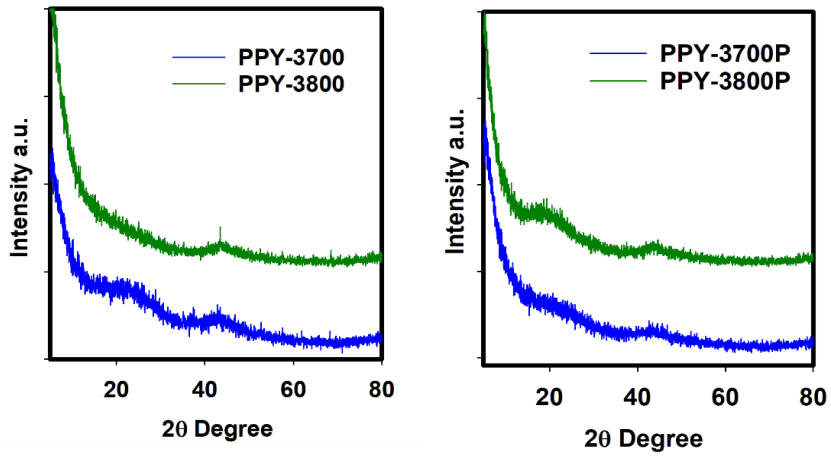


Figure 6. XRD patterns of PPY-derived activated carbons prepared at a PO/PPY ratio of 3 at 700 and 800°C.

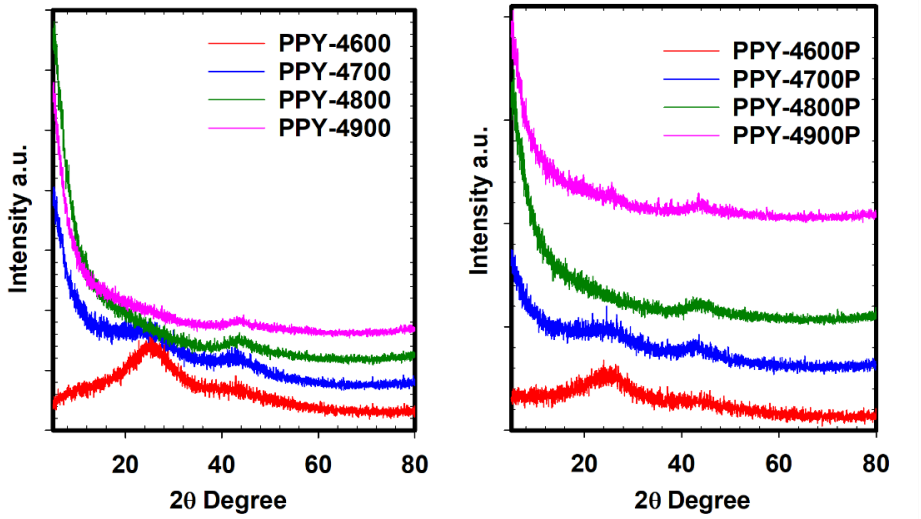


Figure 7. XRD patterns off PPY-derived activated carbons prepared at a PO/PPY ratio of 4 at activation temperatures ranging between 600 and 900˚C.

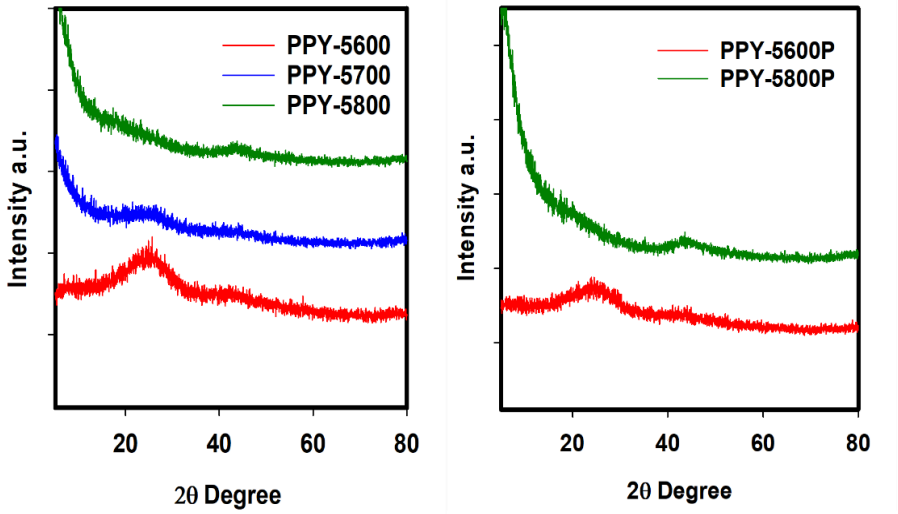


Figure 8. XRD patterns of PPY-derived activated carbons prepared at a PO/PPY ratio of 5 at activation temperatures between 600 and 800˚C.

The changes of PPY morphology were studied before and after activation. Images in Fig. 2 (21, 2a) above show that PPY exhibits a sponge-like structure with interconnected microparticles that are 1 μm in diameter. This structure is favourable for good pore development, which is the target of the work in this chapter. The activated samples exhibit a variety of shapes that depend on the degree of activation. Thus, the mildly activated samples combine into sponge-like structures that are similar to PPY (Fig.9 b, and c) with highly vesiculated particles (2b). In contrast, more highly activated carbons are exclusively made up of particles exhibiting irregular shapes with sharp corners (Fig. 9

1d). The sponge-like structure is completely destroyed, which results in porous carbons particles (as shown in the image for sample PPY-4900).

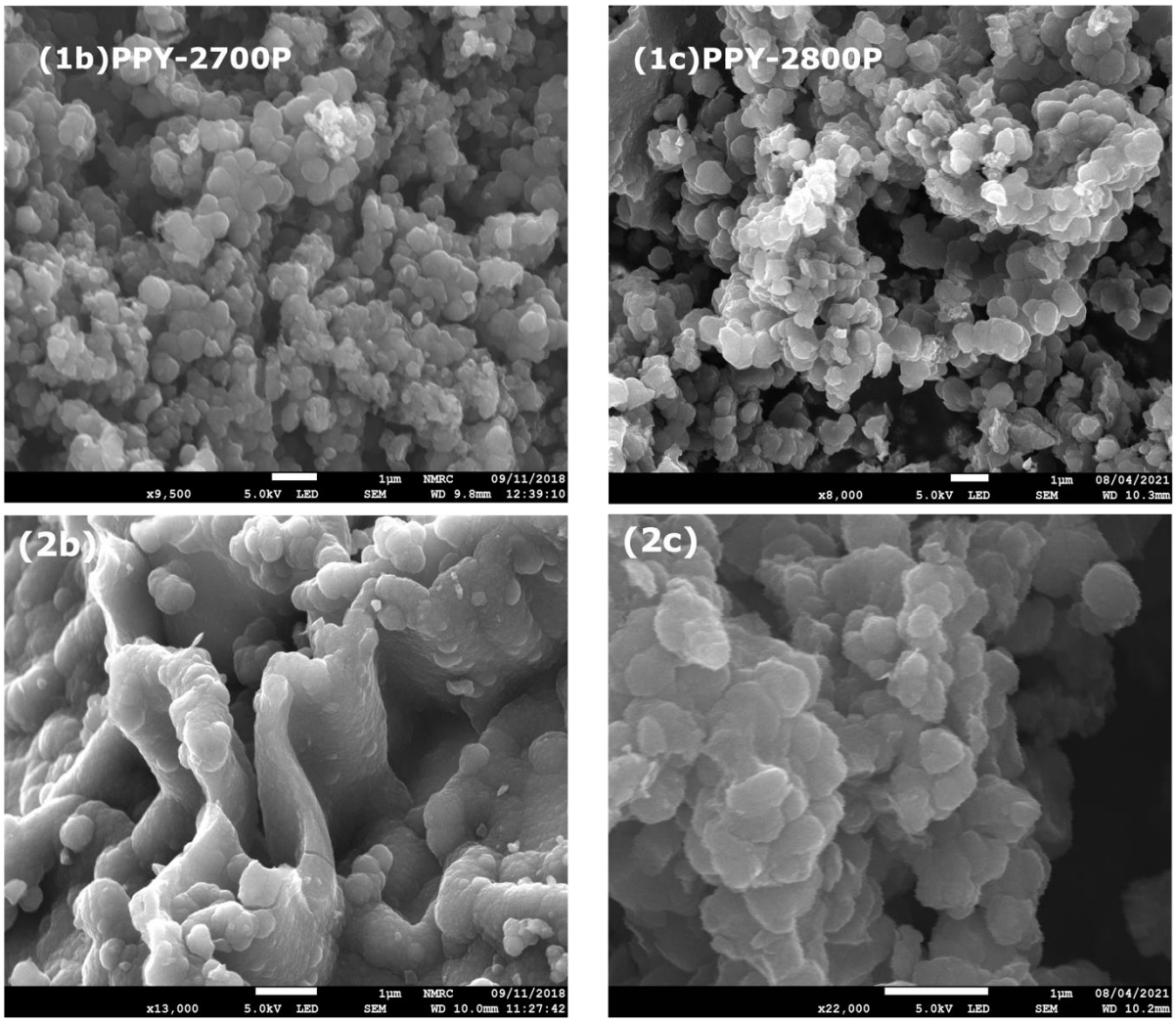


Figure 9. SEM images of PPY before and after being activated (PPY-2700P, PPY-2800P, and PPY4900).

3.3.2. Porosity and textural properties analysis

Porosity analysis was performed using a Micromeritics 3 Flex with nitrogen sorption at 196 °C. The surface area and pore volumes were calculated using BET theory from the adsorption data for the P/P_o = 0.04–0.25. Pore size distributions (PSDs) were calculated using density functional theory (DFT). The degassing step was performed by Micromeritics Smart Vac Prep prior to the analysis in order to ensure that the surface of the material was clean of any molecules that may affect the evaluation of porosity.

As shown in Figure 10, most of the carbons prepared at PO/PPY ratio of 2 exhibit a type **I** isotherm. This type of isotherm indicates a microporous solid adsorbent with a small percentage of external surfaces wherein N_2 sorption is limited by the accessibility of the micropore volume rather than the internal surface area. Samples prepared at higher activation temperature (PPY-2800P, PPY-2900 and PPY2900P) exhibit type IV isotherms that are indicative of significant mesoporosity as confirmed by the pore size distribution curves in Figure 9. This change in isotherm type and shift to mesoporosity indicates the important role that activation plays in determining the porosity of the activated carbons. Some of the isotherms exhibit minor hysteresis effect but overall, most of the samples have present reversible sorption.[22]

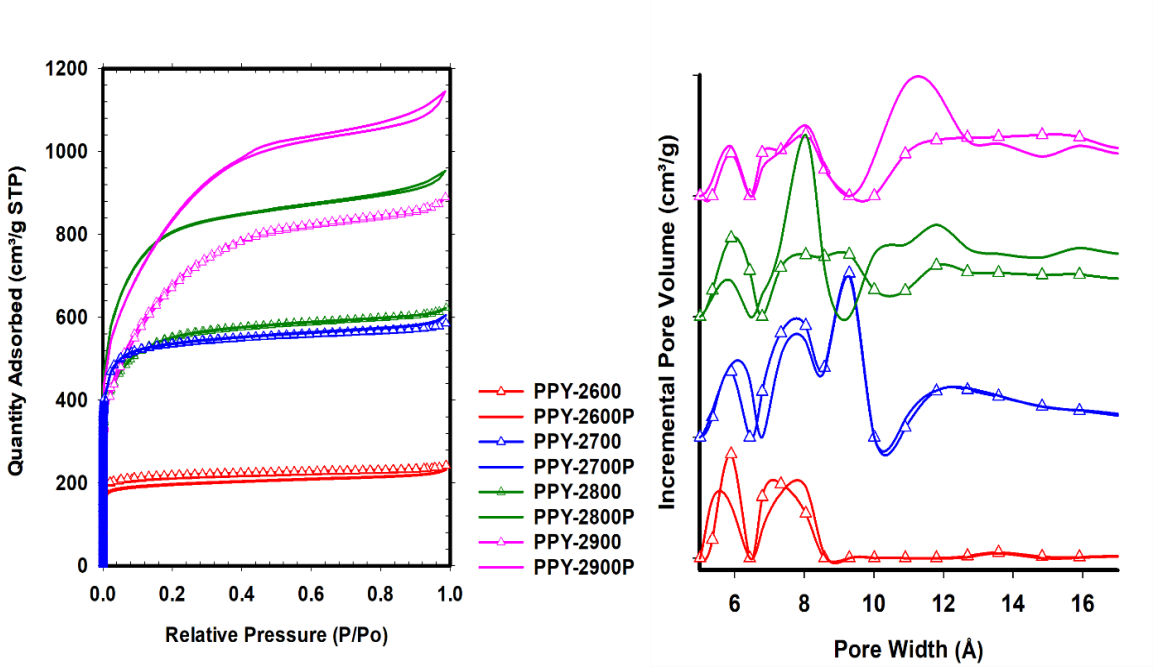


Figure 10. Nitrogen sorption isotherm (left) and corresponding pore size distribution curves (right) of PPY-2X samples prepared at 600–900 ºC and PO/PPY ratio of 2.

The textural properties of the PPY-2X carbons are given in Table 2. The surface area (730 – 3100 m^2/g) and pore volume (0.36 – 1.8 cm^3/g) increase significantly with activation temperature. There is a particularly significant increase in porosity between 600 and 700 ºC, which is related to the mechanism of activation with PO; As shown by equation 2 above, the redox reaction between carbon and the potassium carbonate produced from PO occurs at T $\geq$ 700 °C, which causes carbon etching

and accelerates the generation of porosity. The level of mesoporosity, as indicated by the proportion of micropore surface area and pore volume, decreases at higher activation temperature.

At PO/PPY ratio of 2, activated (powder) and compactivated (pellet) samples show no differences in surface area at activation temperatures of 600 ^{o}C and 700 ^{o}C. However, at higher activation temperatures, compactivated samples have higher surface area. For instance, PPY-2900P has surface area of 3022 m^2/g, which is va. 17% higher than 2461 m^2/g for PPY-2900. The difference between PPY-2800 and PPY-2800P is larger at ca. 31% higher for the former. It is likely that the effects of equation 2 above mean that the impact of compactivation is unleashed at temperature above 700 ^{o}C. On the other hand, at 600 and 700 ^{o}C, the extent of activation remains low due to the mild nature of PO and therefore the impact of compactivation is limited. However, despite the higher nitrogen sorption for compactivated samples (e.g., PPY-2800P and 2900P), there is no significant change in the shape of the isotherm, which indicates that activated and compactivated carbons have comparable pore size distribution. PSD curves (Fig. 10) demonstrate that the size of the pores generated in activated and compactivated carbons is comparable and in the range of range 0.6 – 1.1 nm. We further confirmed that the compactivation process has no effect on the existence, distribution, or proportion of bigger pores (mesopores and/or macropores); the pore size distribution for activated and compactivated samples remains identical.

Table 2. Textural properties of PPY-derived carbons prepared at PO/PPY ratio of 2.

Sample	Yield %	BET surface area[a] (m^2/g)	Pore volume[b] (cm^3/g)	Pore size[c] (Å)	Packing density (g/cm^3)
PPY-2600	60	812 (701)	0.38 (0.29)	6/ 7	1.20
PPY-2700	38	2038 (1739)	0.91 (0.70)	6/ 8/ 9	0.73
PPY-2800	25	2021 (1811)	0.97 (0.77)	6/ 8/ 9	0.70
PPY-2900	24	2461 (1683)	1.38 (0.76)	6/ 7/ 11	0.55
PPY-2600P	62	734 (614)	0.36 (0.25)	6/ 7	1.22
PPY-2700P	41	2036 (1718)	0.94 (0.67)	6/ 8/ 9	0.72
PPY-2800P	24	3098 (2396)	1.77 (1.03)	6/ 8/ 11	0.45
PPY-2900P	18	3022 (1869)	1.77 (0.85)	6/ 8/ 11	0.45

[a]: The values in the parentheses are micropore surface area. *[b]: The values in the parentheses are micropore volume.*[c:] Pore size that extracted from the PSD curves using DFT model.

Similar trends are observed for carbons prepared at PO/PPY ratio of 3 as shown in Figure 11 and Table 3. There is no difference in surface area between the activated and compactivated samples for activation at 700°C. However, the surface area of PPY-3800P is 6% higher than that of PPY-3800.

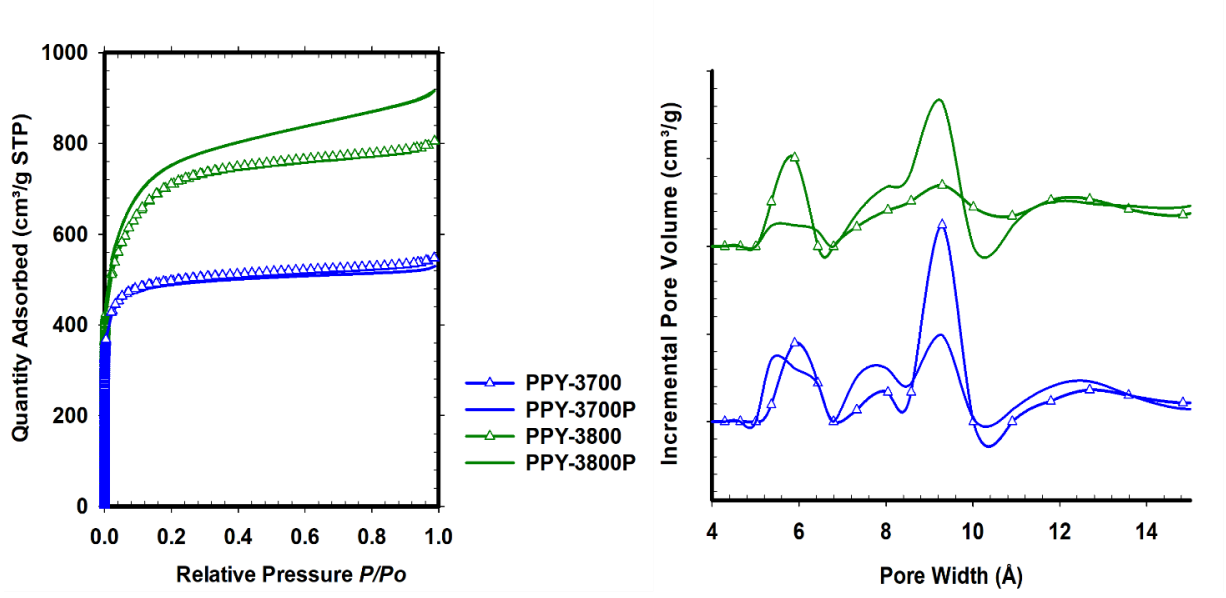


Figure 11. Nitrogen sorption isotherms (left) and corresponding pore size distribution curves (left) of PPY-derived carbons prepared at PO/PPY ratio of 3.

Table 3. Textural properties of PPY-derived carbons prepared at PO/PPY ratio of 3.

Sample	Yield %	BET surface area[a] (m^2/g)	Pore size (Å)	Pore volume[b] (cm^3/g)	Packing density (g/cm^3)
PPY-3700	38	1906 (1613)	6/ 8/ 9	0.85 (0.64)	0.77
PPY-3800	26	2596 (2291)	6/ 9/ 12	1.25 (0.98)	0.59
PPY-3700P	43	1862 (1586)	6/8/9	0.82 (0.63)	0.78
PPY-3800P	30	2751 (2270)	6/9/12	1.42 (0.97)	0.53

For activation at PO/PPY PPY–PO ratio of 4, the porosity of both powder and pellet samples increases at higher activation temperatures as shown in Figure 12 and Table 4. However, at 900 °C, there is a decrease in surface area, which may be due to overactivation arising from the high amount of PO along with closer contact and therefore more efficient activation. Nevertheless, despite the higher nitrogen adsorption of compactivated samples, there is no observed change in the isothermal shape compared with activated samples, which means that both carbons have the same pore size distribution as confirmed by the pore size distribution curves in Figure 12.

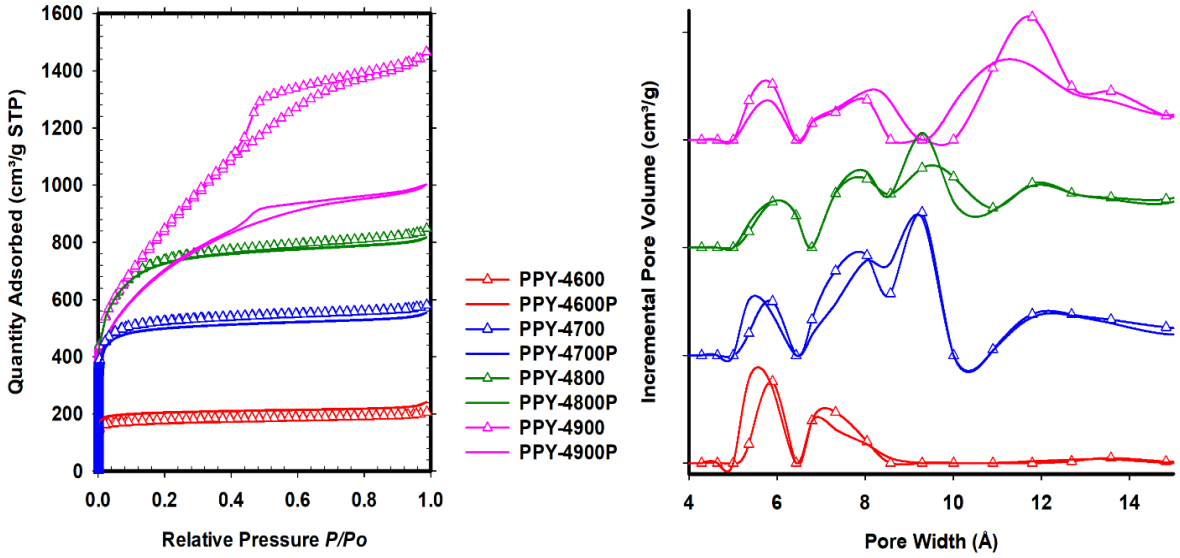


Figure 12. Nitrogen sorption isotherms (left) and corresponding pore size distribution curves (left) of PPY-derived carbons prepared at PO/PPY ratio of 4.

Table 4. Textural properties of PPY-derived carbons prepared at PO/PPY ratio of 4.

Sample	Yield %	BET surface area[a] (m^2/g)	Pore size (Å)	Pore volume[b] (cm^3/g)	Packing density (g/cm^3)
PPY-4600	64	665 (563)	6/ 7	0.32 (0.23)	1.29
PPY-4700	42	1989 (1672)	6/ 8/ 9	0.90 (0.67)	0.74
PPY-4800	31	2720 (2420)	6/ 8	1.32 (1.03)	0.56
PPY-4900	8	3098 (639)	6/ 8/ 10	2.27 (0.27)	0.37
PPY-4600P	63	769 (667)	6/ 7	0.37 (0.27)	1.21
PPY-4700P	34	1898 (1606)	6/ 8/ 11	0.86 (0.64)	0.76
PPY-4800P	32	2653 (2373)	6/ 8/ 9	1.27 (1.02)	0.58
PPY-4900P	11	2518 (1269)	6/ 8/ 11	1.55 (0.57)	0.50

Samples activated at PO/PPY ratio of 5 show good development of microporosity at higher activation temperatures. For e.g., PPY-5800 has microporosity of 88% while PPY-5700 has a microporosity of ~82%. In addition, there were no significant changes in PSD between powder and compacted activated carbons.

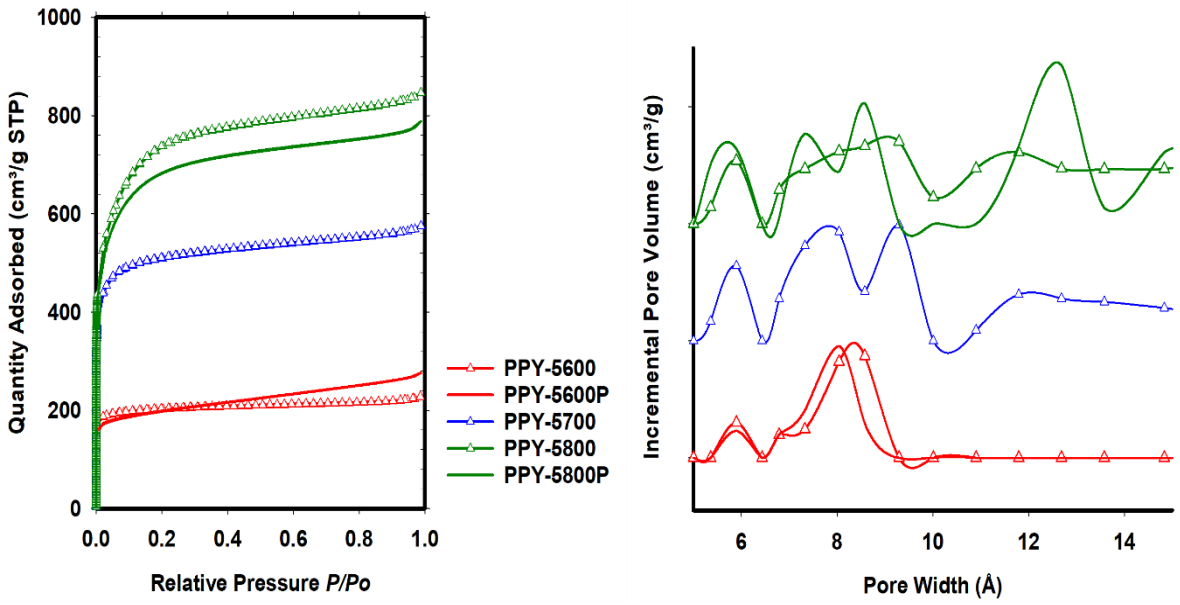


Figure 13. Nitrogen sorption isotherms (left) and corresponding pore size distribution curves (left) of PPY-derived carbons prepared at PO/PPY ratio of 5.

Table 5. Textural properties of PPY-derived carbons prepared at PO/PPY ratio of 5.

Sample	*Yield %*	*BET surface area[a] (m^2/g)*	*Pore size (Å)*	*Pore volume[b] (cm^3/g)*	*Packing density (g/cm^3)*
PPY-5600	60	763 (659)	6/ 7/ 8	0.35 (0.27)	1.24
PPY-5700	41	1934 (1587)	6/ 8/ 9	0.89 (0.64)	0.74
PPY-5800	31	2709 (2389)	6/ 9/ 11	1.31 (1.02)	0.57
PPY-5600P	62	730 (484)	6/8	0.43(0.20)	1.13
PPY-5800P	31	2499 (2226)	6/9/13	1.22(0.95)	0.60

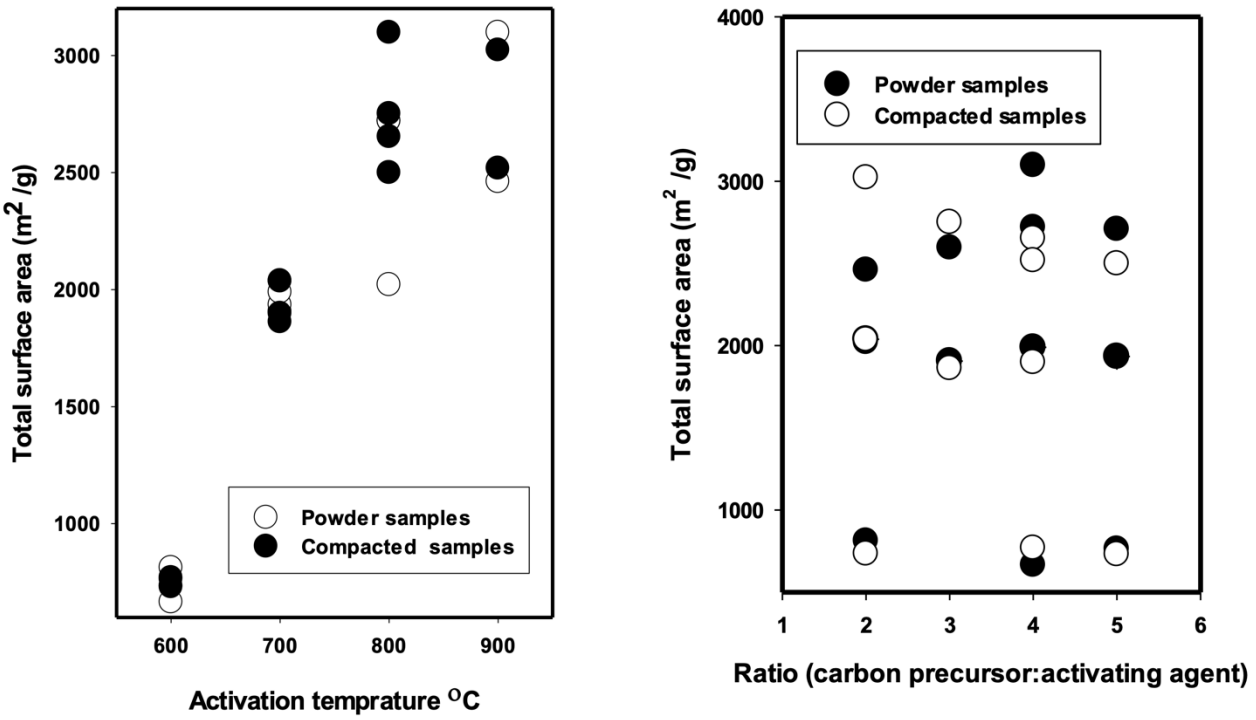


Figure 14: The effects of ratio(right), temperature(left) for powder and compacted samples on the samples surface area.

Overall, the pore size and volumes were seen to increase with increasing activation temperatures. The textural values are comparable to previous work.[23] Comparing powder and pellet samples across Tables 2–5, it can be observed that the method of preparation does not always lead to significant differences in micropore surface areas, pore sizes, or volumes. In general, there is no clear trend observed between mode of activation and porosity especially at activation temperature of 600 and

700 °C. However, for activation at 800 and 900°C, compactivated samples generally have higher porosity meaning that the compaction step aids in achieving more efficient use of the PO activating agent. The lack of compaction effects at 600 and 700°C is due to the mild nature of PO, and the fact that the mechanism of PO activation is such that significant etching of the PPY precursor only kicks in at temperature above 700°C. This is in contrast to previous studies with KOH as activating agent, wherein pellet samples (compaction) were found to reliably give higher surface area than powder forms (conventional activation).[13] The reason for this is that KOH is a harsher activating agent, and that the mechanism of KOH activation of PPY includes significant etching at much lower temperature.[13]

Although the redox reaction between carbon and potassium carbonate occurs at temperatures > 700 °C, the porosity of samples activated at 600 °C (and PO/PPY ratio of 2, 3, 4, or 5) increases from ~70 m^2/g (of PPY) to ca. 800 m^2/g. In this regard, the effect of thermal treatment of PPY at 600 °C was ascertained (Figure 15). PPY was placed in an alumina boat and heated to 600 °C at the ramp rate of 3 °C/min on a horizontal furnace tube under a nitrogen flow for one hour. The resulting thermal-treated PPY (PPY-600) had surface area of 257 m^2/g compared to ca. 70 m^2/g for PPY (Figure 13). This confirmed that some PO activation takes place even at activation temperatures of < 700 °C.

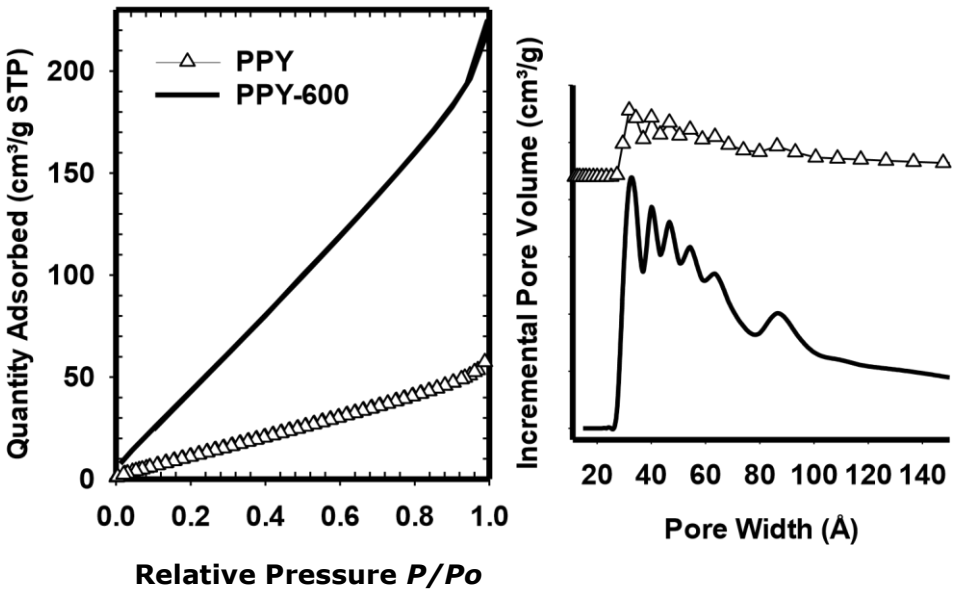


Figure 15. N_2 sorption isotherm (left) and corresponding pore size distribution curves of PPY and thermally treated PPY-600 pyrolysed at 600 ^oC.

3.3.3. CO_2 uptake measurements

A XEMIS instrument was used to measure the CO_2 uptake of at room temperature and pressures ranging from 0 to 40 bar. The uptake isotherms are shown in Figure 16, and Table 7 summarizes the CO_2 capture capacities in the pressure range 0.15–40 bar.

The CO_2 uptake of conventional activated samples at 1 bar, which is frequently employed as a performance metric for post-combustion capture from flue gas streams of fossil fuel power plants, ranges from 2.4 to 4.1 mmol/g. For compactivated carbons, the CO_2 uptake at 1 bar ranges from 2.4 to 4.1 mmol/g, with PPY-277 PPY-2700P exhibiting the highest uptake~ 4.1 mmol/g. These samples have high total surface area (2038 m^2/g and 2036 m^2/g) combined with high percentage of microporosity up to 85% and 84%. In contrast, the samples with the highest total surface area PPY-2800P and PPY-4900 up to ~3100 m^2/g and lower microporosity 77% and 20%, showed lower CO_2 uptake up to 3.2 mmol/g and 2.4 mmol/g. Therefore, the uptake indicates that at 25 $^\circ$C and 1 bar, the total surface area does not dictate CO_2 adsorption capacity. Rather, samples with the highest proportion of micropore surface area and narrowest micropore perform better. This is consistent with previous reports,[24,25] which found that pores of size 0.6 – 0.8 nm are most efficient for low pressure CO_2 uptake. Overall, compacted samples demonstrate slightly better performance

for samples activated at 600–800°C. For instance, at 1 bar and 25°C, the PPY-3800 sample has uptake of 3.0, while PPY-3800P can capture up to 3.3 mmol /g.

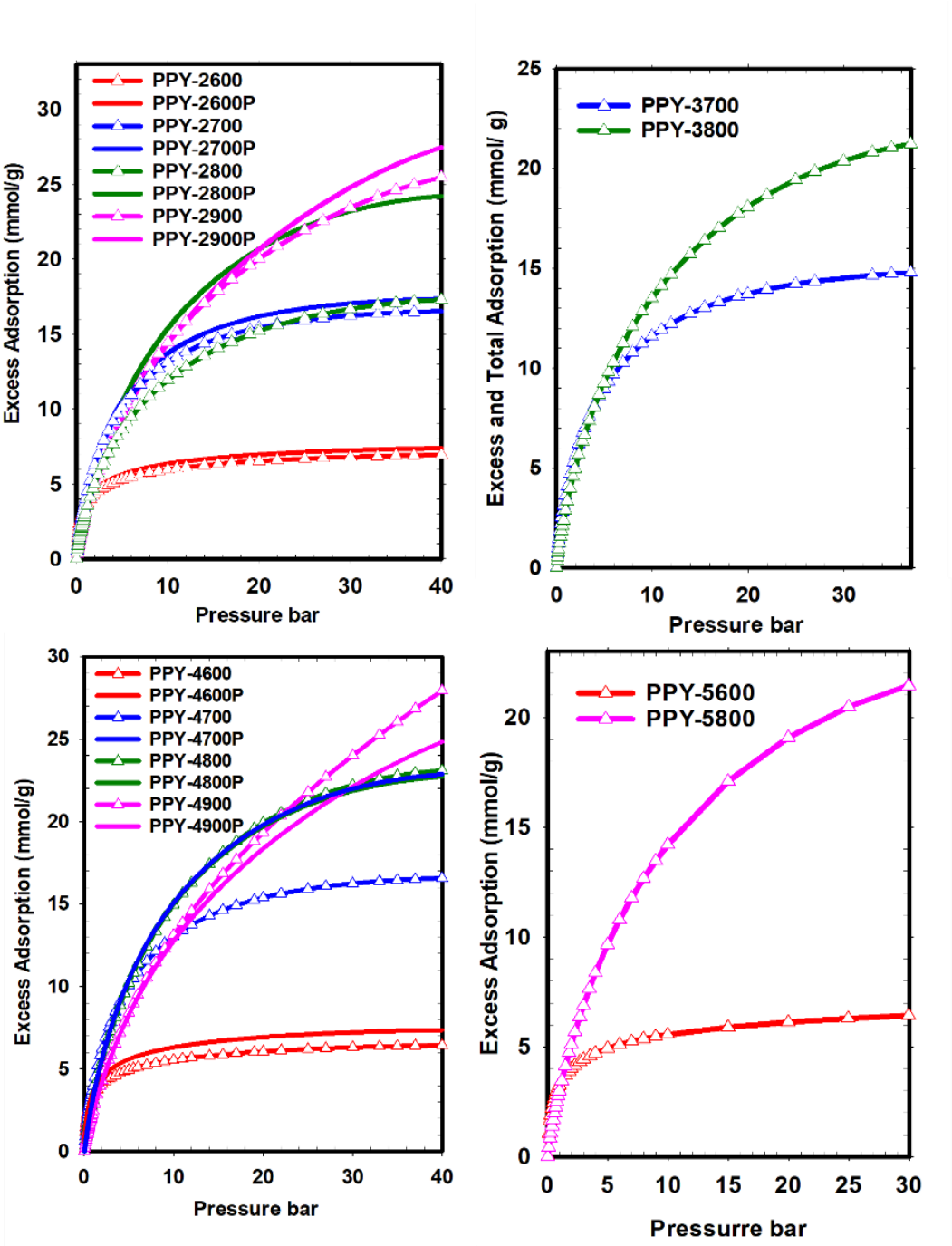


Figure 16. Excess CO_2 uptake at 25 °C for PPY derived carbons.

On the other hand, the CO_2 uptake capacity at high pressure depend on the total surface area and the pore volume. PPY-4900 (SA~ 3100 m^2/g and V_t 2.27 cm^3/g) and PPY-2900P (~3022 m^2/g and 1.77 cm^3/g) showed the best CO_2 uptake performance at high pressure. Up to 24.0 mmol/g @30

bar, and 28.0 mmol/g @40 bar for PPY-4900, and up to 25.0 mmol/g @30bar, and 27.6 mmol/g @40 bar for PPY-2900P.

Table 7. Excess CO_2 uptake at 25 °C for PPY derived carbons over the pressure range 1– 40 bar.

Sample	*0.15 bar*	*1 bar*	*20 bar*	*30 bar*	*40 bar*
PPY-2600	1.4	3.5	6.8	7.0	7.0
PPY-2600P	1.2	3.6	7.0	7.2	7.4
PPY-2700	0.9	4.1	15.3	16.2	16.7
PPY-2700P	0.6	4.1	16.1	17.0	17.2
PPY-2800	0.7	3.1	15.2	17.0	17.5
PPY-2800P	0.5	3.2	20.8	23.1	24.1
PPY-2900	0.6	3.1	20.0	23.5	25.3
PPY-2900P	0.4	2.7	20.7	25.0	27.6
PPY-3700	1.0	3.8	13.7	14.6	15.0
PPY-3800	0.6	3.0	18.0	20.3	22.0
PPY-3800P	0.7	3.3	19.5	21.6	22.5
PPY-4600	1.4	3.4	6.0	6.2	6.5
PPY-4600P	1.3	3.6	6.9	7.1	7.5
PPY-4700	0.9	4.0	15.2	16.1	16.8
PPY-4700P	0.5	3.2	19.9	22.0	23.0
ppy-4800	0.5	3.2	20.0	22.1	23.0
ppy-4800P	0.5	3.2	19.8	21.9	22.9
ppy-4900	0.4	2.4	19.2	24.0	28.0
ppy-4900p	0.5	2.4	18.3	22.1	24.9
PPY-5600	1.4	3.3	6.1	6.3	6.7
PPY-5800	0.7	3.1	19.0	21.0	23.0

Recent studies have attempted to determine the influence of N-doping on the CO_2 absorption of carbons, but the outcomes have been inconsistent. Some researchers have hypothesised that the nitrogen functionalities contained in N-doped carbons have no significant effect on CO_2 adsorption.[26,27] In contrast, several studies hypothesised that incorporation of N into a carbon surface increases hydrogen-bonding interactions between the carbon surface and the CO_2

molecules, which explains the superior CO_2 uptake of N-doped activated carbons. This contradicts the long-held belief that acid–base interactions between N-containing basic functional groups and acidic CO_2 gas are responsible for the improved CO_2 uptake of N-doped carbons.[28–31] This study observed that samples with a high nitrogen content showed higher CO_2 uptakes at low pressure. For example, at 1 bar, PPY-2600 gives a higher CO_2 uptake (up to 3.5 mmol/g) than PPY-2900 (3 mmol/g). This is despite the smaller surface area of PPY-2600. The nitrogen content of PPY-2600 and PPY-2900 were determined to be ~12% and ~1%, respectively, by elemental analysis. This trend is reversed at higher gas pressures. On the other hand, uptake at 1 bar is critically sensitive to pore size, and, in particular, to minute changes in micropore size distribution within the pore size range 6−10 Å.[27] Samples with pore volumes of 0.67-0.70 cm^3/g and pores of size 0.6 – 0.9 nm (PPY-2700, PPY-2700P, and PPY-4700) show the highest CO_2 uptake at 1 bar, up to ~4.1 mmol/g. The result also suggested that carbons with dominant, large micropore and mesopore structures could be ideal targets to achieve high CO_2 uptake capacities at high relative pressures (30 and 40 bar), especially for precombustion capture applications. For instance, samples with a high surface area give a higher CO_2 uptake. PPY-4900 and PPY-2900P demonstrate the highest CO_2 uptake at 30 bar, 24.0 and 25.0 mmol/g, and at 40 bar, 28.0 and 27.6 mmol/g, respectively.

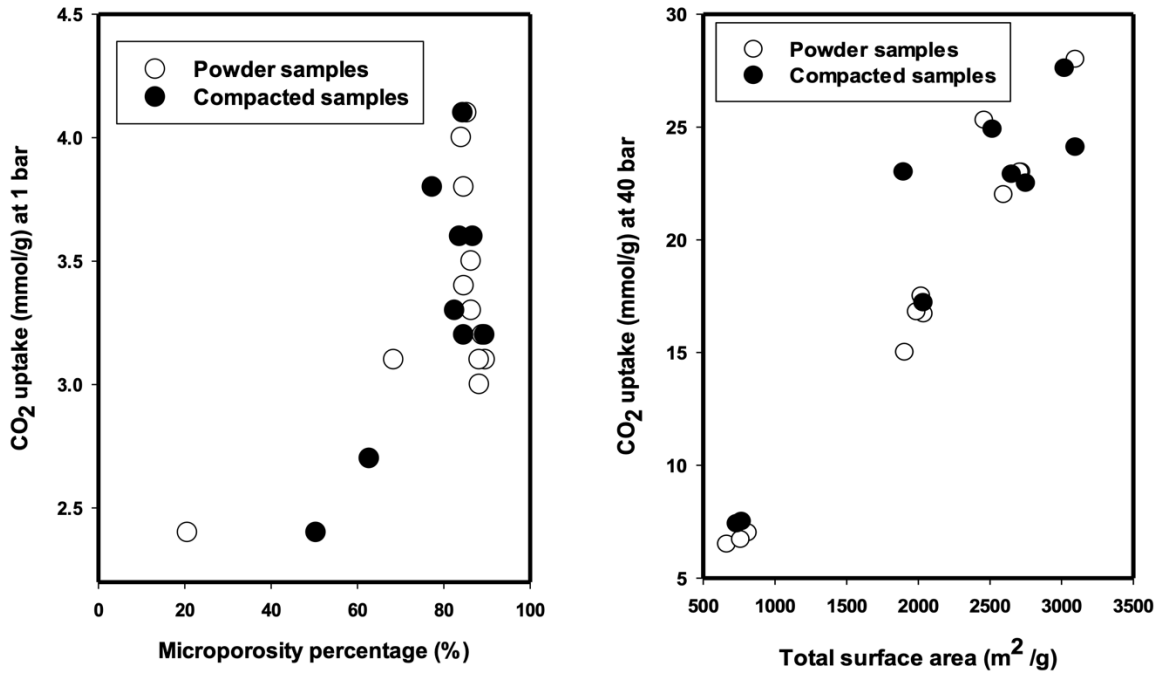


Figure 17: The effects of the amount of microporosity of samples on the CO_2 uptake at 1 bar and 25°C (left), and the effect of total surface area on the CO2 uptake at high pressure ~40 bar and 25°C (right).

The CO_2 uptake at 0.15 bar is regarded to be a near approximation of capture performance from post-combustion flue gas streams emerging from power stations, which typically contain 15–20% CO_2 together with primarily N_2 (70–75%) and water (~10%).[32,33] Samples activated at 600°C show the greatest CO_2 adsorption at 0.15 bar, with uptake between 1.2 and 1.4 mmol/g which is comparable to the highest values reported in literature of activated carbons.[18,27,34] However, as samples include up to 12.0 % N-content, it is hypothesised that incorporating nitrogen-containing functional groups into the pore structure of carbons improves the CO_2-adsorption capacity by a significant amount.[36] For instance, PPY-4600 (N- content of ~11.3 %) has a slightly better uptake performance than PPY-4600P (N- content of ~10.1 %).

Table 8. Excess gravimetric (mmol/g, and g/g), and volumetric (cm^3/cm^3) CO_2 uptake at 30 bar and 25 °C.

Sample	Excess CO_2 uptake at 30 bar		
	mmol/g	g/g	cm^3/cm^3
PPY-2800P	23.1	1.02	232.99
PPY-2900	23.5	1.03	289.70
PPY-2900p	25.0	1.1	252.16
PPY-4700P	22.0	0.97	374.76
PPY-4800	22.1	0.97	277.40
PPY-4900	24.0	1.05	199.04
PPY-4900p	22.1	0.97	247.67

3.3.4. Methane uptake

Methane is a small gas molecule with a kinetic diameter of approximately 3.8, so it can readily diffuse into activated carbons' micropores. Therefore, activated carbons with a high microporosity are typically more effective at storing methane. However, at high pressures, methane gas can condense into a liquid or solid, which necessitates the presence of larger mesopores or macropores.[10,37]

Multiple studies suggest that the optimal pore size range for methane storage on activated carbons is between 0.5 and 2 nm. This size range corresponds to micropores and small mesopores, which offer a high surface area and microporosity for methane absorption. At moderate pressures, the micropore volume and surface area of activated carbon are typically the most influential factors on methane uptake. At higher pressures, however, the mesopore and macropore volumes of activated carbons play a greater role in methane storage. [37,38]

As mentioned in the porosity and textural properties in tables 2-5 above, some the PPY-derived activated carbon samples contain high levels of microporosity along with some mesoporosity. Such a mix of porosity is a good indicator for good performance in CH_4 storage at pressures of 35–100 bar.[37,38] In addition, pore channels ranging in size from 0.8 to 1.5 nm are considered to be optimally suited for the adsorption of two or three methane molecules, which optimises the packing of the adsorbed phase within the pores. Additionally, it has been suggested that pores with a 1.1 nm diameter are the most suitable for methane storage. Based on their porosity (surface area > 2000 m^2/g and pore size range of 0.8–1.3 nm), the samples listed in Table 9 were assessed for CH_4 storage capacity. An initial focus was on the uptake at 35 bar, a pressure used widely in previous research that allows easy comparisons with benchmark materials. The excess and total gravimetric methane uptake isotherms are shown in Fig. 18. The total methane storage capacity can be calculated from the excess obtained experimentally by considering the methane density (under any given temperature and pressure conditions) and the total pore volume of the activated carbon according to equation 5.

$$\theta_{Tol} = \theta_{Exc} + d_{CH4} * v_t \quad \textit{Equation 5}$$

Where θ_{Exc} is the excess methane uptake, d_{CH4} is the density of the methane, and v_t is total pore volume.

Table 9. Textural properties and methane working capacity of PPY-derived carbons.

Sample	Packing density *g/cm³*	Volumetric surface area[a] m^2/cm^3	Surface area density[b] *m^2/cm^3*	Working capacity[c] cm^3/cm^3
PPY-2800	0.70	1415	2084	123
PPY-2900	0.55	1354	1783	112
PPY-2700P	0.72	1466	2166	109
PPY-2800P	0.45	1394	1750	95
PPY-2900P	0.45	1360	1707	99
PPY-3800P	0.53	1458	1937	105
PPY-4700	0.74	1472	2210	98
PPY-4800	0.56	1523	2211	111
PPY-4800P	0.58	1539	2089	110
PPY-4900P	0.50	1259	1625	92
PPY-5800	0.57	1544	2068	108

[a]Volumetric surface area = Surface area X packing density. [b]Surface area density = Total surface area/Total pore volume. [c]Working capacity is the difference in CH_4 uptake between 35 and 5 bar.

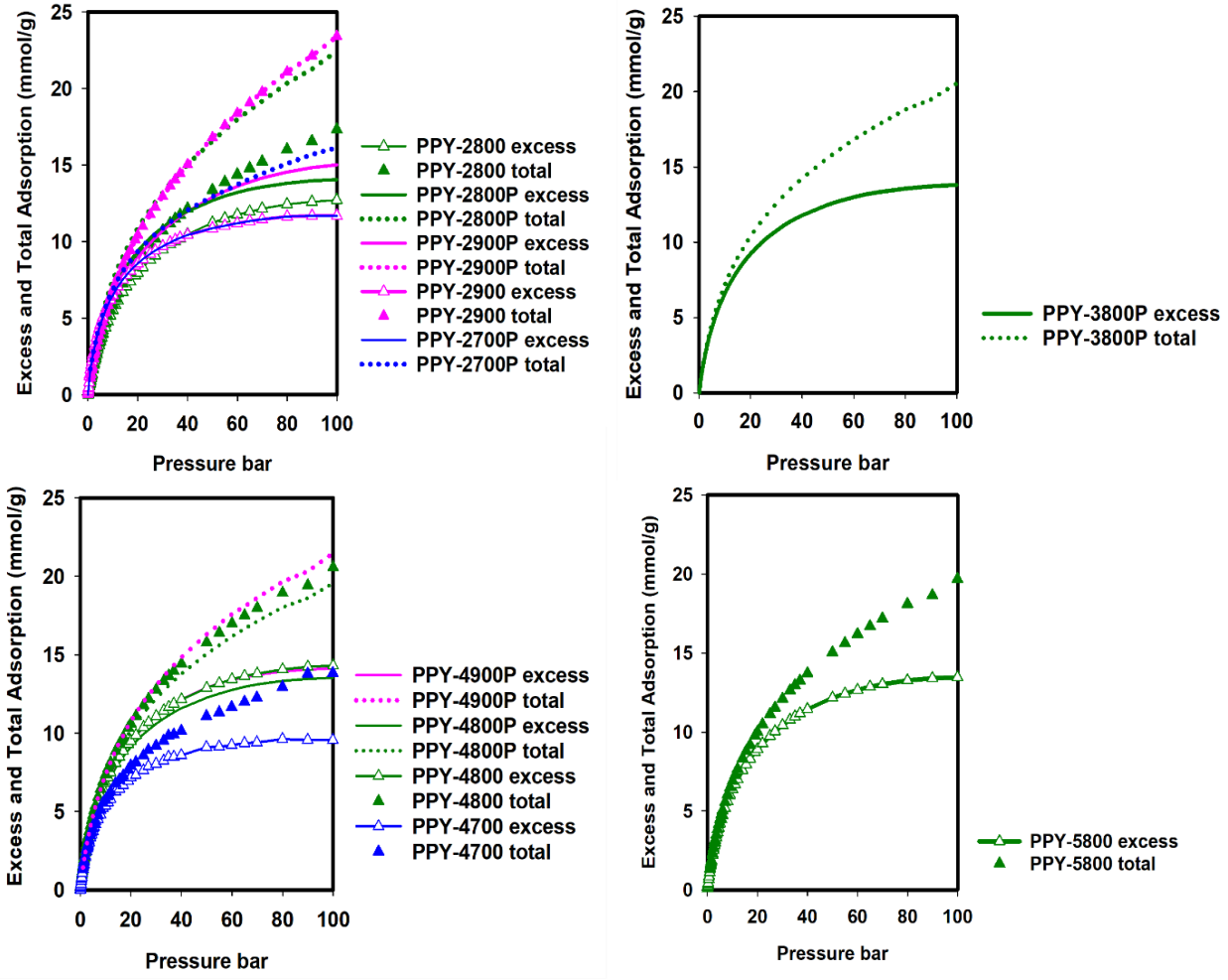


Figure 18. Excess and total CH_4 uptake for PPY-derived activated carbon at 25 °C.

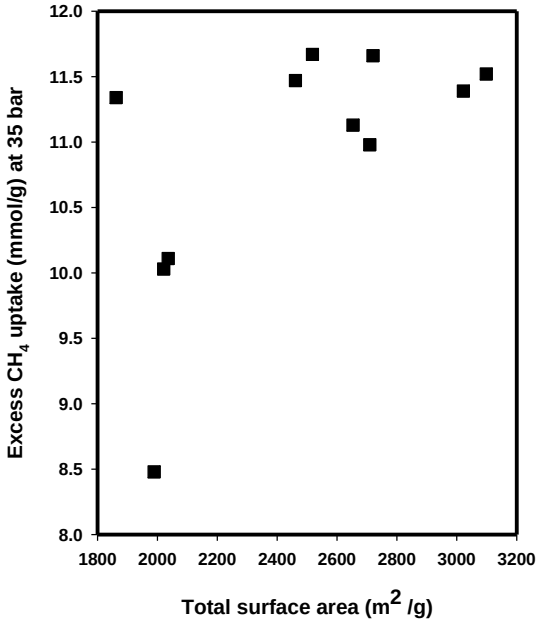


Figure 19: The correlation between the total surface area and methane uptake at 35 bar and 25°C.

The methane uptake at pressures up to 100 bar was fully reversible and exhibited no hysteresis for any samples. The excess and total gravimetric isotherms (Fig. 18) indicate that saturation was not reached in the pressure range of 0–100 bar, indicating that the present carbons have the potential to store more methane at higher pressures. Table 10 summarizes the amount of methane adsorbed at 5 and 35 bar; expressed as gravimetric (mmol/g and g/g) or volumetric (cm^3 (STP) / cm^3) uptake. At 35 bar, the excess uptake ranges from 8.5 to 11.7 mmol/g (equivalent to 0.14–0.19 g/g) and the total uptake is in the range of 9.8 -14.2 mmol/g (equivalent to 0.16–0.23 g/g). At 25 °C and 35 bar, the best performing samples with respect to excess methane gravimetric uptake are PPY2800P (11.5 mmol/g), and both PPY-4800 and PPY-4900 with uptake of 11.7 mmol/g. Such uptake is amongst the highest reported to date for any porous material.[37–41] On the other hand, the samples with the best total gravimetric uptake are PPY-2800P (14.2 mmol/g), PPY-2900P (14.1 mmol/g) and PPY-4900P (14.0 mmol/g). Such uptake is comparable or better than that reported to date for any porous material, i.e., up to ~12.0 mmol/g of ACDS4800 amongst others.[10,37–39,41] Volumetric uptake, which takes into the packing density of the carbons, is regarded as being the most crucial indicator of the methane storage capacity of any solid. The US Department of Energy (DOE) has set the target of the volumetric methane uptake at ambient temperature (25°C) and moderate pressure (35 – 100 bar) to be 263 cm^3(STP)/cm^3. A more optimised combination of porosity (84% microporosity, pore size of 0.9 nm, and pore volume of 0.94 cm^3/g) and packing density (0.72 g/cm^3) is responsible for the superior volumetric uptake performance of sample PPY-2700P (~186cm^3/cm^3). At 25 °C, the present PPY-derived carbons have volumetric methane uptake of 142 to 186 cm^3/cm^3 at 35 bar and 175 – 271 cm^3/cm^3 at 100 bar (Figure 20). Such storage capacity is comparable with the highest volumetric uptake previously reported for porous carbons, which at 35 bar is the best uptake to date is 222 cm^3 (STP) cm^{-3} for an activated carbon (ACDS4700) from aircarbonised date seed.[10,37,42,43]

Table 10. Excess and total gravimetric (mmol/g, and g/g) and volumetric (cm^3/cm^3) methane uptake at 25 °C and pressure of 5 and 35 bar of PPY-derived activated carbons.

Sample	Excess uptake						Total uptake					
	mmol/g		g/g		cm^3/cm^3		mmol/g		g/g		cm^3/cm^3	
	@5	@35	@5	@35	@5	@35	@5	@35	@5	@35	@5	@35
PPY-2800	3.48	10.03	0.06	0.16	54.6	157.4	3.7	11.5	0.06	0.18	57.7	180.3
PPY-2900	4.16	11.47	0.07	0.18	51.3	141.4	4.4	13.5	0.07	0.22	54.7	167.0
PPY-2700P	4.60	10.11	0.07	0.16	74.2	163.2	4.8	11.5	0.08	0.18	77.3	185.9
PPY-2800P	4.46	11.52	0.07	0.18	45.0	116.2	4.8	14.2	0.08	0.23	48.6	143.1
PPY-2900P	3.84	11.39	0.06	0.18	38.7	114.9	4.2	14.1	0.07	0.23	42.3	141.7
PPY-3800P	4.38	11.34	0.07	0.18	55.4	134.7	4.7	13.5	0.08	0.22	55.4	160.1
PPY-4700	3.74	8.48	0.06	0.14	62.0	140.7	3.9	9.8	0.06	0.16	65.1	163.1
PPY-4800	4.51	11.66	0.07	0.19	56.6	146.4	4.8	13.6	0.08	0.22	60.0	171.3
PPY-4800P	4.35	11.13	0.07	0.18	56.6	144.7	4.6	13.0	0.07	0.21	59.9	169.5
PPY-4900P	4.42	11.67	0.07	0.19	49.5	130.8	4.7	14.0	0.08	0.22	55.9	147.6
PPY-5800	4.21	10.98	0.07	0.18	53.8	140.3	4.5	13.0	0.07	0.21	57.2	165.5

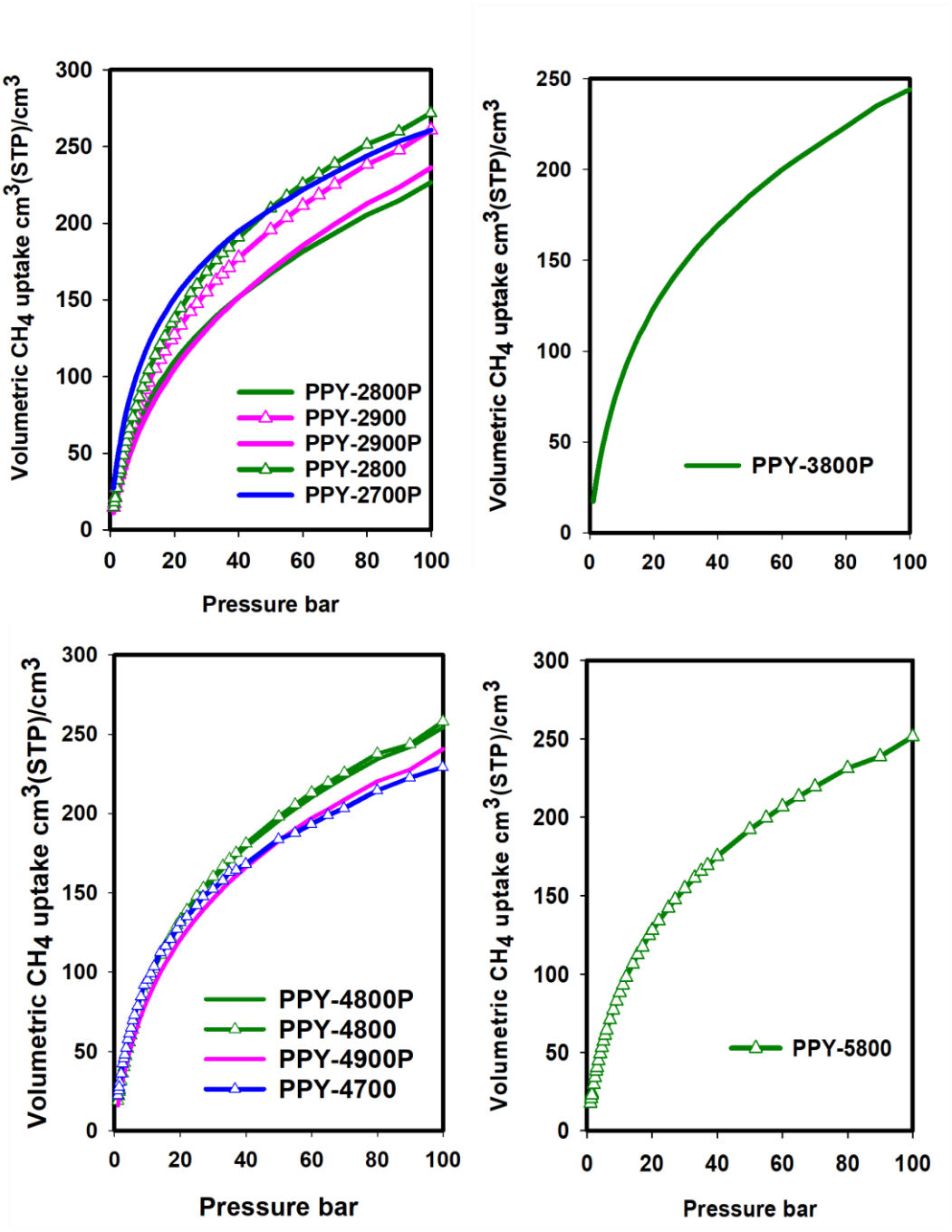


Figure 20. Volumetric CH_4 uptake for PPY-derived activated carbon at 25 °C.

The working capacity, which is the difference in uptake between the adsorption and desorption (regeneration) pressures, is also an important performance metric for porous materials. For methane storage, a desorption pressure of 5.8 bar is recommended, while we used an adsorption pressure of 35 bar. PPY-XY samples show moderate-to-high working capacity (92–123 cm^3/cm^3) as

shown in Table 9. At the high end, such working capacity for a 35 to 5 bar pressure swing is one of the highest reported to date.[10,37,42,43]

3.4. Conclusion

We have demonstrated that PO is an efficient activator for the generation of activated carbons from PPY using a direct, simplified method of synthesis. This is notable because PO is less corrosive and hazardous than conventional KOH. Carbons were activated with PO as powders or by including a compaction stage (compactivation), where a combination of PO and PPY was compressed prior to thermal activation. The majority of samples had a type I N_2 sorption isotherm, which is characteristic of microporous materials. The microporosity ranged from moderate to high (67 – 86% of surface area and/or pore volume) accompanied with pores of size 0.6 – 1.2 nm, along with high pore volume (>0.5 cm^3 g^{-1}). The PPY-derived activated carbons have excellent CO_2 capture and storage capabilities at both low pressures (up to 1.4 and 4.1 mmol/g at 0.15 and 1 bar, respectively), and high pressure (up to 25.0 and 28 mmol/g at 30 and 40 bar, respectively). In addition, the volumetric properties of the carbons (pore volume, packing density, volumetric surface area, and surface area density) acted simultaneously to ensure that they are a promising option for methane storage. At 25 ^oC, the carbons have volumetric methane uptake of 142 to 186 cm^3/cm^3, and 175-271 cm^3/cm^3 at 35 and 100 bar, respectively. This volumetric uptake is comparable with the highest values reported to date for porous carbons. At the same time, the carbons also have high total methane uptake up to 14.2 mmol/g (equivalent to 0.23 g/g), at 35 bar and 25°C.

3.5. References

1 J. Przepiórski, M. Skrodzewicz and A. W. Morawski, *Appl Surf Sci*, 2004, **225**, 235–242.

2 M. M. Maroto-Valer, Z. Tang and Y. Zhang, *Fuel Processing Technology*, 2005, **86**, 1487– 1502.

3 C. Pevida, M. G. Plaza, B. Arias, J. Fermoso, F. Rubiera and J. J. Pis, *Appl Surf Sci*, 2008, **254**, 7165–7172.

4 J. A. Thote, K. S. Iyer, R. Chatti, N. K. Labhsetwar, R. B. Biniwale and S. S. Rayalu, *Carbon N Y*, 2010, **48**, 396–402.

5 C. Pevida, T. C. Drage and C. E. Snape, *Carbon N Y*, 2008, **46**, 1464–1474.

6 M. Sevilla, P. Valle-Vigõn and A. B. Fuertes, *Adv Funct Mater*, 2011, **21**, 2781–2787.

7 M. Sevilla and A. B. Fuertes, *Energy Environ. Sci*., 2011, **4**, 1765-1771.

8 A. B. Fuertes and T. A. Centeno, *J Mater Chem*, 2005, **15**, 1079–1083.

9 M. Lezanska, P. Pietrzyk and Z. Sojka, *Journal of Physical Chemistry C*, 2010, **114**, 1208–1216.

10 A. Altwala and R. Mokaya, *Energy Environ Sci*, 2020, **13**, 2967–2978.

11 Y. He, W. Zhou, G. Qian and B. Chen, *Chem Soc Rev*, 2014, **43**, 5657–5678.

12 B. Li, H. M. Wen, W. Zhou, J. Q. Xu and B. Chen, *Chem*, 2016, **1**, 557–580.

13 B. Adeniran and R. Mokaya, *Nano Energy*, 2015, **16**, 173–185.

14 A. M. Aljumialy and R. Mokaya, *Mater Adv*, 2020, **1**, 3267–3280.

15 J. Li, Q. Jiang, L. Wei, L. Zhong and X. Wang, *J Mater Chem A Mater*, 2020, **8**, 1469– 1479.

16 Q. Jiang, Y. Wang, Y. Gao and Y. Zhang, *Environmental Science and Pollution Research*, 2019, **26**, 30268–30278.

17 M. Sevilla, N. Alam and R. Mokaya, *Journal of Physical Chemistry C*, 2010, **114**, 11314– 11319.

18 A. Altwala and R. Mokaya, *Energy Advances*, 2022, **1**, 216–224.

19 M. Sevilla, A. B. Fuertes and R. Mokaya, *Energy Environ Sci*, 2011, **4**, 1400–1410.

20 M. Sevilla, A. S. M. Al-Jumialy, A. B. Fuertes and R. Mokaya, *ACS Appl Mater Interfaces*, 2018, **10**, 1623–1633.

21 L. Shao, Y. Li, J. Huang and Y. N. Liu, *Ind Eng Chem Res*, 2018, **57**, 2856–2865.

22 K. S. W. Sing and R. T. Williams, *Adsorption Science and Technology*, 2004, **22**, 773– 782.

23 N. Balahmar, A. S. Al-Jumialy and R. Mokaya, *J Mater Chem A Mater*, 2017, **5**, 12330– 12339.

24 Y. Li, T. Ben, B. Zhang, Y. Fu and S. Qiu, *Sci Rep*, 2013, **3**, 1–6.

25 K. C. Yung, W. M. Wu, M. P. Pierpoint and F. v. Kusmartsev, *Contemp Phys*, 2013, **54**, 233–251.

26 M. Sevilla, J. B. Parra and A. B. Fuertes, *ACS Appl Mater Interfaces*, 2013, **5**, 6360– 6368.

27 B. Adeniran and R. Mokaya, *Chemistry of Materials*, 2016, **28**, 994–1001.

28 W. Xing, C. Liu, Z. Zhou, L. Zhang, J. Zhou, S. Zhuo, Z. Yan, H. Gao, G. Wang and S. Z. Qiao, *Energy Environ Sci*, 2012, **5**, 7323–7327.

29 K. V. Kumar, K. Preuss, L. Lu, Z. X. Guo and M. M. Titirici, *Journal of Physical Chemistry C*, 2015, **119**, 22310–22321.

30 B. Ashourirad, A. K. Sekizkardes, S. Altarawneh and H. M. El-Kaderi, *Chemistry of Materials*, 2015, **27**, 1349–1358.

31 L. Wang and R. T. Yang, *Journal of Physical Chemistry C*, 2012, **116**, 109–1106.

32 J. D. Figueroa, T. Fout, S. Plasynski, H. McIlvried and R. D. Srivastava, *International Journal of Greenhouse Gas Control*, 2008, **2**, 9–20.

33 Z. Zhang, K. Wang, J. D. Atkinson, X. Yan, X. Li, M. J. Rood and Z. Yan, *J Hazard Mater*, 2012, **229–230**, 183–191.

34 A. Almasoudi and R. Mokaya, *J Mater Chem A Mater*, 2014, **2**, 10960–10968.

35 A. Wahby, J. M. Ramos-Fernández, M. Martínez-Escandell, A. Sepúveda-Escribano, J. Silvestre-Albero and F. Rodríguez-Reinoso, *Chem Sus Chem*, 2010, **3**, 974–981.

36 A. H. Assen, Y. Belmabkhout, K. Adil, A. Lachehab, H. Hassoune and H. Aggarwal, *Chemical Engineering Journal*, 2021, **419**, 129569.

37 T. A. Makal, J. R. Li, W. Lu and H. C. Zhou, *Chem Soc Rev*, 2012, **41**, 7761–7779.

38 C. M. Simon, J. Kim, D. A. Gomez-Gualdron, J. S. Camp, Y. G. Chung, R. L. Martin, R. Mercado, M. W. Deem, D. Gunter, M. Haranczyk, D. S. Sholl, R. Q. Snurr and B. Smit, *Energy Environ Sci*, 2015, **8**, 1190–1199.

39 I. Angelidaki, L. Treu, P. Tsapekos, G. Luo, S. Campanaro, H. Wenzel and P. G. Kougias, *Biotechnol Adv*, 2018, **36**, 452–466.

40 J. A. Mason, M. Veenstra and J. R. Long, *Chem Sci*, 2014, **5**, 32–51.

41 J. Romanos, S. Sweany, T. Rash, L. Firlej, B. Kuchta, J. C. Idrobo and P. Pfeifer, *Adsorption Science & Technology*, 2014, **32**, 681-691.

42 M. E. Casco, M. Martínez-Escandell, E. Gadea-Ramos, K. Kaneko, J. Silvestre-Albero and F. Rodríguez-Reinoso, *Chemistry of Materials*, 2015, **27**, 959–964.

43 M. E. Casco, M. Martínez-Escandell, K. Kaneko, J. Silvestre-Albero and F. RodríguezReinoso, *Carbon N Y*, 2015, **93**, 11–21.

4. Mesoporous hierarchical carbon nanocages with high CH4 and CO2 adsorption under high pressure.

4.1. Introduction

Porous materials are of scientific and technological interest due to their ability to interact with atoms, ions and molecules at both their surface and throughout their bulk. Pore size has been classified according to its diameter into micropore (> 2 nm), mesopore (2 nm– 50 nm) and macropore (>5 0nm). The distribution of sizes, shapes and volumes of the pores in porous materials is linked to their ability to perform desired functions in specific applications. For instance, optimal pore characteristics provide maximum efficiency in separation or catalysis applications.

Porous activated carbons, ACs, which represent a class of non-oxide porous materials, are of great importance due to their applications in water and air purification, and as gas hosts, templates, or electrode components. The widespread use of ACs is due to their notable properties, such as the hydrophobicity of their surfaces, high surface area, large pore volume, chemical inertness, good thermal stability and mechanical stability, easy handling, and low manufacturing cost. Most ACs are primarily microporous with narrow pore size distribution (PSD)[1–7], and their natural composition makes them well suited to many applications involving small molecules, such as molecular sieving, adsorption and catalysis.

Since the preparation of activated carbons enables the fabrication of materials with a regulated architecture, template synthesis of materials has lately attracted a lot of interest.[8–16]By using template synthesis, a significant number of novel materials of considerable relevance for emerging applications have been created e.g., mesostructured silica materials (MSM), which have been synthesised by using surfactant micelles as templating agents[10,17,18]. The rigid structure and well-structured pore network of MSM make them appropriate for use as templates in the synthesis of materials with controlled structures and distinctive properties e.g., mesoporous carbons.[8,19–21]

Mesoporous carbon (MC) has attracted an enormous amount of scientific and technological interest due to its exceptional and intriguing properties such as: high specific surface area, high porosity, good thermal stability, stable mechanical durability, and unique mesoporous structure.[12,14,20,22,23] To synthesise MC materials with adjustable pore diameter and particle size, well-designed functionalities, uniform morphology, relatively high graphitization, and excellent repeatability remains a formidable challenge.

There are a number of potential uses in which the presence of mesopores would be preferable; for example, chromatographic separations, electrochemical double-layer capacitor applications, or in the adsorption of large hydrophobic molecules such as vitamins, dyes, and polymers. Therefore, the development of mesoporous and macroporous, as well as microporous carbon materials is of great importance for fundamental research and practical applications. Large pore volume is advantageous in high pressure gas storage applications such as CO_2 and CH_4 storage. Porosity of carbons can be developed and tailored via the chemical or physical activation of a carbon precursor. The latter can be obtained via the chemical activation of rich carbon chemicals (e.g., polypyrrole),[24] the chemical activation of biochar,[14,25] or via the activation of template-assisted carbon.

Mesoporous carbon MC can be prepared via templating method using different technologies to introduce the carbon precursor such as carbon vapour deposition, liquid impregnation and nanocasting that are explained in detail in the introduction chapter. Many templates have been employed including metals oxides e.g., SiO_2 [12]and MgO[26].

This carbon nanomaterial classification is based on the number of material dimensions that exceed the nanoscale (100 nm) range. Consequently, in zero-dimensional (0D) nanomaterials, all dimensions are measured on the nanoscale (none are greater than 100 nm). 0D nanomaterials are typically nanoparticles e.g., fullerene (1985). One dimension of one-dimensional nanomaterials (1D) exceeds the nanoscale. This category consists of nanotubes, nanorods, and nanowires. Two dimensions exceed the nanoscale in two-dimensional nanomaterials (2D). This category consists of graphene, nanofilms, nanolayers, and nanocoatings with plate-like structures. Three-dimensional nanomaterials (3D) are materials whose dimensions are not limited to the nanoscale. This category can include bulk granules, nanoparticle dispersions, nanowire bundles, nanotubes, and multi-

nanolayers. Currently, 3D hierarchical carbon nanostructures are gaining popularity because they can combine various advantages of individual building blocks, presenting unprecedented collaborative effects and vast potential applications.[27–31]

Hierarchical carbon nano cages are a variety of carbon-based material that forms cage-like hierarchical structures. These structures are composed of carbon atoms arranged in a three-dimensional network to create nanometer to micrometer sized enclosures that are interconnected. The hierarchical architecture of these structures refers to the fact that smaller enclosures are contained within larger cages. This configuration generates a complex and porous network with potential applications in numerous disciplines, such as energy storage, catalysis, and drug delivery. Typically, the synthesis of hierarchical carbon nano cages requires the use of a template, which can be a sacrificial material that is subsequently eliminated, leaving behind the carbon nano cages. These templates can be constructed from a variety of substances, such as silica, polymers, and biological molecules. [27–31]

Templating with MgO is known to be a useful technique for creating hierarchical mesoporous carbons with controlled pore sizes.[11,13,26,30,32] Studies have recently established an in-situ MgO template approach for producing hierarchical carbon nanocages (hCNCs). The studies have demonstrated that hCNCs functioned well in supercapacitor and battery applications.[29,30] The unique 3D structure of hCNCs, combined with the high surface area and large pore volume, are promising for gas storage applications. MgO was selected as a substrate due to its chemical and thermal stability, absence of structural and compositional changes or reactions with carbon, and easy dissolvability in acidic solutions for template removal.[14] The 3D hierarchical structure of MgO was replicated in the hCNCs carbons. The structure obtained is favourable due to its structural stability; for example, it avoids the agglomeration or restacking generally associated with 2D graphene due to the intrinsic π− π interaction. The resulting hCNCs had surface area of 1276 m^2/g and pore volume of 4.18 cm^3/g (Fig. 1).

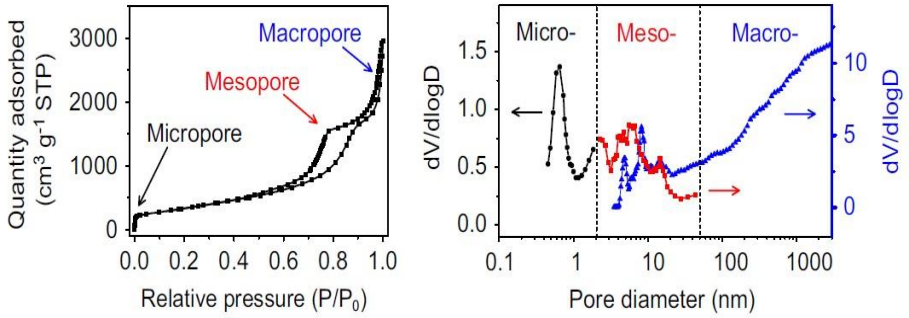


Figure 1: N_2 sorption isotherm (left) and PSD (right) of hCNCs prepared by Lyu et al.[29]

This chapter describes how to construct 3D hierarchical carbon nanocages (hCNCs) with a large surface area, network geometry, and coexisting micro-, meso-, and macro-pores. Preparation methods were developed to attain the target of having pore volume of up to 4.0 cm^3/g, to provide a high storage capacity for CO_2 and CH_4 at high pressure. The development includes: (i) studying the effect of chemical vapour deposition (CVD) duration on the hCNCs porosity and textural properties, (ii) employ the liquid impregnation technique and study the effect of that on the resultant hCNCs porosity in comparison with that prepared via (CVD) technique. In addition, the impact of chemical activation on the resulting templated carbons is also investigated. Furthermore, purity, thermal stability, textural characteristics, structural shape, and CO_2/CH_4 uptake capabilities are all determined using a variety of analytical techniques.

4.2. Experimental Section

4.2.1. The formation of hierarchical carbon nanocages (hCNCs)

Two methods were used to prepare hierarchical carbon nanocages (hCNCs). First, the magnesium oxide (MgO) template was formed by the thermal treatment of commercial magnesium carbonate pentahydrate ($MgCO_3.Mg(OH)_2.5H_2O$) at 800 □C with heating ramp rate 10 °C/min, followed by the introduction of benzene vapour, via CVD technique, for a specific time duration (30- 120 minutes) under an inert medium of nitrogen. Subsequently, the sample was allowed to cool under a flow of nitrogen. The MgO-hCNCs were then washed with 10% HCl to remove the template, followed by thorough washing with deionised water at until the filtrate achieved pH~7. The resultant hCNCs were dried at 60 °C for several hours and designated as Vap-hCNCs-x, where Vap indicates the form of benzene during deposition and ***x*** indicates the CVD duration in minutes.

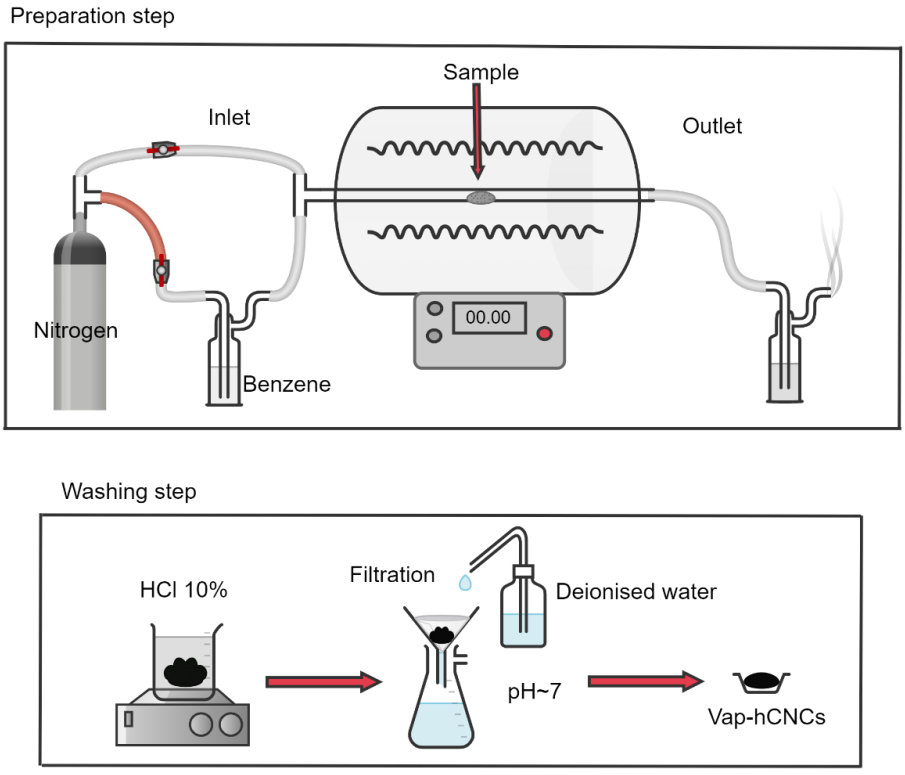


Figure 2: Preparation of Vap-hCNCs-X using the chemical vapour deposition CVD technique.

The second method was divided into two steps. The first step involved forming the MgO through the thermal treatment of commercial magnesium carbonate pentahydrate ($MgCO_3.Mg(OH)_2.5H_2O$) at

800□C for 1 h. The second step involved mixing the MgO with benzene via liquid impregnation (LI) and heating the resulting mixture to 800□C at ramp rate 10°C/min and holding for 120 minutes under a flow of nitrogen. Subsequently, the sample was allowed to cool under a flow of nitrogen. The resulting MgO-hCNCs were washed with 10% HCl to remove the template, followed thorough washing with deionised water until the filtrate achieved pH~7. The resultant hCNCs were dried at 60°C for several hours and designated as LI-hCNCs-120, where LI is the method of introducing benzene to the MgO and 120 is the carbonisation duration in minutes.

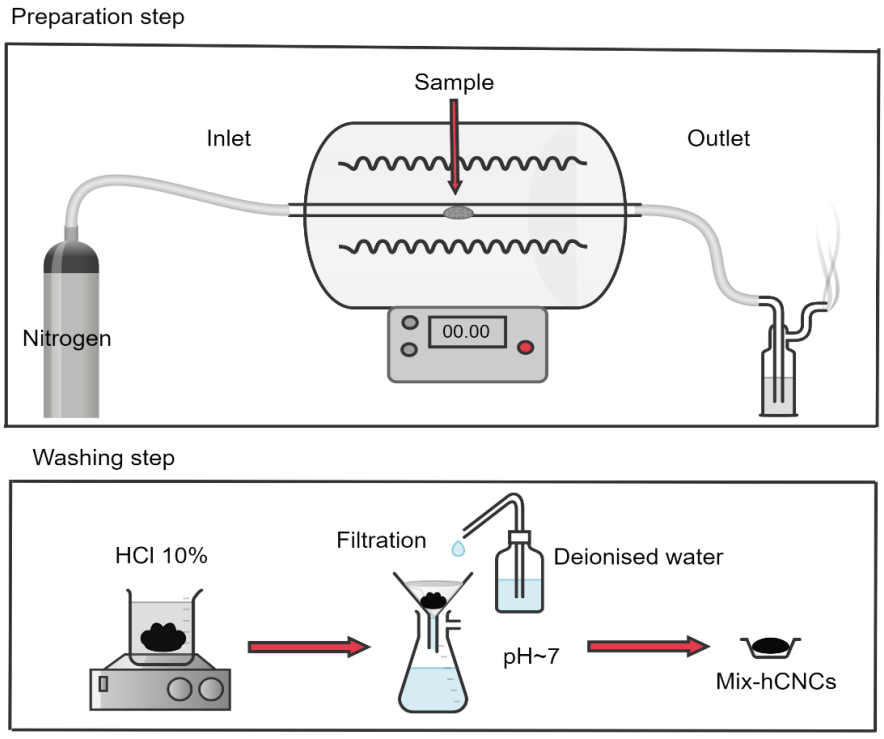


Figure 3: Preparation of LI-hCNCs-120 via the liquid impregnation LI technique.

4.2.2. The activation of hCNCs

For activation, 0.5 g of LI-hCNCs-120 was mixed with KOH at KOH/LI-hCNCs-120 ratio of 2, 4, or 6 and thermally treated at 800□C for 1 h following a heating ramp rate of 5°C/min. The activated hCNCs obtained were then washed with 10% HCl to remove any inorganic salts. Subsequently, multiple washes were performed with deionised water, until the water achieved pH~7. The resulting carbons were designated as AX-LI-hCNCs-120, where A indicates the activation process and X denotes the KOH/hCNCs ratio (2, 4 or 6).

4.2.3. Structural analysis

Thermogravimetric analysis (TGA) was performed to assess the purity and thermal stability of hCNCs. Powder X-ray diffraction (P-XRD) analysis was performed to confirm that the hCNCs produced were fully carbonaceous. Scanning electron microscopy (SEM) was performed using a JEOL 7100F FEG-SEM to study hCNCs morphology. Raman spectra were acquired using a HORIBA LabRAM HR Raman microscope (660 nm laser, <0.2 mW power). This was performed to confirm whether graphitisation had occurred. Porosity analysis was performed via nitrogen sorption with Micromeritics 3-FLEX and TriStar II PLUS sorptometers. For porosity analysis, ca. 0.15 g of sample was degassed under vacuum to eliminate any volatile matter that could be present in the pores of the carbons. Physisorption was then performed at -196 °C.

4.2.4. CH_4 and CO_2 uptake measurements

CH_4 and CO_2 uptake were determined using a Hiden Isochema XEMIS Analyser. Before the uptake measurements, the carbon samples were degassed at 240°C under vacuum for several hours. Adsorption-desorption isotherms were obtained at 25 °C, over methane (CH_4) pressure range of 0 – 100 bar, and (CO_2) pressure range 0-40 bar.

4.3. Results and Discussion

4.3.1. Nature and structure of MgO

In this study, commercial magnesium carbonate pentahydrate ($MgCO_3.Mg(OH)_2.5H_2O$) was used to generate the MgO template via thermal treatment up to 800 °C. Thermogravimetric analysis (TGA) was performed to assess the thermal stability of the resulting MgO template. As illustrated in the TGA curve in Fig. 4, the magnesium carbonate pentahydrate was dehydrated by removing four molecules of water at approximately 250 °C, followed by the elimination of another water molecule via the dihydroxylation of $MgCO_3.Mg(OH)_2$ at between 250 °C and 350 °C. The resulting $MgCO_3$ was decarbonised by the elimination of four molecules of CO_2 at temperatures greater than 350 °C.

$$4MgCO_3 \cdot Mg(OH)_2 \cdot 5H_2O \longrightarrow 4MgCO_3 \cdot Mg(OH)_2 + 5H_2O \quad \textit{Equation 2}$$

$$4MgCO_3 \cdot Mg(OH)_2 \longrightarrow 4MgCO_3 + MgO + H_2O$$ *Equation 3*

$$4MgCO_3 \longrightarrow 4MgO + 4CO_2$$ *Equation 4*

At 500°C, the resultant MgO was stable, with no weight decrease up to 1000°C. The MgO yield was calculated by the following equation:

$$Product\ yield\ (\%) = \frac{mass\ of\ dry\ MgO}{mass\ of\ dry\ Magnesium\ carbonate\ pentahydrate} \times 100$$ *Equation 5*

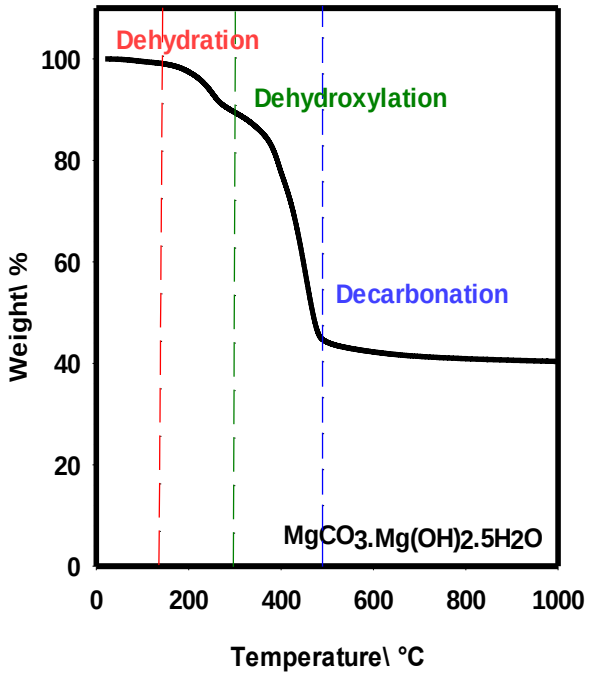


Figure 4: Thermogravimetric analysis for a commercial magnesium carbonate pentahydrate under air flow at heating ramp rate of 10°C /min.

Approximately 50% yield of MgO was obtained. The basic magnesium carbonate has 3D hierarchical morphological character.[29] This distinctive structure is retained in the MgO template, as shown in Fig. 5.

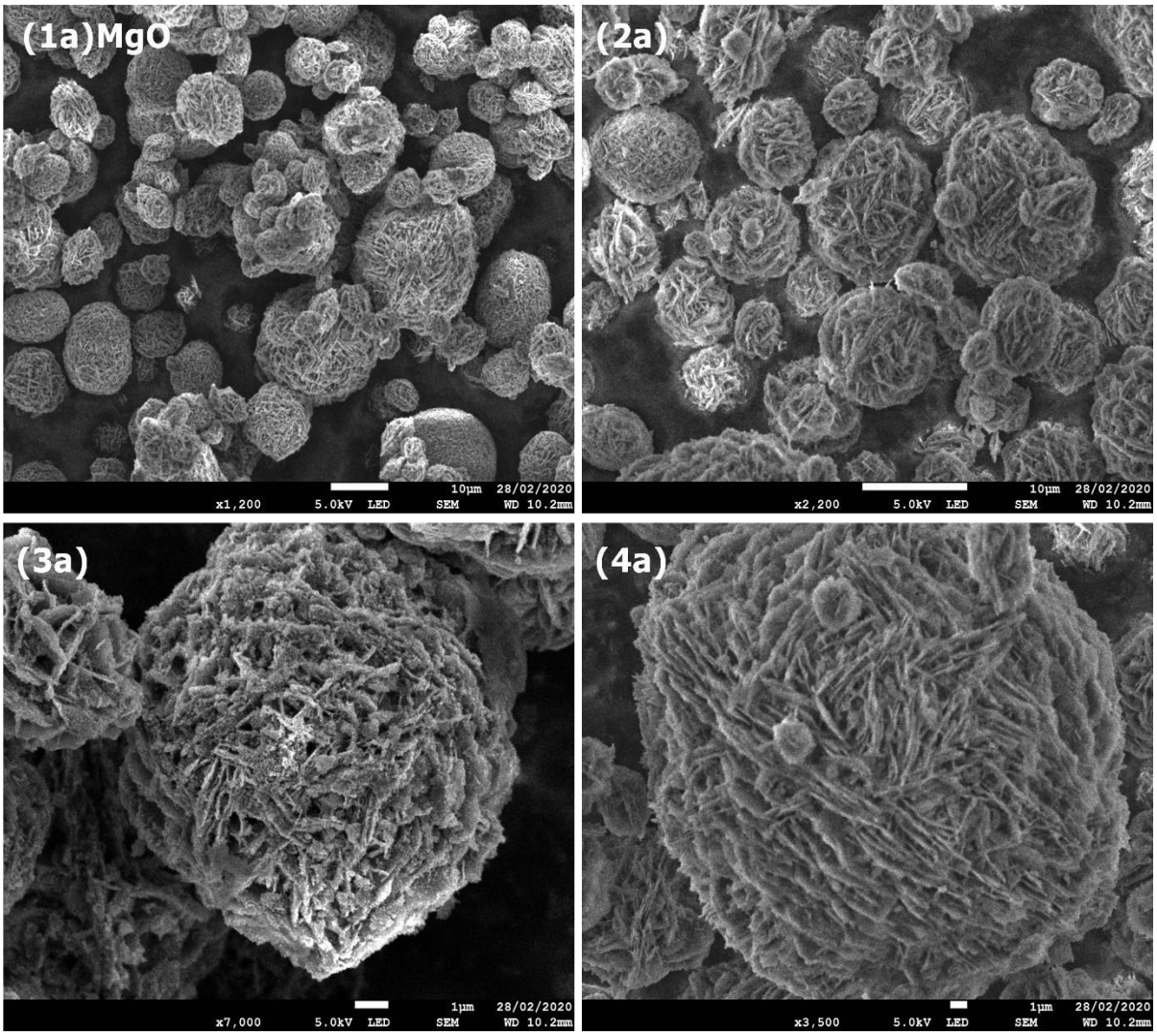


Figure 5: SEM images of MgO used as template.

Porosity and textural analysis

Nitrogen sorption analysis was then performed to verify the meso-structural properties of the MgO. As shown in Fig. 6, the sorption isotherm is IV type. Characteristic features of the type IV isotherm are a hysteresis loop, which is associated with capillary condensation taking place in mesopores, as well as the limiting uptake over a range of high P/P_o.

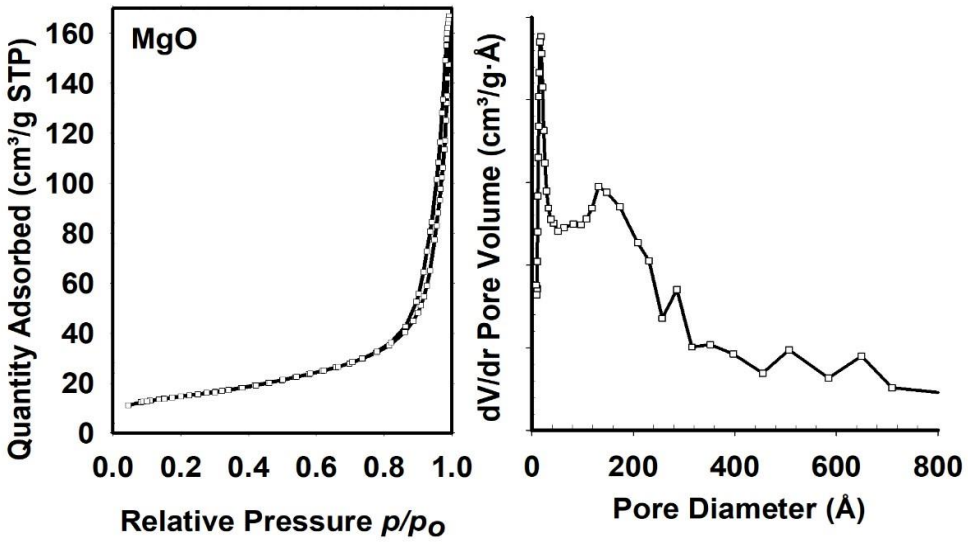
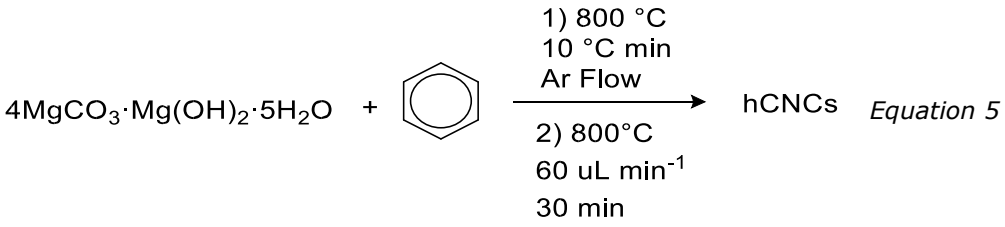


Figure 6: N_2 sorption isotherm of MgO (left) and corresponding pore size distribution curve.

The MGO had surface area of 51 m²/g and pore volume of 0.25 cm³/g, with pores of size between 2 and 14 nm.

4.3.2. Structure of hCNCs carbons

Previously, hCNCs have been synthesised using MgO as a template and benzene as a carbon source via the CVD technique,[29] as illustrated in the following equation:



Equation 5

The 3D hierarchical structure of MgO was replicated in the hCNCs carbons. The structure obtained is favourable due to its structural stability; for example, it avoids the agglomeration or restacking generally associated with 2D graphene due to a particular type of dispersion force from Van der Waals forces, which is established between unsaturated (poly)cyclic molecules that called intrinsic π– π interaction.

In this study, the method of Lyu et al.[29] was employed to prepare 3D hCNCs, which were found to have surface area of 1552 m^2/g, which is higher than that reported by Lyu *et.al.,* However, the pore volume 1.5 cm^3/g, was much lower. The synthesis method was then modified in an attempt to achieve surface area above 1500 m^2/g and pore volume greater than 3 cm^3/g. For this purpose, two methods were proposed. In the first method, hCNCs were prepared via chemical vapour deposition (CVD) of the carbon precursor (benzene) onto the MgO template, and the CVD duration was varied between 30 and 120 minutes. In the second method, deposition of benzene onto the MgO template was achieved via liquid impregnation (LI).

4.3.3. Vap-hCNCs carbons prepared via chemical vapour deposition.

As mentioned in the experimental section, carbon nanocages were obtained via two different systems that introduced benzene. The first system, CVD, had a poor yield of hCNCs (see below), which was not sufficient for any subsequent activation. The VaphCNCs, however, exhibited significant porosity depending on synthesis conditions as described below.

Nature of Vap-hCNCs carbons

TGA was performed to assess the thermal stability and purity of all samples. The TGA curves in Figure 7 confirmed the fully carbonaceous nature of the Vap-hCNCs. The TGA curves show a significant mass decrease between 500–650°C, indicating that Vap-hCNCs have high thermal stability. Samples had differences in thermal stability depending on differences in CVD duration, with a higher deposition duration providing more carbon content, and higher thermal stability. At ~650°C, the carbon content was burned off in all samples with no residual mass.

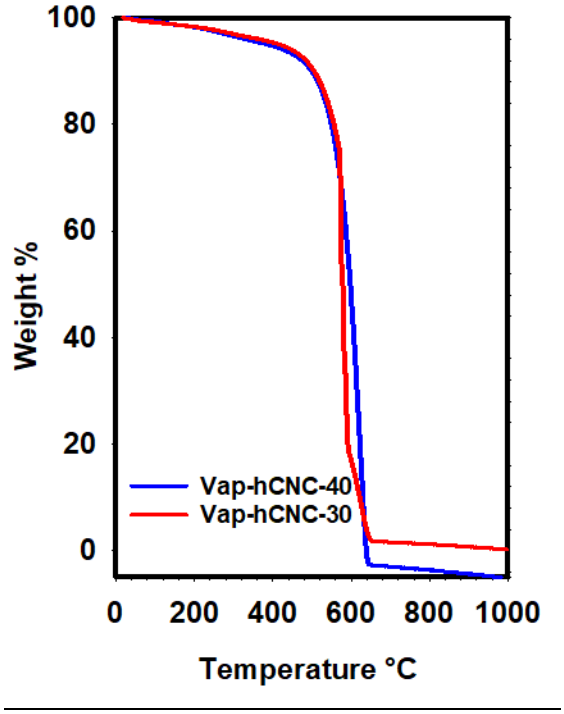


Figure 7: TGAs curves of representative Vap-hCNCs samples under air flow and heating ramp rate of 10 °C/min.

Table 1 below shows the elemental composition of Vap-hCNCs-X samples. The C content ranges from 85.6 to 97.3 % while the O content is relatively low at between 2.7% and 14.4 %. The C-content increased as the duration of benzene deposition increased. The longest deposition duration resulted in the highest C-content of 97.3 %, accompanied with the lowest O-content of 2.7 %.

Table 1. Yield and elemental composition of Vap-hCNCs-X samples. O-content is calculated as O %= 100 - (C%+ H%+ N%).

Sample	*C%*	*H%*	*N%*	*O%*
Vap-hCNCs-30	90.8	0.2	0.0	9.1
Vap-hCNCs-40	85.6	0.1	0.0	14.4
Vap-hCNCs-60	90.6	0.1	0.0	9.3
Vap-hCNCs-90	94.5	0.3	0.0	5.2
Vap-hCNCs-120	97.3	0.0	0.0	2.7

XRD was performed to determine whether amorphous materials had been made, and to assess the level of graphitisation. The XRD patterns in Figure 8 show that the Vap-hCNCs are non-graphitic. No graphitic XRD diffractions are observed for any of the samples.

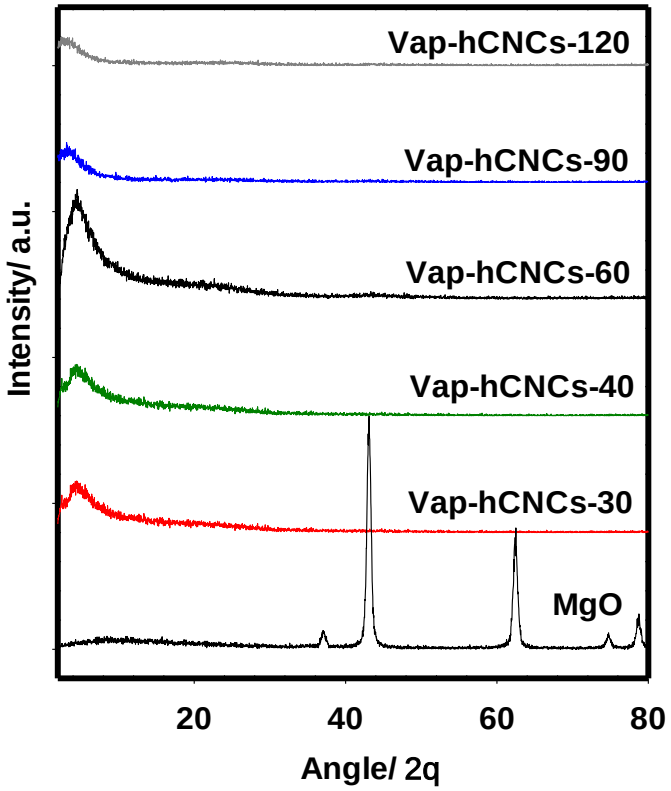


Figure 8: XRD patterns for MgO and Vap-hCNCs samples.

SEM images (Fig. 9) show that the structural features of MgO (Fig. 5) are replicated in Vap-hCNCs-60, which retains the unique 3D hierarchical structure of MgO.

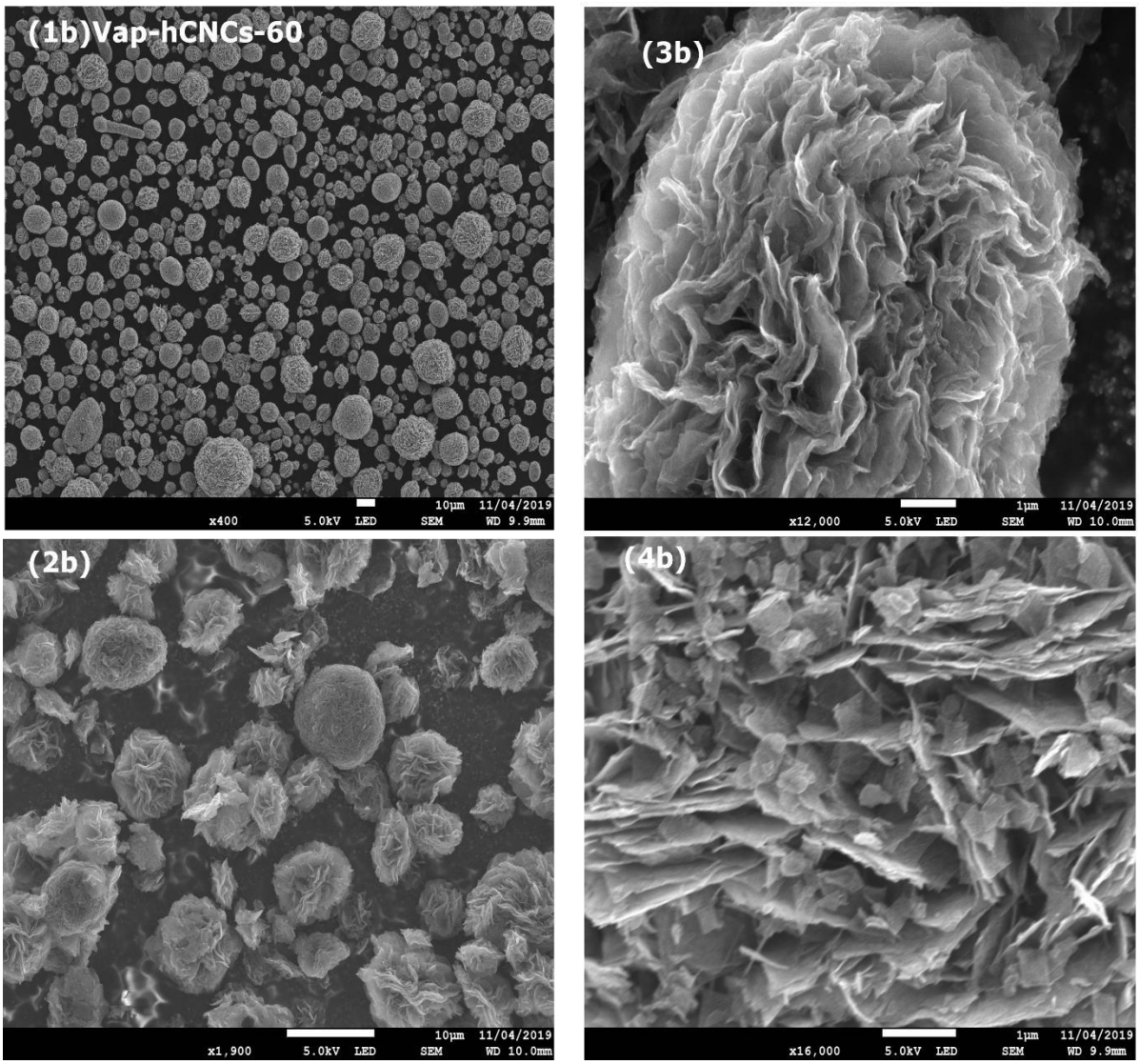


Figure 9: SEM images of Vap-hCNCs-60.

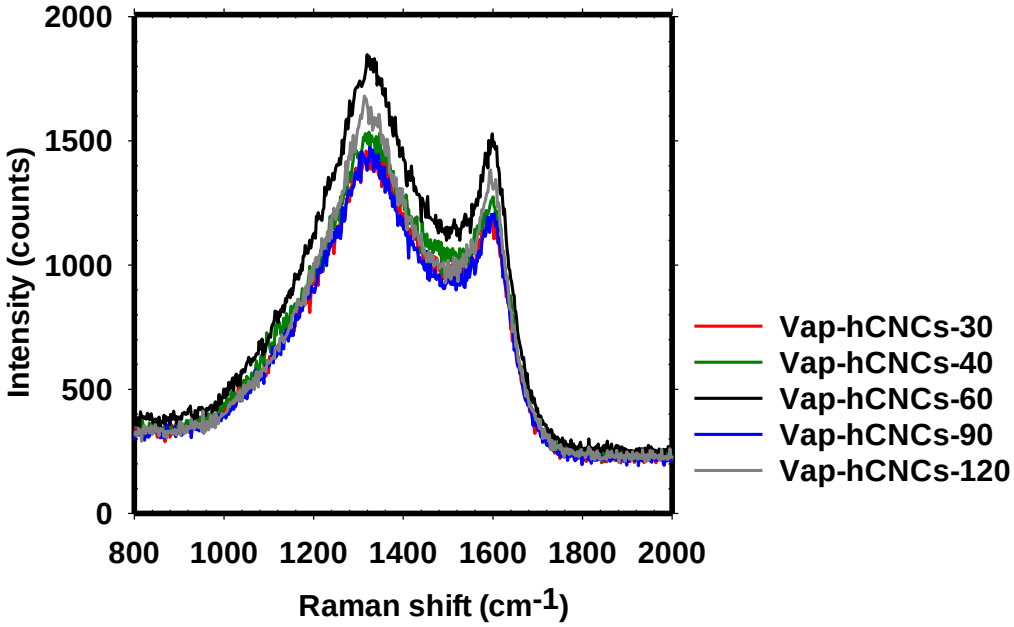


Figure 10: Raman spectra of Vap-hCNCs-X samples.

Raman spectra for the Vap-hCNCs carbons are shown in Fig.10, and exhibit bands at 1300 cm^{-1} and 1600 cm^{-1}, which are the D-peak (disordered carbon) and the G-peak (graphitic domains), respectively. The Raman spectra reveals the homogeneous nature of VaphCNCs-X samples. It shows that Vap-hCNCs-X carbons are not graphitic, which is consistent with the XRD patterns. The Raman spectra are dominated by bands 1332–1337 cm^{-1}, which are the so-called D-peaks arising from disordered carbon. The G peaks (1590– 1598 cm^{-1}) from graphitic domains are much diminished. The ratio of peak intensity (i.e., area) of the G-peak to D-peak (I_G/I_D ratio) is 0.83 for Vap-hCNCs-120, Vap-hCNCs-90 and Vap-hCNCs-60, and 0.84 for Vap-hCNCs-30 and Vap-hCNCs-40.

Table 2: The ratio of peak intensity of the G-peak to D-peak (I_G/I_D ratio) of Vap-hCNCs-x samples.

Sample	I_D	I_G	I_G/I_D
Vap-hCNCs-30	1338	1594	0.84
Vap-hCNCs-40	1334	1596	0.84
Vap-hCNCs-60	1328	1595	0.83
Vap-hCNCs-90	1326	1594	0.83
Vap-hCNCs-120	1323	1590	0.83

Porosity and textural properties analysis

Nitrogen sorption isotherms of the Vap-hCNCs-X and the derived pore size distributions PSD are shown in Fig. 11. All the isotherms are type IV indicating that the Vap-hCNCs-X are mesoporous as expected.[29] Hysteresis loops are observed, suggesting that there exist a variety of pore shapes.[33] It is important to mention that the duration of the chemical vapour deposition (CVD) process can have a substantial impact on the porosity of the resultant carbons.[34,35] The greater the duration of the CVD process, the denser the carbon layer deposited on the template, which has multiple effects on the porosity. The carbon layer may not be dense enough to form a porous structure if the CVD process duration is too short. In this instance, the carbon material is dense and impermeable. Therefore, extending the duration of the CVD process can result in the deposition of a denser carbon layer, which increases the likelihood that fissures will form in the material. Moreover, as the duration of the CVD process increases, the carbon atoms can become more densely compressed, resulting in a more compact structure. This can contribute to a reduction in the material's porosity. However, if the processing conditions are meticulously managed, the CVD process duration can be used to create a material with the desired level of porosity.[29,30,34,35]

The duration of the CVD procedure can also influence the pore size and distribution of carbon materials. As the carbon atoms have more time to diffuse and rearrange to produce larger cavities, longer deposition durations can result in apertures that are larger. Conversely, shortened deposition

durations can result in smaller apertures because diffusion and rearrangement have less time to occur.[34,35] As illustrated in Table 3 below, the surface area and pore volume are increased with benzene deposition duration from 1552 m^2/g and 1.5 cm^3/g (Vap-hCNC-30) to 1711 m^2/g and 1.6 cm^3/g (Vap-hCNC-40). However, the surface area decreased slightly at durations of 60, 90 and 120 minutes, with significant rises in pore volume to between 2.9 and 3.9 cm^3/g. The increase in porosity occasioned at longer benzene deposition duration was accompanied by a decrease in the packing density of the Vap-hCNCs carbons.

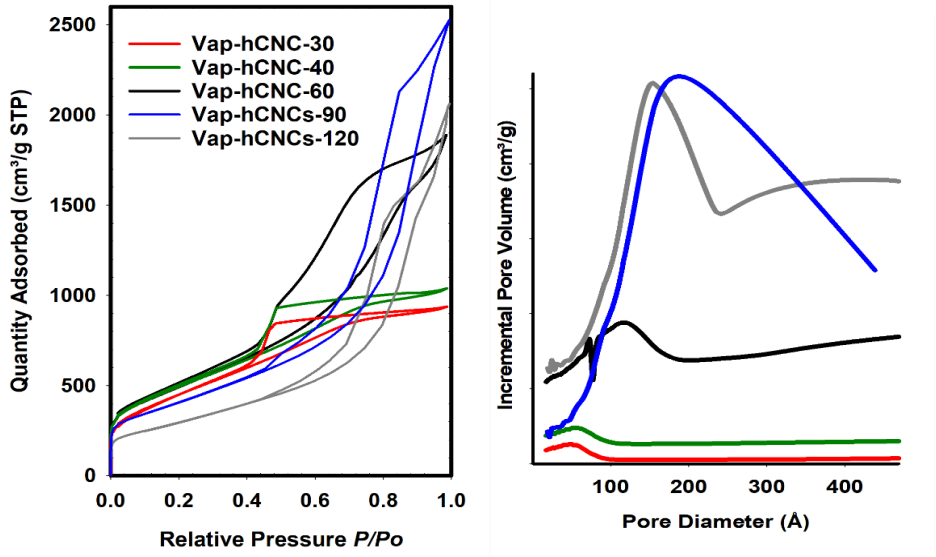


Figure 11: N_2 sorption isotherms (left) and corresponding pore size distribution curves (right) for all Vap-hCNCs-X samples.

Table 3: Yield and textural properties of Vap-hCNCs-X carbons.

Sample	C-deposition period (min)	*Yield (%)*	surface area (m^2/g)	Pore size (nm)	Pore volume (cm^3/g)	Packing density (g/cm^3)
MgO	-	50	51	2/14	0.25	-
Vap-hCNC-120	120	6.6	1071	15	3.2	0.27
Vap-hCNC-90	90	3.5	1465	19	3.9	0.23
Vap-hCNC-60	60	3.0	1685	12	2.9	0.29
Vap-hCNC-40	40	2.2	1711	49	1.6	0.48
Vap-hCNC-30	30	1.6	1552	49	1.5	0.50

CO_2 uptake

Increases in surface area and pore volume enhance the adsorption of an adsorbate by providing adsorbed molecules with an increased surface with which to interact and more space to occupy, respectively. This is nonetheless constrained by pore size, which can make one adsorbent more suitable for storing a gas than another.[23,36–38] In particular, high mesoporosity and high pore volume (> 2.0 cm^3/g) are thought to be suited for precombustion CO_2 capture.[39,40] The CO_2 uptake isotherms of the Vap-hCNCs samples are shown in Figure 12. Both excess and total uptake show continuous, in some cases almost linear, increase as pressure rises. This may be ascribed to the high pore volume of the carbons, meaning that high CO_2 uptake occurred at the greater pressures and that the uptake does not approach saturation even at 40 bar. The CO_2 uptake, in general, correlates with the CVD duration and surface area. Vap-hCNCs-60 shows the highest excess uptake (23.4 mmol/g) at 40 bar on account of possessing a suitable mix of surface area, pore volume and pore size distribution. Vap-hCNCs-120 has both the lowest excess uptake at 40 bar, and the lowest surface area, suggesting a putative link between total surface area and excess CO_2. Due to their mesoporosity, as shown in Table 4, the present carbons have low CO_2 uptake at low pressure with

storage capacity of 1 – 1.9 mmol/g at 1 bar. The uptake then rapidly increases in line with surface area with no apparent saturation up to 40 bar.

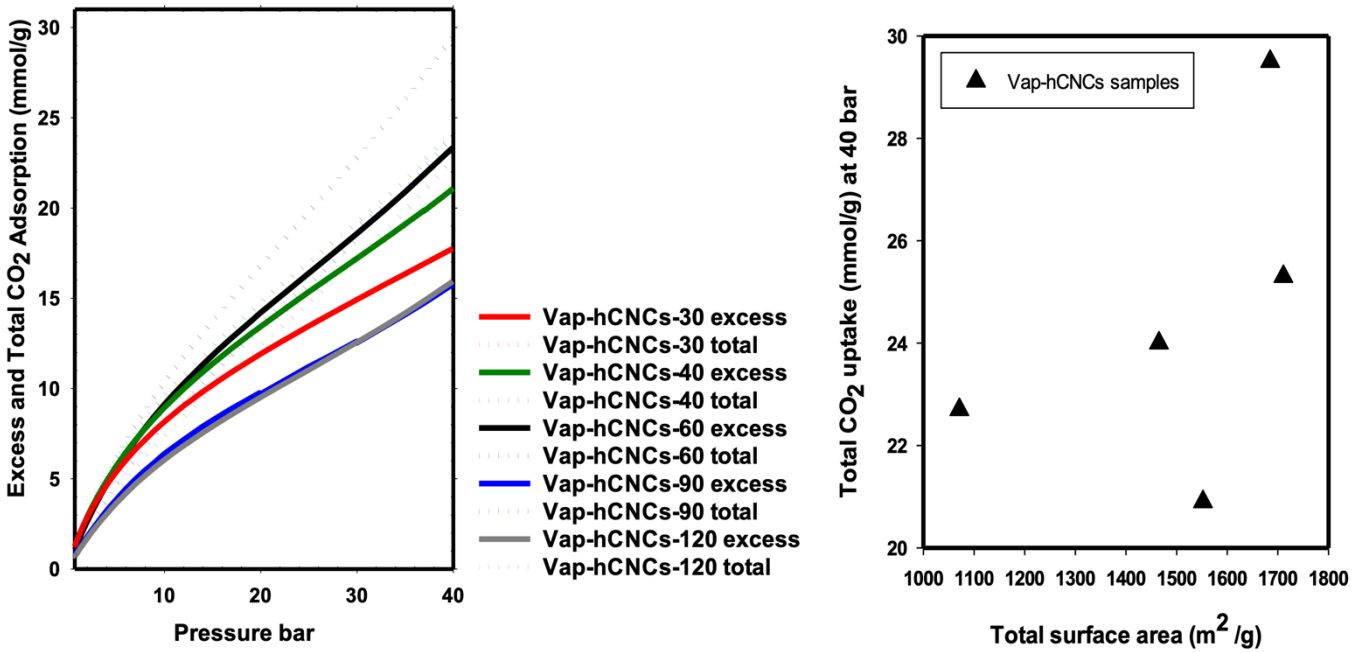


Figure 12: Excess and total gravimetric CO_2 uptake of Vap-hCNCs-X samples at 25 °C (left), and the effect of the increase of total surface area in the total CO_2 uptake at 40 bar and at 25 °C (right).

Table 4: Excess CO_2 uptake of Vap-hCNCs-X samples at 25°C.

Sample	*1 bar*	*20 bar*	*30 bar*	*40 bar*
Vap-hCNCs-120	1.0	6.5	8.3	16.0
Vap-hCNCs-90	1.0	9.5	12.5	15.7
Vap-hCNCs-60	1.7	15.0	19.0	23.4
Vap-hCNCs-40	1.9	13.4	17.6	21.9
Vap-hCNCs-30	1.8	11.9	14.9	17.8

Table 5 gives the excess gravimetric uptake (as g/g) and the excess volumetric uptake, which takes into account the packing density. At 1 bar, the g/g excess uptake is low at 0.04 to 0.08 but increases to impressive values of up to 1 g/g at 40 bar. The dependence of excess volumetric uptake on both

the gravimetric capacity and packing density means that Vap-hCNCs-40 has the highest (236 cm^3 STP/cm^3) value at 40 bar.

Table 5: Excess gravimetric CO_2 uptake (mmol/ g and g/g), and volumetric (cm^3 (STP)/ cm^3) uptake of Vap-hCNCs carbons at 25°C.

Sample	Excess CO_2 uptake					
	mmol/g		g/g		cm^3(STP)/cm^3	
	1 bar	40 bar	1 bar	40 bar	1 bar	40 bar
Vap-hCNCs-120	1.0	16.0	0.04	0.70	3.8	61
Vap-hCNCs-90	1.0	15.7	0.04	0.69	3.8	60
Vap-hCNCs-60	1.7	23.4	0.07	1.03	11.1	152
Vap-hCNCs-40	1.9	21.9	0.08	0.96	20.4	236
Vap-hCNCs-30	1.7	17.8	0.08	0.78	20.2	200

The total uptake of the present carbons is a good indicator of their potential for high pressure CO_2 capture applications. For instance, the separation of CO_2 from natural gas typically occurs at elevated CO_2 partial pressures of up to 30 bar.[41,42] Table 6 shows the total CO_2 uptake of Vap-hCNCs-X samples. The samples show high levels of total capacity at high pressure of up to 29.5 mmol/g at 40 bar. The total uptake is significantly higher than the excess values due to the high pore volume of the present carbons. Vap-hCNC-60 has total uptake of 22.8 mmol/g at 30 bar, which is close to the best porous carbons reported in the literature (e.g. SU-AC-400 with capacity of 28.3 mmol/g at 30 bar).[42] The uptake of Vap-hCNC-60 is even more impressive at 40 bar reaching exceptional storage capacity of close to 30 mmol/g. As shown in Figure 13 and Table 6, the present carbons, on account of their high total gravimetric uptake at 40 bar, have impressive volumetric uptake that reaches 272 cm^3 STP/cm^3 for Vap-hCNC-40. This high volumetric uptake shows that the enhanced pore volume allows for high gravimetric uptake of CO_2 at relatively high pressure (40 bar), which

compensates for the relatively low packing density. These findings illustrate how large pore volume carbons, such as the present nanocages, may be applied to gas storage applications at high pressure.

Table 6: Total gravimetric (mmol/g and g/g), and volumetric (cm^3(STP)/cm^3) CO_2 uptake of VAP-hCNCs samples at 25°C.

Sample	Total CO_2 uptake								
	mmol/g			g/g			cm^3(STP)/cm^3		
	1 bar	30 bar	40 bar	1 bar	30 bar	40 bar	1 bar	30 bar	40 bar
Vap-hCNC-120	1.1	17.2	22.7	0.05	0.8	1.0	6.7	104	137
Vap-hCNC-90	1.1	18.9	24.0	0.05	0.8	1.1	5.8	97	124
Vap-hCNC-60	1.8	22.8	29.5	0.08	1.0	1.3	10.4	148	192
Vap-hCNC-40	2.0	19.5	25.3	0.09	0.9	1.1	18.3	210	272
Vap-hCNC-30	1.8	17.1	20.9	0.08	0.8	1.0	20.2	192	234

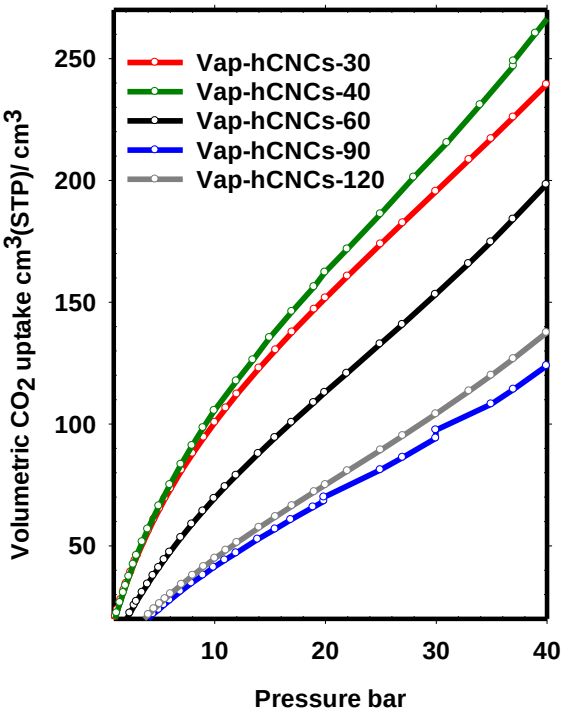


Figure 13: Volumetric CO_2 uptake of Vap-hCNCs-X samples at 25 °C.

Methane uptake measurements

Adsorbed natural gas (ANG) is a superior option to cryogenic or compressed methane storage. As illustrated in Table 4, Vap-hCNCs carbons have moderate to high surface area, accompanied by large pore volume. Generally, at high pressure (i.e., 100 bar), methane gravimetric uptake is dependent on surface area and pore volume.[43–45] As shown in Figure 14 and summarised in Table 7, the Vap-hCNCs carbons have moderate to high excess gravimetric uptake, in the range of 4.3 - 8.4 mmol/g at 35 bar, and 5.3 - 11.5 mmol/g at 100 bar. Vap-hCNC-60 has the highest excess gravimetric uptake of 8.4 mmol/g (~0.13 g/g) and 11.5 mmol/g (~0.18 g/g) at 35 and 100 bar, respectively. However, the porosity properties suggested that low pressure adsorption of CH_4 would be limited due to the fact that adsorption at low pressure is governed by micropore surface area and volume, which are at low levels for the Vap-hCNCs carbons. On the other hand, Vap-hCNCs carbons have large pore volume, which plays a significant role in total uptake at higher pressures. VaphCNC-90 shows the highest total uptake, 13.4 and 29.9 mmol/g (equivalent to 0.21 and 0.48 g/g) at 35 and 100 bar, respectively.

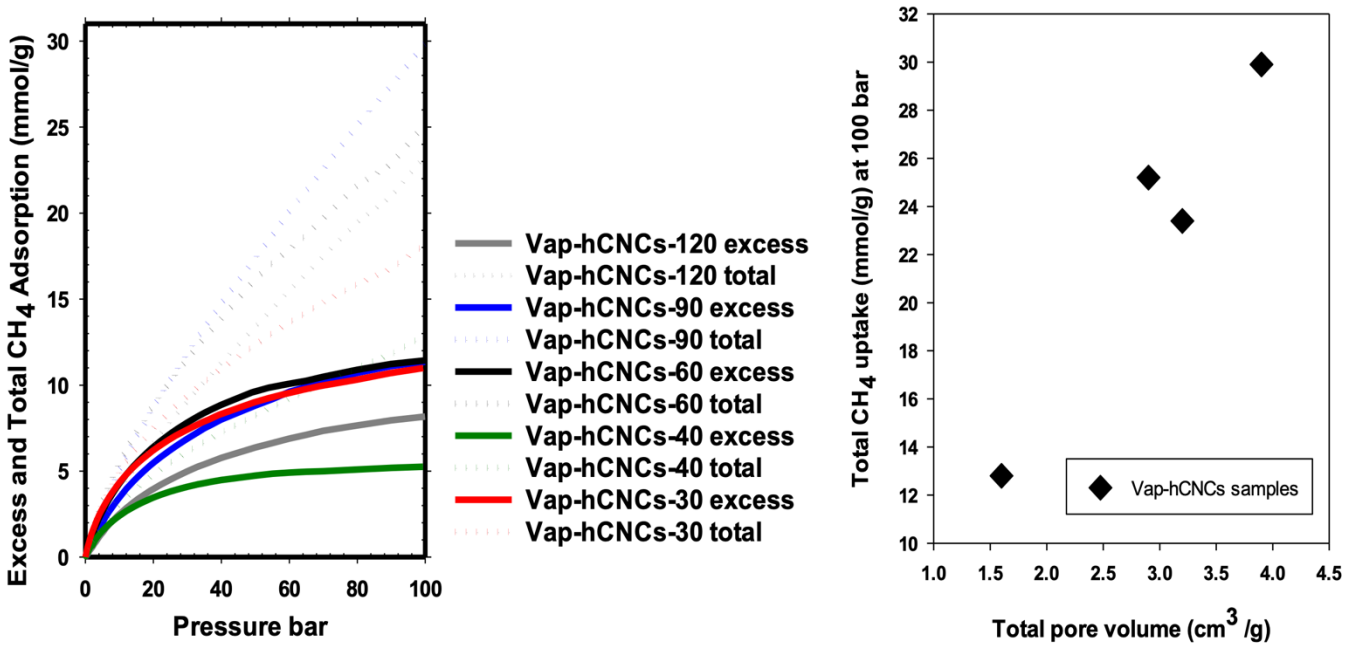


Figure 14: Excess and total CH_4 uptake of Vap-hCNCs-X samples at 25°C (left), and the correlation between the total pore volume and totalCH_4 uptake at 100 bar and 25°C (right).

Table 7: Gravimetric excess and total CH_4 uptake at 25 °C and pressures of 5, 35 and 100 bar.

Sample	Gravimetric Methane uptake											
	@5				@35				@100			
	mmol/g		g/g		mmol/g		g/g		mmol/g		g/g	
	Excess	Total	Excess	Total	Excess	Total	Excess	Total	Excess	Total	Excess	Total
Vap-hCNC-120	1.4	2.1	0.02	0.03	4.6	10.2	0.09	0.16	8.2	23.4	0.13	0.37
Vap-hCNC-90	2.0	2.8	0.03	0.05	7.5	13.4	0.12	0.21	11.4	29.9	0.12	0.48
Vap-hCNC-60	2.7	3.3	0.04	0.05	8.4	12.8	0.13	0.21	11.5	25.2	0.18	0.40

Vap-hCNC-40	1.5	1.9	0.02	0.03	4.3	6.7	0.07	0.11	5.3	12.8	0.08	0.21
Vap-hCNC-30	2.8	3.1	0.04	0.05	7.8	10.1	0.13	0.16	11.0	18.1	0.18	0.29

The uptake of Vap-hCNCs carbons is higher than that of mesoporous carbon derived from MOFs,[46] COFs,[47,48] and MOFs, including benchmark examples such as MOF-177 and HKUST-1.[49] In addition, the gravimetric uptake of 0.4 and 0.48 g/g, respectively, for VaphCNC-90 and Vap-hCNC-60 is very close to the gravimetric uptake target set by the US Department of Energy (DoE) of 0.5 g/g at ambient temperature and pressure of 35 – 100 bar.[44]

In fact, due to its poor correlation with volumetric capacity, gravimetric surface area is becoming a less important factor for CH_4 storage [43–46,50,51]. As a result, measurements such as packing density and volumetric surface area (surface area * packing density) are frequently mentioned in addition to, or in place of, the conventional gravimetric value[32–].[52] The DoE has recently revised the methane storage target volumetric capacity of 263 (cm^3/cm^3) at pressure range (35-100). The volumetric uptake of Vap-hCNCs-X samples at 100 bar and 25°C are range 141-207 cm^3 (STP)/cm^3), The highest volumetric uptake is observed in Vap-hCNCs-30 which has volumetric uptake of 207 cm^3 (STP)/cm^3).

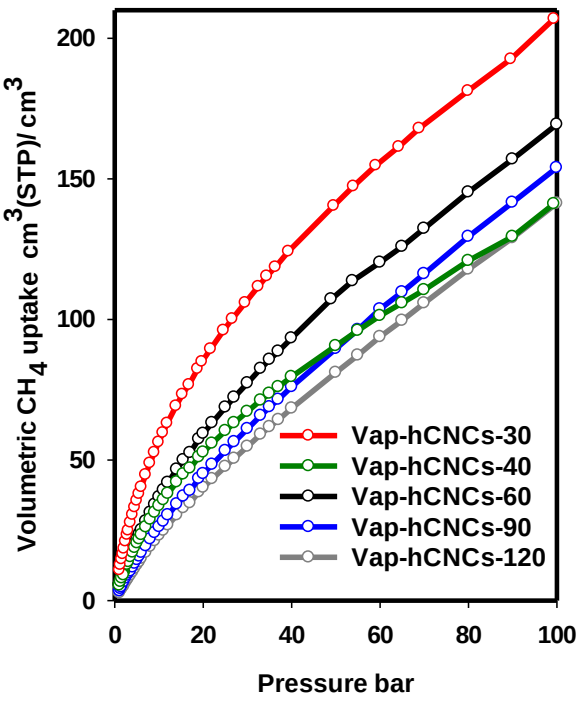


Figure 15: Volumetric CH_4 uptake measurements of Vap-hCNCs-X samples at 25°C and pressures at a range of 1–100 bar.

Table 8: Volumetric excess and total CH_4 uptake at 25 °C and pressures of 5 and 35 bar.

Sample	Volumetric uptake @5 bar $cm^3(STP)/cm^3$		Volumetric uptake @100 bar $cm^3(STP)/cm^3$		Volumetric surface area m^2/cm^3	surface area density m^2/cm^3
	Excess	Total	Excess	Total		
Vap-hCNCs-120	8.5	12.6	50	141.3	289	335
Vap-hCNCs-90	10.3	14.5	59	154.0	337	376
Vap-hCNCs-60	16.3	21.9	74	169.5	489	581
Vap-hCNCs-40	15.1	20.4	57	141.1	821	1069
Vap-hCNCs-30	29.1	35.6	123	207.0	776	1035

* Volumetric surface area = Surface area*packing density *Surface area density = Total BET SA/total pore volume.

4.3.4. LI-hCNCs-120 templated carbon prepared via liquid impregnation.

The liquid impregnation approach was used in an effort to address the low yield via the CVD route. The LI method is also likely to be more amenable to scale up. As mentioned in the experimental section, 30 g of $MgCO_3.Mg(OH)_2.5H_2O$ was thermally treated at 800 □C to yield 12 g (~40% yield) of MgO. The MgO was then mixed with 20 ml of benzene and the resulting LI-hCNCs-120 was washed with 10% HCl to remove the MgO template, followed by multiple washes with deionised water until the water achieved a level of pH 7.

Nature and structure of LI-hCNCs-120

The TGA curve in Fig. 16 confirms the carbonaceous nature of LI-hCNCs carbons and shows a large mass decrease between 590 and 670 °C, indicating significant thermal stability for the LI-hCNCs. At ~680 °C, the carbon content was burned off, and no carbon or residual weight remained.

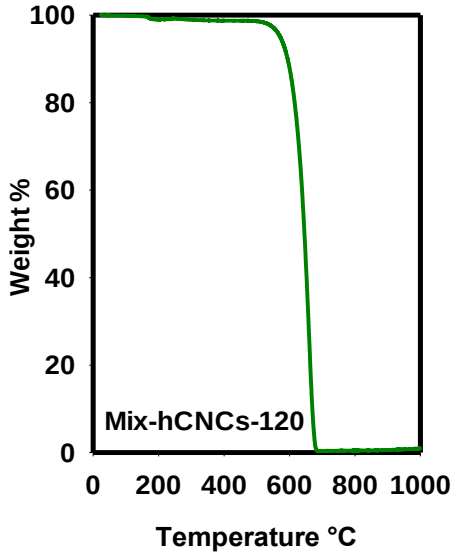


Figure 16: TGA curve for LI-hCNCs sample under air flow and heating ramp rate of 10 °C/min.

XRD was performed to determine whether amorphous materials had been created, and/or the level of graphitisation if any. The XRD patterns in Fig. 17 show peaks centred at ca. 2θ = 26° and 44°, the peak at 2θ = 26° corresponds to the (002) diffraction of graphitic planes. The intensity of this peak corresponds to the regularity of the graphene structure within the sample. The weak and low

intensity peak at 2 θ = 23– 26° indicates a very low level of graphitisation that is similar to that of Vap-hCNCs samples. The morphology of LIhCNCs-120 (Fig. 18) shows 3D hierarchical carbon nanocages similar to cages prepared via the CVD technique.

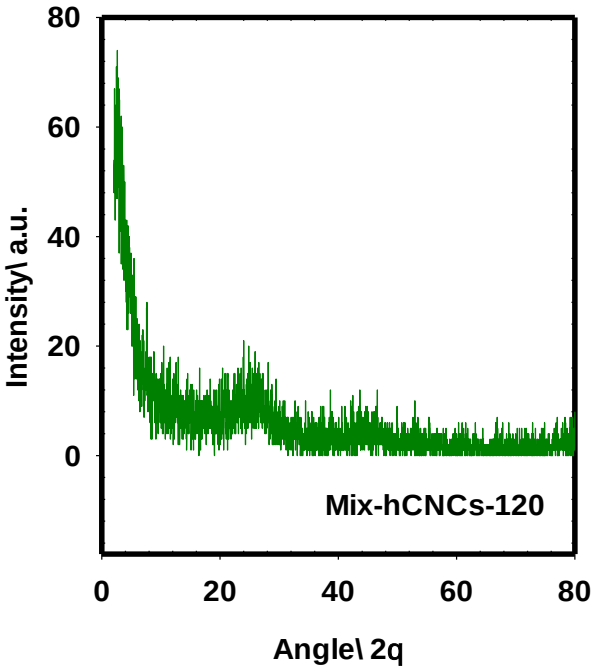


Figure 17: XRD patterns for LI-hCNC-120.

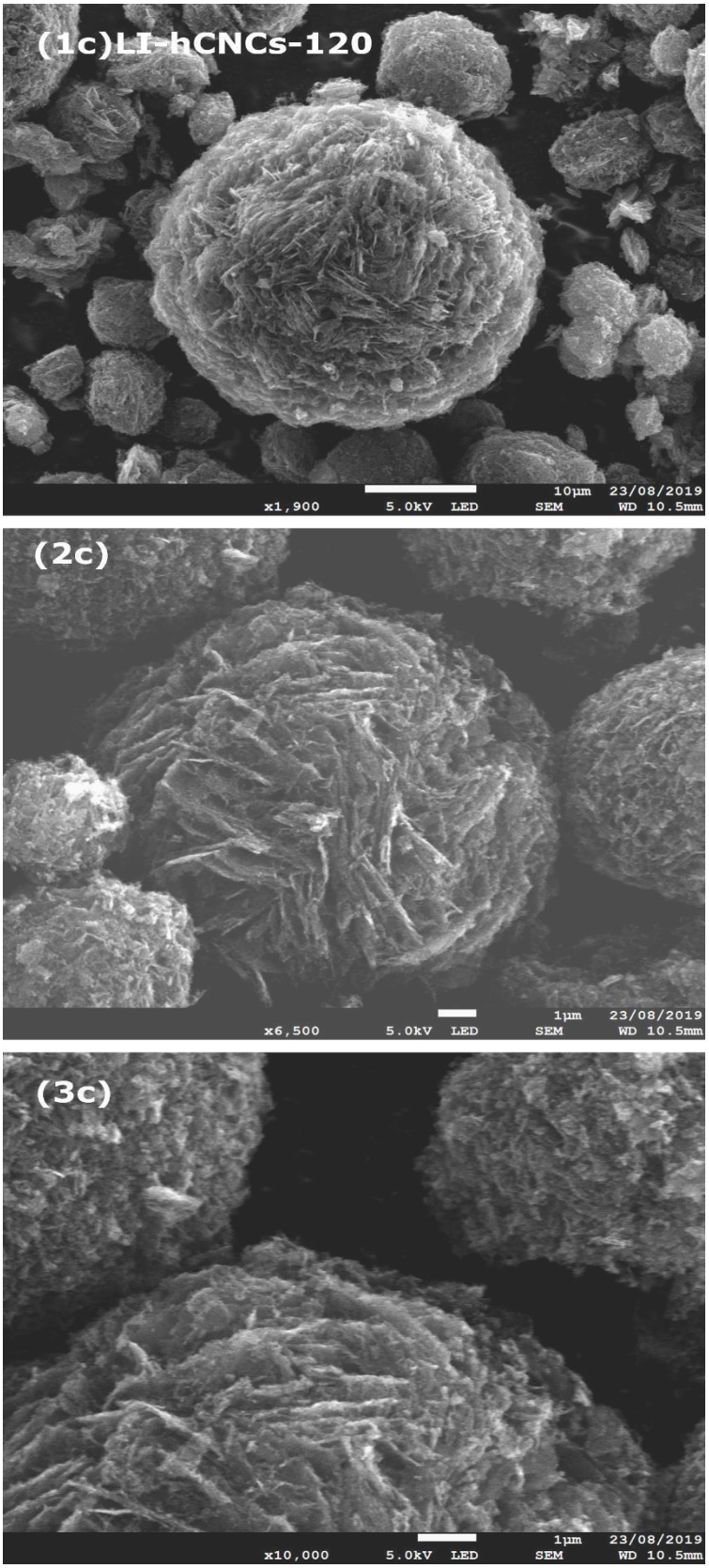


Figure 18: SEM images of LI-hCNCs-120.

Porosity and textural properties analysis

As shown in Figure 19, LI-hCNCs-120 exhibits a type IV isotherm that is typical of a mesoporous material. This type of isotherm denotes a mesoporous material featuring capillary condensation. As shown below in Fig.19, the adsorption/ desorption isotherm of LI-hCNCs-120 samples have a narrow capillary pore, and following from that, occurrence of the capillary condensation phenomenon is expected. Initially, the formation of the monolayer occurs. Then, with increased pressure, the formation of the multilayer takes place. In this process, the monolayer begins to condense inside the capillary pore, and the incoming layer will sit on the monolayer, then the multilayer will form on the monolayer. In the case of capillary condensation occurring in LI-hCNCs-120, the desorption path will be different from that of adsorption, resulting in the formation of a hysteresis loop. This type of loop is mostly associated with the pore shape. LI-hCNCs have a uniform distribution of spherical and cylindrical narrow mesopores exhibiting the H1 type of hysteresis loop. Along with the simplicity of hCNCs preparation, the LI approach is able to produce cages with a pore volume of up to 4.6 cm^3/g.

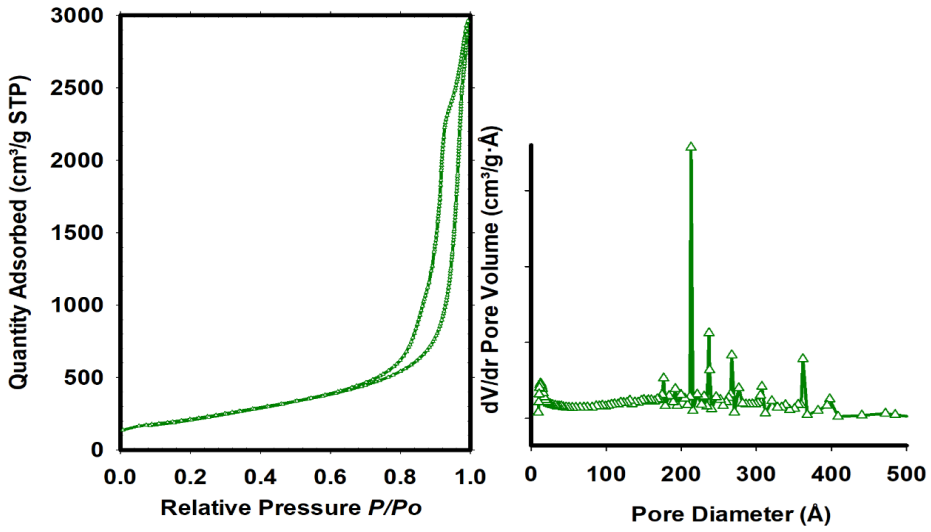


Figure 19: Nitrogen physisorption isotherms for LI-hCNCs-120 sample at -196 °C and 1 bar (left), and PSD curve using the BJH model (right).

4.3.5. The chemical activation of LI-hCNCs-120

Ax-LI-hCNCs analysis

In order to develop the porosity of LI-hCNCs, activation was attempted with KOH as activating agent.[53–55] 0.5g sample of LI-hCNCs-120 was chemically activated using KOH at KOH/LI-hCNCs-120 ratio of 2, 4 or 6 at 800□C. In KOH activation, the oxidation of carbon to carbonate ions leads to the intercalation of potassium compounds in etched pores, which are easily removed in the acid washing step.[45] After the contact with the KOH, the LI-hCNCs were activated at a high KOH/LI-hCNCs ratio of 4 and 6, the cages were partially collapsed by chemical reaction to form a level of microporosity. In the activation

process, main reactions are occurred:[54,56]

$$4\,KOH + C \rightarrow K_2CO_3 + K_2O + 2\,H_2 \qquad Equation\ 6$$

The carbon is eroded by KOH, releasing hydrogen, leaving voids on the carbon frame. At temperature ≤500°C, Dehydration (7) may occur due to the presence of potassium oxide, which can catalyse the occurrence of water gas (8) and transformation reaction (9), then the carbon dioxide and potassium oxide can produce potassium carbonate according to (10) [57,58]. Therefore, the main products are mainly hydrogen, as well as a small amount of carbon monoxide, carbon dioxide, etc.

$$2\,KOH \rightarrow K_2O + H_2O \qquad Equation\ 7$$

$$C + H_2O \rightarrow H_2 + CO \qquad Equation\ 8$$

$$CO + H_2O \rightarrow H_2 + CO_2 \qquad Equation\ 9$$

$$K_2O + CO_2 \rightarrow K_2CO_3 \qquad Equation\ 10$$

After the removal of the intercalated metallic K and other K compounds by HCl washing, the expanded carbon lattices cannot return to their previous nonporous structure.

As mentioned above, the XRD patterns of hCNCs suggest a low level of graphitisation, which may limit the extent to which they can be activated by KOH. The porosity of carbon materials is developed

in line with the level of activation meaning that hCNCs may be somewhat resistant to activation.[25,54,57]

Table 9: Elemental composition for LI-hCNCs-120 and activated AX-LI-hCNCs-120.

Sample	*C%*	*H%*	*N%*	*%O*
LI-hCNCs-120	78.4	0.0	0.0	21.6
A2-LI-hCNCs	67.6	0.3	0.0	32.0
A4-LI-hCNCs	90.1	0.0	0.1	9.8
A6-LI-hCNCs	88.8	0.0	0.1	11.1

Powder X-ray diffraction (P-XRD) was performed to determine the graphitic (or not) nature of the activated LI-hCNCs carbons. The activated LI-hCNC carbons (Figure 20) show peaks centred at 2θ = 26° and 44°, which arise the graphitic/turbostratic nature of the carbons. The peak at 2θ = 26° corresponds to the (002) plan of graphite. The low intensity of this peak indicates that any graphitic ordering in the activated carbons is very limited. By comparing the peak intensity of samples, the sample activated at KOH/LI-hCNCs-120 ratio of 4 has the most irregular structure.

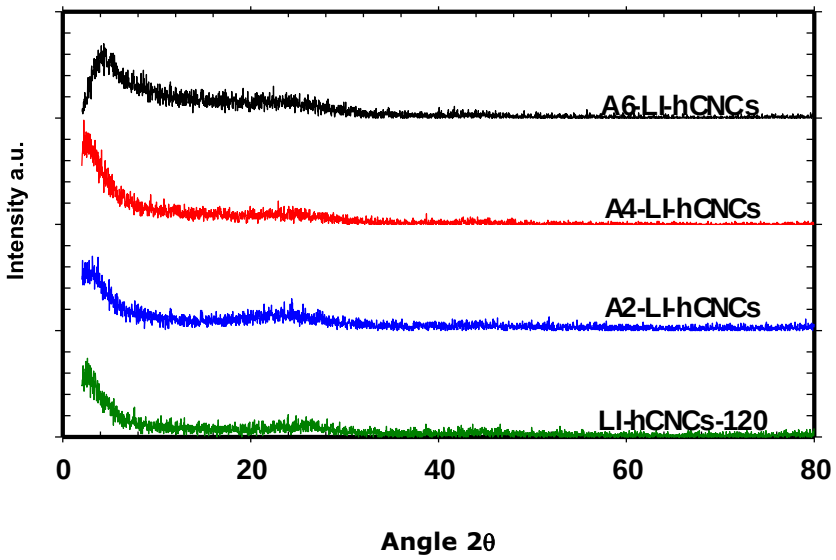


Figure 20: P-XRD pattern of LI-hCNCs-120 before and after KOH activation.

Raman spectra for the activated carbons are shown in Fig.21, and exhibit bands at 1300 cm^{-1} and 1600 cm^{-1}, which are the D-peak (disordered carbon) and the G-peak (graphitic domains), respectively. The Raman spectrum reveals the homogeneous nature of LIhCNCs-120 and the activated LI-hCNCs samples. It indicates that the carbons are not graphitic. The Raman spectra exhibit bands at 1323–1334 cm^{-1} and 1596–1601 cm^{-1} from the D-peak (disordered carbon) and the G peak (graphitic domains), respectively. The ratio of peak intensity (i.e., area) from the G-peak to D-peak (I_G/I_D ratio) is 0.83 for LIhCNCs-120, A2-LI-hCNCs and A6-LI-hCNCs, and 0.84 for A4-LI-hCNCs as shown in Table 10. A ratio of 0.78–0.87 is consistent with the amorphous (i.e., non-graphitic) nature of the carbons.

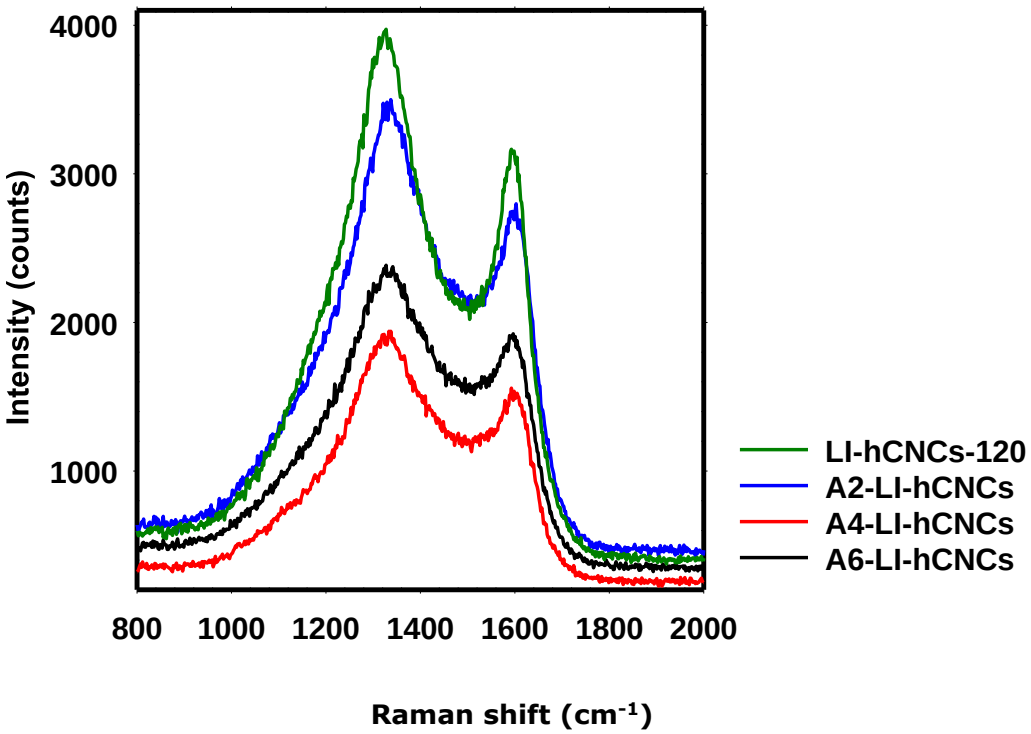


Figure 21: Raman spectra of LI-hCNCs-120 and activated LI-hCNCs-120.

Table 10: The ratio of peak intensity from the G-peak to D-peak (I_G/I_D ratio) of LIhCNCs-120 and activated LI-hCNCs-120 samples.

Sample	I_D	I_G	I_D/I_G
LI-hCNCs-120	1323	1596	0.83
A2-LI-hCNCs	1332	1598	0.83
A4-LI-hCNCs	1334	1596	0.84
A6-LI-hCNCs	1328	1601	0.83

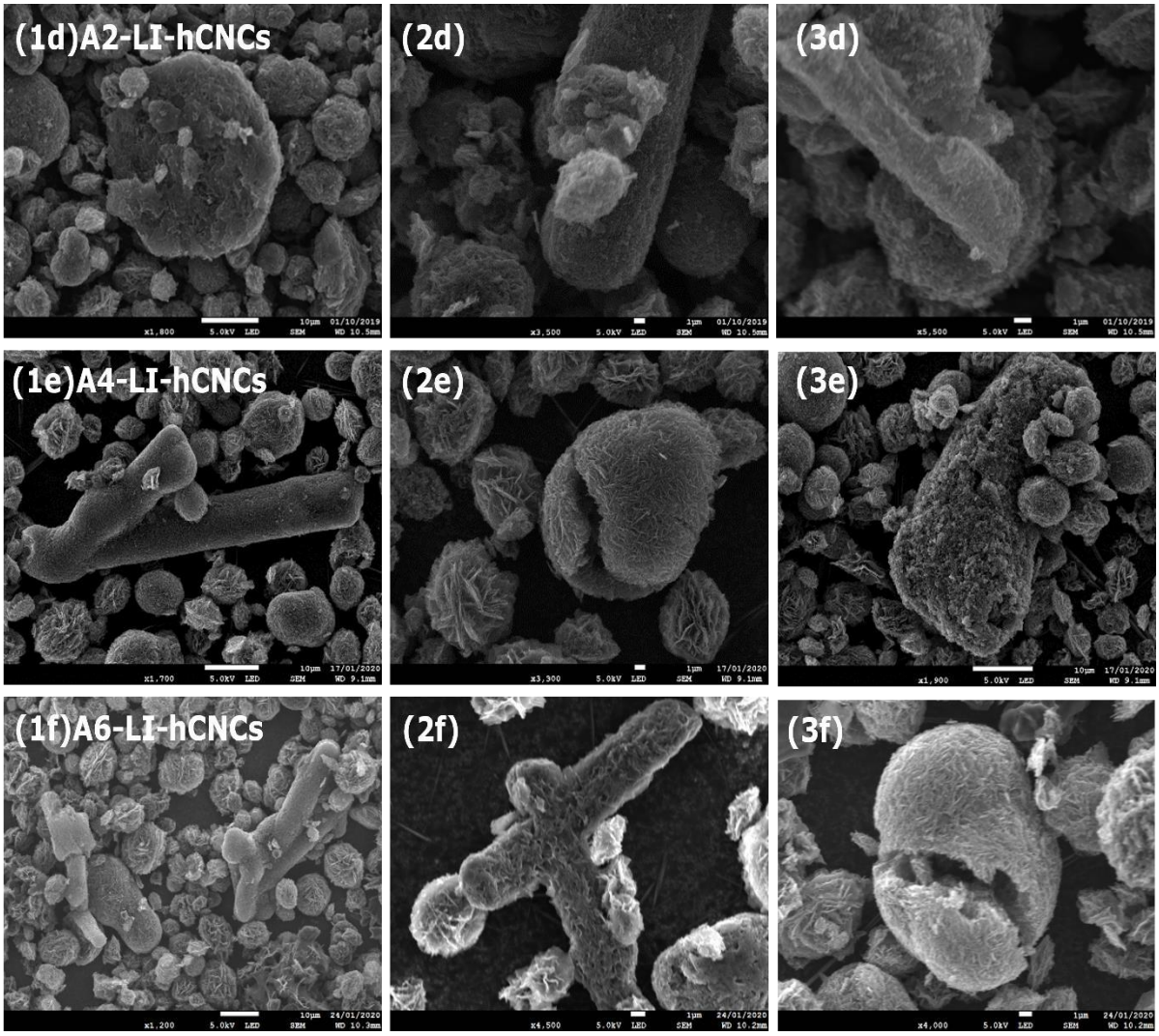


Figure 22: SEM images of activated LI-hCNCs-120 carbons.

As previously observed in the preparation of activated carbons, activation develops the

porosity and leads to a more irregular amorphous structure.[23,53,56–63]For hCNCs samples, KOH activation is assumed to create etches in cage walls or develop potential etches into pores that lead to a loss in structural stability, thereby resulting in the structure collapsing to form small carbonaceous sheets. Indeed, SEM images reveal that after activation, the cages partially collapse (Fig. 22, 1d) or develop transverse fissures (Fig. 22, 2e and 3f). In addition, samples exhibit the formation of stick-like structures (Fig. 22, 1e, 2f, 3d) that may be attributed to the aggregation of carbon sheets.

Porosity and textural properties analysis

The nitrogen sorption isotherms (Figure 23) show that A2-LI-hCNCs, A4-LI-hCNCs and A6LI-hCNCs retain the mesoporous nature, exhibiting the type IV sorption isotherm. At a higher level of activation of A4-LI-hCNCs and A6-LI-hCNCs, the level of microporosity increased slightly. Thus, as shown in Table 11, the surface area of these two samples (A4LI-hCNCs and A6-LI-hCNCs) rose by 29%, and 37%, respectively. Interestingly, the packing density of activated Li-hCNCs increased from 0.20 g/cm^3 for LI-hCNCs-120 to 0.35 g/cm^3 for A6-LI-hCNCs, which is expected with the increase in microporosity. Pore volume decreased at higher KOH/LI-hCNCs-120 ratio, from 3.33 cm^3/g to 2.4 cm^3/g.

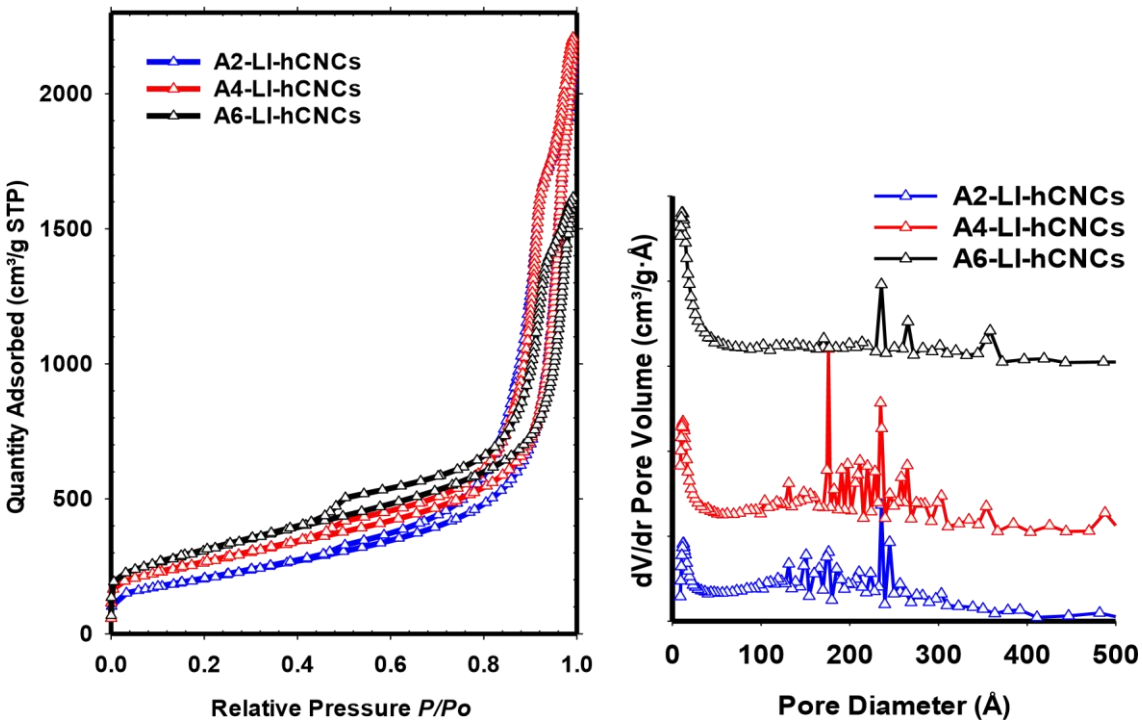


Figure 23: N_2 sorption isotherms and corresponding pore size distribution curves for LIhCNCs-120 before and after KOH activation.

Table 11: Porosity and Textural properties of LI-hCNCs-120 precursor and activated LIhCNCs-120 carbons.

Sample	*BET surface area m^2/g*	*Pore volume cm^3/g*	*Pore size (nm)*	*Packing density g/cm^3*
LI-hCNC-120	779	4.6	21/24/28	0.20
A2-LI-hCNCs	734	3.3	24/25	0.27
A4-LI-hCNCs	937	3.3	23/24	0.27
A6-LI-hCNCs	1069	2.4	25/27	0.35

CO_2 uptake measurements

At high pressure, the pore volume and pore size of a material can have a significant effect on its total CO_2 adsorption. This is because the adsorption of CO_2 onto the surface of a material is a function of both the surface area and the available pore volume, which determines how much gas the material can contain. A material with a high pore volume will typically have a greater capacity to adsorb CO_2 at high pressure than one with a low pore volume. This is because the larger pore volume provides more capacity for the gas to be adsorbed, enabling the storage of a greater total amount of CO_2. The gas molecules may not be able to access all of the available pores, so a material with a high pore volume may not inherently have a high CO_2 adsorption capacity per unit surface area.[38,55,64–66]

Pore size is also crucial in determining the CO_2 absorption capacity of a material at high pressure. A material with smaller pore sizes may have a greater CO_2 adsorption capacity per unit surface area than one with larger pore sizes. This is because small apertures can provide a greater surface area per unit volume, resulting in a greater concentration of CO_2 adsorption sites. However, a material with small pore sizes may also have a reduced pore volume, thereby limiting the quantity of CO_2 that can be stored.[38,55,64]

As LI-hCNCs-120 has low surface area (779 m^2/g), it exhibited lower excess CO_2 uptake compared to the cages prepared via CVD. The uptake of Vap-hCNCs-120 was 16.0 mmol/g at 40 bar, while LI-hCNCs-120 can store only up to ~ 8.2 mmol/g at 40 bar. In contrast, LI-hCNCs-120 has a

relatively large pore volume of 4.6 cm^3/g with pores of size 21, 27 and 28 nm, which enhanced the total CO_2 uptake up to 17.9 mmol/g at 40 bar. After activation with KOH, the surface is increased, which allowed for more storage capacity at high pressure. The excess CO_2 uptake (Fig. 24 and Table 12) increased as the amount of KOH activating agent increased, (i.e., 10.1 mmol/g for A2-LI-hCNCs, 11.9 mmol/g for A4-LI-hCNCs, and 12.7 mmol/g for A6-LI-hCNCs. As shown in Table 13, the highest total CO_2 uptake at 40 bar was observed with A4-LI-hCNCs (18.8 mmol/g), which has the largest pore volume (3.33 cm^3/g).

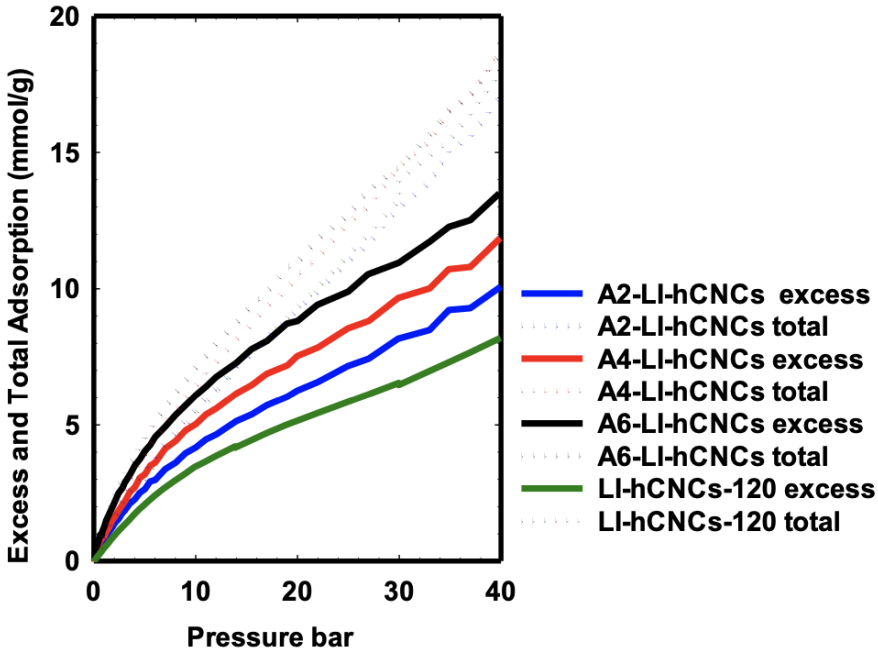


Figure 24: Excess and total CO_2 uptake at 25 °C of LI-hCNCs before and after activation.

Table 12: Excess gravimetric (mmol/g and g/g) and volumetric (cm^3(STP)/cm^3) CO_2 uptake of LI-hCNCs-120 and activated LI-hCNCs-120.

Sample	Excess CO_2 uptake @1 bar					
	mmol/g		g/g		cm^3(STP)/cm^3	
	1 bar	40 bar	1 bar	40bar	1 bar	40 bar
LI-hCNCs-120	0.5	8.20	0.02	0.36	2.5	36.8
A2-LI-hCNCs	0.8	10.1	0.04	0.44	4.8	61.1
A4-LI-hCNCs	0.9	11.9	0.04	0.52	5.4	72.0
A6-LI-hCNCs	1.9	12.7	0.08	0.56	14.9	99.6

Table 13: Total gravimetric (mmol/g and g/g) and volumetric (cm^3(STP)/cm^3) CO_2 uptake of LI-hCNCs-120 and activated LI-hCNCs-120.

Sample	Total CO_2 uptake @1 bar					
	mmol/g		g/g		cm^3(STP)/cm^3	
	1 bar	40 bar	1 bar	40bar	1 bar	40 bar
LI-hCNCs-120	0.6	17.9	0.03	0.79	3.0	80.4
A2-LI-hCNCs	0.9	17.1	0.04	0.75	5.7	103.3
A4-LI-hCNCs	1.0	18.8	0.04	0.83	6.3	114.0
A6-LI-hCNCs	1.4	18.6	0.06	0.82	10.7	145.8

As illustrated in Fig. 25, LI-hCNCs-120 before or after activation has low volumetric uptake due to having mesoporous structure and associated low packing density. A6-LI-hCNCs, which has the highest packing density (~0.35 g/cm^3) exhibits the highest volumetric CO_2 storage capacity (up to ~145.8 cm^3(STP)/cm^3) at 100 bar.

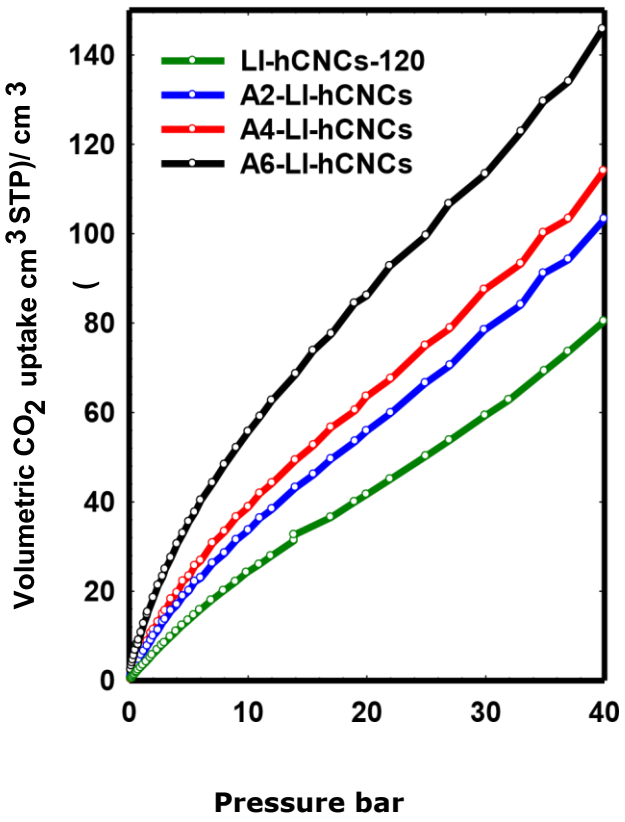


Figure 25: Volumetric CO_2 uptake at 25°C of LI-hCNCs before and after activation.

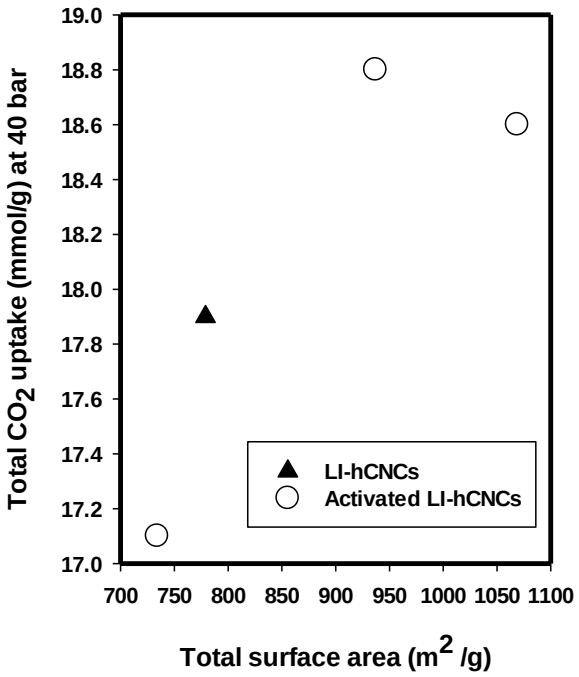


Figure 26: The effect of total surface area in the CO_2 uptake of LI-hCNCs and the activated LI-hCNCs at high pressure ~40 bar and 25°C.

4.4. Conclusion

This work discussed the modification of existing technology for the preparation of 3D hierarchical nanocage structures in order to tailor porosity and pore volume and thus maximise gas storage capacity. The template (MgO) was prepared via the thermal treatment of commercial magnesium carbonate pentahydrate. The resulting MgO (yield of 40 - 50%) had very high thermal stability, as well as a very stable hierarchical 3D structure, with surface area of 51 m^2/g and pore volume of 0.25 cm^3/g. The 3D hierarchical structure was then passed successfully to the resulting templated carbon. The template nanocages have moderate surface area of 779 - 1465 m^2/g, while the pore volume ranged from 1.5 - 4.6 cm^3/g. We explored a liquid impregnation approach and were successful in improving the yield of nanocages. The nanocages prepared via the LI technique were activated by KOH, and surface area was enhanced by up to 37% depending on the level of activation. Nanocage carbons prepared via CVD-technique (Vap-hCNCs-X) exhibited good performance for CO_2 uptake at high pressure. The total uptake of up to 22.8 mmol/g at 30 bar and 25°C indicates that the nanocage carbons are a promising candidate for pre-combustion CO_2 storage applications. Additionally, the Vap-hCNCs-X samples showed very high total CH_4 uptake of up to ~13.4 and 29.9 mmol/g (equivalent to 0.21 and 0.48 g/g) at 35 and 100 bar, respectively. However, due to their low packing density, the VaphCNCs-X samples showed modest volumetric uptake. A nanocage sample, Vap-hCNCs-30, with moderate packing density (0.50 g/cm^3) and CH4 gravimetric uptake showed the highest volumetric uptake up to 207 $cm^3(STP)/cm^3$ at 100 bar and 25 °C.

4.5. References

1 A. S. Ello, L. K. C. De Souza, A. Trokourey and M. Jaroniec, *Microporous and Mesoporous Materials*, 2013, **180**, 280–283.

2 T. S. Blankenship, N. Balahmar and R. Mokaya, *Nat Commun*, , DOI:10.1038/s41467-017-01633-x.

3 R. Dawson, A. I. Cooper and D. J. Adams, *Polym Int*, 2013, **62**, 345–352.

4 Q. Wang, H. Li, L. Chen and X. Huang, *Novel spherical microporous carbon as anode material for Li-ion batteries*, .

5 J. Ludwinowicz and M. Jaroniec, *Carbon N Y*, 2015, **82**, 297–303.

6 C. Nieto-Delgado, M. Terrones and J. R. Rangel-Mendez, *Biomass Bioenergy*, 2011, **35**, 103–112.

7 J. Jagiello, C. Ania, J. B. Parra and C. Cook, *Carbon N Y*, 2015, **91**, 330–337.

8 R. Ryoo, S. H. Joo and S. Jun, *J Phys Chem B*, 1999, **103**, 7743–7746.

9 R. Ryoo, S. H. Joo and S. Jun, , DOI:10.1021/jp991673a.

10 J. S. Beck, J. C. Vartuli, W. J. Roth, M. E. Leonowicz, C. T. Kresge, K. D. Schmitt, C. T. W. Chu, D. H. Olson, E. W. Sheppard, S. B. McCullen, J. B. Higgins and J. L. Schlenker, *J Am Chem Soc*, 1992, **114**, 10834–10843.

11 Y. Xia, Z. Yang and R. Mokaya, *Nanoscale*, 2010, **2**, 639–659.

12 A. B. Fuertes, *J Mater Chem*, 2003, **13**, 3085–3088.

13 V. Malgras, Q. Ji, Y. Kamachi, T. Mori, F. K. Shieh, K. C. W. Wu, K. Ariga and Y. Yamauchi, *Bull Chem Soc Jpn*, 2015, **88**, 1171–1200.

14 M. Inagaki, M. Toyoda, Y. Soneda, S. Tsujimura and T. Morishita, *Carbon N Y*, 2016, **107**, 448–473.

15 A. B. Fuertes and T. A. Centeno, *J Mater Chem*, 2005, **15**, 1079–1083.

16 C. Pevida, T. C. Drage and C. E. Snape, *Carbon N Y*, 2008, **46**, 1464–1474.

17 D. Zhao, Q. Huo, J. Feng, B. F. Chmelka and G. D. Stucky, *J Am Chem Soc*, 1998, **120**, 6024–6036.

18 S. A. Bagshaw, E. Prouzet and T. J. Pinnavaia, *Science (1979)*, 1995, **269**, 1242–1244.

19 S.-S. Kim and T. J. Pinnavaia, *Chemical Communications*, 2001, 2418–2419.

20 R. Ryoo, S. H. Joo, M. Kruk and M. Jaroniec, *Advanced Materials*, 2001, **13**, 677–681.

21 S. Jun, S. H. Joo, R. Ryoo, M. Kruk, M. Jaroniec, Z. Liu, T. Ohsuna and O. Terasaki, *J Am Chem Soc*, 2000, **122**, 10712–10713.

22 H. Tamon, H. Ishizaka, T. Yamamoto and T. Suzuki, *Carbon N Y*, 1999, **37**, 2049–2055.

23 K. Huang, S. H. Chai, R. T. Mayes, S. Tan, C. W. Jones and S. Dai, *Microporous and Mesoporous Materials*, 2016, **230**, 100–108.

24 M. Cox and R. Mokaya, *Sustain Energy Fuels*, 2017, **1**, 1414–1424.

25 N. Balahmar, A. S. Al-Jumialy and R. Mokaya, *J Mater Chem A Mater*, 2017, **5**, 12330–12339.

26 X. Li, W. Xiao, G. He, W. Zheng, N. Yu and M. Tan, *Colloids Surf A Physicochem Eng Asp*, 2012, **408**, 79–86.

27 S. L. Candelaria, Y. Shao, W. Zhou, X. Li, J. Xiao, J. G. Zhang, Y. Wang, J. Liu, J. Li and G. Cao, *Nano Energy*, 2012, **1**, 195–220.

28 S. Jin, N. Li, H. Cui and C. Wang, *Nano Energy*, 2013, **2**, 1128–1136.

29 Z. Lyu, D. Xu, L. Yang, R. Che, R. Feng, J. Zhao, Y. Li, Q. Wu, X. Wang and Z. Hu, *Nano Energy*, 2015, **12**, 657–665.

30 K. Xie, X. Qin, X. Wang, Y. Wang, H. Tao, Q. Wu, L. Yang and Z. Hu, *Advanced Materials*, 2012, **24**, 347–352.

31 K. S. Novoselov, A. K. Geim, S. V Morozov, D. Jiang, Y. Zhang, S. V. Dubonos, I. V Grigorieva and A. A. Firsov, *Science (1979)*, 2004, **5**, 1–12.

32 H. Wang, J. Deng, Y. Chen, F. Xu, Z. Wei and Y. Wang, *Nano Res*, 2016, **9**, 2672–2680.

33 C. Weidenthaler, *Nanoscale*, 2011, 3, 792–810.

34 J.-O. Carlsson and P. M. Martin, in *Handbook of Deposition Technologies for Films and Coatings*, Elsevier, 2010, pp. 314–363.

35 M. Ohring, in *Materials Science of Thin Films*, Elsevier, 2002, pp. 277–355.

36 E. García-Díez, S. Schaefer, A. Sanchez-Sanchez, A. Celzard, V. Fierro, M. M. Maroto-Valer and S. García, *ACS Appl Mater Interfaces*, 2019, **11**, 36789–36799.

37 M. Sevilla, J. B. Parra and A. B. Fuertes, *ACS Appl Mater Interfaces*, 2013, **5**, 6360–6368.

38 L. S. Blankenship and R. Mokaya, *Mater Adv*, 2022, 3, 1905–1930.

39 A. H. Assen, Y. Belmabkhout, K. Adil, A. Lachehab, H. Hassoune and H. Aggarwal, *Chemical Engineering Journal*, 2021, 419.

40 H. M. Coromina, D. A. Walsh and R. Mokaya, *J Mater Chem A Mater*, 2015, **4**, 280–289.

41 C. C. Hwang, J. J. Tour, C. Kittrell, L. Espinal, L. B. Alemany and J. M. Tour, *Nat Commun*, 2014, 5.

42 J. He, J. W. F. To, P. C. Psarras, H. Yan, T. Atkinson, R. T. Holmes, D. Nordlund, Z. Bao and J. Wilcox, *Adv Energy Mater*, , DOI:10.1002/aenm.201502491.

43 K. Mosher, J. He, Y. Liu, E. Rupp and J. Wilcox, *Int J Coal Geol*, 2013, **109–110**, 36–44.

44 D. Saha, T. M. Fieback and B. Tom, *Energy Technology*, 2016, **4**, 1392–1400.

45 T. Ohkubo, J. Miyawaki, K. Kaneko, R. Ryoo and N. A. Seaton, *Journal of Physical Chemistry B*, 2002, **106**, 6523–6528.

46 W. Wang and D. Yuan, *Sci Rep*, , DOI:10.1038/srep05711.

47 W. A. Goddard, J. L. Mendoza-Cortés, S. S. Han, H. Furukawa and O. M. Yaghi, *Journal of Physical Chemistry A*, 2010, **114**, 10824–10833.

48 H. Furukawa and O. M. Yaghi, *J Am Chem Soc*, 2009, **131**, 8875–8883.

49 Y. Peng, V. Krungleviciute, I. Eryazici, J. T. Hupp, O. K. Farha and T. Yildirim, *J Am Chem Soc*, 2013, **135**, 11887–11894.

50 X. Liu, L. Zhou, J. Li, Y. Sun, W. Su and Y. Zhou, *Carbon N Y*, 2006, **44**, 1386–1392.

51 B. P. Prajwal and K. G. Ayappa, *Adsorption*, 2014, **20**, 769–776.

52 C. Guan, L. S. Loo, K. Wang and C. Yang, *Energy Convers Manag*, 2011, **52**, 1258–1262.

53 Y. Lv, F. Zhang, Y. Dou, Y. Zhai, J. Wang, H. Liu, Y. Xia, B. Tu and D. Zhao, *J Mater Chem*, 2012, **22**, 93–99.

54 T. Otowa, R. Tanibata and M. Itoh, *Gas Separation and Purification*, 1993, **7**, 241–245.

55 M. Sevilla, A. S. M. Al-Jumialy, A. B. Fuertes and R. Mokaya, *ACS Appl Mater Interfaces*, 2018, **10**, 1623–1633.

56 E. Raymundo-Piñero, P. Azaïs, T. Cacciaguerra, D. Cazorla-Amorós, A. Linares-Solano and F. Béguin, *Carbon N Y*, 2005, **43**, 786–795.

57 D. Lozano-Castelló, J. M. Calo, D. Cazorla-Amorós and A. Linares-Solano, *Carbon N Y*, 2007, **45**, 2529–2536.

58 J. Wang and S. Kaskel, *J Mater Chem*, 2012, 22, 23710–23725.

59 A. Khasri, O. S. Bello and M. A. Ahmad, *Research on Chemical Intermediates*, 2018, **44**, 5737–5757.

60 F. Suárez-García, A. Martínez-Alonso and J. M. D. Tascón, *Carbon N Y*, 2004, **42**, 1419–1426.

61 P. E. Hock and M. A. A. Zaini, *Acta Chimica Slovaca*, 2018, **11**, 99–106.

62 ´ A Huidobro, A. C. Pastor, F. Rodrıguez- and R. Reinosó, *Preparation of activated carbon cloth from viscous rayon Part IV. Chemical activation*, 2001, vol. 39.

63 W. Qiao, S. H. Yoon and I. Mochida, *Energy and Fuels*, 2006, **20**, 1680–1684.

64 M. Sevilla, W. Sangchoom, N. Balahmar, A. B. Fuertes and R. Mokaya, *ACS Sustain Chem Eng*, 2016, **4**, 4710–4716.

65 A. M. Aljumialy and R. Mokaya, *Mater Adv*, 2020, **1**, 3267–3280.

66 E. A. Hirst, A. Taylor and R. Mokaya, *J Mater Chem A Mater*, 2018, **6**, 12393–12403.

5. Highly porous biomass-derived activated carbon with enhanced CO2 and methane uptake.

5.1. Introduction

To address the challenges posed by a growing population and excessive consumption of fossil fuels, technologies for the future storage and use of renewable and green energy must be developed. Gravimetric/volumetric energy densities, cost, and cycle stability are the most important performance measures for evaluating these energy storage materials. .[1–5] Carbon serves a crucial role in the development of human civilisation in terms of the materials used. Similarly, carbon materials play an increasingly vital role in energy storage due to their large specific surface area (SSA), tuneable pore size, high electric conductivity, and robust mechanical property. [6–17]

Biomass compounds, which are predominantly constituted of carbohydrates, have the potential to serve as a renewable source for the production of carbon-based materials. In recent years, lignin, carbohydrates, cellulose, chitin, and proteins have been widely utilised to produce carbon-based materials. e.g., pyrolysis combined with the activation of coconut obtained activated carbons (ACs) with an ultrahigh SSA and micropore-predominant structure. Direct Activation of sawdust with uniform diameters. In addition, biomass-derived carbon contains an abundance of functionality, and one of the challenges in this field of study is the development of techniques for controlling carbon functionality. Creating an integrated biomass refinery that combines the production of carbon and the disposal of biomass refuse would drastically reduce the price of carbon, which is one of the primary obstacles to widespread biomass use. The elemental composition such carbons depend on the type of carbonaceous material (henceforth referred to as the precursor) and activation conditions. [15,17–28]

Hydrothermal carbonisation (HTC) or pyrolysis are the usual methods of carbonising biomass prior to activation. More recently, it has been demonstrated that, for carbons produced from biomass, the manner of carbonisation prior to activation, or lack thereof, has a considerable effect on the properties of both the activatable carbonaceous matter and the final activated carbons.[16,29–32]A

simpler, relatively low-temperature approach for biomass carbonisation incorporating flash carbonisation was investigated. Compared to carbons produced by hydrothermal carbonisation or conventional pyrolysis, activated carbons produced by flash carbonisation have larger microporosity and greater yield.[15,33]

Activation is the most practical technique for increasing the surface area of carbon materials and adjusting the ratio of meso/micropores. Chemical activation, physical activation, and self-activation are the three categories of activation mechanisms based on the activation mechanism. The activation of biomass precursors rich in heteroatoms provides a straightforward and simple method for producing heteroatom-functionalized porous carbon, which has promising applications in energy storage material and devises. The chemical activation reagent potassium hydroxide (KOH) is well-known. The KOH activation mechanisms can be summarised as follows: (i) the carbon matrix is etched by K-containing species (KOH, K_2CO_3, K_2O) through a redox reaction, resulting in abundant micro/mesopores; (ii) the water vapour produced in the activation process contributes to the gasification of carbon, which further aids in the development of porosity; and (iii) the intermediate products (metallic K) can intercalate into the carbon framework and expand the carbon lattices, resulting in a highly porous structure. [18–21,34–38]

After the activation procedure, the obtained porous carbon has a high SSA ranging from several hundreds to thousands of square metres per gramme. In addition, the porous structure can be modified by controlling the activation conditions (i.e., the proportion of the precursor/activation agent, activation temperature, activation duration, etc.). Natural biomass precursors, such as plants, animal organs, and refuse materials, have been activated with KOH to produce a variety of porous carbon materials with distinct morphologies and pore textures.

In this study, prickly pear peels (PPPS) are chosen as the feedstock since they are readily accessible and affordable. It presents the flash carbonisation methodology of PPPs, and examine the effect of change pyrolysis temperature on the resultant char. Char that prepared at 350, 400, 500, and 600 are activated using KOH at different ratio and temperatures. The porosity and textural properties of

the four sets of samples are investigated, and their use as CO_2 and CH_4 storage materials is also investigated.

5.2. Experimental section

Prickly pear peels (PPPs) were used as the non-carbonised feedstock or starting material.

They were collected from a farm from Taif city, Saudi Arabia.



Figure 1: Prickly pear plant, Photo taken in Taif city, Saudi Arabia.

5.2.1. Material synthesis

Step1: Biomass carbonisation

PPPSs were thoroughly washed with water and dried, and then placed in an alumina boat and heated in a horizontal tube furnace at carbonisation temperatures of 350°C, 400°C,

500°C and 600°C within an atmosphere of nitrogen with a heating ramp rate of 5°C/min. At desired carbonisation temperatures (T=350°C, 400°C, 500°C and 600°C), the PPPs were exposed to a flow of air for 5 minutes, after which the furnace was left to cool under a flow of nitrogen gas. The resulting carbonaceous matter was designated as **Char-A**, where **A** = 350°C, 400°C, 500°C and 600°C.

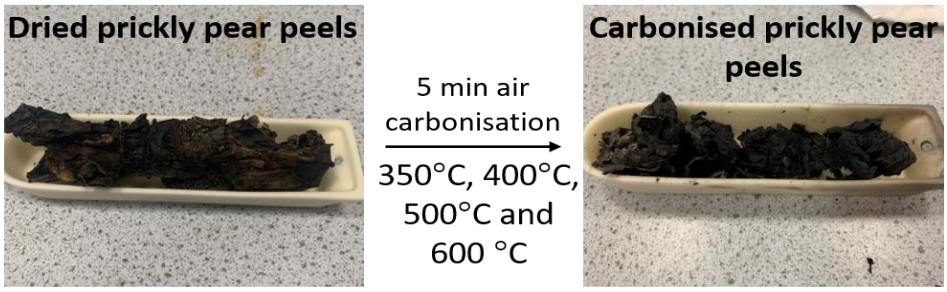


Figure 2: Carbonisation of dried prickly pear peels using flash carbonisation technique.

Step 2: Chemical activation of Char

X g of Char-A was mixed and ground with KOH at KOH/Char ratio of 2, 3 and 4, at activation temperatures of 700°C, 800°C and 900°C, and a ramp rate of 5ºC min^{-1}, under nitrogen flow for 1 h. The resulting activated carbons were washed with 10% HCl for several days to remove any inorganic salts. Samples were designated as ACX-Y-Z where **X** indicates KOH/precursor ratio, **Y** is the char carbonisation temperature and **Z** is the activation temperature.

5.2.2. Characterization methods

Thermogravimetric analysis (TGA) was performed using a TA Instruments SDT Q600 analyser at a heating rate of 10 ºC/min under flowing air conditions. Powder XRD patterns were obtained using a PANalytical X'Pert PRO diffractometer with CuKa radiation (l = 1.5406 Å) (40 kV, 40 mA), 0.02 step size and 2s step time for values of 2y between 21 and 801. Elemental analysis (CHNO) was performed using an Exeter Analytical CE-440 Elemental Analyser. Analysis of porosity and determination of textural properties was performed via nitrogen sorption using a Micromeritics 3Flex Flex sorptometer. Prior to analysis (at 196°C), the carbon samples were degassed under vacuum at 200°C for 12hours. The surface area was calculated using the Brunauer–Emmett–Teller (BET) method applied to adsorption data at a relative pressure (*P/Po*) range of 0.02–0.22. The total pore volume was determined from the total nitrogen uptake at close to saturation pressure (*P/Po* ~0.99). The micropore surface area and micropore volume were determined via t-plot analysis. Non-local density functional theory (NL-DFT) was applied to nitrogen adsorption data to determine the pore size distribution. Scanning electron microscopy (SEM) analysis was performed using a JEOL 7100F microscope. The carbon samples were loaded on a carbon-conductive sticky tape prior to analysis.

5.2.3. CO_2 and CH_4 uptake measurements

CO_2 uptake was determined using a Hiden Isochema XEMIS instrument at 25 ºC and a pressure of up to 40 bar. The carbons were outgassed for 3 hours under vacuum at 240 ºC prior to performing the CO_2 uptake measurements. These measurements directly determined the excess CO_2 uptake. Methane uptake was determined using a Hiden Isochema XEMIS Analyser. Before the uptake measurements, the carbons were degassed at 240 ^oC under vacuum for several hours. Adsorption–desorption isotherms were obtained at 25 ^oC, over methane (CH_4), at a pressure range of 0–100 bar.

5.3. Results and Discussion

5.3.1. Study of the nature of Char

Char is a solid product that is obtained from the pyrolysis of biomass with an absence of oxygen. However, a partial combustion would be possible to provide thermal energy for the process. Depending on pyrolysis duration variation, the decomposition of biomass will vary in the percentage of resulting products (gas, liquid and solid). In this study, the role of pyrolysis temperature on resulting char, and on the activated carbon produced has been examined. In addition, the effect of amount of activating agent used and the activation temperature on the porosity of the resulting activated carbons and their capacity for methane storage and CO_2 uptake have been investigated. To this end PPPs were flash carbonised at 350°C, 400°C, 500°C and 600°C. The resulting chars were activated at different KOH/char ratios and activation temperatures, yielding four sets of activated carbon: ACX-Y-350, ACX-Y-400, ACX-Y-500 and ACX-Y-600.

As shown in the Table 1 below, ca. half of the PPPs mass was burnt off during carbonisation. However, a yield of 37 – 48% compares favourably with yields from conventional pyrolysis and hydrothermal carbonisation that tend to be ca. 30%

Table 1: Yield and surface area of flash carbonised PPPs

Sample	*Weight before carbonisation (g)*	*Weight after Carbonisation (g)*	*Yield (%)*	Surface area (m^2/g)
Char-350	10.7	4.3	40.2	17
Char-400	14.6	6.0	42.0	87
Char-500	11.7	5.6	48.0	129
Char-600	12.3	4.6	37.4	3

Elemental analysis of the resultant char in the Table 2 shows that the C content post carbonisation increased by 30 % - 49 %, while the nitrogen content decreased by at least 50%. This was accompanied by a reduction in the apparent O content from 61.2 % to 54.0 %, 55.3 %, 50.9 % and 57.6 % respectively at each of the temperatures (Table 2). These results are as expected based on previous work, which showed that air carbonisation or pyrolysis cause a decrease of the O/C ratio.[15,23,39]

Table 2: Elemental composition of PPPs and chars

Sample	*C%*	*N%*	*H%*	*O%*[a]	*O/C*[b]
Prickly pear peels (PPPS)	31.5	1.4	5.9	61.2	1.5
Char350	42.1	0.8	3.1	54.0	1.0
Char400	41.4	0.5	2.8	55.3	1.0
Char500	46.8	0.6	1.7	50.9	0.8
Char600	40.8	0.5	1.1	57.6	1.1

[a]Nominal O content obtained as O% = 100-C%–H%–N%. Atomic ratio (divide the average atomic mass by the reference standard).

Thermogravimetric analysis (TGA) was conducted to monitor the change in carbon content and the carbonising/demineralisation impacts of the air-carbonised PPPs. Firstly, the TGA curves of the PPPS

under oxidizing conditions was noted. Indeed, as shown in Figure 3, when heated under flowing air conditions, the PPPs are steadily volatilised, leading to a loss in mass of ca. 80% at ~550°C, after which there is a further loss of ca. 5% % due, presumably, to combustion of char. This leaves a non-combustible ash content of about 15 % as residues at 1000°C. According to the TGA data, the PPPs contained a noncarbon mineral content of approximately 15%, which should have been eliminated prior to the activation procedure.

In contrast, as shown in Fig.3, Char-350 is completely burnt off at 1000°C, with most of the carbon combustion occurring between 400 and 800°C. This shows that Char-350 is fully composed of carbonaceous material and that the air carbonization process removed any inorganic residues. However, Char-400, Char-500 and Char-600 show initial mass loss below 100°C due to evaporation of residual moisture from the drying process. This is followed by a further single step mass-loss event at ~550°C- 640°C due to the combustion of carbon. It shows that about 30%-40% of inorganic impurities was rigid and resistant to burn off at 1000°C.

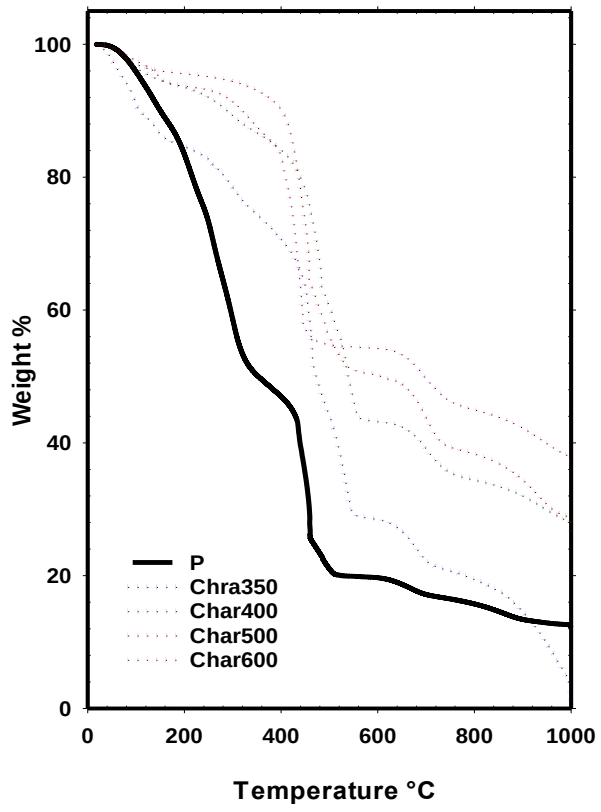


Figure 3: Thermogravimetric analysis curves of prickly pear peel (PPPs) after flash air carbonisation at 350ºC, 400ºC, 500ºC or 600ºC.

The N_2 sorption isotherms in Figure 4 indicate that the chars are lowly porous with surface areas of 17 m^2/g for Char-350, 87 m^2/g for Char-400, 120 m^2/g for Char-500 and 3 m^2/g for Char-600.

Figure 5 below reports the XRD patterns of char samples. The XRD spectral analysis of chars produced at 350–600 °C revealed multiple peaks, confirming the formation of a wide variety of mineral crystals and other inorganic substances. Observations revealed that some peaks overlapped and provided multiple possible combinations of peaks. This peak was assigned a value close to the reference data, and the analysis was qualitative rather than quantitative. Strong peaks at (2θ) 26°, 28°, and 30° were found, which possibly indicated the presence of fluorite, graphite, and chlorapatite. The remaining peaks, which had comparatively low intensities and were attributed to calcite, bayerite, and hydrobiotite, were also found. A few more peaks were found at 29° and 40°, 41° (2θ), which correlate to apophyllite, pyrophyllite, and barite in addition to graphite and fluorite.

The CHN analysis (table 2) and the mineralogical heterogeneity (Figure 5) were shown to be impacted by the pyrolysis temperature. According to Yuan *et al.,* the mineralogical heterogeneity of biochar was altered by the increase in temperature for biochar synthesis from 300°C to 500°C.[40] Other investigations, such as those by Ding *et al.,*[41] and Ahmad *et al.,*[42] noted a change in the mineral composition of biochar as the pyrolysis temperature increased.

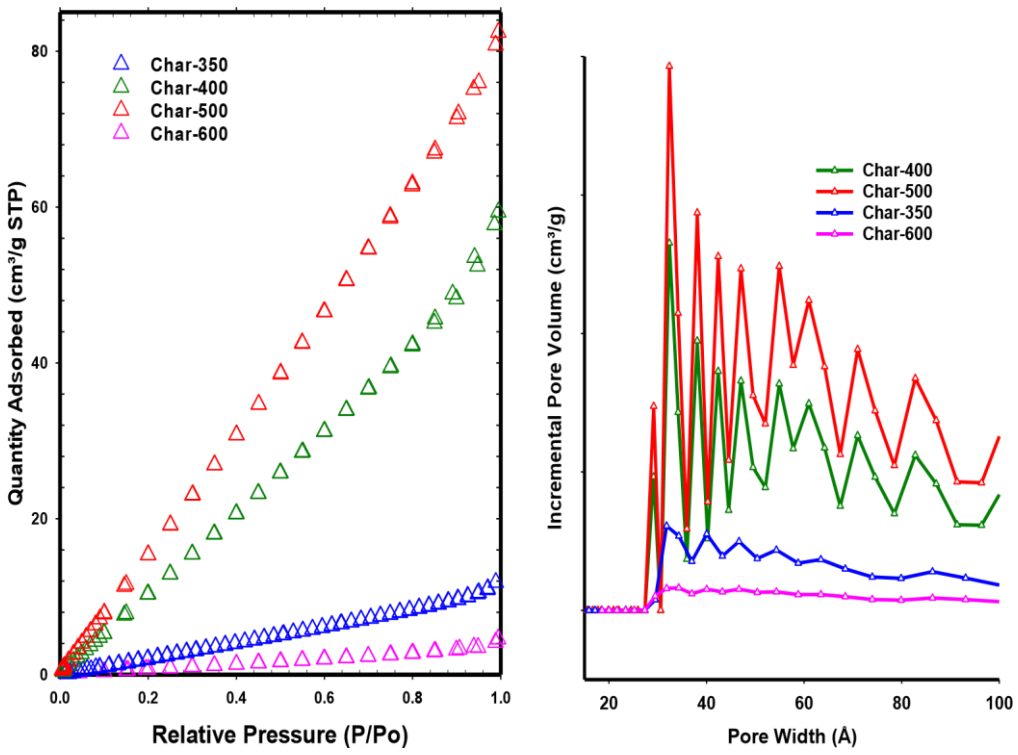


Figure 4: N_2 sorption isotherm (left) and pore size distribution curves (right) of chars prepared at various carbonisation temperatures.

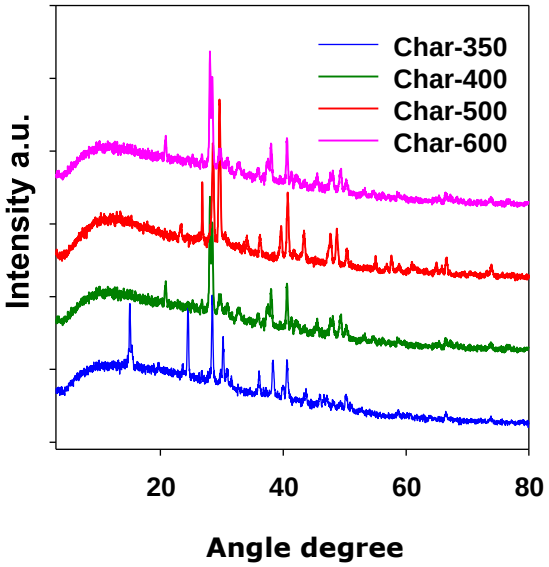


Figure 5: Powder XRD patterns of air-carbonised prickly pear peels at 350°C, 400°C and 500°C.

5.3.2. Study of the PPPS-derived activated carbons

Nature and elemental composition

The porosity of char directly derived from biomass pyrolysis is relatively low, i.e., often < 125 m^2/g.

Activation has been shown to be the most robust method for increasing char porosity.[15,17,22–

[25,27,43,44]Chemical activation, especially using KOH, has been extensively studied and showed successful activation outcomes in terms of increasing surface area up to 3500 m^2/g and beyond, for a variety of biomass, including sawdust,[26,38] rice husks,[19,20]coconut shells,[37,45] olive stones[46] and date seeds.[33] In this chapter, four sample sets of PPPS-derived activated carbon prepared at various KOH/Char ratios and activation temperature were explored.

The yields of the activated carbons are summarised in Table 3 and varies between 7 and 53%. There is no clear trend between the yield and carbonization temperature. In general, however, the yield of activated carbon reduces with the amount of KOH used and the activation temperature. As shown in Table 3, the C content of the PPPS-derived activated carbons increases compared to that of the chars, accompanied with decreases in the N, H and O content. The carbon content rose from 31.5 to 92.4 %. In contrast, the N content (%) and H content (%) decrease from 1.4 to 0.0 for N (%), and from 5.9 to 0.0 for H (%). The O/C ratio plays a role in the activation process, as suggested in some other studies.[13,33] It has been proposed that the elemental composition of activatable carbonaceous matter, and specifically the atomic ratio of oxygen to carbon (i.e., the O/C atomic ratio), plays a role in the activation process, with a high O/C ratio favouring ease of activation and formation of larger mesoporosity.[13]

Table 3: Yield and elemental analysis of PPPs-derived activated carbons.

Sample	Yield [%]	C [%]	N [%]	H [%]	O [%][a]	*O/C*[b]
Prickly pear peels (PPPS)	-	31.5	1.4	5.9	61.2	1.5
AC-4700-350	23	47.4	0.6	0.7	51.3	0.8
AC-2800-350	44	78.1	0.8	0.3	20.8	0.2
AC-4800-350	34	70.0	0.3	0.2	29.5	0.3
AC-2700-400	22	83.1	0.5	0.2	16.2	0.1
AC-3700-400	41	52.3	0.2	0.4	47.1	0.7
AC-4700-400	52	55.3	0.1	0.1	44.5	0.6
AC-2800-400	48	92.4	0.5	0.1	7.0	0.1
AC-3800-400	40	77.5	0.1	0.0	22.4	0.2
AC-4800-400	19	84.6	1.0	0.2	14.2	0.1
AC-2900-400	11	63.6	0.7	0.2	35.5	0.4
AC-2700-500	20	70.3	0.4	0.0	29.3	0.3
AC-4700-500	53	50.0	0.1	0.1	49.8	0.7
AC-2800-500	50	63.3	3.1	0.0	33.6	0.4
AC-4800-500	25	79.4	0.5	0.1	20.0	0.2
AC-2900-500	14	57.7	0.0	0.0	42.3	0.6
AC-4700-600	36	45.6	0.3	0.1	54.0	0.9
AC-4800-600	27	77.3	0.4	0.0	22.3	0.2
AC-2900-600	7	67.9	0.0	0.0	32.1	0.4

[a] Nominal O content obtained as O% = 100-(C+H+N). [b]Atomic ratio *(divide the average atomic mass by the reference standard).*

Regarding specific reactions in the activation of the char, the KOH chemical activation mechanism has been studied in various research.[9,11,47,48] Despite the prevalence of KOH as an activating agent in the scientific literature, the activation mechanism is a matter of some disagreement. Notwithstanding, there is widespread consensus that pores are formed through three fundamental processes: (i) chemical activation wherein redox reactions between K compounds and the carbon framework occur; (ii) formation of the physical activating materials; (iii) the intercalation of metallic K between graphitic sheets. Washing of the sample removes both intercalated K as well as K oxides and carbonates, resulting in a permanently porous carbon. The present chars contain abundant O-content (54.0% for Char-350, 55.3% for Char-400, 50.9% for Char-500 and 57.6% Char-600). This leads to having O-containing groups such as C–O, C–O, –COOH, O–C–O, and –OH, which provide essential active sites for adsorption and reactions.[43,49–51] Chen *et al.* suggested that KOH reaction with active O-containing species in biomass was the main reaction at lower ratios (1:8–1:2) or lower temperatures (400–600 ◦C). The authors found that KOH was completely transformed to K_2CO_3, leading to the formation of large amounts of gaseous products and phenols (reaching 75%). The reaction between KOH and more stable carbon fragments, however, was enhanced at higher ratios (> 1:2) or higher temperatures (700–800◦ C), such that it became the main reaction. With a significant decrease in the phenols and O-species, the hydrocarbons became the dominant species.[21] As shown in Fig. 6, 'active sites' (the functional groups in the carbon matrix) can react with potassium hydroxide at temperature higher than the melting point of KOH (~360°C). This results in the carbon mass consuming process, which generates porosity. At the same time, potassium oxide and carbon dioxide can react to generate potassium carbonate, which plays an important role in developing microporous structure. At high activation temperatures close to the boiling point of potassium > 760°C, the potassium transforms from solid state to gaseous matter. This passes through carbon layers in the carbon matrix, which leads to an increased level of porosity.[21]

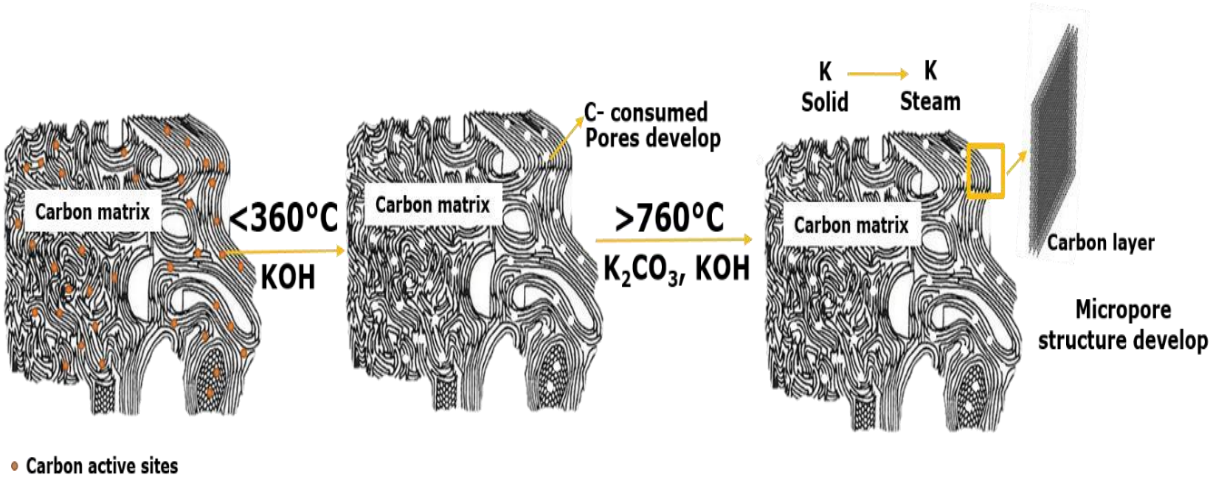


Figure 6: Proposed activation process of biomass carbon matrix by potassium hydroxide at high activation temperature (700°C-900°C).

Powder X-ray diffraction was performed to confirm the nature and purity of the PPPS derived porous carbons. The XRD patterns of representative samples are shown in Figure 7. The broad peak at 2-theta of 22° and 44° in the XRD pattern correspond to the positions at which the (002) and (100) diffractions arising from graphene stacks are expected. This indicates that AC-2800-350, AC-2700-400 and AC-2700-500 have some graphene-like stacking that is greatly reduced or lost for the rest of the PPPS-derived activated carbons. The KO/char ratio appears to have an impact on the level of graphene stacking, with greater amounts of KOH appearing to be more disruptive. The activation temperature does not appear to have any significant or consistent effect on the level of graphene stacking. Overall, it can be inferred from the XRD patterns produced that the PPPs derived activated carbons are essentially amorphous, as is typical of KOH activated carbons. Some carbons' XRD patterns show some strong peaks that could be caused by inorganic residue that was retained from K salts e.g., $KHCO_3$ and K_2CO_3 that didn't washed during the deionised water wash process.(Figure 3).

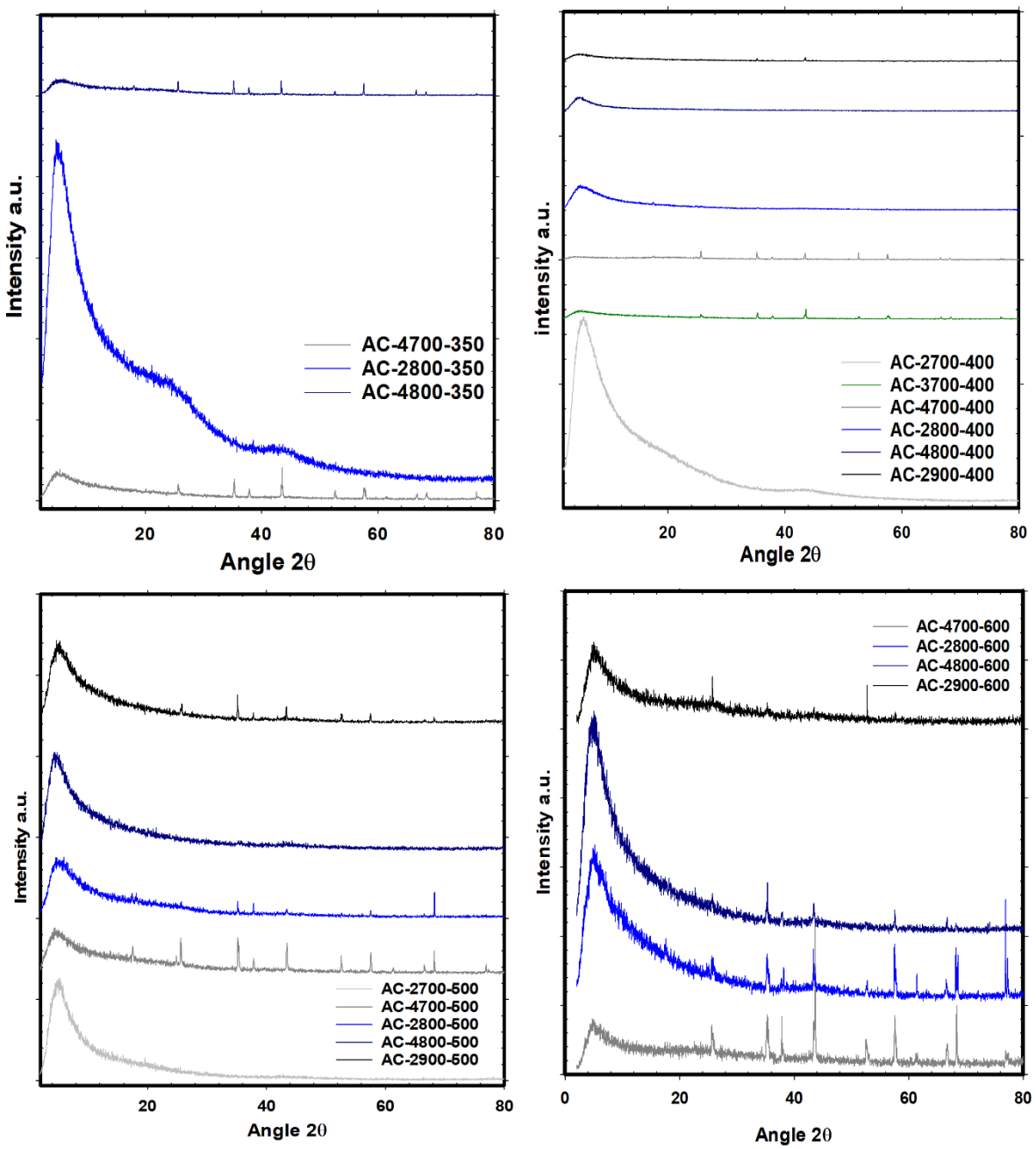


Figure 7. Powder XRD patterns of air-carbonised prickly pear peels-derived (PPPs) derived activated carbons.

Using SEM images of highly porous AC-2800-400 (1, 2, and 3) b, and AC-4800-500 (1, 2, and 3) c, the activation mechanism was investigated further. As illustrated in Figure 8, the shape of these activated carbons is significantly distinct from that of raw PPPs (1, 2, and

3) a. In both the imaged activated carbons, particles with smooth surfaces and extensive conchoidal cavities dominate the morphology of the activated carbons, which is consistent with what has been previously described for char-derived activated carbons.

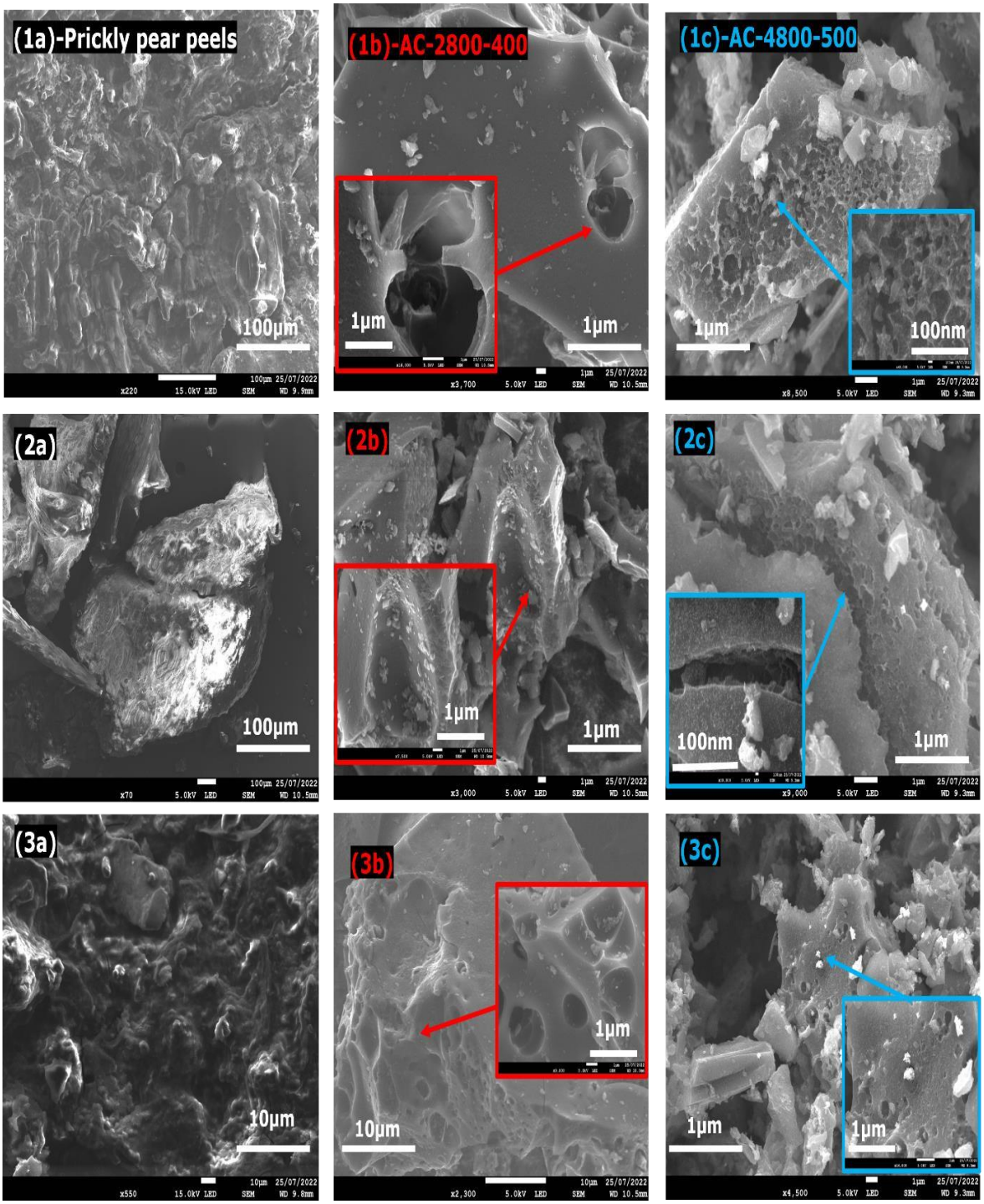


Figure 8: SEM images of (a) raw prickly pear peels (1, 2, 3), (b) AC-2800-400 (1, 2, 3), and (c) AC-4800-500 (1, 2, 3).

The porosity and the textural properties of PPPS-derived activated carbon

As shown in Figure 9 – 12, the nitrogen sorption isotherms for PPPS-derived carbons activated carbons exhibit a range of isotherms including type I, a mix of type I and type IV and type IV, depending on the char and level of activation (amount of KOH and activation temperature). This indicates that the porosity of the PPPS- derived carbons ranges from microporous to mainly mesoporous, although all samples exhibit some microporosity. The range of pores is confirmed by the pore size distribution curves in Figure 9 – 12.

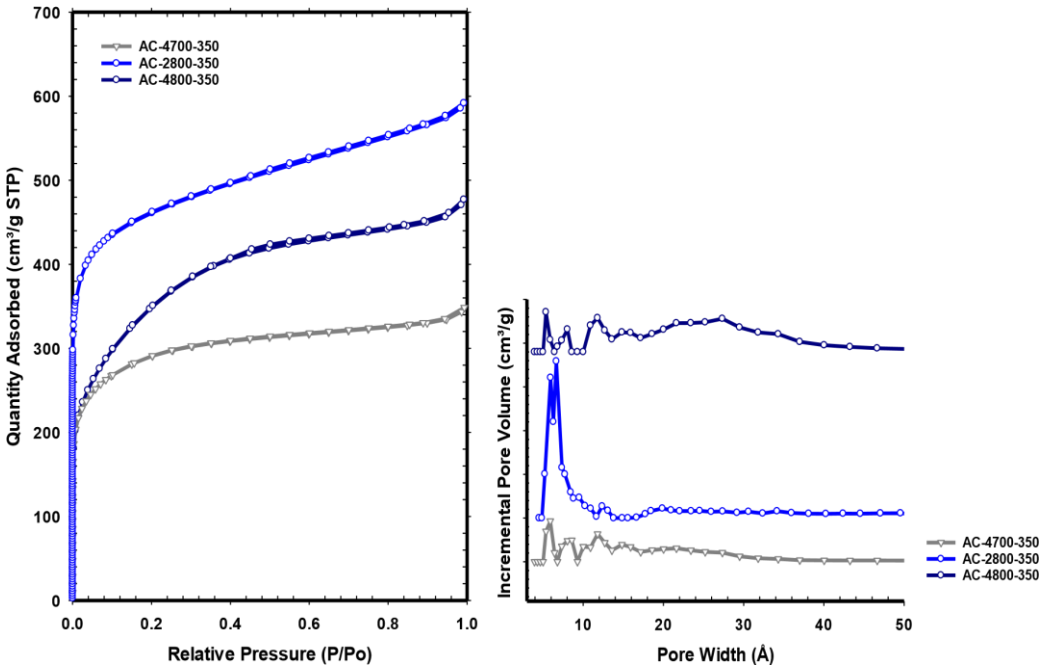


Figure 9: N_2 sorption isotherms (left) and pore size distribution curves (right) of activated carbons prepared from Char-350.

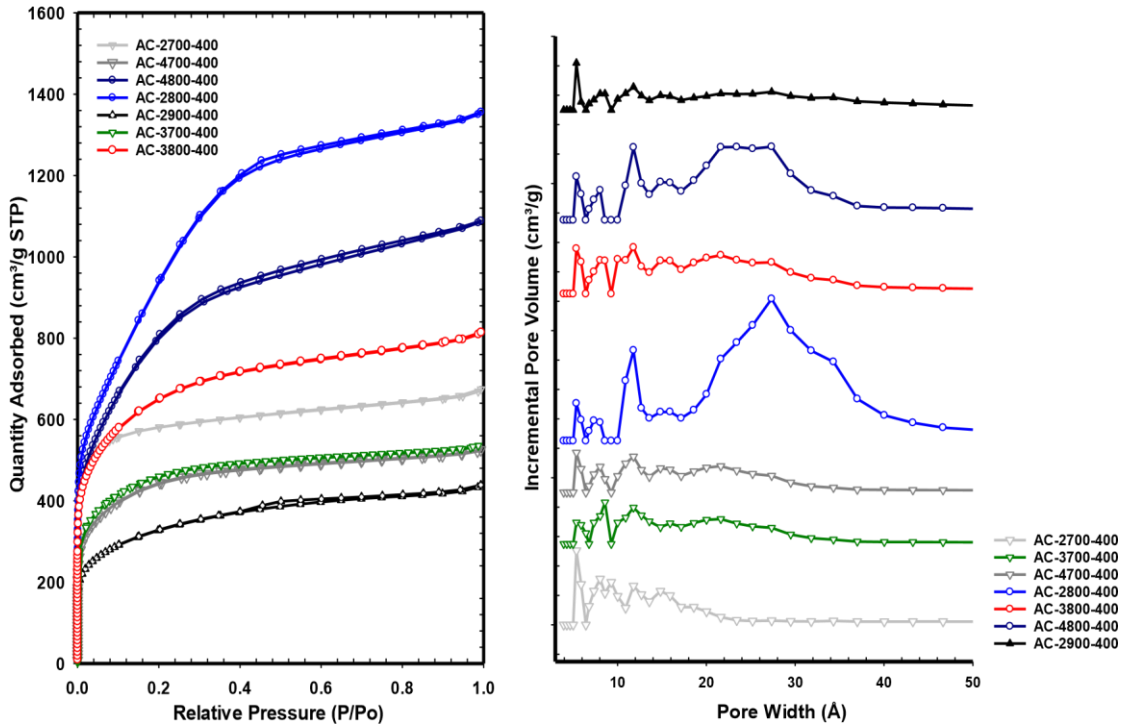


Figure 10: N_2 sorption isotherms (left) and pore size distribution curves (right) of activated carbons prepared from Char-400.

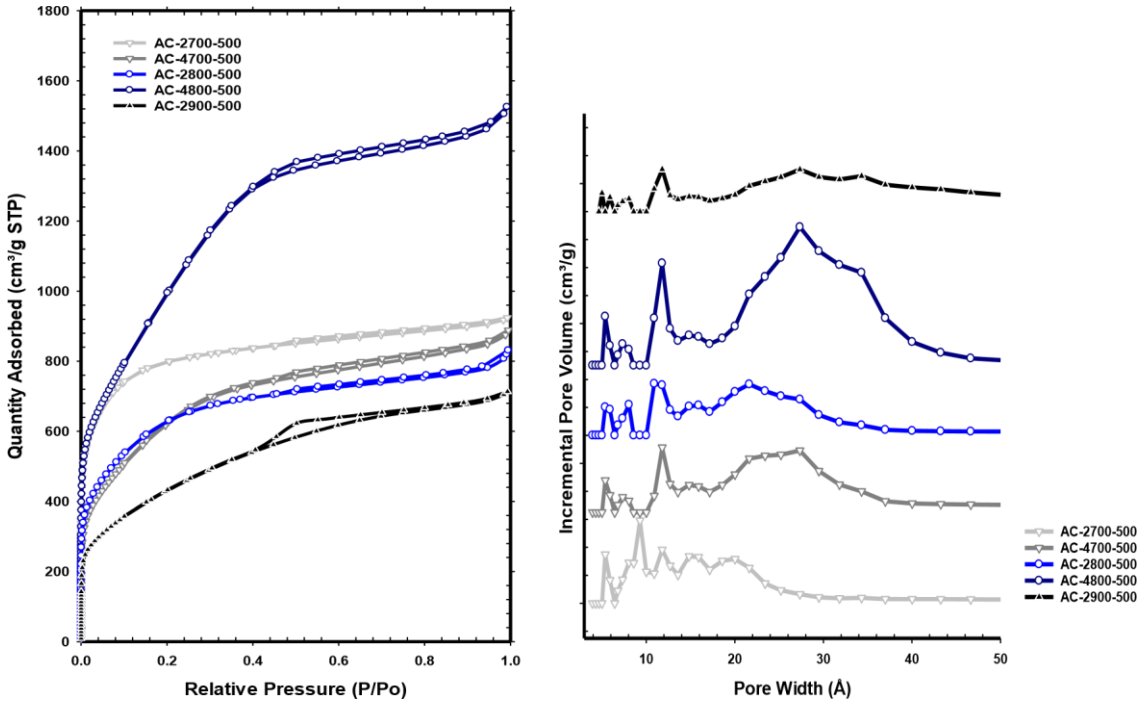


Figure 11: N_2 sorption isotherms (left) and pore size distribution curves (right) of activated carbons prepared from Char-500.

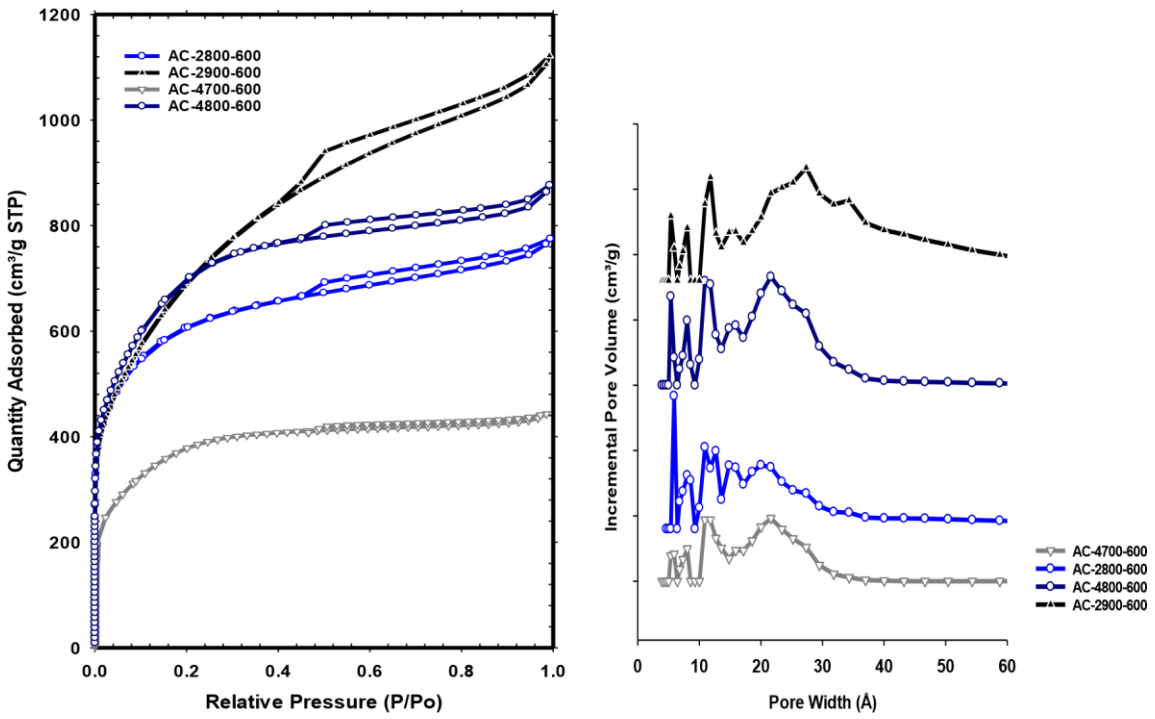


Figure 12: N_2 sorption isotherms (left) and pore size distribution curves (right) of activated carbons prepared from Char-600.

The textural properties of the PPPS-derived activated carbons are summarised in Tables 4, 5, 6 and 7 and for simplicity are grouped according to the char use as precursor for activation. For the AC-XY-350 set of samples (Table 4), the surface area increased with activation temperature as follows; 1075 m^2/g (AC-4700-350) and 1263 m^2/g (AC-4800350), while the microporosity decreased slightly. In contrast, at a similar activation temperature e.g., 800°C, the sample prepared at KOH/char ratio of 2 tended to have a higher surface area. In addition, the increase in activating agent ratio led to an expansion of pore width up to 1.2 nm (Table 4 and Figure 9), with an increase in pore volume from 0.46 (AC-2800-350) to 0.74 (AC-4800-350).

Table 4: Textural properties and packing density of activated carbons prepared from Char-350.

Sample	Surface are[a] (m^2/g)	Pore size *(Å)*	Pore volume[b] (cm^3/g)	Packing density (g/cm^3)
AC4700-350	1075 (973)	6/8/12	0.54 (0.42)	1.01
AC2800-350	1512 (937)	6/7	0.82 (0.46)	0.78
AC4800-350	1263 (916)	5/8/11	0.74 (0.41)	0.84

The values in parentheses are; [a]micropore surface area, and [b]micropore volume

As shown in Table 5, the optimal temperature of activation for the AC-XY-400 is 800 °C. When compared to samples prepared at 700°C and 900°C, samples prepared at 800°C had the highest specific surface area, e.g., 3614 m^2/g (AC-2800-400), 2309 m^2/g (AC3800-400), and 2959 m^2/g (AC-4800-400). The majority of AC-XY-400 samples show similar pore width e.g., 0.5, 0.8 and 1.1 nm. However, AC-2800-400 and AC-4800-400, exhibit the type IV isotherm. This type of adsorption indicates a relatively mesoporous structure, with a small number of micropores; for instance, the surface areas are 3614 m^2/g and 2959 m^2/g, while the micropore areas are 1633 m^2/g and 2127 m^2/g, with pore widths of 2.8 nm and 2.5 nm, and greater pore volumes of 2.19 cm^3/g and 1.68 cm^3/g, respectively.

Table 5: Textural properties and packing density of activated carbons prepared from Char-400.

Sample	*Surface are[a] (m^2/g)*	*Pore size (Å)*	*Pore volume[b] (cm^3/g)*	*Packing density (g/cm^3)*
AC2700-400	2163 (1977)	5/7/11	1.04 (0.83)	0.67
AC3700-400	1620 (764)	5/8/12	0.83 (0.33)	0.78
AC4700-400	1522 (1346)	5/8/11	0.81 (0.63)	0.79
AC2800-400	3614 (1633)	5/11/28	2.19 (0.66)	0.38
AC3800-400	2309 (1936)	5/8/11	1.26 (0.88)	0.58
AC4800-400	2959 (2127)	5/11/25	1.68 (0.91)	0.47
AC2900-400	1167(890)	5/8/12	0.68 (0.41)	0.88

The values in parentheses are; [a]micropore surface area, and [b]micropore volume.

In the case of the AC-XY-500 sample set, samples prepared at KOH/Char ratio of 2 show a decrease in surface area as the temperature increases from 700°C to 900°C, e.g., 2846 m^2/g (AC-2700-500), 2261 m^2/g (AC-2800-500), and 1568 m^2/g (AC-2900-500). In addition, the increase on activation temperature led to a decrease in the microporosity region i.e., from 2498 m^2/g to 730 m^2/g, as well as decrease in pore volume from 1.43 cm^3/g to 1.10 cm^3/g. However, AC-4800-500 shows a similar trend to AC-2800-400, whereby the initial adsorption at low pressure follows a type II isotherm, due to a monolayer moving to a multilayer adsorption. The hysteresis loop shows capillary condensation of nitrogen occurring in the meso cavities at high relative pressure. It exhibits the highest specific surface area in the AC-XY-500 group up to 3720 m^2/g, with a broad pore size distribution centred at ~2.7 nm and a large pore volume of ~2.37 cm^3/g.

Table 6: Textural properties and packing density of activated carbons prepared from Char-500.

Sample	*Surface are[a] (m^2/g)*	*Pore size (Å)*	*Pore volume[b] (cm^3/g)*	*Packing density (g/cm^3)*
AC2700-500	2846 (2498)	5/9/11	1.43 (1.09)	0.53
AC4700-500	2305(1908)	5/7/12	1.36 (0.90)	0.55
AC2800-500	2261 (1801)	6/8/11	1.28 (0.80)	0.58
AC4800-500	3720 (1283)	5/7/27	2.37 (1.78)	0.35
AC2900-500	1568(730)	5/12	1.10 (0.33)	0.64

The values in parentheses are; [a]micropore surface area, and [b]micropore volume.

The AC-XY-600 sample set shows that an increase in amount of activation agent or activation temperature led to increase specific surface area and pore volume, e.g., AC4700-600 < AC-4800-600 and AC-2800-600 < A-4800-600. It is important to note that AC-2900-600 exhibited a high surface area (~2531 m^2/g) and pore volume (~1.74 cm^3/g) compared with samples prepared in similar conditions from the other sample sets, e.g., AC-2900-400 (1167m^2/g and 0.68 cm^3/g) and AC-2900-500 (1568 m^2/g and 1.10 cm^3/g). That may be attributable to the Char-600 thermal stability produced in the first instance (Figure 3).

Table 7: Textural properties and packing density of activated carbons prepared from Char-600.

Sample	*Surface are[a] (m²/g)*	*Pore size (Å)*	*Pore volume[b] (cm³/g)*	*Packing density (g/cm³)*
AC4700-600	1391(1324)	6/8/11	0.69 (0.59)	0.87
AC2800-600	2146(1819)	6/8/11	1.20 (0.82)	0.60
AC4800-600	2520(2107)	6/12/21	1.35 (0.92)	0.55
AC2900-600	2531(1267)	5/12/27	1.74 (0.56)	0.46

The values in parentheses are; [a]micropore surface area, and [b]micropore volume.

Regarding possible application of the PPPS- derived carbons, numerous studies have shed light on the optimal pore sizes that maximise a solid's gas storage capacity.[3,33,52–55] The pore size must be greater than the appropriate adsorbent diameter for gas molecules to enter. In addition, to achieve better diffusion at low temperatures, pore size must be greater than the kinetic diameter of the molecules (dk). For small molecules such as CO_2 and CH_4 (dk= 0.33 and 0.38 nm respectively),[3,56–59] PPPS-derived activated carbon samples show highly micropore structure with pores sizes from 0.5-1.2 nm, which may indicate suitability for their storage. PPPS-derived activated carbons demonstrate that PPPs are a suitable biomass source for medium to high surface area carbons wherein the textural qualities may be tailored for gas storage and capture applications. Various studies have shown that packing density is a good predictor of CH_4 and CO_2 capacity, provided that this is balanced with appropriate pore size, as well as high surface area and pore volume. Packing density can be measured from the pellets compacted in a 1.3 cm die for 5-10 minutes at 7 MPa. Similar values are typically obtained from the Grain Density Equation:

$$ \text{ɖ}carbon = \left(\frac{1}{\rho s} + \nu\tau\right)^{-1} \qquad \textit{Equation 1} $$

where ρ_s is the skeletal density determined via helium pycnometry and $\nu\tau$ is the total pore volume. As shown in Table 4 – 7, the present activated carbons have density values ranging between 0.35 - 1.01 g/ cm^3, which is important in volumetric capacity for gas uptake.

5.3.3. Methane uptake

For effective methane storage at moderate to high pressure (35–100 bar), a porous material must be predominately microporous with a high surface area and low mesoporosity. A high microporous volume is required to achieve robust adsorption of methane molecules, yet a certain amount of mesoporosity is necessary for effective sorption kinetics. In addition, pore channels ranging in size from 0.8 to 1.5 nm are optimally suited for the adsorption of two or three methane molecules by optimising the packing of the adsorbed phase within the pores. Additionally, it has been hypothesised that pore channels of size 1.1 nm are optimal for methane storage.[3,14,54,55,60]With their mixture of microporosity and mesoporosity (Tables 4, 5, 6, and 7), the current activated carbons are suitable for achieving a high methane storage capacity at moderate pressures. The methane adsorption capacity of activated carbons was determined at ambient temperature (25°C) and up to 100 bar pressure.

Fig. 13 displays the excess and total methane uptake isotherms of the AC-XY-Z activated carbons. The current study's measurements of methane uptake allowed for direct determination of the excess uptake. The excess CH_4 adsorption isotherms were measured using ca. 0.15 g of activated carbon, which was degassed at 240 °C for 3 h under vacuum. The CH_4 adsorption isotherms were then determined at 25 °C and pressure of up to 100 bar. The total methane storage capacity can be calculated from the excess values by taking into account the density of the methane (under any given temperature and pressure conditions) and the total pore volume of the activated carbon. This was done by applying the equation:

$$\theta_{Tol} = \theta_{Exc} + \rho_{CH4} * \nu_{\tau} \qquad \textit{Equation 2}$$

where θ_{Tol} is total methane uptake, θ_{Exc} is excess methane uptake, ρ_{CH4} is density (g/cm^3) of methane gas under the prevailing temperature and pressure, and ν_{τ} is total pore volume (cm^3/g) of the activated carbon. The methane density was obtained from the National Institute of Standards and Technology (NIST) website (https://www.nist.gov/).

As shown in Figure 13, the methane uptake isotherms at a pressure of up to 100 bar proved fully reversible with no hysteresis. The isotherms indicate that saturation was not attained in the 0–100 bar pressure range, meaning the present carbons can potentially store greater amounts of methane

at higher pressure. The present carbons have highvery high gravimetric methane storage capacity, with the uptake being superior for samples that have higher surface area and pore volume. The fact that the AC-2800-400, AC-4800-400 and AC-4800-500 samples have high methane uptake at high pressures and relatively lower uptake at low pressures is a preferred combination for achieving better performance with respect to working capacity.

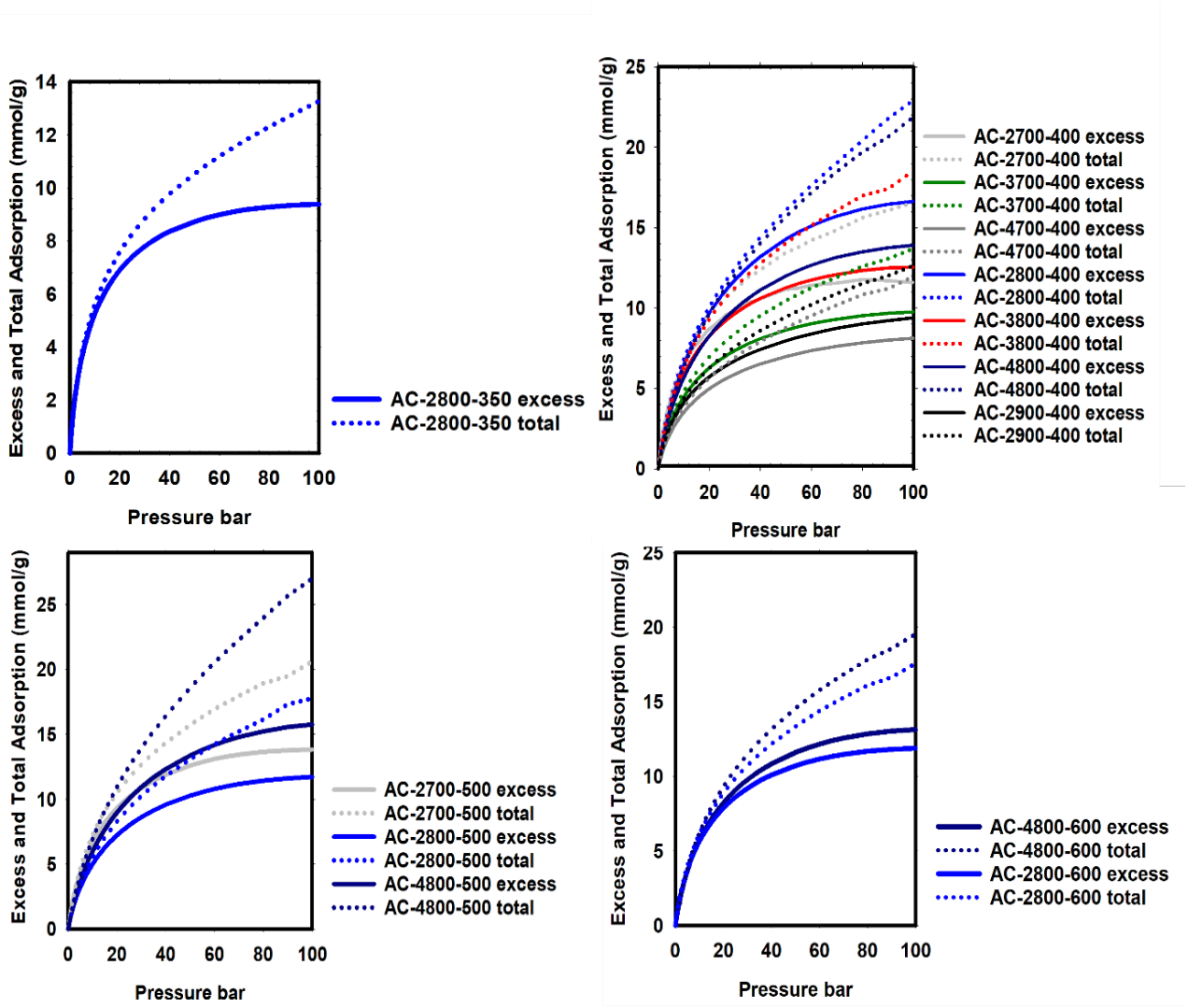


Figure 13: Excess and total gravimetric methane uptake at 25°C of all AC-XY-Z activated carbon samples.

Table 8 and 9 summarise the excess methane uptake at 5, 35 and 100 bar, expressed as gravimetric (mmol/g and g/g) or volumetric (cm^3 (STP)/cm^3) uptake. The resulting activated carbons have a high-extremely high gravimetric methane storage capacity, with greater absorption in samples with a greater surface area and pore volume. The excess gravimetric methane uptake at 35 bar is in the range 6.2 - 12.5 mmol/g (equivalent to 0.10–0.20 g/g). Meanwhile, the excess gravimetric methane uptake at 100 bar is in the range 8.1- 16.6 mmol/g (equivalent to 0.13–0.27 g/g). Samples AC2800-400, AC4800400 and AC-4800-500 have higher gravimetric methane uptake, which is consistent with their greater surface area and pore volume. This can be contrasted with sample AC-4700400 which has both the lowest porosity and methane uptake. It is noteworthy that, at 25°C and 35 bar

pressure, the excess methane uptake of 12.5 mmol/g (0.20 g/g) is among the highest observed for any porous material.

Table 8: Excess gravimetric methane uptake (mmol/g) of all AC-XY-Z activated carbon samples at pressures 1, 5, 35 and 100 bar and 25°C.

Samples	*1 bar*	*5 bar*	*35 bar*	*100 bar*
AC2800-350	1.3	3.7	8.1	9.4
AC4800-350	0.6	1.4	4.0	6.7
AC2700-400	1.6	4.5	10.4	11.6
AC3700-400	1.0	3.0	7.8	9.8
AC4700-400	0.7	2.3	6.2	8.1
AC2800-400	1.1	4.0	12.5	16.6
AC3800-400	1.2	3.9	10.2	12.6
AC4800-400	1.0	3.6	10.6	13.9
AC2900-400	1.0	2.8	7.1	9.4
AC2700-500	1.4	4.5	11.4	13.8
AC2800-500	1.0	3.3	9.2	11.7
AC4800-500	1.0	3.7	11.7	15.8
AC2800-600	1.2	3.9	9.7	11.9
AC4800-600	1.3	3.8	10.4	13.2

Table 9: Excess methane uptake (mmol/g), (g/g), and (cm^3(STP)/cm^{-3}) of AC-XY-Z activated carbons at pressure of 5, 35 and 100 bar and 25°C.

Sample	Excess CH_4 uptake								
	mmol/g			g/g			cm^3(STP)/cm^3		
	@5	@35	@100	@5	@35	@100	@5	@35	@100
AC2800-350	3.7	8.1	9.4	0.06	0.13	0.15	64.7	141.6	164.3
AC2700-400	4.5	10.4	11.6	0.07	0.17	0.19	67.6	156.2	174.2
AC3700-400	3.0	7.8	9.8	0.05	0.12	0.16	52.4	136.4	171.3
AC4700-400	2.3	6.2	8.1	0.04	0.10	0.13	40.7	109.8	143.4
AC2800-400	4.0	12.5	16.6	0.06	0.20	0.27	34.1	106.5	141.4
AC3800-400	3.9	10.2	12.6	0.06	0.16	0.20	50.7	132.6	163.8
AC4800-400	3.6	10.6	13.9	0.06	0.17	0.22	37.9	111.7	146.4
AC2900-400	2.8	7.1	9.4	0.04	0.11	0.15	55.2	140.0	185.4
AC2700-500	4.5	11.4	13.8	0.07	0.18	0.22	53.5	135.4	163.9
AC2800-500	3.3	9.2	11.7	0.05	0.15	0.19	42.9	119.6	152.1
AC4800-500	3.7	11.7	15.8	0.06	0.19	0.25	29.0	91.80	124.0
AC2800-600	3.9	9.7	11.9	0.06	0.16	0.19	52.4	130.5	160.0
AC4800-600	3.8	10.4	13.2	0.06	0.17	0.21	39.2	107.2	136.1

As shown in Table 10, the total methane uptake at 35 bar is between 7.5 and 15.3 mmol/g (equivalent to 0.13 and 0.24 g/g). At 100 bar the total uptake is between 12 and 27 mmol/g (equivalent to 0.19 and 0.43 g/g). The total uptake of sample AC-4800-500 at 100 bar, which is 27.0 mmol/g (0.43 g/g), is highly significant, and compares with the highest benchmark materials reported thus far.[14,54,55,61] However, the volumetric uptake (Figure 14 and Table 10), which considers the packing density of the adsorbent, is the most significant measure of solids performance in

methane storage. The primary goals for methane storage in porous materials are based on the volumetric uptake capacity, which is measured in cm^3 (STP) cm^{-3} (i.e., cm^3 of methane per unit tank volume occupied by the adsorbent). Frequently cited is the US Department of Energy's (DOE) target of 263 cm^3 (STP) cm^{-3} at ambient temperature (25°C) and standard pressure (35–100 bar).

Table 10: Total methane uptake (mmol/g), (g/g), and (cm^3(STP)_cm^{-3}) of AC-XY-Z activated carbons at pressures of 5, 35 and 100 bar, and 25°C.

Sample	TotalCH_4 uptake									Working capacity
	mmol/g			g/g			cm^3(STP)\cm^3			
	@5	@35	@100	@5	@35	@100	@5	@35	@100	cm^3/cm^3
AC2800-350	3.9	9.3	13.3	0.06	0.15	0.21	68	163	232	95
AC2700-400	4.7	11.9	16.5	0.08	0.19	0.26	70	179	248	109
AC3700-400	3.1	9.0	13.7	0.05	0.14	0.22	55	158	240	102
AC4700-400	2.5	7.5	12.0	0.04	0.12	0.19	44	132	212	88
AC2800-400	4.3	13.5	22.9	0.07	0.22	0.37	37	115	195	78
AC3800-400	4.2	12.1	18.5	0.07	0.19	0.30	54	157	241	103
AC4800-400	4.0	13.1	21.9	0.06	0.21	0.35	42	138	231	97
AC2900-400	2.3	8.1	12.6	0.04	0.13	0.20	57	160	249	103
AC2700-500	4.7	13.5	20.6	0.08	0.22	0.32	62	177	268	115
AC2800-500	3.5	11.1	17.8	0.06	0.18	0.29	46	144	231	98
AC4800-500	4.2	15.3	27.0	0.07	0.24	0.43	33	120	212	87
AC2800-600	3.8	11.5	17.6	0.06	0.18	0.28	51	155	237	104
AC4800-600	4.0	12.4	19.5	0.06	0.20	0.31	49	153	241	104

Although, the best excess gravimetric uptake was obtained for the following samples which also have the highest surface area and pore volume: AC-2800-400 (~16.6 mmol/g), and AC-4800-500 (~15.8 mmol/g) had the highest surface areas of 3614 m^2/g, and 3720 m^2/g, and pore volumes of 2.19 cm^3/g, and 2.37cm^3/g respectively, whereas samples AC2800-350, AC4700-400, and AC2700-500 had the highest total volumetric uptake up to 179.1 cm^3(STP)/ cm^3 at 35 bar, and 268.1

cm^3(STP)/ cm^3 at 100 bar . The enhanced volumetric uptake efficiency of sample AC-2700-500 is attributable to a more optimal combination of porosity and packing density. The present carbons have excess volumetric methane uptake (at 25°C and 35bar) up to 156.2 cm^3 (STP) cm^{-3} (AC2700-400), which is higher than the best performing porous carbons for volumetric methane storage at 25°C and 35 bar i.e., mesophase pitch derived activated carbons, LMA738 and DO00-3:1_700 that store 142 cm^3 (STP) cm^{-3} methane[46] , and zeolite templated carbons, ZTC, (BEA-ZTC) and thermally treated BEA-ZTC (BEA-ZTC-873), that store 125 and 145 cm^3 (STP) cm^{-3} methane[62], respectively. It is also comparable to DO00-3:1_700 that store that store ~160 cm^3 (STP) cm^{-3} of methane and the greatest uptake recorded for ACDS4700, which stores 196 cm^3 (STP) cm^{-3} of excess methane.[33]

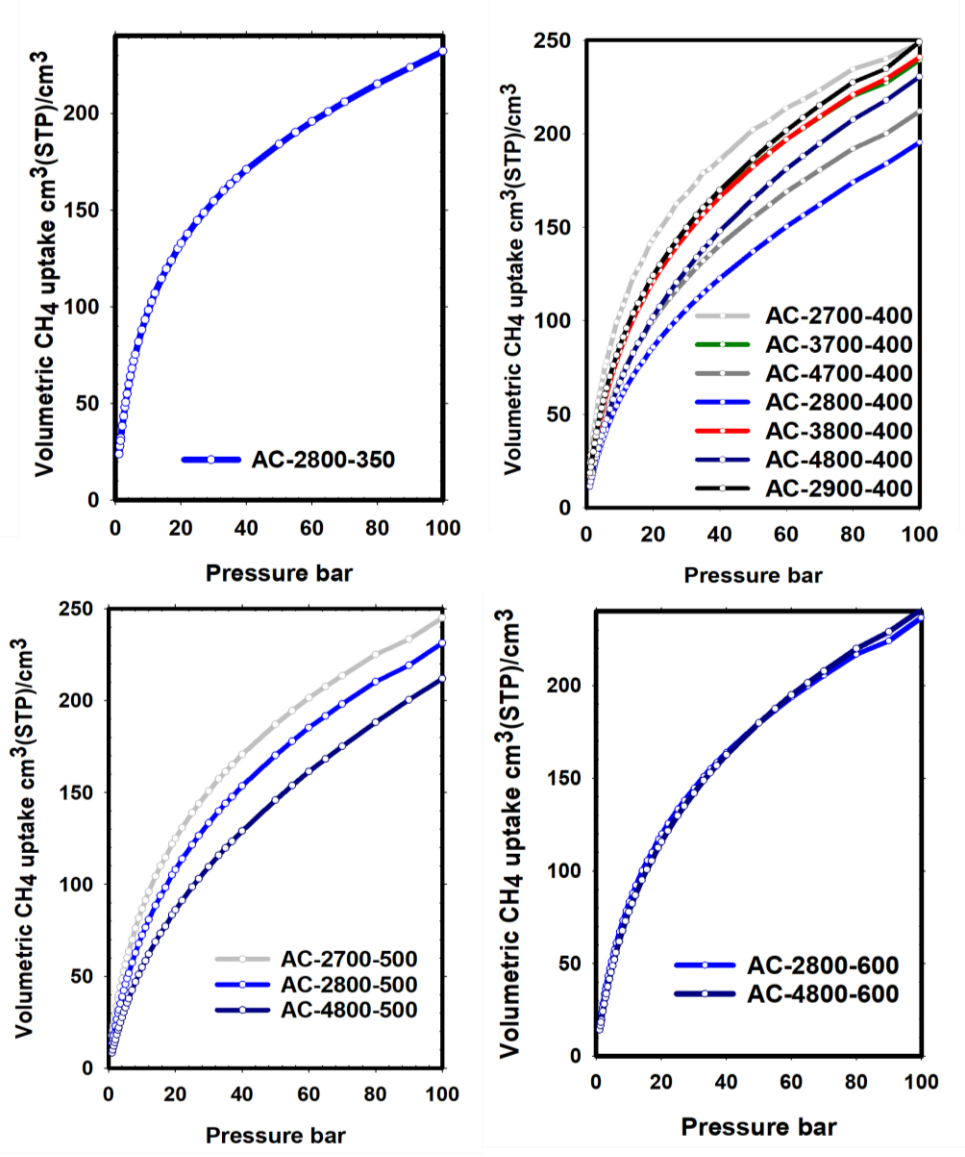


Figure 14: Volumetric methane uptake isotherms of AC-XY-Z carbons at 25°C.

The working capacity, which is the difference in uptake between the adsorption and desorption (regeneration) pressures, is a crucial indicator of how much a porous material will store methane. A desorption pressure of 5.8 bar is recommended for methane storage, and an adsorption pressure of 35 bar was used in this study. Samples have a working capacity of up to 115 cm^3/cm^3, which is good compared with the highest working capacity (135 cm^3/cm^3) recorded in the literature for activated carbon generated from biomass.[33]

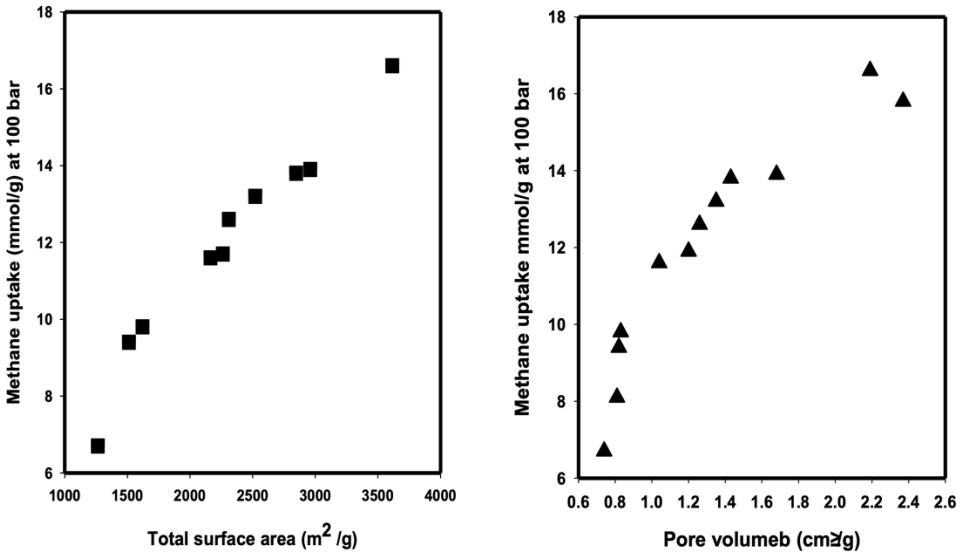


Figure 15: The effect of total surface area and total pore volume on the CH_4 uptake at high pressure ~100 bar and 25C°.

5.3.4. CO_2 uptake

Natural gas is the cleanest source of fossil fuel. However, natural gas wells generally include substantial quantities of CO_2, necessitating on-site CO_2 capture. Due to their comparatively modest regeneration energies and non-corrosive nature, solid sorbents are preferable to conventional amine scrubbing. To enhance the sorbent's CO_2 capacity at elevated pressures relevant to natural gas purification remains difficult. The capacity for CO_2 capture and storage for the PPPS-derived carbons was measured at 25°C and a pressure range of 1 to 40 bar. The CO_2 uptake isotherms are shown in Fig. 16, and the storage capacity at various pressures (1, 20, and 40 bar) is stated in Table 11. For the AC-XY-350 samples set, AC-2800-350 exhibits the highest CO_2 uptake performance at low and high pressure: ~3.7 mmol/g at 1 bar and ~13.6 mmol/ g at 40 bar. For the AC-XY400 sample set, samples prepared at 700°C showed that uptake was inversely proportional with the KOH/char

ratio. Samples prepared at a KOH/char ratio of 2 showed high performance for low pressure CO_2 uptake. On the other hand, uptake at 40 bar was 18.8 mmol/ g (AC-2700-400), > 15.4 mmol/ g (AC-3700-400) and >12.5 mmol/ g (AC4700-400). However, the uptake of samples prepared at a KOH/char ratio of 2 indicated that 800 °C is the best activation temperature to highly porous carbons with high surface area (3614 m^2/g), capable of storing 31.7 mmol/g of CO_2 at high pressure, which is the highest uptake in the AC-XY-400 set of samples.

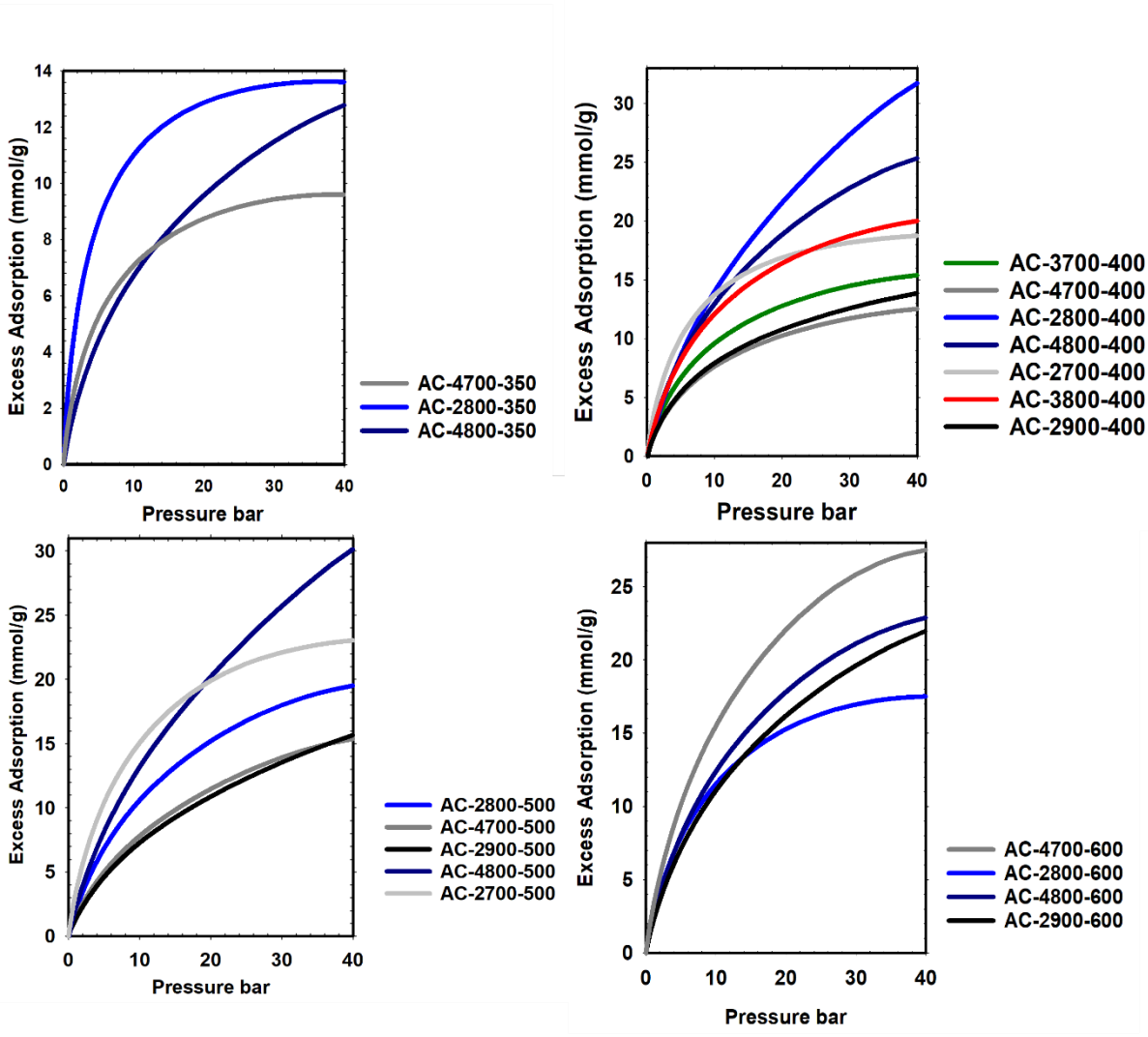


Figure 16: Excess gravimetric CO_2 uptake isotherms of AC-XY-Z at ~25°C.

Table 11: Excess gravimetric CO_2 uptake for PPPS-derived activated carbon at 25°C and pressure range of 1, 20 and 40 bar.

Sample	*1 bar*	*20 bar*	*30 bar*	*40 bar*
AC4700-350	2.1	8.8	9.4	9.6
AC2800-350	3.7	12.9	13.5	13.6
AC4800-350	1.4	9.6	11.5	12.8
AC2700-400	3.7	17.0	18.2	18.8
AC3700-400	2.2	12.8	14.5	15.4
AC4700-400	1.8	10.3	11.7	12.5
AC2800-400	2.2	21.6	27.3	31.7
AC3800-400	2.5	16.4	18.5	20.0
AC4800-400	2.6	18.9	22.8	25.3
AC2900-400	1.7	10.8	12.7	13.9
AC2700-500	3.5	15.7	21.9	23.1
AC4700-500	1.5	11.8	14.0	15.4
AC2800-500	2.0	15.3	18.3	19.5
AC4800-500	2.2	20.3	25.7	30.1
AC2900-500	1.4	10.9	13.5	15.7
AC4700-600	3.2	22.1	25.8	27.5
AC2800-600	3.0	15.5	16.9	17.5
AC4800-600	2.3	17.9	21.0	22.9
AC2900-600	2.1	16.2	19.8	22.0

The AC-XY-500 sample set showed a similar trend to AC-XY-400, where CO_2 uptake is inversely proportional with KOH/carbon ratio at samples prepared at the same activation temperature. For example, the excess uptake at 40 bar is 23.1 mmol/g (AC-2700-500) and >15.4mmol/g (AC-4700-500). Furthermore, samples prepared at a KOH/carbon ratio of 2 and activation temperatures ranging from 700 to 900°C demonstrated that CO_2 uptake decreases when the activation temperature is raised, e.g., at 40 bar the excess CO_2 uptake was ~23.1 mmol/ g (AC-2700-500), ~19.5 mol/ g (AC-2800-500) and ~15.7 mmol/ g (AC-2900-400). Finally, AC-4800-500 showed the highest CO_2 uptake ability: up to ~30.1 mmol/ g at 40 bar. At 40 bar, the CO_2 uptake of AC-XY-600

samples ranged from 17.5 mmol/g to 27.5 mmol/g. At a KOH/carbon ratio of 4, the CO_2 uptake of the samples reduced as the activation temperature increased. For example, AC-4700-600 > AC-4800600. In addition, at the same temperature, the CO_2 uptake capacity is increased as the KOH/carbon ration is increased, e.g., 17.5 mmol/g (AC-2800-600) < 22.9 mmol/g (AC-4800-600).

The findings indicate that PPPS-derived activated carbon presents a potential option for high-pressure CO_2 storage. The carbons have optimal CO_2 uptake at moderate to high pressure, for example up to 22 mmol/g at 20 bar, 27.3 mmol/g at 30 bar, and 31.5 mmol/g at 40 bar, at 25°C. It can be deduced that CO_2 uptake capacity at moderate to high pressure is more closely connected to total surface area rather than the narrow micropore structure. Many studies emphasise that increases in surface area and pore volume typically enhance CO_2 adsorption by providing adsorbed molecules with more surface to interact with and more space to fill, respectively. This is, however, restricted by pore size.[56,63–65]

Pore size is an essential metric that might indicate the probability of CO_2 adsorption. Pore width should be more than the kinetic diameter of CO_2 (dk) = 0.33 nm. Where the width less than the CO_2 diameter, this means that CO_2 adsorption will not occur. A slightly larger width than the CO_2 diameter will lead to extremely slow diffusion at low temperatures, meaning that equilibrium may take a long time (hours) to achieve.[3,64,65] For instance, AC2800-400 and AC-4800-500, which showed the highest uptake at 40 bar, have a high pore width (up to 2.8 and 2.7 nm respectively).

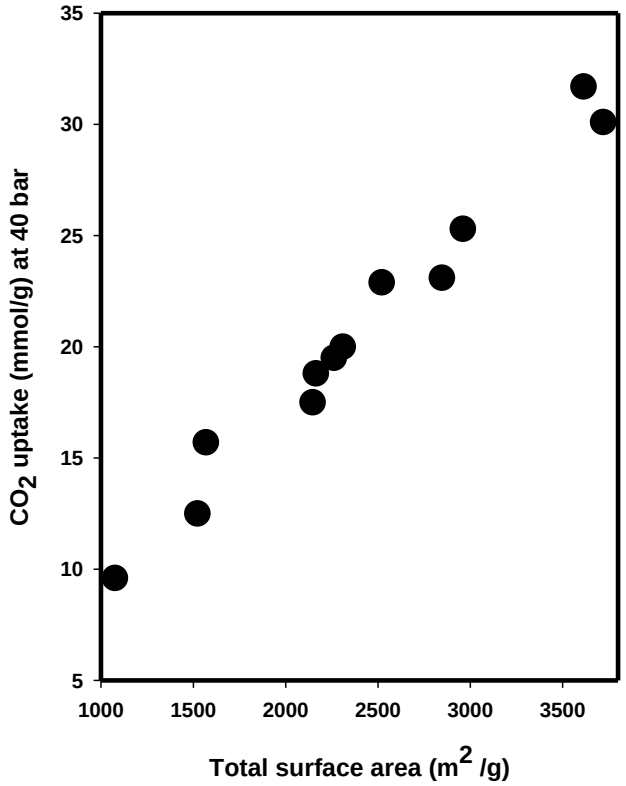


Figure 17: The effect of the increase of total surface area on the excess CO_2 uptake at high pressure ~40 bar and 25 °C.

5.4. Conclusion

In summary, this study sought to investigate the chemical activation of cheap, readily available, and renewable prickly pear peel-derived char with potassium hydroxide. PPPS activated carbons were successfully produced via an air carbonisation (flash carbonisation) route, that offers simplicity by removing the need for extended hydrothermal carbonisation or pyrolysis. The flash carbonisation route involved the introduction of air for 5 minutes, at a low to moderate temperature (350°C, 400°C, 500°C and 600°C) prior to activation. The results showed that the activation process can significantly develop the pore structure of the PPPS-derived char to generate porosity ranging from a narrow, small micropore size distribution to a larger micropore and small mesopore range. Resultant activated carbons of the four sample sets exhibited moderate to high surface area and pore volume, in the range 1075-1512 m^2/g and 0.54-0.82 cm^3/g (AC-XY-350), 1167-3614 m^2/g and 0.68-2.19 cm^3/g (AC-XY-400), 1568-3720 m^2/g and 1.10-2.37 cm^3/g (AC-XY-500), and 1391-2531 m^2/g and 0.69-1.74 cm^3/g (AC-XY-600).

All samples demonstrated a microporous/mesoporous structure dominated by pores of size 0.6 - 1.2 nm and were therefore capable of enhanced CO_2 uptake of up to 31.7 mmol/g at 25°C and 40 bar. Moreover, samples with higher surface area and pore volume exhibited enhanced CH_4 excess uptake at moderate to high pressure of up to 12.5 mmol/g at 35 bar and 16.6 mmol/g at 100 bar, at 25°C. Moreover, the samples had impressive total CH_4 uptake of up to ~15.3 mmol/g at 35 bar, and 27.0 mmol/g at 100 bar. The best performing samples have levels of volumetric storage that reaches up to 179 cm^3(STP)/cm^3 at 35 and 268 cm^3(STP)/cm^3 at 100 bar.

5.5. References

1 S. Choi, J. H. Drese and C. W. Jones, *ChemSusChem*, 2009, **2**, 796–854.

2 U. Eberle, B. Müller and R. Von Helmolt, *Energy Environ Sci*, 2012, **5**, 8780–8798.

3 L. S. Blankenship and R. Mokaya, *Mater Adv*, 2022, **3**, 1905–1930.

4 K. V. Kumar, K. Preuss, M. M. Titirici and F. Rodríguez-Reinoso, *Chem Rev*, 2017, **117**, 1796–1825.

5 I. Angelidaki, L. Treu, P. Tsapekos, G. Luo, S. Campanaro, H. Wenzel and P. G. Kougias, *Biotechnol Adv*, 2018, **36**, 452–466.

6 M. Sevilla and A. B. Fuertes, *J Mater Chem A Mater*, 2013, **1**, 13738–13741.

7 M. Inagaki, M. Toyoda, Y. Soneda, S. Tsujimura and T. Morishita, *Carbon N Y*, 2016, **107**, 448–473.

8 M. Sevilla, A. B. Fuertes and R. Mokaya, *Energy Environ Sci*, 2011, **4**, 1400–1410.

9 J. Wang and S. Kaskel, *J Mater Chem*, 2012, **22**, 23710–23725.

10 Y. Xia, Z. Yang and Y. Zhu, *J Mater Chem A Mater*, 2013, **1**, 9365–9381.

11 M. Sevilla and R. Mokaya, in *Energy and Environmental Science*, Royal Society of Chemistry, 2014, **7**, 1250–1280.

12 A. Alabadi, S. Razzaque, Y. Yang, S. Chen and B. Tan, *Chemical Engineering Journal*, 2015, **281**, 606–612.

13 N. Balahmar and R. Mokaya, *J Mater Chem A Mater*, 2019, **7**, 17466–17479.

14 D. Lozano-Castelló, J. Alcañiz-Monge, M. A. De La Casa-Lillo, D. Cazorla-Amorós and A. Linares-Solano, *Fuel,* 2002, **81**, 1777-1803.

15 E. A. Hirst, A. Taylor and R. Mokaya, *J Mater Chem A Mater*, 2018, **6**, 12393–12403.

16 M. Paneque, J. M. De la Rosa, J. Kern, M. T. Reza and H. Knicker, *J Anal Appl Pyrolysis*, 2017, **128**, 314–323.

17 E. Haffner-Staton, N. Balahmar and R. Mokaya, *J Mater Chem A Mater*, 2016, **4**, 13324–13335.

18 Y. Li, T. Ben, B. Zhang, Y. Fu and S. Qiu, *Sci Rep*, 2013, **3**, 1–6.

19 S. Wang, Y. R. Lee, Y. Won, H. Kim, S. E. Jeong, B. Wook Hwang, A. Ra Cho, J. Y. Kim, Y. Cheol Park, H. Nam, D. H. Lee, H. Kim and S. H. Jo, *Chemical Engineering Journal,* 2022, **437**, 135378.

20 S. Lv, C. Li, J. Mi and H. Meng, *Applied Surface Science,* 2020, **10**,145425.

21 W. Chen, M. Gong, K. Li, M. Xia, Z. Chen, H. Xiao, Y. Fang, Y. Chen, H. Yang and H. Chen, *Environ Sci Technol, 2018, 52, 9414–9521.*

22 M. Sevilla, A. S. M. Al-Jumialy, A. B. Fuertes and R. Mokaya, *ACS Appl Mater Interfaces*, 2018, **10**, 1623–1633.

23 N. Balahmar, A. S. Al-Jumialy and R. Mokaya, *J Mater Chem A Mater*, 2017, **5**, 12330–12339.

24 J. Wang, P. Nie, B. Ding, S. Dong, X. Hao, H. Dou and X. Zhang, *J Mater Chem A Mater*, 2017, **5**, 2411–2428.

25 T. Rogalinski, T. Ingram and G. Brunner, *Journal of Supercritical Fluids*, 2008, **47**, 54–63.

26 C. Quan, R. Su and N. Gao, *Int J Energy Res*, 2020, **44**, 4335–4351.

27 H. Pińkowska, P. Wolak and A. Złocińska, *Biomass Bioenergy*, 2011, **35**, 3902–3912.

28 Y. Liu, S. Ma and J. Chen, *J Clean Prod*, 2018, **176**, 187–195.

29 Z. Kaczor, Z. Buliński and S. Werle, *Renew Energy*, 2020, **159**, 427–443.

30 M. M. Titirici, R. J. White, C. Falco and M. Sevilla, *Energy Environ Sci*, 2012, **5**, 6796–6822.

31 M. M. Titirici, A. Thomas, S. H. Yu, J. O. Müller and M. Antonietti, *Chemistry of Materials*, 2007, **19**, 4205–4212.

32 C. K. Rojas-Mayorga, A. Bonilla-Petriciolet, I. A. Aguayo-Villarreal, V. Hernández-Montoya, M. R. Moreno-Virgen, R. Tovar-Gómez and M. A. Montes-Morán, *J Anal Appl Pyrolysis*, 2013, **104**, 10–18.

33 A. Altwala and R. Mokaya, *Energy Environ Sci*, 2020, **13**, 2967–2978.

34 E. Raymundo-Piñero, P. Azaïs, T. Cacciaguerra, D. Cazorla-Amorós, A. Linares-Solano and F. Béguin, *Carbon N Y*, 2005, **43**, 786–795.

35 Y. Lv, F. Zhang, Y. Dou, Y. Zhai, J. Wang, H. Liu, Y. Xia, B. Tu and D. Zhao, *J Mater Chem*, 2012, **22**, 93–99.

36 D. Lozano-Castelló, J. M. Calo, D. Cazorla-Amorós and A. Linares-Solano, *Carbon N Y*, 2007, **45**, 2529–2536.

37 C. Song, S. Wu, M. Cheng, P. Tao, M. Shao and G. Gao, *Sustainability (Switzerland)*, 2014, **6**, 86–98.

38 A. Khasri, O. S. Bello and M. A. Ahmad, *Research on Chemical Intermediates*, 2018, **44**, 5737–5757.

39 M. Sevilla and A. B. Fuertes, *Energy Environ Sci*, 2011, **4**, 1765–1771.

40 J.-H. Yuan, R.-K. Xu and H. Zhang, *Bioresour Technol*, 2011, **102**, 3488–3497.

41 Z. Ding, Y. Wan, X. Hu, S. Wang, A. R. Zimmerman and B. Gao, *Journal of Industrial and Engineering Chemistry*, 2016, **37**, 261–267.

42 M. Ahmad, M. Ahmad, A. R. A. Usman, A. S. Al-Faraj, A. Abduljabbar, Y. S. Ok and M. I. Al-Wabel, *Environ Geochem Health*, 2019, **41**, 1687–1704.

43 W. Chen, H. Yang, Y. Chen, K. Li, M. Xia and H. Chen, *Environ Sci Technol*, 2018, **52**, 9414–9521.

44 F. Lian and B. Xing, *Environ Sci Technol*, 2017, 51, 13517–13532.

45 I. Mufandi, S. Jamilatun, D. A. A. Purnama and R. U. Melani Putri, *al-Kimiya*, 2020, **7**, 62–66.

46 M. E. Casco, M. Martínez-Escandell, K. Kaneko, J. Silvestre-Albero and F. Rodríguez-Reinoso, *Carbon N Y*, 2015, **93**, 11–21.

47 H. Wang, Q. Gao and J. Hu, *J Am Chem Soc*, 2009, **131**, 7016–7022.

48 W. Qiao, S. H. Yoon and I. Mochida, *Energy and Fuels*, 2006, **20**, 1680–1684.

49 X. Xiao, B. Chen, Z. Chen, L. Zhu and J. L. Schnoor, *Environ Sci Technol*, 2018, **52**, 5027–5047.

50 T. Ishii and J. ichi Ozaki, *Carbon N Y*, 2020, **161**, 343–349.

51 X. Yang, Y. Wan, Y. Zheng, F. He, Z. Yu, J. Huang, H. Wang, Y. S. Ok, Y. Jiang and B. Gao, *Chemical Engineering Journal*, 2019, **366**, 608–621.

52 H. Furukawa and O. M. Yaghi, *J Am Chem Soc*, 2009, **131**, 8875–8883.

53 T. A. Makal, J. R. Li, W. Lu and H. C. Zhou, *Chem Soc Rev*, 2012, **41**, 7761–7779.

54 J. Romanos, S. Sweany, T. Rash, L. Firlej, B. Kuchta, J. C. Idrobo and P. Pfeifer, .

55 D. A. Gómez-Gualdrón, C. E. Wilmer, O. K. Farha, J. T. Hupp and R. Q. Snurr, *Journal of Physical Chemistry C*, 2014, **118**, 6941–6951.

56 J. Jagiello, C. Ania, J. B. Parra and C. Cook, *Carbon N Y*, 2015, **91**, 330–337.

57 A. Vishnyakov, P. I. Ravikovitch and A. V. Neimark, *Langmuir*, 1999, **15**, 8736–8742.

58 J. M. Martin-Martinez, R. Torregrosa-Maci6 and M. C. Mittelmeijer-Hazeleger, *Fuel,* 1995, **74**, 111-114.

59 B. E. Poling, J. M. Prausnitz, J. P. O'connell, Properties of gases and liquids, McGRAWHILL, New York, 2001.

60 C. Guan, L. S. Loo, K. Wang and C. Yang, *Energy Convers Manag*, 2011, **52**, 1258–1262.

61 C. M. Simon, J. Kim, D. A. Gomez-Gualdron, J. S. Camp, Y. G. Chung, R. L. Martin, R. Mercado, M. W. Deem, D. Gunter, M. Haranczyk, D. S. Sholl, R. Q. Snurr and B. Smit, *Energy Environ Sci*, 2015, **8**, 1190–1199.

62 S. Choi, M. A. Alkhabbaz, Y. Wang, R. M. Othman and M. Choi, *Carbon N Y*, 2019, **141**, 143–153.

63 M. Sevilla, J. B. Parra and A. B. Fuertes, *ACS Appl Mater Interfaces*, 2013, **5**, 6360–6368.

64 J. Jagiello and M. Thommes, in *Carbon*, Elsevier Ltd, 2004, **42**, 1227–1232.

65 J. Jagiello, J. Kenvin, A. Celzard and V. Fierro, *Carbon N Y*, 2019, **144**, 206–215.

6. Highly microporous activated carbon cloth as a versatile material for CH_4 and CO_2 storage at low pressure

6.1. Introduction

Activated carbons are widely employed as effective adsorbent materials for the storage of adsorbates such as H_2, CH_4, and CO_2 due to their large specific surface areas (SSA), good chemical stability and low cost. When nanoporous activated carbon is used for these applications, it must still be treated to generate a functional material (e.g., membranes, thin films) from carbon powder. This results in a lowering of the specific surface area and pore volume, due to the effects of aggregation and pore blockage.[1] Since these textural properties play a key role in energy related gas storage and other energy storage applications, it would be highly desirable to develop a cost-effective and simple processing procedure for a lightweight, mechanically and chemically stable, flexible, non-fragile material without losing porosity. This may exist in the form of activated carbon cloth (ACC),[2–7] whose conformability and flexibility make it much more versatile and robust as a potential liner in gas storage tanks.[6,7]

Furthermore, the large surface areas of activated carbon cloth enable faster adsorption kinetics and mass transfer as compared to the powder and granular forms of activated carbon. This is in addition to the safe handling benefits, with regard to health, and the convenient commercialisation opportunities that tank processes offer. Dehydrating agents are used during activation to create pathways of pores and prevent tar production. Upon activation, the salts left in the pores are eliminated with an acid wash.Click or tap here to enter text.

Recently, activated carbon cloth has been suggested as such a flexible form of activated carbon that may function as an efficient gas adsorbent. In the case of use as absorbents for energy related gases (e.g., CO_2, CH_4 and H_2), such flexible activated carbon cloth would be much easier to handle than powder and granular forms. They would offer the process ability and mechanical properties required for the construction of more efficient storage tank designs incorporating the carbons as

coatings or liners inside tanks. This is in addition to the safe handling benefits with regard to health, and convenient commercialisation opportunities during tank processes.[2,3,5–7,9]

At the present time, the preparation of activated carbon cloth (ACC), which retains the flexibility of the original cloth, involves a number of steps, which include polymerisation, stabilisation and physical or chemical activation.[2–5,7,10] For, example, Huidobro *et al.,* investigated the chemical activation of viscose rayon fabric via impregnation with solutions of different chemicals (NH_4Cl, $AlCl_3$, $ZnCl_2$, $CuCl_2$, $FeCl_3$, H_3PO_4 or Na_2HPO_4), followed by carbonisation in an inert atmosphere. The authors argued that impregnation modifies the pyrolysis of the precursor, favouring dehydration over depolymerisation resulting in a larger ACC yield.[5]

The conversion of regenerated cellulose-based fibres to carbon is a complicated process, which to-date requires treatment to modify the chemical and physical properties of the cellulose such as thermal stability and chemical composition. Such treatment has been typically accomplished by impregnating the cellulose with a variety of chemicals, the most common of which are $ZnCl_2$, NH_4Cl and H_3PO_4.[3,9]For this reason, the current state-ofte-art methods for preparing cellulose-based activated carbon cloths (ACCs) involve a number of steps that consume significant energy, chemicals and time.

In general, cellulose-based and polyacrylonitrile (PAN) fibres are the most prevalent precursors for carbon fibre manufacturing. Particularly attractive characteristics of cellulosic precursors include their high thermal conductivity, high mechanical flexibility and low cost. However, natural cellulose-based materials (such as cotton, linen, ramie etc.) are not considered suitable precursors for carbonisation due to their discontinuous filaments, low degree of orientation among fibres, and high impurity arising from the complex structure of natural cellulose sources such as lignin and hemicellulose. These traits may finally result in a low yield of carbon fibres with poor porosity properties. Instead, semi-synthetic (regenerated) cellulose-based fibres such as viscose rayon are favoured for carbonisation and activation applications due to their possible transformation into nanoporous structures with a large surface area.[6,7,11,12]

The main obstacle in producing ACC is linked to the lack of a simple and inexpensive synthesis route to a lightweight, mechanically flexible and non-fragile carbon-based structure. Furthermore,

the development of porosity is also fundamental, especially if the ACCs are to be used in gas capture and storage applications. For this reason, the development of sustainable synthesis methods of ACCs are needed, and which involve fewer steps, less chemical usage and lower energy consumption. Viscose rayon (VR), which was used as carbon precursor contains cellulose fibres, as shown in Figure 1, and has a C content of ca. 41 %. Porosity generation and development of carbon materials from VR has been investigated previously via chemical activation, either directly[13] or after precursor carbonisation. The latter has been used mainly to increase C-content.[2,3,5,9,10,14–21]

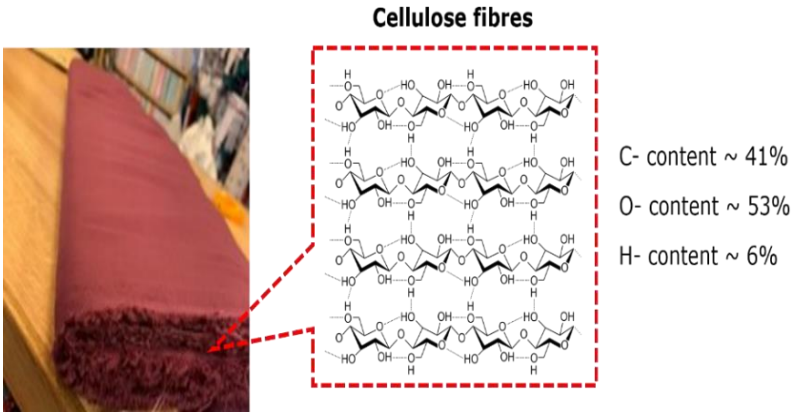


Figure 1: Viscose rayon (VR), which was used as carbon precursor.

Comparison to benchmark materials

To date, the state-of-the-art in the preparation of ACCs is based on two recent reports by (i) Kostoglou and co-workers,[7] and (ii) Attia and co-workers.[6] reported the preparation of ACCs via a complicated process involving several steps, namely, (i) stabilisation of VR with NH_4Cl and $ZnCl_2$, followed by (ii) carbonisation of the stabilised VR at 630 ^oC under N_2, and then (iii) physical activation of the resulting carbonised matter with CO_2 at 930 ^oC. They obtained microporous ACC with maximum surface area and pore volume of 1200 m^2/g and 0.5 cm^3/g, respectively, with pores of size ca. 0.6 nm.[4] On the other hand, Attia and co-workers more recently developed ACCs via an even longer synthesis route including the following steps; (i) preparation of VR/polypyrrole nanoparticle composite involving the use of pyrrole and ammonium persulfate, and then (ii) stabilisation of VR/polypyrrole composite with NH_4Cl and $ZnCl_2$, followed by (ii) carbonisation of

the stabilised VR/polypyrrole composite at 850 °C under N_2, and then (iv) activation of the resulting carbonised matter via physical activation with CO_2 at 900 °C or chemical activation with KOH at 900 °C.[6] They obtained ACCs with surface area of up to 1922 m^2/g and pore volume of 0.85 cm^3/g, which were obtained via the chemical activation (with KOH) route.

As stated above, the aim of the present work was to simplify the preparation of ACCs. This has been successfully achieved as we have been able to prepare fully flexible, cloth-like ACCs via a much simpler route that negates the need for stabilisation and only requires carbonisation of VR followed by conventional activation with PO. The use of PO, as a milder activating agent rather than KOH, which is harsher, is key in achieving flexible ACCs. Our route simplifies the synthesis route (fewer steps, fewer reagents as only PO is needed), and lower energy use. Despite the advantage of a simpler process, our route yields ACCS with enhanced porosity with surface are and pore volume of up to 2253 m^2/g and 1.2 cm^3/g, respectively. These textural properties are higher than those previously achieved for ACCs from more complicated synthesis routes.[6,7] In the next section we explore the gas (CH_4 and CO_2) uptake of the present ACCs and compare them to previous benchmark ACC materials.

In this chapter, an innovation in preparing ACC is reported in the context of the extant literature. This innovation involves reduction or minimisation of the following: (i) energy consumption, (ii) chemicals and (iii) preparatory steps. In particular, the innovation proposes a novel synthesis method that eliminates the stabilising step that has to date been considered to be a crucial step in the preparation of ACCs that preserve the flexibility of activated carbon fabric. Additionally, the innovation involves activation using a mild activating agent, namely potassium oxalate.

There is currently limited experimental data in the scientific literature regarding the CO_2 and CH_4 adsorption capabilities of nanopore-sized carbon cloth, fabric, or textile-like materials.[1] Hence, the activated carbon cloth explored in this study was extensively studied with respect to morphological, structural and elemental composition properties using several characterization methods, including scanning electron microscopy (SEM) and X-ray diffraction (XRD). The porosity of the developed ACCs was determined from nitrogen (N_2) sorption data collected at 77 K. To assess the ACCs

potential for use in energy relevant applications, the CO_2 storage performance was evaluated at pressure range of 1– 40 bar at ambient temperature, and the methane uptake capacity was evaluated at a higher-pressure range of 1- 100 bar at ambient temperature.

6.2. Experimental Section

6.2.1. Material synthesis

6.2.1.1. Direct Activation of Rayon.

A strip of viscose rayon (VR) was immersed in KOH solution (0.2M, 100 mL), then dried at 60 °C. This impregnated rayon was then spread in an alumina boat and placed in a horizontal tube furnace and heated to 650 °C, at ramp rate 5 °C/min, under a flow of nitrogen gas, and held at the final temperature for 1 h before cooling under a nitrogen gas flow. The resulting samples were designated as ACVR-K650, where AC indicated activated carbon, VR stands for viscose rayon and **K** was the KOH/ratio mass ratio.

6.2.1.2. Stabilisation prior to activation with KOH

A strip of viscose rayon was immersed in $ZnCl_2$ and NH_4Cl solution (1.5 g (0.28 M) and 1.8 g (0.13 M), respectively) for 1 h and then dried at 60 °C for half an hour to yield impregnated rayon (IVR) that retained cloth-like flexibility. The impregnated rayon was immersed in 2g KOH (0.2 M) for 5 minutes, then dried at 60 °C for half 1 h. The resulting KOH/IVR (impregnated rayon) material retained clothlike flexibility. The treated rayon (KOH/impregnated ($ZnCl_2$ + NH_4Cl) rayon was then spread in an alumina boat in a tube furnace and heated to 700°C, at ramp rate 5°C\min under N_2 flow and held at the final temperature for 1 h. The carbon obtained from this process were washed with 10% HCl to remove any inorganic salts, followed by washing with deionised water until pH~7 was attained by the filtrate. The sample was then dried and designated as AC-VR-F, with AC indicating activated carbon, VR stands for viscose rayon and **F** indicates the level of cloth-like flexibility.

6.2.1.3. Stabilisation prior to thermal treatment

A strip of viscose rayon was immersed in $ZnCl_2$ and NH_4Cl solution for 1 h, and then dried at 60°C for half an hour to yield impregnated rayon (IVR) that retained cloth-like flexibility. The IVR was then spread in an alumina boat in a tube furnace and heated to target temperature 700 °C, at ramp rate 5°C\min, under a flow of nitrogen gas and held at the final temperature for 1 h. The resulting carbons were washed with deionised water until pH~7 was attained by the filtrate. This sample was dried and designated as **ACC-VR-W-Y**, with AC indicating activated carbon, VR stands

for viscose rayon, **W** is the amount of deionised water used and **Y** is the thermal treatment temperature.

6.2.1.4. Stabilisation followed by activation with potassium oxalate (PO)

Viscose rayon was stabilised with NH_4Cl (0.28 M) for 1 h at room temperature, and then dried at 60 °C. The stabilised rayon (SVR) was mixed with PO to achieve a PO/SVR ratio of 2 (SVR was immersed PO solution 1.2 M for 30 minutes). The resulting PO/SVR mixture then spread in an alumina boat in a tube furnace and heated to 750 °C, 800 °C or 900 °C, at ramp rate 5°C\min under a flow of nitrogen gas and held at the final temperature for 1 h. The resulting ACCs were washed with deionised water until pH~7, and then dried at 60°C for 30 minutes. The resulting ACCs was assigned as **ACC-2:X-S**, where 2 is PO/VR ratio and X is the activation temperature and S stands for with stabiliser.

6.2.1.5. Carbonisation followed by activation with potassium oxalate (PO)

Viscose rayon was carbonised under a flow of N_2, 60 mL min^{-1} for 1 h at 800 °C following a heating ramp rate 5°C/min to generate a sample designated as VR-800. The flexible VR800 was mixed with PO to achieve a PO/VR-800 ratio of 2 (i.e., soaked in 1.2 M aqueous PO solution then dried at 60 ◦ C for 30 min). The resulting PO/VR-800 mixture was then spread in an alumina boat in a tube furnace and heated to between 650 and 900 °C, at ramp rate 5°C\min under a flow of nitrogen gas and held at the final temperature for 1 h. The resulting ACCs were washed with deionised water until pH~7, and then dried at 60°C for 30 minutes. The resulting ACC was designated as **ACC-2:Y-NS**, where 2 is PO/VR-800 ratio, **Y** is the activation temperature, and NS stands for no stabiliser.

6.2.2. Material Characterisation

Thermogravimetric analysis (TGA) was performed using a TA Instruments Discovery analyser or TA Instruments SDT Q600 analyser under flowing air conditions (100 mL/min). A PANalytical X'Pert PRO diffractometer was used to perform powder XRD analysis using CuK ◦ light source (40 kV, 40 mA) with step size of 0.02° and 50 s time step. Elemental, CHN, analysis was performed on an Exeter Analytical CE-440 Elemental Analyser. Nitrogen sorption (at 77 K) with a Micromeritics 3FLEX sorptometer was used for porosity analysis and to determination textural properties. Prior to analysis the carbon samples were degassed under vacuum at 200°C for 12 h. Surface area was

calculated using the Brunauer-Emmett-Teller (BET) method applied to adsorption data in the relative pressure (*P/Po*) range of 0.02 – 0.22, and pore volume was estimated from the total nitrogen uptake at close to saturation pressure (*P/Po* ≈ 0.99). The micropore surface area and micropore volume were determined via t-plot analysis. The pore size distribution was determined using non-local density functional theory (NL-DFT) applied to nitrogen adsorption data. Scanning electron microscopy (SEM) images were recorded using a Microscopy JEOL 7100F FEG-SEM, operating at a 15 kV accelerating voltage.

6.2.3. Methane and CO_2 uptake measurements

Methane and CO_2 uptake were determined using a Hiden Isochema XEMIS Analyser. Before the uptake measurements, the carbon samples were degassed at 240°C under vacuum for several hours. Adsorption-desorption isotherms were obtained at 25°C, over methane (CH_4) pressure range of 0 – 100 bar, and CO_2 pressure range 0 – 40 bar.

6.3. Results and Discussion

We first explored the nature of the viscose rayon (VR) used as precursor. The nitrogen sorption isotherm of the VR is shown in Figure 2 and indicates that the VR is non-porous.

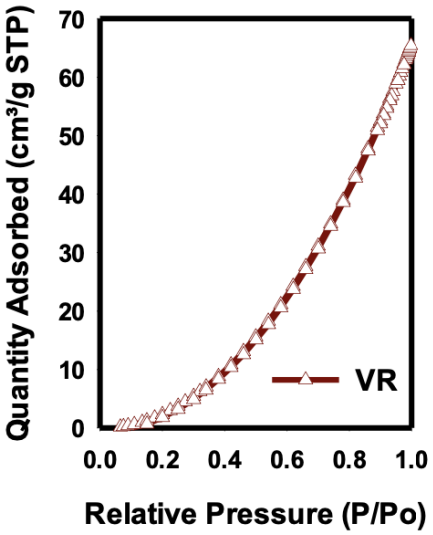


Figure 2: N_2 sorption isotherm of viscose rayon.

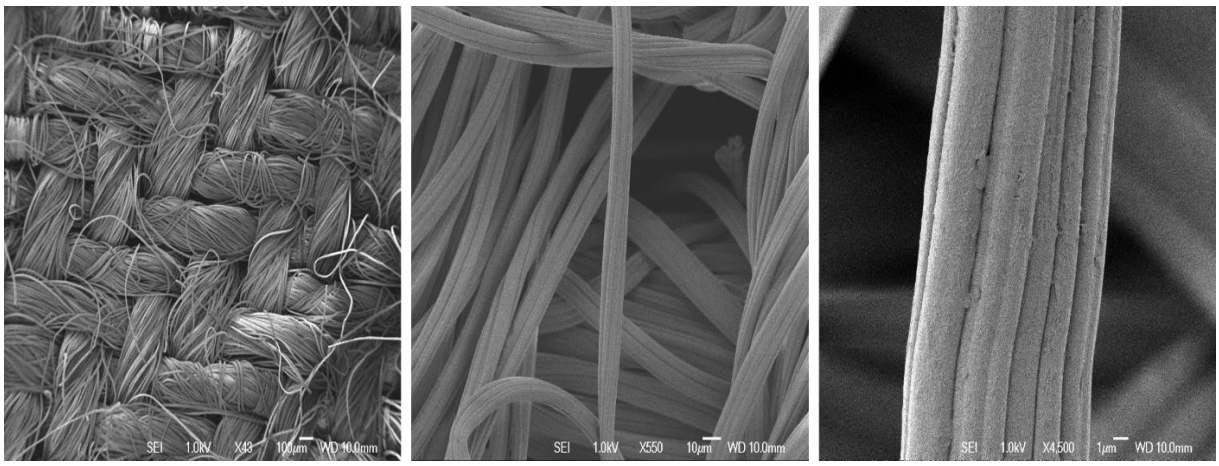


Figure 3: Shows SEM images of the hierarchical structure of viscose rayon material over a wide range of magnifications, revealing a chain-like weaving morphology.

6.3.1. Direct Activation of Viscose Rayon

To generate and develop the porous carbon structure of VR, direct activation was initially attempted, with KOH as the activating agent. This process led to the conversion of VR into totally powdered forms of activated carbons, as shown in Figure 4 below. The VR fabric was bleached and dehydrated after the VR was soaked in KOH solution. This process highlighted the fact that the KOH was harsh, and therefore not a suitable choice as activating agent for the production of the flexible activated carbon cloths.

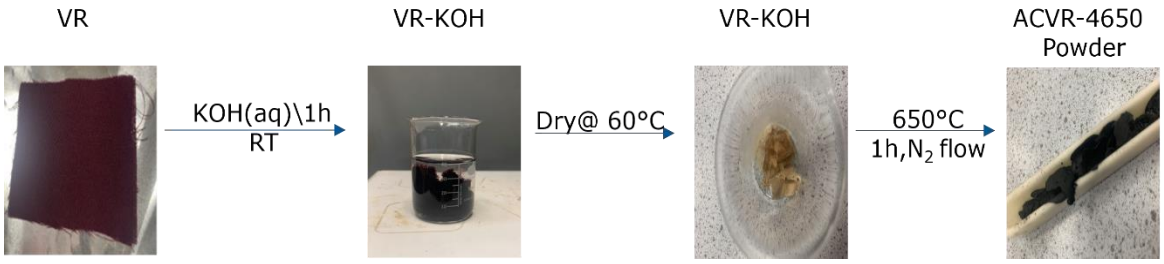


Figure 4: Transforming of viscose rayon into activated carbons via direct activation route.

The P-XRD pattern of ACVR-4650, shown in Figure 5, exhibits peaks centred at 2θ = 26° and 44°. The peak at the 2θ = 26° corresponds to the (002) diffraction of graphitic domains. The intensity of this peak corresponds to the regularity of the graphene structure within the sample. The nature of the peak - weak, broad and of low intensity – means that the level of graphitisation is very low.

The sharp peaks in the XRD pattern indicate that the sample may contain a small amount of inorganic mineral matter with crystalline properties. Impurity is likely to originate from some potassium containing compounds that were not completely washed out during the synthesis process.

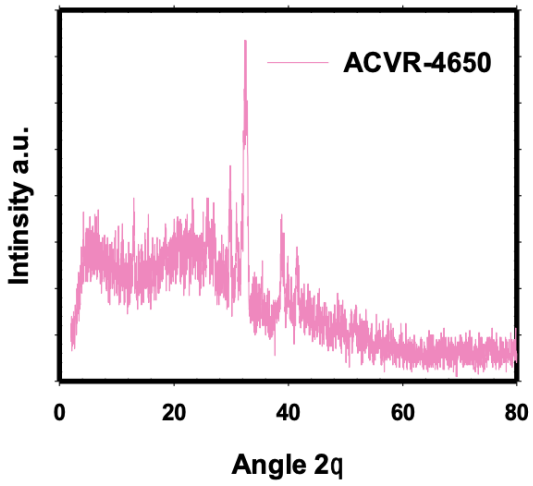


Figure 5: XRD pattern of activated viscose rayon at prepared at KOH/VR ratio of 4 and 650°C.

The C-content of resulting activated carbon rose from ~41 to 72.4%, while the O and H-content were reduced from 53 to 26 % and 6 to 1 %, respectively.

The nitrogen sorption isotherm of sample ACVR-4650 is a fully reversible type I isotherm. This is characteristic of microporous materials (i.e., pore sizes below 2 nm) as confirmed by the PSD curves (Figure 6).

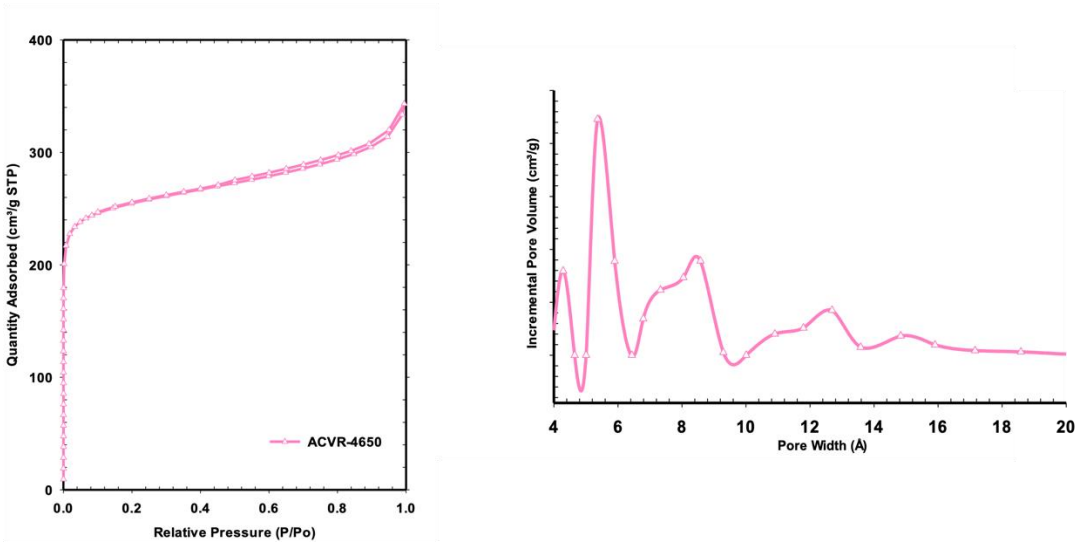


Figure 6: N_2 sorption isotherm of ACVR-4650 at 77K and 1 bar (left), and pore size distribution (PSD) for ACVR-4650 sample using density functional theory (DFT).

Sample ACVR-4650 had a surface area of 944 m^2/g, with 80% (753 m^2/g) arising from micropores, along with pore volume of 0.5 cm^3/g of which 0.3 cm^3/g (60%) was from micropores. As shown by the PSD curves in Figure 6, the sample had hardly any pores larger than 2 nm, with most pores being of size smaller than 1.0 nm.

In conclusion, it can be inferred that viscose rayon does not possess the strength (i.e., it is delicate) to be directly activated. In addition, the harshness of KOH was highlighted, suggesting that it is an unsuitable as an activating agent. To avoid total dehydration of VR, it needs a prior treatment to modify its physical properties. Kostoglou, *et al.,* have suggested that the impregnation of VR in NH_4Cl and $ZnCl_2$ can increase the thermal stability of rayon, as well as reducing the ash and volatile carbon content upon carbonisation.[7]

6.3.2. ACC prepared via KOH activation following stabilisation with NH_4Cl and $ZnCl_2$

The existing literature has shown that the physical properties of VR can be modified to improve stability during the activation process. In the next synthesis attempt, VR was stabilized with NH_4Cl and $ZnCl_2$, followed by KOH activation. The stabilized VR produced using this approach had not lost its flexibility after drying. However, following activation and washing, a partial loss in the flexibility of VR was noted, as illustrated in Fig. 8. The elemental composition of hard and flexible

parts differed markedly, especially in O and N content. The flexible part had higher C and N content (~68.6 and 5.8 % respectively), and lower O-content (~24.1%) as shown in Table 1.

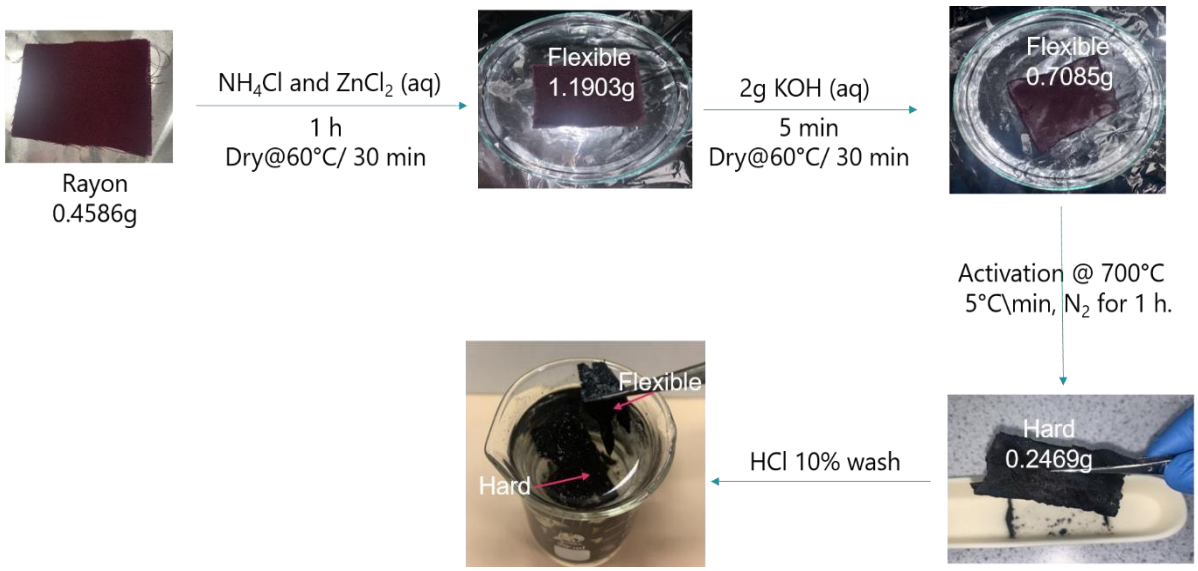


Figure 7: Transforming of viscose rayon into activated carbons via stabilization and KOH activation.

Table 1: Elemental composition of ACVR-4650, ACC-VR-hard and ACC-VR-flexible.

Sample	*C%*	*H%*	*N%*	*O%*
ACVR-4650	72.4	1.0	0.5	26.1
ACC-VR-hard	55.7	0.5	0.0	43.8
ACC-VR-flexible	68.6	1.5	5.8	24.1

ACC-VR-hard and ACC-VR-flexible have nitrogen sorption isotherms of similar shape, as shown in Figure 8, but the former has higher surface area (Table 2). Both parts have similar pores size distribution curves.

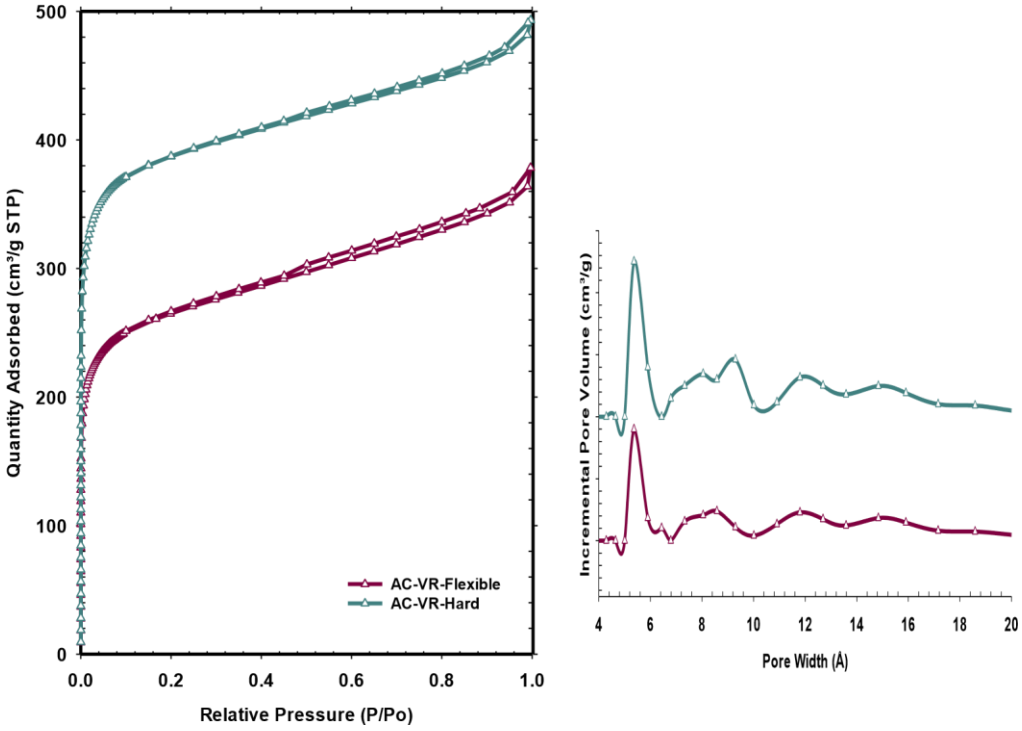


Figure 8: N_2 sorption isotherm of ACC-VR-Hard and ACC-VR-Flexible, and corresponding pore size distributions curves.

Table 2: Surface area and textural properties of ACVR-4650, AC-VR-Flexible and AC-VR-Hard.

Sample	*Surface area* m^2/g	*Pore volume* cm^3/g	*Pore size* Å
ACVR-4650	944 (753)	0.5 (0.3)	4/ 5/ 8
AC-VR-Flexible	847 (647)	0.6 (0.3)	5/8/12
AC-VR-Hard	1263 (1076)	0.8 (0.5)	5/9/12

As stated in many studies, $ZnCl_2$ has been used as an activating agent.[14,22] This may suggest that impregnation with $ZnCl_2$ followed by activation with KOH may have the effect of exposing the VR to two activating agents, which may lead to over activation. This may explain the fragile nature of the final activated sample and loss of cloth-like flexibility.

In the subsequent attempt, KOH was eliminated, but certain factors needed to be considered to ensure a successful $ZnCl_2$ activation process. The impregnation step was kept at 60 min. to avoid over exposure to $ZnCl_2$ and associated VR dehydration. The activation temperature was set above the $ZnCl_2$ melting point (~290 °C), and lower than the boiling point (~730°C) so as to ensure the intercalation of Zn into the carbon matrix. In addition, the thermal activation duration was in the range of 30 to 90 min. to avoid any sintering effect where pores are sealed off.

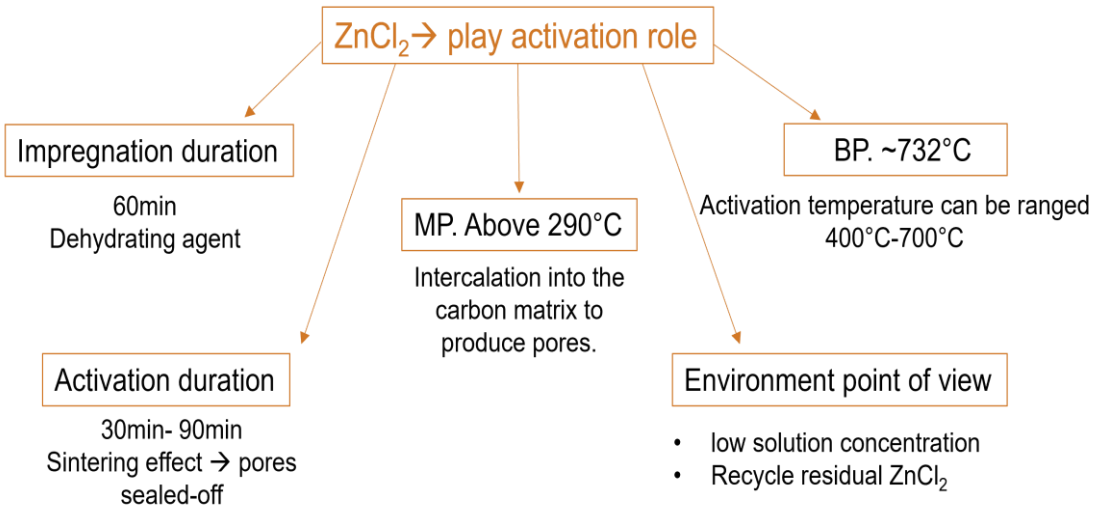


Figure 9: Suggested $ZnCl_2$ activation conditions.

6.3.3. ACC via simultaneous stabilisation and activation with NH_4Cl and $ZnCl_2$

The stabilisation of VR with NH_4Cl and $ZnCl_2$ was followed by thermal treatment during which carbonisation and activation occurred simultaneously. The application of $ZnCl_2$ in chemical activation generally improves the carbon content through the formation of aromatic graphitic structure. The most simplified mechanism of the carbonisation of semisynthetic (regenerated) cellulose-based fibres was suggested by Bacon and Tang.[23] Depending on the processing temperature range, the carbonisation process consists of four stages: (1) physical desorption of water (25–150°C), (2) dehydration from the cellulose unit (150–240 °C), (3) thermal cleavage of the glycosidic linkage and scission of C–O and C–C bonds via free radical reaction (240–400 °C) and (4) aromatisation (from 400 °C and above).

Mechanisms of Zinc Chloride Activation

In zinc chloride activation, the molten salt is intercalated into the carbon matrix and acts to generate pores during subsequent thermal treatment. The reaction between the carbon atoms and dehydrating agent is promoted in the extended interlayers of carbon. The application of $ZnCl_2$ in chemical activation generally improves the carbon content through the formation of aromatic graphitic structures. The carbon content of viscose rayon VR increased from 40.1 to 80.6% after stabilisation and thermal activation with $ZnCl_2$. A high amount of activating agent increases the removal of volatile matter through the collapsed of aliphatic and aromatic bonds, and thereafter causes a reduction in carbon yield. Activation at a higher temperature also results in a lower yield. The cellulose turns into activated carbon due to the decomposition of hemicellulose, splitting-off of cellulose and decomposition of the lignin structure at the high temperature. The tar-containing phenolic compounds are stripped out, causing a reduction in material weight.

Consequently, the yield of the final ACCs is dependent on the thermal treatment process and the type of starting material.[6,7] The impregnation step prior to carbonisation, involving a combination of NH_4Cl and $ZnCl_2$, drastically modifies the pyrolysis mechanism of the cellulose precursor by primarily favouring dehydration over depolymerization, thereby reducing the treatment time and yielding a higher carbon content. As illustrated in Fig. 11, this approach successfully provided a flexible ACC. The carbon content of the resulting

ACC-VR-W-Y samples increased by approximately 100% compared with VR as shown in Table 4. The C content increases as thermal treatment temperature rises i.e., 60% increase (compared to VR) at 630°C and ~73% at 700°C, while N-content decreases from 6.1% to 3.8%.

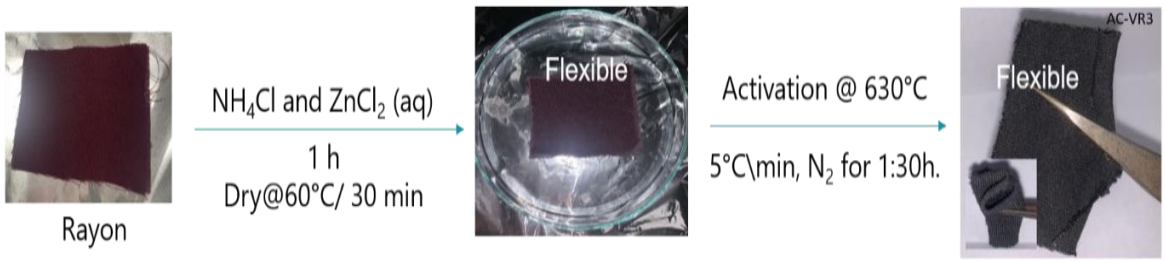


Figure 10: Transforming of viscose rayon into activated carbons via one step simultaneous stabilisation and activation.

Elemental composition shows that O and N content increases at high NH_4Cl and $ZnCl_2$ concentration. N may be introduced onto the carbons during impregnation with NH_4Cl impregnation, meaning that higher NH_4Cl concentration offers more nitrogen.

Table 3: Weight of rayon post-NH_4Cl & $ZnCl_2$ impregnation and post-thermal treatment.

Sample	*Rayon weight (g)*	*Weight with $ZnCl_2$ & NH_4Cl (g)*	*Weight after wash (g)*	*Yield (%)*
ACC-VR-100-630	0.4277	0.4711	0.1612	38
ACC-VR-50-630	0.6585	0.7699	0.2589	39
ACC-VR-10-630	0.4621	0.5103	0.2142	46
ACC-VR-10-700	0.4420	0.4964	0.1600	37
ACC-VR-50-700	0.7352	0.9619	0.2786	38

Table 4: Elemental composition of ACC-VR-W-Y activated carbon cloth.

Sample	***C%***	***H%***	***N%***	***O%***
VR	40.1	5.9	0.1	53.9
ACC-VR-10-630	58.0	1.5	6.8	33.7
ACC-VR-50-630	60.0	1.5	6.1	32.4
ACC-VR-100-630	80.6	1.5	4.3	13.6
ACC-VR-10-700	68.6	1.5	5.8	24.1
ACC-VR-50-700	74.3	0.5	3.8	21.4

The SEM images in Fig. 11 show the morphology of ACC-VR-X-630 for three different NH_4Cl/Zn_2Cl concentrations. As presented in the images in Fig.11 (1a,2a,3a), ACC-VR100-630 has a fractured surface, which appears to be dense in the interior, suggesting that the presence of porosity should

exist at even smaller scales, and most probably at the level of nanometres which, however, cannot be resolved by SEM.

At higher concentrations of $NH_4Cl/ZnCl_2$, activated fibres of ACC-VR-50-630 have more deeply etched surfaces, as illustrated in Fig. 11 (b), which may be related to generation of greater porosity. However, for ACC-VR-10-630, the fibres appear to maintain their structure.

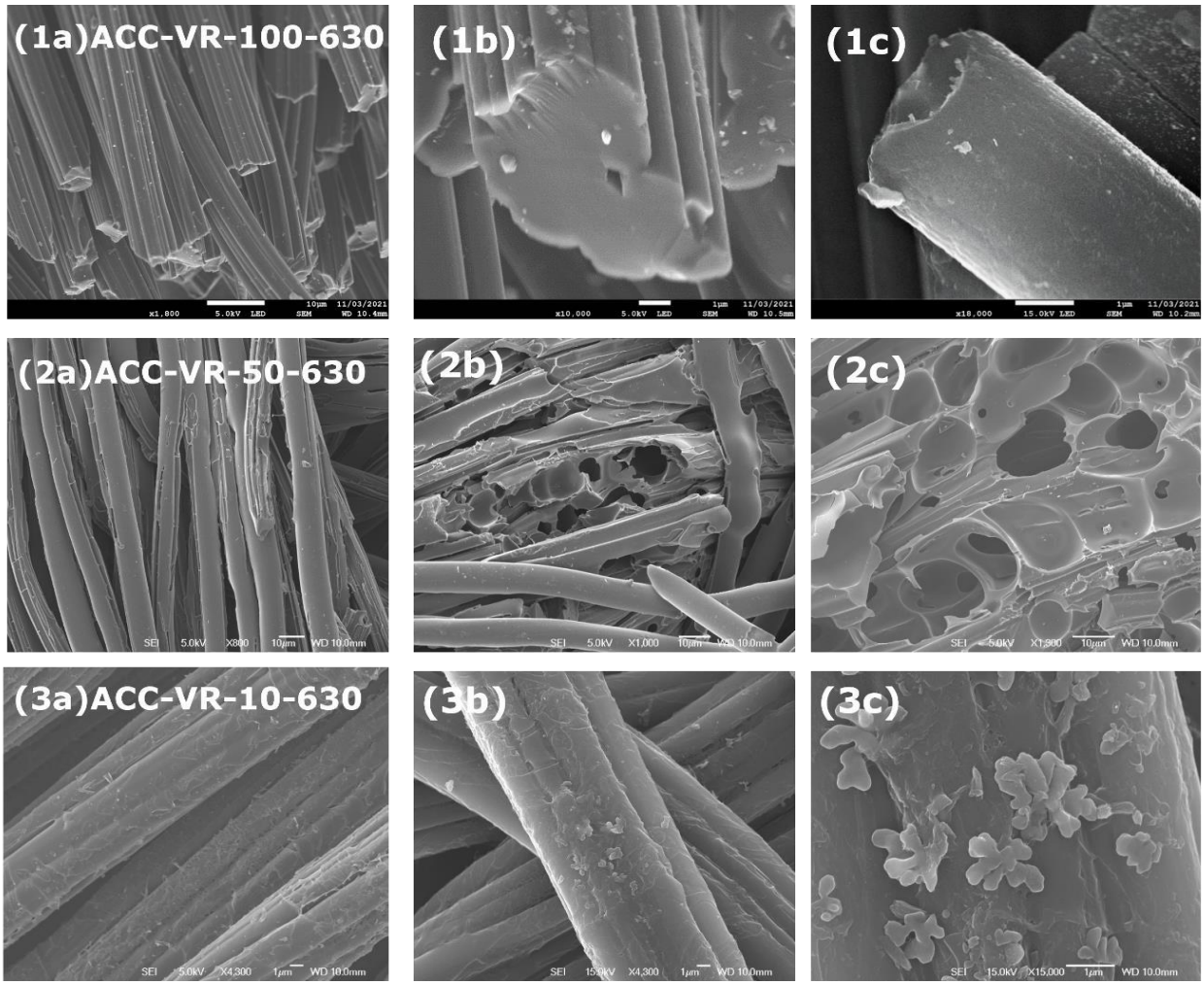


Figure 11: SEM images of activated carbon cloth (ACC-VR-100-630) 1a, 1b, and 1c, (ACCVR-5-630) 2a, 2b, and 2c, and (ACC-VR-10-630) 3a, 3b, and 3c.

Fig. 12 shows the morphology of ACC-VR-X-700 samples. It is apparent that a high concentration of $NH_4Cl/ZnCl_2$ and high activation temperature led to the destruction of some ACC fibres (Fig. 12d). At lower concentrations, (Fig. 12e) fibres keep their structure, with the appearance of roughness on their surfaces.

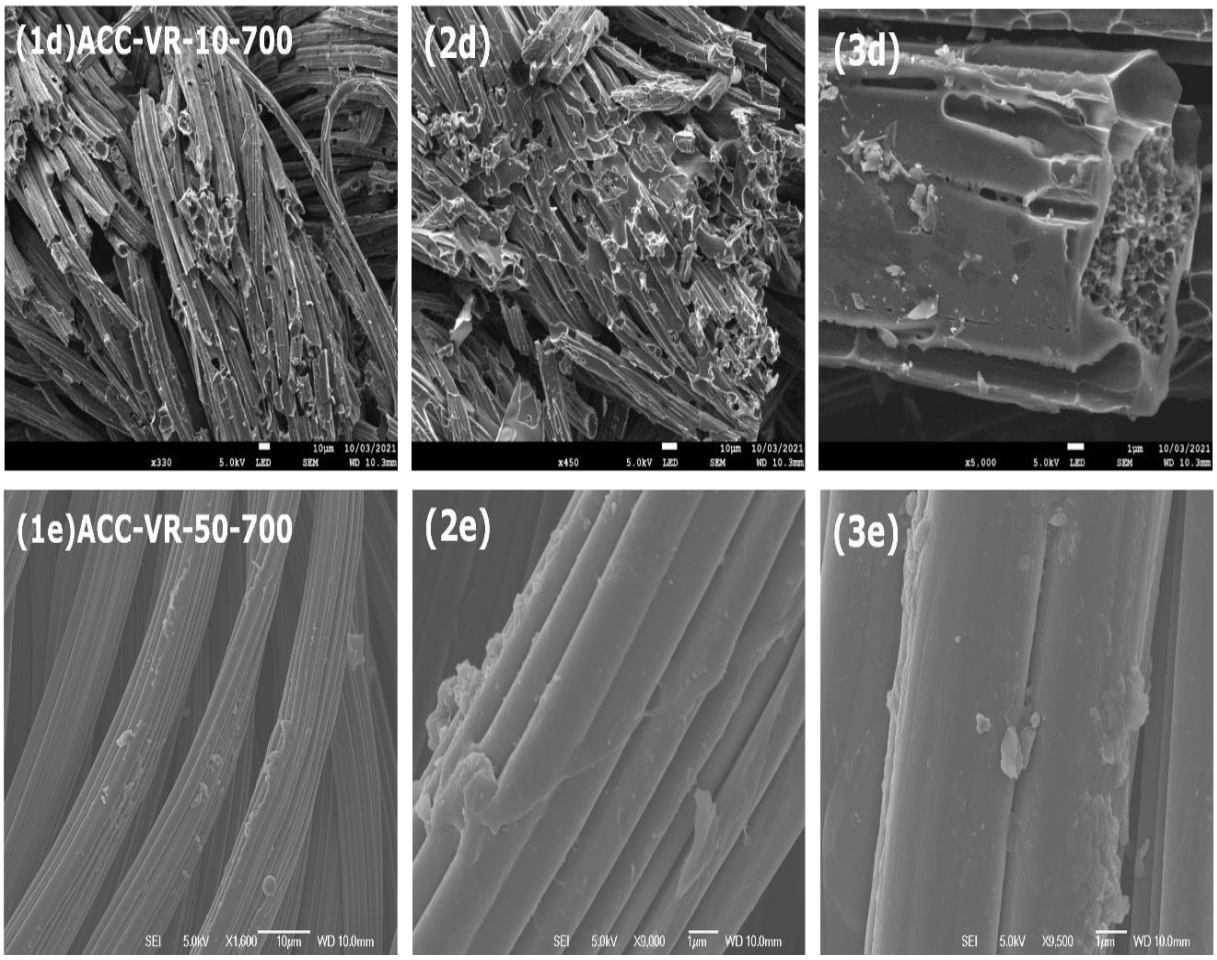


Figure 12: SEM images of activated carbon cloth (AC-10-700) 1d, 2d, 3d, and (ACC-VR50-700) 1e, 2e, and 3e.

In the XRD patterns in Fig. 13, the broad peaks at 2θ of 23° and 43° correspond to the (002) and (100) reflections of turbostratic carbon. At any given temperature, the lower the $NH_4Cl/ZnCl_2$ concentration, the lower the graphitisation level. Sample ACC-VR-10-630, for example, has a higher graphitisation level than ACC-VR-50-630 and ACC-VR-100-630. In addition, ACC-VR-100-630 XRD pattern indicate that the sample contain a small amount of inorganic mineral matter with crystalline properties. Impurity is likely to originate from some Zinc containing compounds that were not completely washed out during the synthesis process.

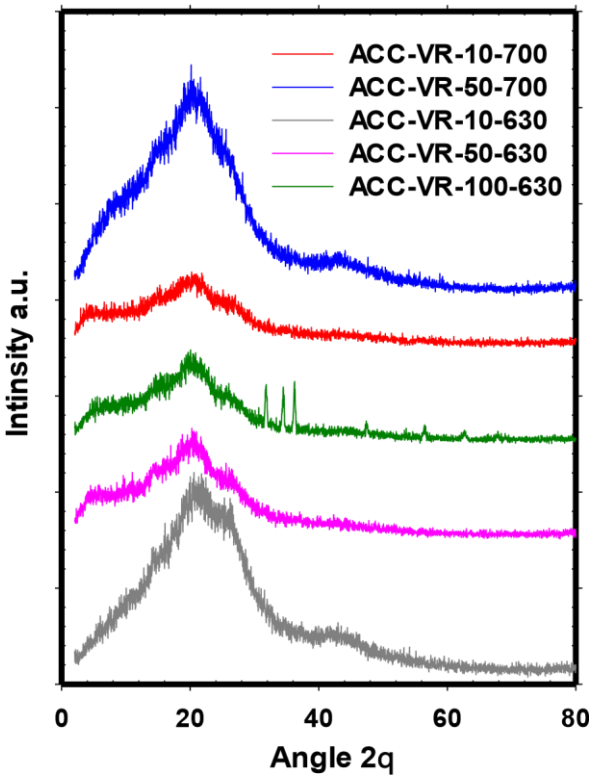


Figure 13: XRD patterns of ACC-VR-W-Y activated carbon cloth prepared via simultaneous stabilisation and activation with NH_4Cl and $ZnCl_2$.

The nitrogen sorption isotherms of the carbons prepared via simultaneous stabilisation and activation with NH_4Cl and $ZnCl_2$ are shown in Figure 14. The samples exhibit fully reversible type I isotherms, which are characteristic of microporous materials. The steep N_2 uptake at the lower relative pressures (P/Po < 0.01) is indicative of the enhanced gas-solid interactions in narrow micropores (i.e., pore sizes below 1 nm) due to the micropore filling mechanism. The adsorption isotherm reaches a plateau beyond the point of $P/P^o \sim 0.01$, and the equivalent amount of adsorbed N_2 is attributed to the accessible micropore volume. Table 5 gives a summary of the textural properties. The surface area is in the range of 516 to 1193 m^2/g being highest for sample ACC-VR-50-630. The pore volume is between 0.25 and 0.43 cm^3/g, which gives surface area density of between 2064 and 2435 m^2/cm^3. The high surface area density is consistent with the high microporosity of the carbons with the proportion of microporosity ranging from 84 – 97% for surface area and 75 – 92% for pore volume.

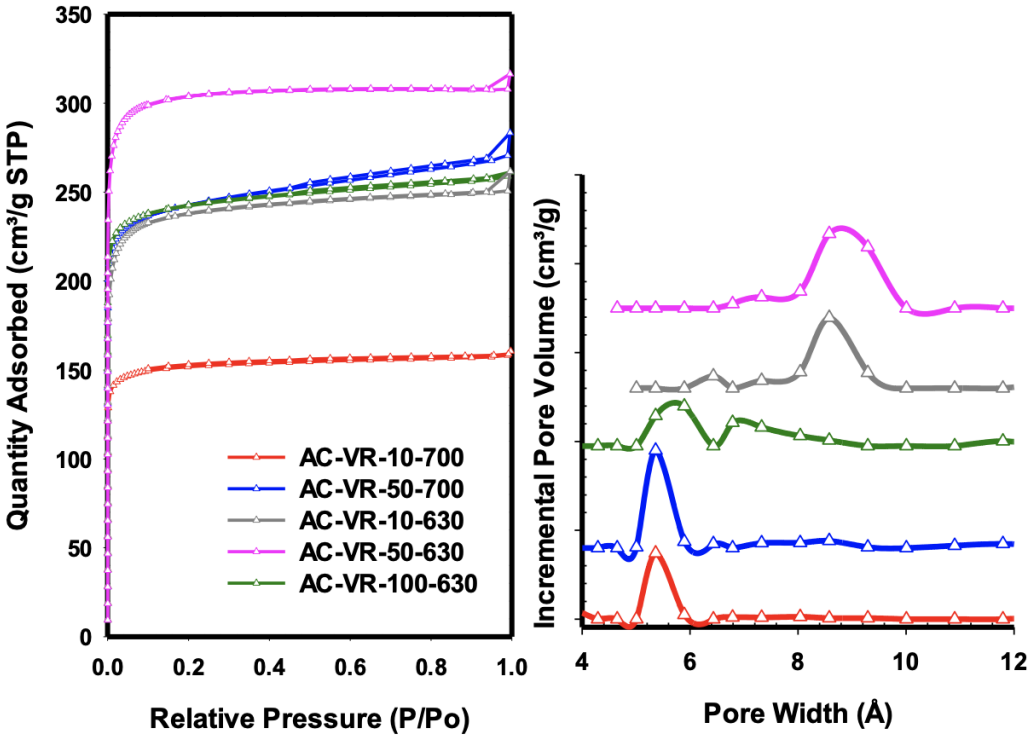


Figure 14: N_2 sorption isotherms (left) and corresponding pore size distributions curves (right) for activated carbons prepared via simultaneous stabilisation and activation with NH_4Cl and $ZnCl_2$.

Table 5: Surface area and textural properties of activated carbon cloth ACC-VR-W-Y samples prepared via simultaneous stabilisation and activation with NH_4Cl and $ZnCl_2$.

Sample	*Surface area (m^2/g)*	*% micropore Surface area*	*Pore volume (cm^3/g)*	*% micropore volume*	*Pore size (Å)*	*SAD[a] m^2/cm^{-3}*
ACC-VR-10-700	516 (501)	97	0.25 (0.23)	92	5	2064
ACC-VR-50-700	936 (885)	95	0.43 (0.36)	84	5	2177
ACC-VR-10-630	926 (777)	84	0.40 (0.30)	75	6/9	2315
ACC-VR-50-630	1193 (1051)	88	0.49 (0.41)	84	9	2435
ACC-VR-100-630	965 (927)	96	0.40 (0.36)	90	5/6	2413

[a]SAD is surface area density, which is given as ratio of surface area to pore volume.

Generally, the porosity of this set of activated carbons depends on the impregnation ratio and activation temperature. The release of volatiles due to the dehydrating effect of $ZnCl_2$ at elevated temperatures commonly results in the development of pores and channels in the matrix of activated carbon. However, the new pores are prone to collapse and become larger at higher temperatures, which can act to reduce the surface area. This is also true for the excessive use of $ZnCl_2$ in impregnation and activation. The boiling point of $ZnCl_2$ (732 °C) is another concern that is worthy of consideration in selecting the operating conditions. As the temperature of activation is normally below the boiling point, some traces of the salt may remain on the activated carbon. Consequently, the washing step would drain off the chemical, hence polluting the environment because of the hazardous nature of $ZnCl_2$. From a process-economics point of view, and to minimise the release of $ZnCl_2$ into the environment, the residual activator on activated carbon can be recovered using Soxhlet extraction and reused for subsequent activation.

It is important to reiterate that $ZnCl_2$ is not an environmentally friendly material, particularly for aquatic life. However, the residual $ZnCl_2$ on activated carbon can be recovered and reused using a Soxhlet unit.[24,25] This particular subject has received little discourse or research focus in the majority of the extant literature.

It should also be noted that by substituting $ZnCl_2$ with a mild, environmentally friendly activator, such as potassium oxalate (PO), the activation process can be improved by increasing its sustainability. Many studies have investigated potassium oxalate (PO) activation performance in developing porosity in activated carbons.[26–28] The samples obtained have been shown to have a high surface area and significant potential to act as adsorbents for various applications including CO_2 capture.[26,28] Moreover, as shown in Chapter 3, PO was successfully utilised as activating agent in preparing activated carbons from polypyrrole with high surface area and robust textural properties for CO_2 and methane uptake.

6.3.4. ACC prepared via stabilisation with NH_4Cl and PO activation.

This synthesis approach, as illustrated in Figure 16, involved stabilisation of VR with NH_4Cl followed by activation with PO at a PO/VR ratio of 2 and temperatures between 750 °C and 900 °C. As shown in Figure 15, the final activated carbon cloth was totally flexible and fully retained cloth-like

characteristics. The elemental composition is presented in Table 6 below. The C content increased from 40 % for VR to between 76 and 84%; the content increases with activation temperature. On the other hand, the O-content decreased as the activation temperature is increased.

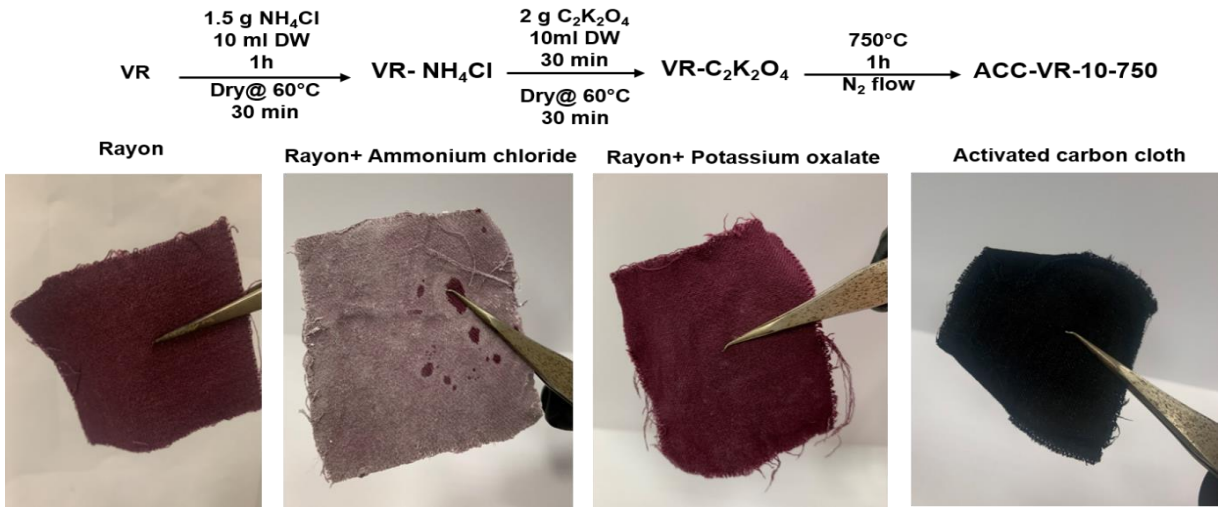


Figure 15: Transformation of viscose rayon into activated carbons via stabilisation with NH_4Cl and PO activation.

Table 6: Elemental composition of VR and ACC-2:X-S activated carbon cloth prepared via stabilisation with NH_4Cl and activation with PO.

Sample	***C%***	***H%***	***N%***	***O%***
VR	40.1	5.9	0.1	53.9
ACC-2:750-S	76.1	0.1	0.0	23.8
ACC-2:800-S	82.2	0.9	0.3	16.6
ACC-2:900-S	84.0	1.0	0.5	14.5

The XRD patterns of the PO activated carbons, Figure 16, indicate that they are amorphous with very low levels of graphitisation. The patterns show broad peaks at 2θ of ca. 23° and 43°, which correspond to the (002) and (100) diffractions of turbostratic carbon, respectively. The sample prepared at a low activation temperature (750 °C) appears to have a higher level of level of graphitisation, which is consistent with higher temperatures disrupting any graphitic domains that may be present.

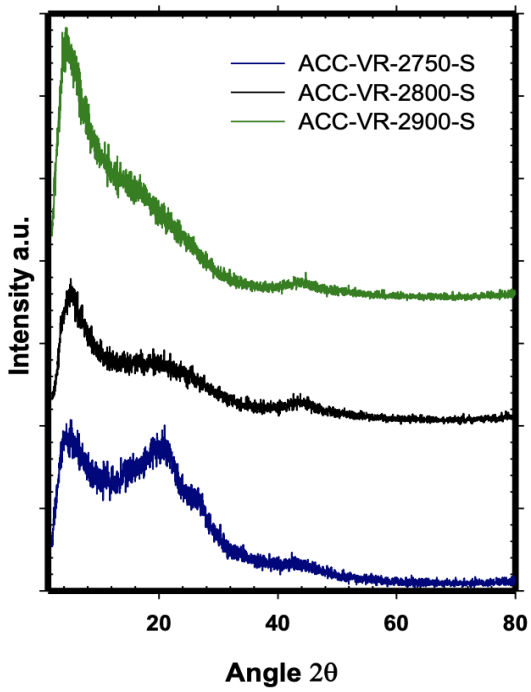


Figure 16: XRD pattern of ACC-VR-2:X-S activated carbon cloths prepared via stabilisation with NH_4Cl and PO activation.

As shown in Fig. 17, the isotherms of this set of ACCs are type I suggesting that the samples are microporous. The significant nitrogen uptake at the relative pressure $p/p_o < 0.01$ indicates a significant presence of micropores. For ACC-2:800-S and ACC-2:900-S, the isotherms plateau as the relative pressure, p/p_o increases, which suggests the presence of limited mesopores. However, a steady increase in nitrogen uptake up to P/Po = ~0.5 as well as a minor hysteresis loop are observed for the samples of ACC-2:750-S, which can be attributed to mesoporosity. The pore size distribution curves in Fig. 18 shows that the porosity of the carbons is mainly from micropores. The PSD curves are similar for all three samples, with two main maxima, i.e., 0.5-0.6 nm, and 0.7–0.9 nm.

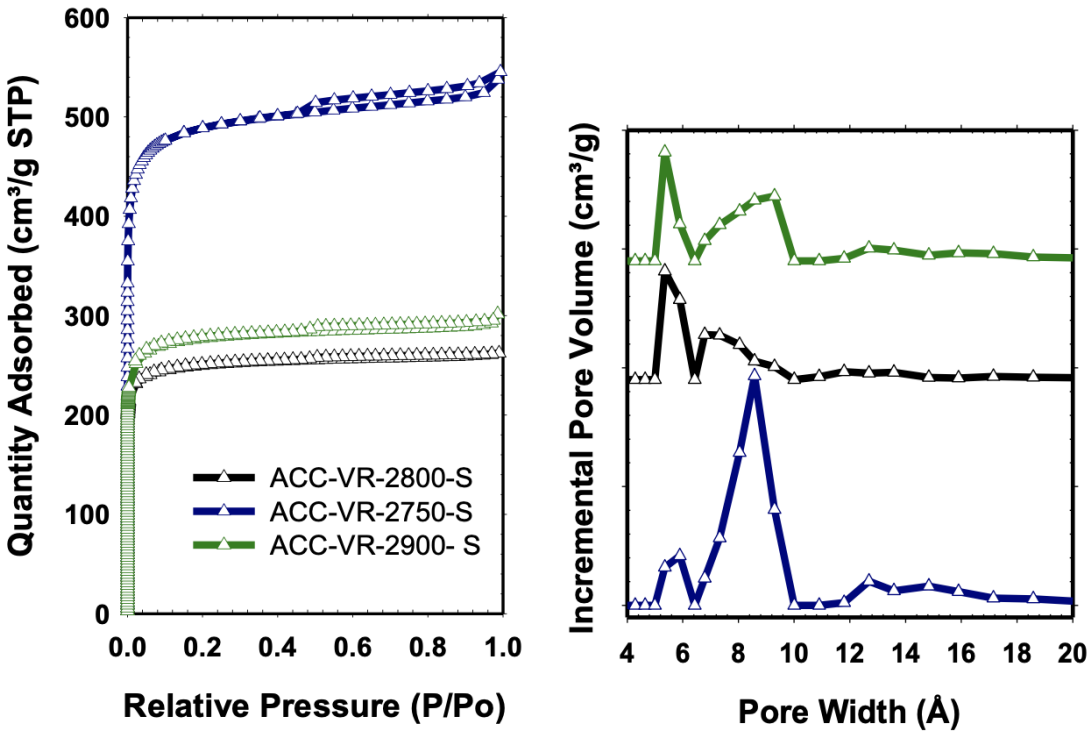


Figure 17: N2 sorption isotherm (left) and corresponding pore size distribution curves (right) of ACC-VR-2X-S activated carbon cloths prepared via stabilisation with NH4Cl and PO activation.

The textural properties of carbons prepared via stabilisation with NH_4Cl and PO activation are summarised in Table 7. The surface area is in the range of 923 to 1892 m^2/g while the pore volume is between 0.25 and 0.43 cm^3/g. This gives surface area density (SAD) of between 2046 and 2365 m^2/cm^3 with the ADS decreasing at higher activation temperature. The surface area density of this set of carbons is consistent with their high microporosity with the proportion of micropore surface area in the range of 82 – 87% and between 75 and 80% of pore volume arising from micropores. The textural data in Table 9 suggests that a temperature of ~750°C is most suitable for activation via this route as the resulting carbons have surface area and pore volume that is almost double that achieved at 800 and 900 °C but without loss of microporosity. Activation at 750 °C enables much better retention of the fibrous morphology of the VR, as shown by the SEM images in Figure 18, which is important in retaining cloth-like flexibility in the activated carbon cloths.

Table 7: Textural properties of activated carbon cloth ACC-2:X-S prepared via stabilisation with NH_4Cl and PO activation.

Sample	*Surface area (m^2/g)*	*% micropore surface area*	*Pore volume (cm^3/g)*	*% micropore volume*	*Pore size (Å)*	*SAD[a] m^2/cm^3*
ACC-2:750-S	1892 (1542)	82	0.8 (0.6)	75	6/9	2365
ACC-2:800-S	923 (813)	88	0.4 (0.3)	75	5/7	2308
ACC-2:900-S	1028 (895)	87	0.5 (0.4)	80	5/9	2046

[a]SAD is surface area density, which is given as ratio of surface area to pore volume.

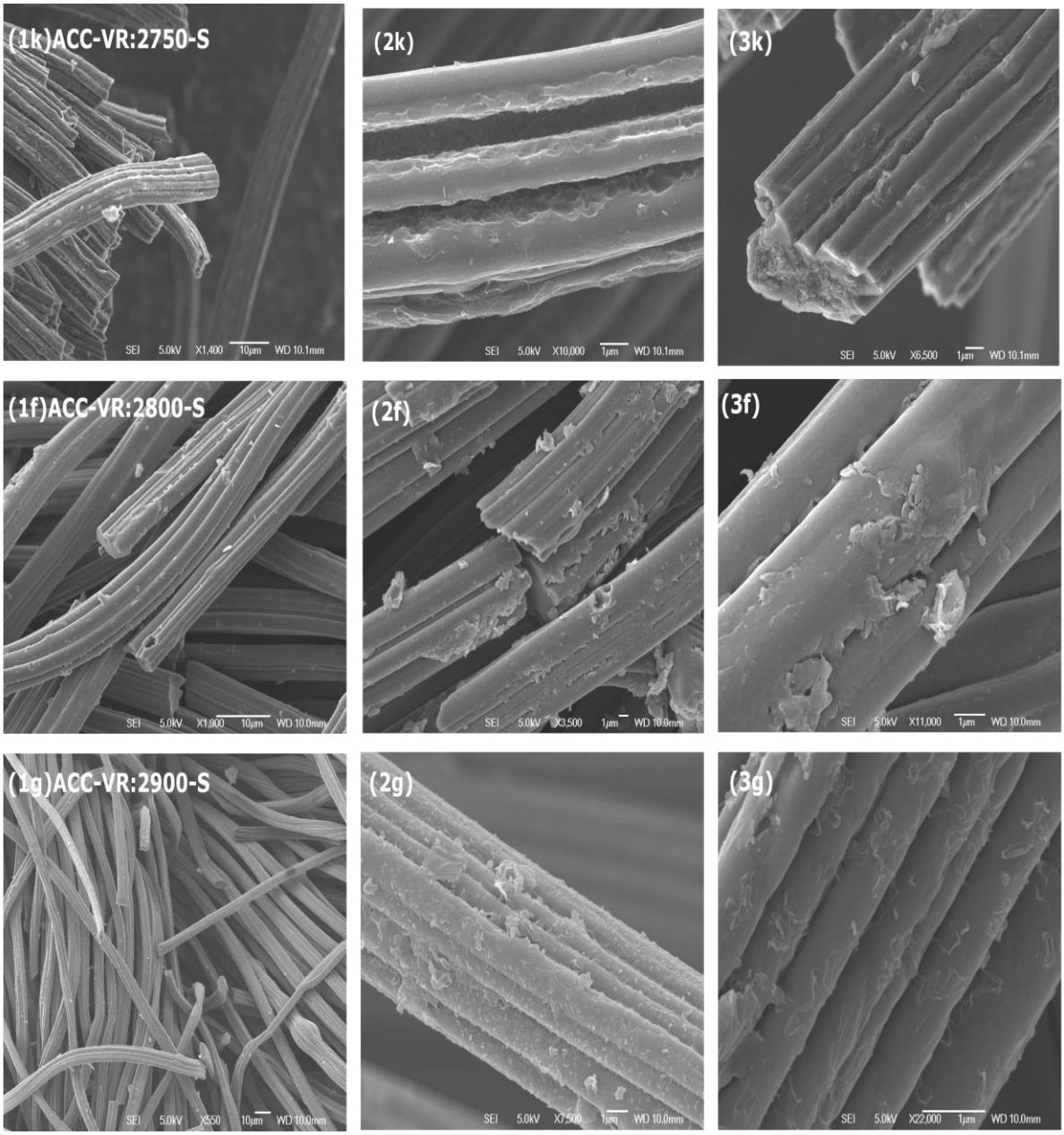


Figure 18: SEM images of activated carbon cloth, ACC-2:X-S, prepared via stabilisation with NH_4Cl and PO activation.

6.3.5. ACC via carbonisation and PO activation

The aim of the work in this chapter was to make the synthesis of activated carbon cloth as simple as possible. A key aim was to reduce the number of steps and to limit the use of reagents. As shown above, the experimental set up followed a systematic plan that gradually simplified the synthesis routes that were able to yield flexible cloth-like ACC. A key question is whether the stabilisation step can be removed from the synthesis route.

At the present time, all previous reports on successful synthesis of cloth-like ACCs have included a stabilisation step. However, our use of a mild activating agent may make it possible to exclude the stabilisation step. Thus, section reports on a simpler route that excludes the stabilisation step by activation of VR following pyrolysis. To better understand the direct activation of VR with PO, we first ascertained the behaviour of VR under thermal treatment at likely pyrolysis and activation temperatures. In choosing he activation temperature, we considered that carbonisation at low temperatures is known to preserve the mechanical integrity of VR.[29] When VR was carbonised at 800°C under N_2 for 1 h, it yielded a lowly porous carbon (designated as VR-800) with surface area of 90 m^2/g. The C content of the VR-800 was ca. 85 % compared to 40 % for VR.

Viscose rayon is composed of cellulose fibres, which are a naturally occurring polymer composed of repeating glucose units. Cellulose has a crystalline structure, and its XRD pattern typically displays multiple peaks that correspond to its crystal planes. The most prominent peaks in the cellulose XRD pattern are typically located at approximately 14°, 16°, and 22° 2 angles. cellulose's (110) crystal plane corresponds to the apex at 2 = 14°, while the peak at 2 = 16° corresponds to the (200) plane. Plane (040) corresponds to the apex at 2 = 22°.[30,31]

When cellulose is elevated to high temperatures in the absence of oxygen, it degrades thermally and produces a charred residue. Typically, the XRD pattern of cellulose char is substantially distinct from that of the original cellulose material. A broad ridge in the low-angle region of the XRD pattern of cellulose char indicates the presence of amorphous carbon in the charred material. The intensity of this ridge can intensify as temperature and char yield increase.[23,30–32]

In addition to the broad amorphous ridge, the XRD pattern of cellulose char may also display residual peaks corresponding to the char's remaining crystalline regions. These residual peaks can reveal the degree to which the original structure of cellulose has been preserved during the thermal degradation process.[30,31]The XRD pattern of VR-800 (Fig. 19) is consistent with that of carbonaceous matter but with some crystalline regions that appear as sharp peaks in the 2θ range of 20° to 50°.

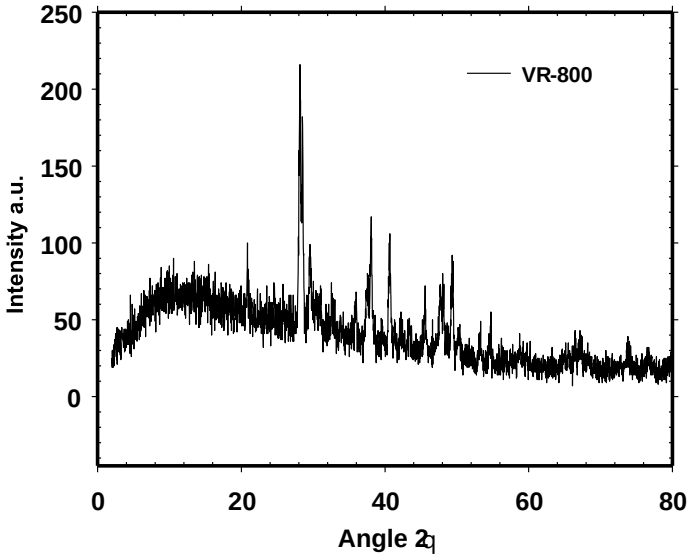


Figure 19: XRD pattern of VR-800.

SEM images and surface morphologies of viscose rayon VR before and after carbonisation (VR-800) are shown in Fig. 20 (a) and (b), respectively. It is apparent that the VR's morphology changed; it showed signs of roughness on fibre surfaces, caused by carbon accumulation. It can be deduced, therefore, that calcination at 800 ^{o}C did not affect the woven yarn’s structure carbon-fibre corrugations.

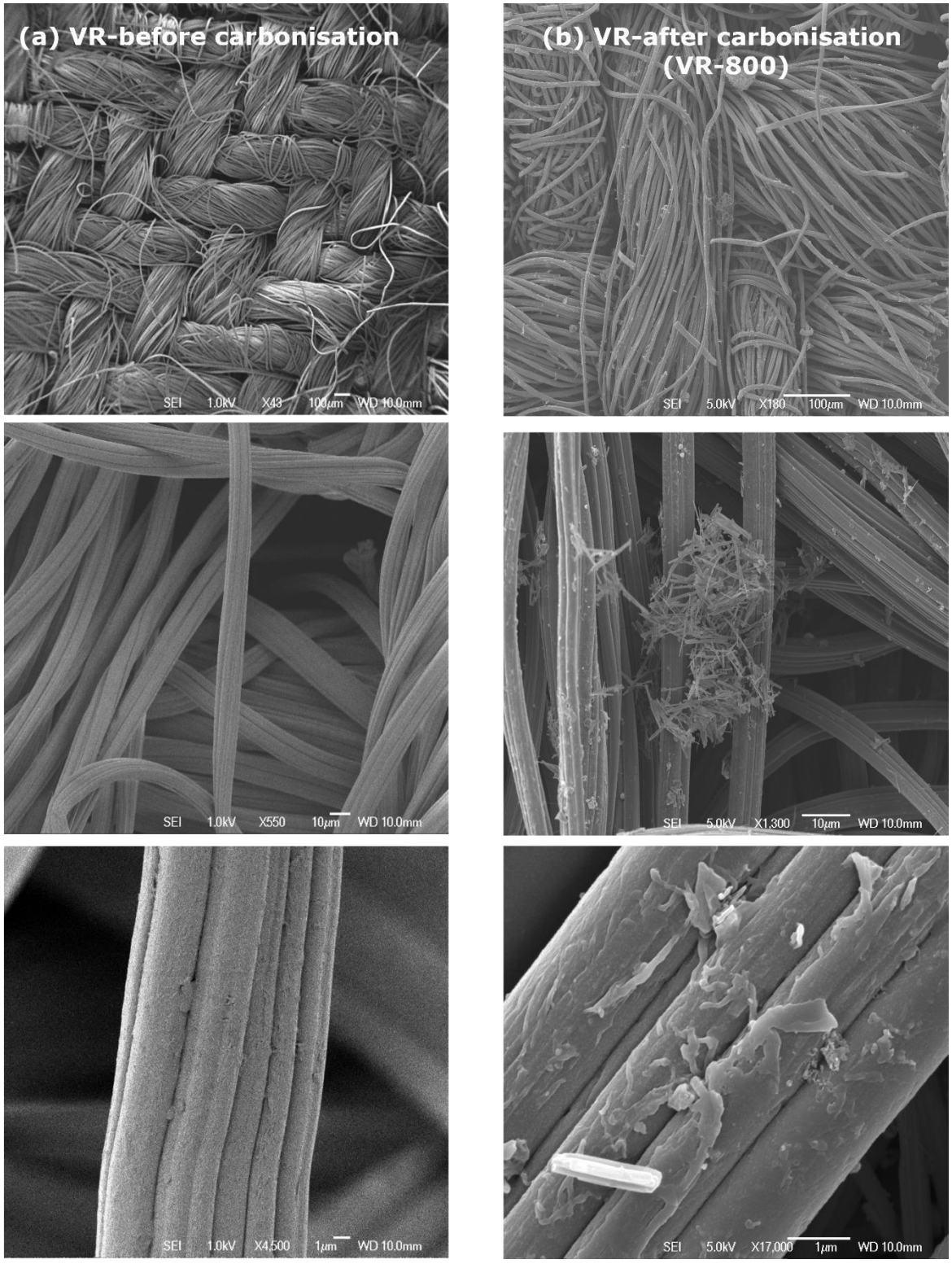


Figure 20: SEM images of viscose rayon (VR) before and after (VR-800) calcination at 800 °C under nitrogen.

After activation of VR-800 with PO, the elemental composition of the resulting carbon was generally similar to that of the starting material as shown in Table 8. The C content is in the range 81.5 to

89.7 % and appears to increase to a maximum for activation at 750 °C and then decreases. On the other hand, the O-content decreased from 17.3 % to 10.2 % as the activation temperature rose to 750 °C, and then increased to 11.8 % and 18.0 % as the activation temperature was raised to 800°C and 900°C, respectively.

Table 8: Elemental composition of VR-800 and PO activated ACC-2:Y-NS ACCs.

Sample	***C%***	***H%***	***N%***	***O%***
Char-VR-800	84.9	0.5	0.2	14.4
ACC-2:650-NS	82.0	0.3	0.4	17.3
ACC-2:700-NS	82.9	0.3	0.3	16.5
ACC-2:750-NS	89.7	0.0	0.1	10.2
ACC-2:800-NS	87.6	0.3	0.3	11.8
ACC-2:900-NS	81.5	0.2	0.3	18.0

The XRD patterns of the PO activated ACCs are shown in Figure 21. The broad peaks at 2θ of approximately 23° and 43° correspond to the (002) and (100) diffractions graphitic domains in the turbostratic carbon. These two peaks are shifted to lower 2θ values compared to those of crystalline graphite, which are located at 26.5° and 44.3°, respectively. This means that the in-plane crystallographic structure of the graphene layers and their stacking are significantly distorted in the present carbons, which is consistent with their being largely turbostratic or tending to amorphous.

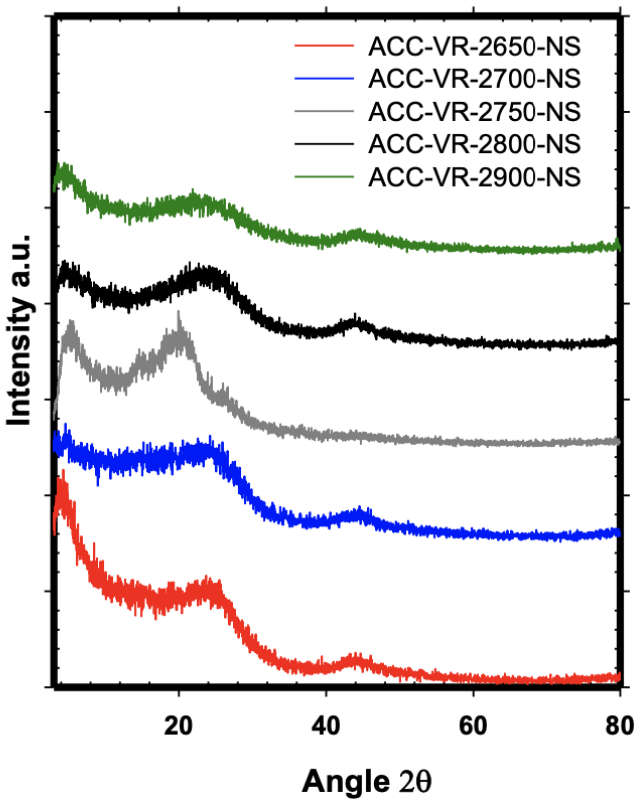


Figure 21: XRD patterns of PO activated ACC-2:Y-NS ACCs.

As shown in Fig. 22, the nitrogen sorption isotherms of the PO activated ACCs are mainly type I, indicative of microporosity. The high nitrogen uptake at the relative pressure *p/po*< 0.01 indicates a significant presence of micropores. For ACC-2:650-NS, ACC-2:700-NS, ACC-2:800-NS and ACC-2:900-NS, the isotherms plateau as the relative pressure, *p/po* increases, which suggests absence of mesopores. However, a steady increase in nitrogen uptake up to *p/po* = ~0.5, as well as a minor hysteresis loop are observed for ACC-2:750-NS, which may be attributed to the presence of some limited mesoporosity.

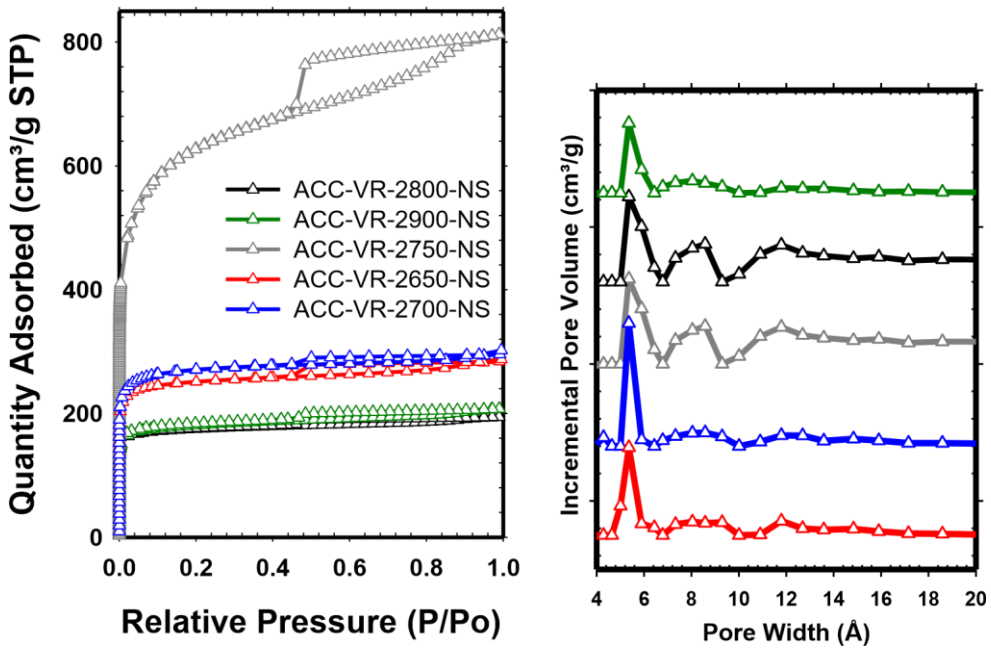


Figure 22: N_2 sorption isotherm (left) and corresponding pore size distribution curves (right) of PO activated ACC-2:Y-NS ACCs.

The textural properties of the ACC-2:Y-NS samples are summarised in Table 9. The surface area significantly increases with a rise in activation temperature from 650 °C (809 m^2/g), 700 °C (867m^2/g), and 750 °C (2253 m^2/g), followed by a decrease at the higher activation temperature of 800 °C and 900 °C with surface area of 654 m^2/g at 800 °C and 658 m^2/g at 900°C. The pore volume follows a similar trend. Sample ACC-2:750-NS has the highest porosity, which agrees with observations discussed above for ACCs prepared via stabilisation with NH_4Cl and PO activation. The surface area density of the ACC-2:Y-NS samples is between 1734 and 2193 m^2/cm^3. The surface area density is consistent with the microporous nature of the carbons with the proportion of microporosity ranging from 80 – 93% for surface area and 67 – 80% for pore volume.

Table 9: Surface area and textural properties of activated carbon cloth ACC-2:Y-NS carbons.

Sample	*Surface area (m^2/g)*	*% micropore surface area*	*Pore volume (cm^3/g)*	*% micropore volume*	*Pore size (Å)*	*SAD[a]*
VR-800	90 (42)	47	0.04 (0.02)	50	6	2250
ACC-2:650-NS	809 (755)	93	0.4 (0.3)	75	5	2023
ACC-2:700-NS	867 (819)	94	0.5 (0.4)	80	5	1734
ACC-2:750-NS	2253 (1089)	48	1.2 (0.5)	42	5/8	1878
ACC-2:800-NS	654 (544)	83	0.3 (0.2)	67	5/8	2180
ACC-2:900-NS	658 (562)	85	0.3 (0.2)	67	5	2193

[a]SAD is surface area density, which is given as ratio of surface area to pore volume.

The pore size distribution curves in Fig. 22 show that the porosity of the ACC-2: Y-NS carbons is mainly from micropores. The PSD curves are similar for all three samples, with two main maxima, i.e., 0.5-0.6 nm, 0.7–0.9 nm, and 1.2 nm. Broadening of the pore size for samples activated at higher temperature is attributed to greater evolution of CO_2 and CO due to the decomposition of PO through the activation process.[13,33–35] Sample ACC2:750-NS exhibited higher porosity, as shown in Figure 22; the nitrogen sorption isotherm is typical of a material that possesses both micropores and a level of mesopores. It appears therefore, that activation at ~750°C leads to greater porosity development. A widening of the adsorption isotherm 'knee' at low relative pressure is observed for ACC-2:750-NS, indicating the presence of a significant proportion of small mesopores.

Fig. 23 presents SEM images of ACC-2:750-NS, ACC-2:800-NS and ACC-2:900-NS. The images reveal the hierarchical structure of the ACC fibres over a wide range of magnifications. From a macroscopic view, the ACCs appear to maintain the original woven chain-like morphology of the VR precursor upon carbonisation and PO activation. Samples ACC-VR:2800-NS and ACC-VR:2900-NS showed similar signs of roughness on the fibres surface. However, ACC-VR:2750-NS showed defined circular itches in ACC fibre surfaces.

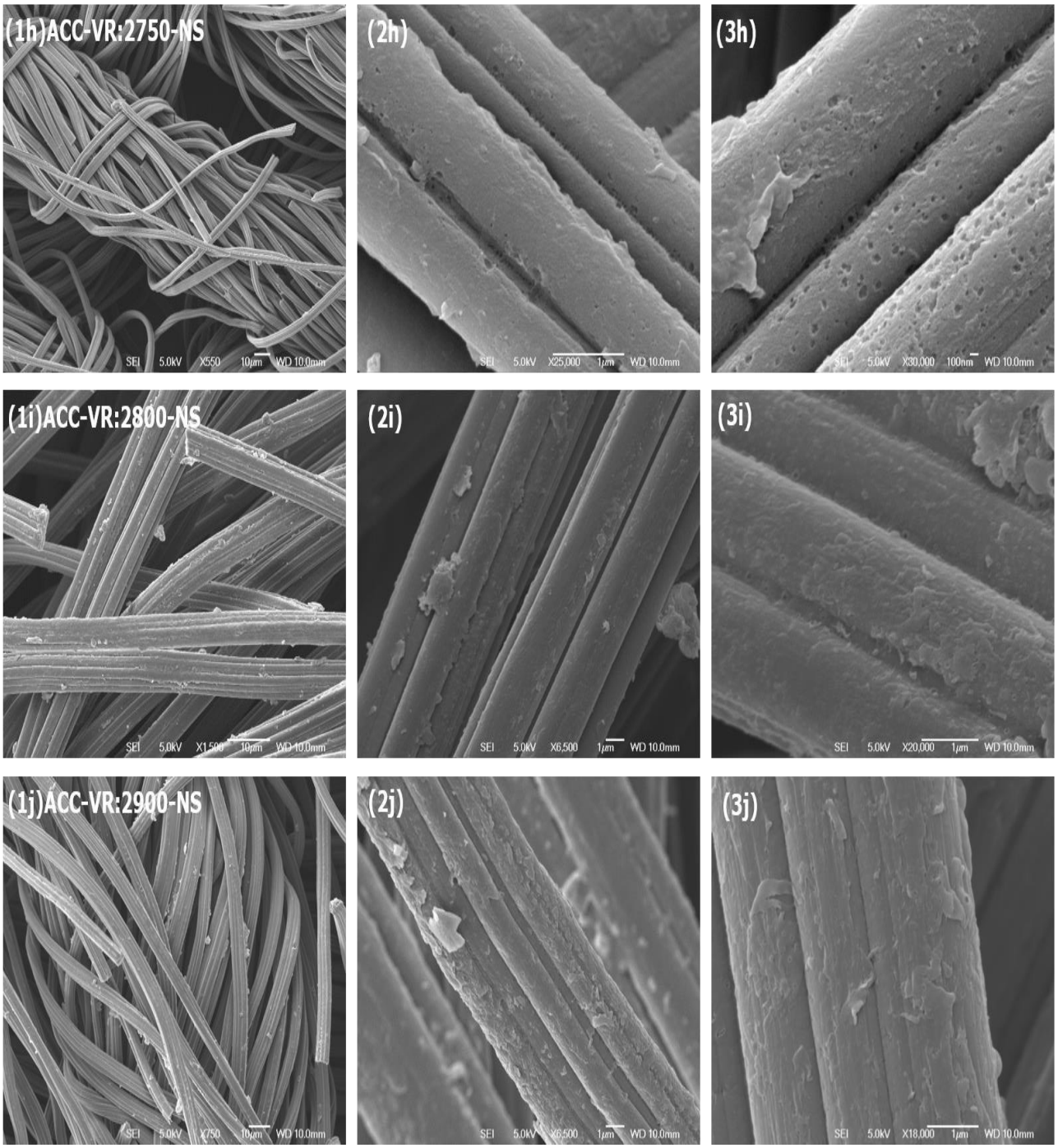


Figure 23: SEM images of activated carbon cloth ACC-2:Y-NScarbons.

6.4. Methane storage and CO_2 uptake

An innovative approach was developed for the synthesis of flexible nanoporous ACCs with superior textural properties. We therefore investigated the gas (CH_4 and CO_2) uptake capacity of the present ACCs and compared them to previously reported ACCs and commercially available carbon cloths.[1,4,6,7,10,36] The capacity of these newly developed flexible ACCs for reversible storage of CH_4 was evaluated at 25°C and pressure of up to 100 bar. Figure 25 shows the CH_4 adsorption isotherms of ACC-VR-W-Y series of ACCs, ACC-2:750-S and ACC-2:750-NS with the corresponding uptake summarised in Table 10. At 100 bar, all the samples exhibited good excess CH_4 storage capacity in the context of the previously reported capacity of ACCs, i.e., excess uptake of 6.7 mmol/g (AC-VR-10-700), 7.1 mmol/g (AC-VR-50-630), 9.9 mmol/g (ACC-2:750-S) and 8.4 mmol/g (ACC2:750-NS). The total uptake is even more impressive at 7.9 mmol/g (AC-VR-10-700), 9.4 mmol/g (AC-VR-50-630), 13.7 mmol/g (ACC-2:750-S) and 14.1 mmol/g (ACC-2:750-NS). Furthermore, AC-VR-10-700 and AC-VR-50-630 did not reach saturation at 100 bar, and thus higher CH_4 uptake can be expected at higher pressures.

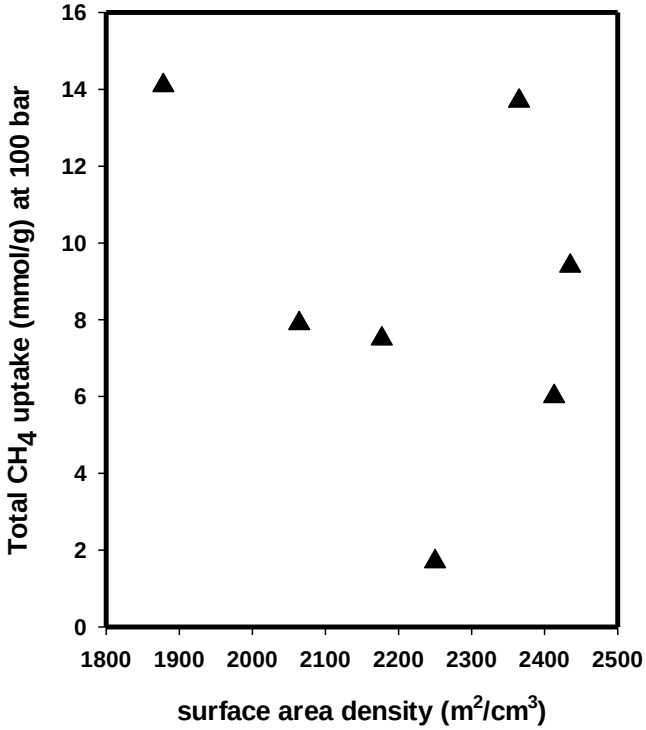


Figure 24: The effect of surface density on CH_4 uptake at 100bar and 25 °C.

In particular, exceptionally high (for ACCs) CH_4 storage capacity was achieved for the ACCs prepared via PO activation, which we ascribe to their high surface area; 2253 m^2/g (ACC2:750-NS) and 1892 m^2/g (ACC-2:750-NS). It is important to note that ACC-2:750-NS also has the highest capacity for CH_4 storage at low pressure in addition to impressive uptake at high pressure. This may be ascribed to the significant microporosity of this sample in addition to overall high porosity. Significantly, the CH_4 uptake of the much simpler to prepare ACC-2:750-NS (8.4 mmol/g at 25°C and 20 bar) is higher than the storage capacity of the best benchmark ACC reported to date, i.e., 7.5 mmol /g for C60CC-PNP.[6]

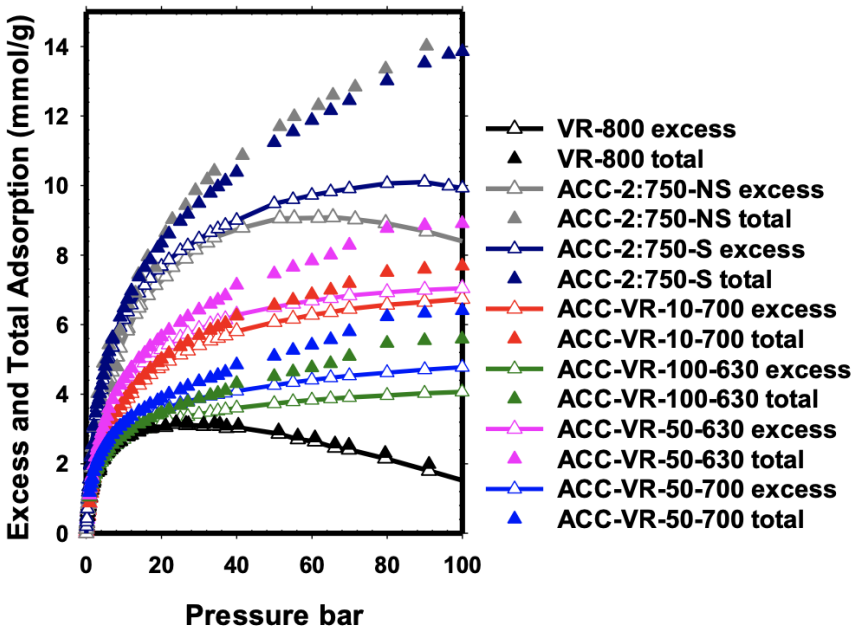


Figure 25: Excess and total CH_4 uptake at 25 °C of ACC-VR-W-Y activated carbon cloths, VR-800, ACC-2:750-S and ACC-2:750-NS.

Table 10: Excess and total CH_4 uptake at 25 °C of ACC-VR-W-Y activated carbon cloths, VR-800 and ACC-2:750-WS and ACC-2:750-NS. The values in parenthesis are the total uptake.

Sample	*1 bar*	*20 bar*	*35 bar*	*100 bar*
AC-VR-10-700	1.1 (1.11)	4.9 (5.1)	5.6 (6.0)	6.7 (7.9)
AC-VR-50-700	1.2 (1.22)	2.5 (2.9)	3.2 (3.8)	5.5 (7.5)
AC-VR-50-630	1.2 (1.22)	5.3 (5.7)	6.0 (6.7)	7.1 (9.4)
AC-VR-100-630	1.0 (1.02)	3.2 (3.5)	3.6 (4.2)	4.1 (6.0)

Char-VR-800	1.1 (1.10)	3.0 (3.0)	3.1 (3.2)	1.5 (1.7)
ACC-2:750-S	2.0 (2.03)	7.7 (8.4)	8.9 (10.1)	9.9 (13.7)
ACC-2:750-NS	1.5 (1.55)	7.3 (8.3)	8.6 (10.4)	8.4 (14.1)

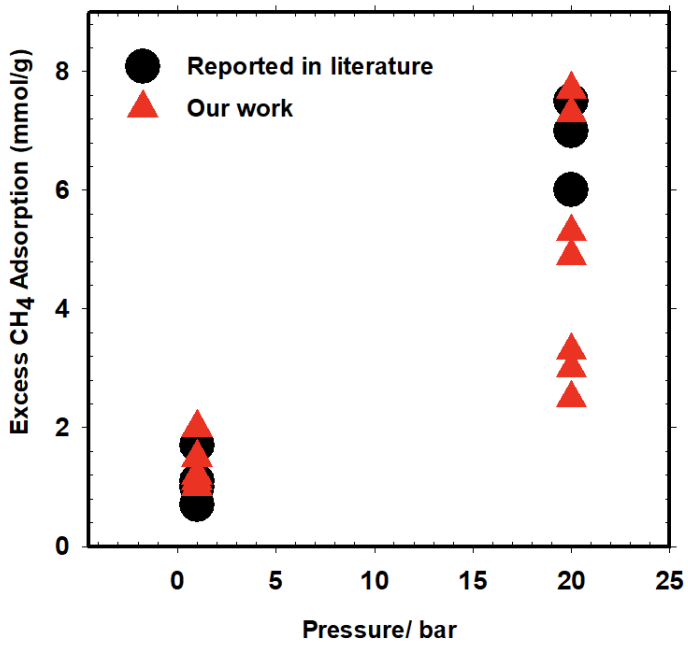


Figure 26: Benchmarking of methane uptake with previously reported activated carbons cloths.[1,3,4,6,8,9]

The role of micropores in CO_2 capture by carbons has been investigated by analysing the CO_2 adsorption properties at 25°C and pressure up to 40 bar in many studies.[6,16,37–44] Recently, Presser *et al.,* empirically deduced that, in the case of microporous carbons, CO_2 capture at atmospheric pressure largely depends on the number of micropores smaller than 0.8 nm.[37] Following their initiative, Wei *et al*., and Sevilla *et al*., found similar results for a variety of activated carbons.[21,45]

Table 11: CO_2 uptake (mmol/g) at 25°C and various pressures of rayon-derived activated carbon.

Sample	*0.25 bar*	*1 bar*	*20 bar*	*40 bar*
AC-VR-10-700	1.3	3.0	8.6	9.4
AC-VR-50-700	1.2	2.5	3.2	5.5
AC-VR-50-630	1.6	3.5	8.9	9.6
AC-VR-100-630	1.1	2.4	4.6	4.9
Char-VR-800	1.0	2.3	5.0	4.7
ACC-2:750-S	2.0	4.2	12.2	13.4
ACC-2:750-NS	1.0	3.0	14.0	16.2

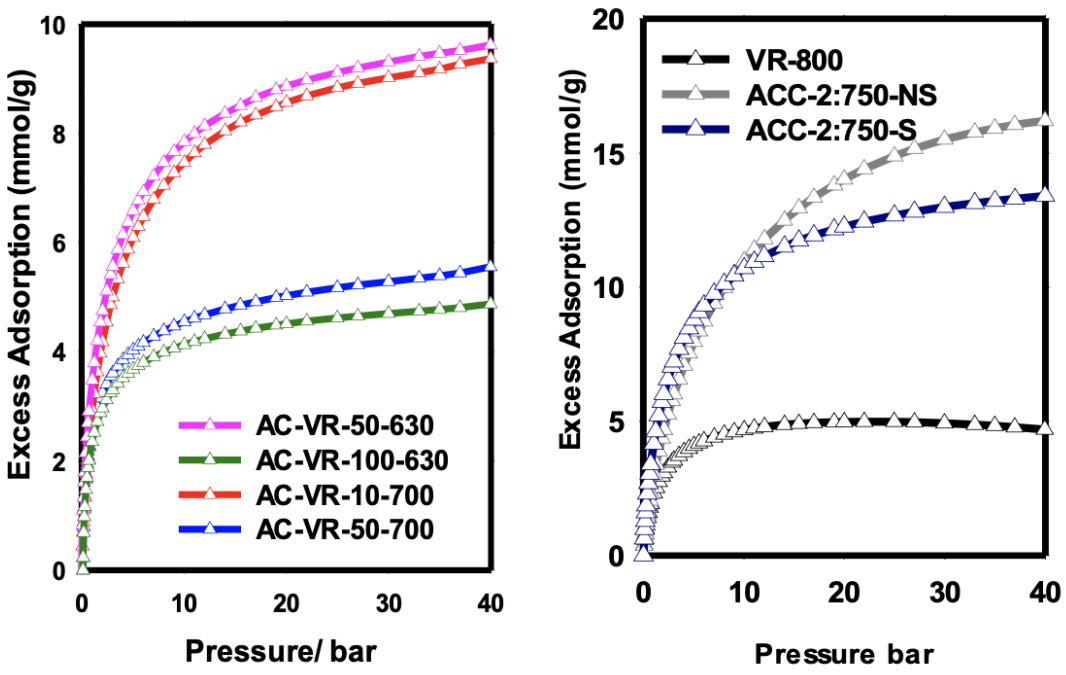


Figure 27: The CO_2 adsorption isotherm for ACC-VR-W-Y at 25°C and 40 bar (left), and The CO_2 adsorption isotherm for VR-800. ACC-2:750 with and-NS at 25°C and 40 bar (right).

The CO_2 uptake capacity of the ACCs was evaluated at 25 °C and pressure of up to 40 bar. The uptake isotherms are shown in Figure 27 and the uptake at various pressures is summarised in Table 11. Uptake values of up to 4.2 mmol/g at 1 bar, and 13.4 mmol/g at 40 bar were observed for sample ACC-2:750-S, which had the best performance at low pressure. This compares with an uptake of 3.0 mmol/g at 1 bar and 16.2 mmol/g at 40 bar for sample ACC-2:750-NS. The better performance of ACC-2:750-S at low pressure (1 bar) may be ascribed to a higher level of

microporosity and smaller micropores. Conversely, ACC-2:750-NS exhibited a higher CO_2 uptake at higher pressure (40 bar) due its overall larger surface area.

Uptake capacity at low pressure (~1 bar) is an important indicator for CO_2 capture performance under post-combustion conditions. Hence, the CO_2 uptake of 3.0 and 4.2 mmol/g at 1 bar for ACC-2:750-NS and ACC-2:750-S, respectively, indicates that the present easily synthesised ACCs can be effective for high performance CO_2 uptake in regard of relevant carbon capture and storage (CCS) applications. It is important to note that the CO_2 uptake of the present carbons and in particular ACC-2:750-S (4.2 mmol/g at 1 bar, 25°C) is similar to the highest CO_2 uptake reported so far for benchmark ACCs, namely C30-CC-PNP.[6] Thus the CO_2 uptake of the present ACCs represents some of the highest values reported for activated carbon cloths, conventional activated carbons,[17,46] and MOFs.[40,41,47,48]

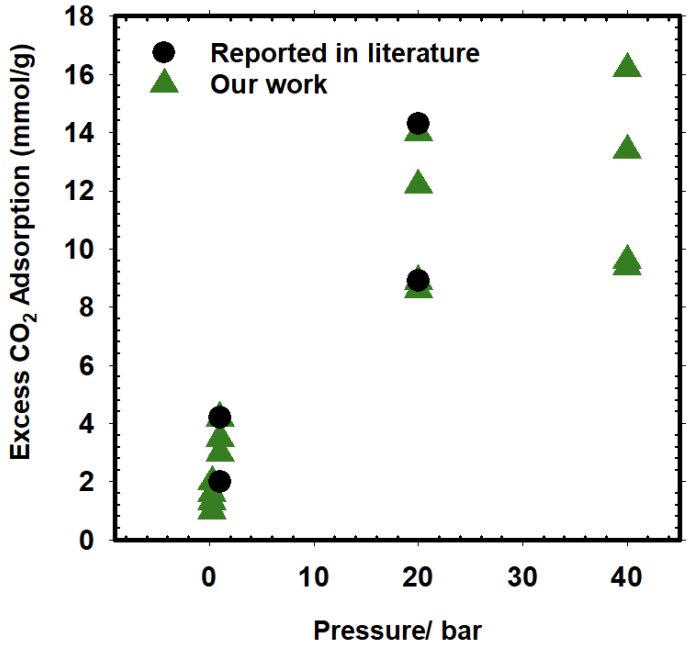


Figure 28: Benchmarking of CO_2 uptake with previously reported ACCs.

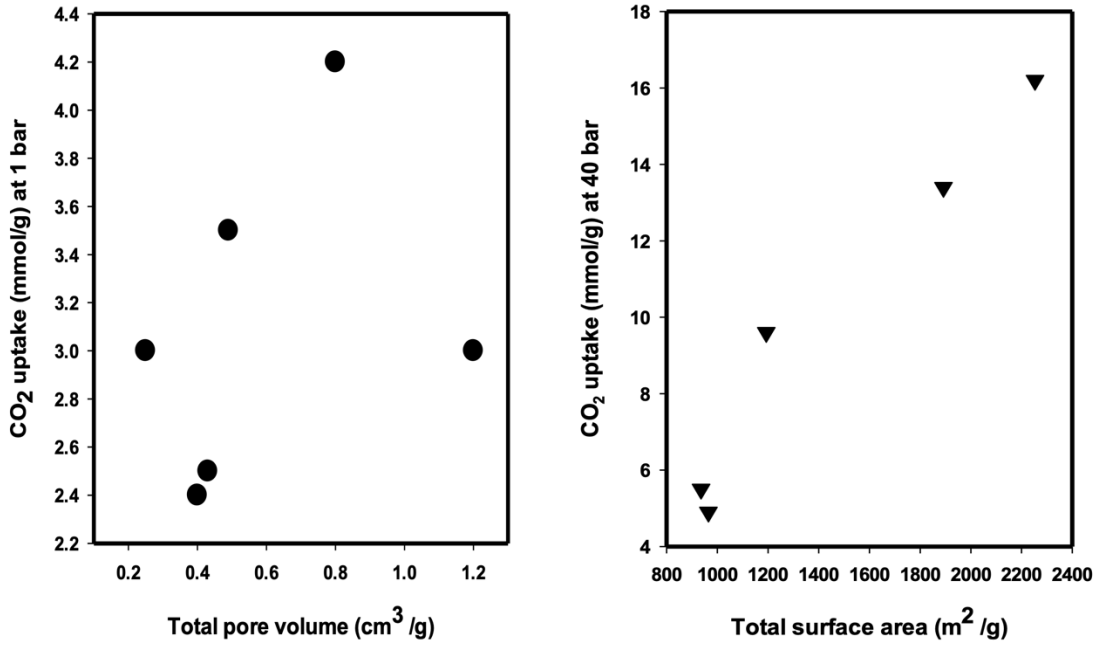


Figure 28: The effect of total pore volume in CO_2 uptake at 1 bar and 25°C *(left), and the effect of the increase of total surface area in CO_2 uptake at 40 bar and* 25°C *(right).*

6.5. Conclusion

The development of nanoporous and high surface-area carbon materials showing strong performance for a variety of applications is a significant challenge, as the textural, porosity and surface chemistry features may exert different influences. However, the average pore size and pore size distribution, as well as the surface area and pore volume appear to be the most important parameters with respect to adsorption of both gaseous molecules and charged ions. In the context of this study, a mechanically stable and flexible activated carbon cloth (ACC) material was prepared without the need for chemical impregnation, which has to date been accomplished using an aqueous mixture of $ZnCl_2$ and NH_4Cl. Previously reported ACC has been synthesized via complicated methodologies that required many steps, energy, time, and reagents.[2–7]

In this work, an examination has been undertaken of a sustainable synthesis route in terms of minimising preparation steps, energy, time and chemicals. ACC has been successfully prepared using three increasingly simple, sustainable and scalable methodologies.

The resulting ACCs have moderate to high surface areas of 516 m^2/g - 2253 m^2/g, with pore volumes of 0.25 cm^3/g - 1.26 cm^3/g. The ACCs exhibited high methane uptake capacity at both low (1 bar) and high (20 bar) pressures at 25°C, of 2.0 and 8.4 mmol/g, respectively. These are

higher than the values of ACC reported in literature to date. The ACC also exhibited the ability to store high amounts of CO_2 at a pressure of 2.0 mmol/g at 0.25 bar and 25°C, which is indicates good potential for use in post-combustion technology applications. It also showed a similar capacity to store CO_2 compared to benchmark ACC types reported in previous studies but prepared via longer and more complicated synthesis routes. At 25 °C, the present ACCs can store up to 4.2 mmol/g and 14.0 mmol/g at 1 and 20 bar, respectively.

6.6. References

1 D. Lozano-Castelló, J. Alcañiz-Monge, M. A. De La Casa-Lillo, D. Cazorla-Amorós and A. Linares-Solano, *Advances in the study of methane storage in porous carbonaceous materials q*, 2002.

2 B. Babic, S. Milonjic, M. Polovina and B. V Kaludierovič Kaludierovič, *Point of zero charge and intrinsic equilibrium constants of activated carbon cloth*, 1999, vol. 37.

3 A. C. Pastor, F. Rodrıguez-Reinoso, H. Marsh and M. A. Martınez, *Preparation of activated carbon cloths from viscous rayon. Part I. Carbonization procedures*, 1999, vol. 37.

4 G. Rodríguez-Blanco, L. Giraldo and J. C. Moreno-Piraján, *Appl Surf Sci*, 2010, **256**, 5221–5225.

5 ´ A Huidobro, A. C. Pastor, F. Rodrıguez- and R. Reinosó, *Carbon, 2001, **39**, 389-398.*

6 N. F. Attia, M. Jung, J. Park, H. Jang, K. Lee and H. Oh, *Chemical Engineering Journal*, 2020, **379**, 122367.

7 N. Kostoglou, C. Koczwara, C. Prehal, V. Terziyska, B. Babic, B. Matovic, G. Constantinides, C. Tampaxis, G. Charalambopoulou, T. Steriotis, S. Hinder, M. Baker, K. Polychronopoulou, C. Doumanidis, O. Paris, C. Mitterer and C. Rebholz, *Nano Energy*, 2017, **40**, 49–64.

8 ´ A Huidobro, A. C. Pastor, F. Rodrıguez- and R. Reinosó, *Carbon, 2001, **39**, 389-398.*

9 P. T. Williams and A. R. Reed, *J Anal Appl Pyrolysis*, 2004, **71**, 971–986.

10 F. Suárez-García, A. Martínez-Alonso and J. M. D. Tascón, *Carbon N Y*, 2004, **42**, 1419–1426.

11 E. Frank, L. M. Steudle, D. Ingildeev, J. M. Spörl and M. R. Buchmeiser, *Angewandte Chemie - International Edition*, 2014, **53**, 5262–5298.

12 A. G. Dumanlı and A. H. Windle, *J Mater Sci*, 2012, **47**, 4236–4250.

13 N. Balahmar, A. S. Al-Jumialy and R. Mokaya, *J Mater Chem A Mater*, 2017, **5**, 12330–12339.

14 P. E. Hock and M. A. A. Zaini, *Acta Chimica Slovaca*, 2018, **11**, 99–106.

15 Y. Li, T. Ben, B. Zhang, Y. Fu and S. Qiu, *Sci Rep*, 2013, **3**, 1–6.

16 S. Deng, B. Hu, T. Chen, B. Wang, J. Huang, Y. Wang and G. Yu, *Adsorption*, 2015, **21**, 125–133.

17 G. Singh, I. Y. Kim, K. S. Lakhi, P. Srivastava, R. Naidu and A. Vinu, *Carbon N Y*, 2017, **116**, 448–455.

18 I. Mufandi, S. Jamilatun, D. A. A. Purnama and R. U. Melani Putri, *al-Kimiya*, 2020, **7**, 62–66.

19 J. Jagiello, J. Kenvin, A. Celzard and V. Fierro, *Carbon N Y*, 2019, **144**, 206–215.

20 C. Quan, R. Su and N. Gao, *Int J Energy Res*, 2020, **44**, 4335–4351.

21 H. Wei, S. Deng, B. Hu, Z. Chen, B. Wang, J. Huang and G. Yu, *ChemSusChem*, 2012, **5**, 2354–2360.

22 M. A. A. Zaini and M. S. M. Shaid, *Hungarian Journal of Industry and Chemistry*, 2017, **44**, 129–133.

23 R. Bacon and M. M. Tang, *Carbon N Y*, 1964, **2**, 221–225.

24 M. A. A. Zaini, T. S. Hui, L. L. Zhi and N. Alias, *Aceh International Journal of Science and Technology*, Aceh Int. J. Sci. Tech., 2016, **5**, 18-20.

25 M. Abbas Ahmad Zaini, T. Wee Meng and M. Johari Kamaruddin, *Sains Malaysiana,* 2014, **43**, 1421-1428.

26 M. Sevilla, A. S. M. Al-Jumialy, A. B. Fuertes and R. Mokaya, *ACS Appl Mater Interfaces*, 2018, **10**, 1623–1633.

27 J. Ludwinowicz and M. Jaroniec, *Carbon N Y*, 2015, **82**, 297–303.

28 Y. D. Chen, W. Q. Chen, B. Huang and M. J. Huang, *Chemical Engineering Research and Design*, 2013, **91**, 1783–1789.

29 29 R. Kumar, J. Gunjal and S. Chauhan, Composites Part B: Engineering, 2021, **217**, 108846.

30 H. G. Ingersoll, *J Appl Phys*, 1946, **17**, 924–939.

31 P. H. Hermans and A. Weidinger, *J Appl Phys*, 1948, **19**, 491–506.

32 W. Ruland, *J Appl Phys*, 1967, **38**, 3585–3589.

33 L. Wei and G. Yushin, *Nano Energy*, 2012, **1**, 552–565.

34 M. Sevilla, W. Sangchoom, N. Balahmar, A. B. Fuertes and R. Mokaya, *ACS Sustain Chem Eng*, 2016, **4**, 4710–4716.

35 Y. Xia, Z. Yang and Y. Zhu, *J Mater Chem A Mater*, 2013, **1**, 9365–9381.

36 L. Zubizarreta, E. I. Gomez, A. Arenillas, C. O. Ania, J. B. Parra and J. J. Pis, *Adsorption*, 2008, **14**, 557–566.

37 V. Presser, J. McDonough, S. H. Yeon and Y. Gogotsi, *Energy Environ Sci*, 2011, **4**, 3059–3066.

38 M. Sevilla, J. B. Parra and A. B. Fuertes, *ACS Appl Mater Interfaces*, 2013, **5**, 6360–6368.

39 36 J. He, J. W. F. To, P. C. Psarras, H. Yan, T. Atkinson, R. T. Holmes, D. Nordlund, Z. Bao and J. Wilcox, Adv. Energy Mater, 2016, **6**, 1502491.

40 Y. Chen, D. Lv, J. Wu, J. Xiao, H. Xi, Q. Xia and Z. Li, *Chemical Engineering Journal*, 2017, **308**, 1065–1072.

41 D. Lv, R. Shi, Y. Chen, Y. Chen, H. Wu, X. Zhou, H. Xi, Z. Li and Q. Xia, *Ind Eng Chem Res*, 2018, **57**, 12215–12224.

42 A. Wahby, J. M. Ramos-Fernández, M. Martínez-Escandell, A. Sepúveda-Escribano, J. Silvestre-Albero and F. Rodríguez-Reinoso, *ChemSusChem*, 2010, **3**, 974–981.

43 Y. S. Bae and R. Q. Snurr, *Angewandte Chemie - International Edition*, 2011, **50**, 11586–11596.

44 M. Sevilla and A. B. Fuertes, *Energy Environ Sci*, 2011, **4**, 1765–1771.

45 M. Sevilla, C. Falco, M. M. Titirici and A. B. Fuertes, *RSC Adv*, 2012, **2**, 12792–12797.

46 A. Arami-Niya, T. E. Rufford and Z. Zhu, *Energy and Fuels*, 2016, **30**, 7298–7308.

47 45 K. S. Park, Z. Ni, A. P. Cô, J. Y. Choi, R. Huang, F. J. Uribe-Romo, H. K. Chae, M. O'keeffe and O. M. Yaghi, PNAS, 2006, **103**, 10186-10191.

48 A. R. Millward and O. M. Yaghi, *J Am Chem Soc*, 2005, **127**, 17998–17999.

7. Conclusion and Future work

7.1. Conclusion

This thesis provides synthesis protocols for the preparation of porous activated carbons with tunable porosities that exhibit a high capability for use as gas adsorbents. Preparation methods are developed to ensure sustainability by minimizing the use of chemicals, cost, time, and the consumption of energy. In addition, novel methods have been established to prepare porous carbons. The simplicity of these protocols is promising, as they increase the ease of application on a large scale. The resulting activated carbons demonstrated a range of porosity from ultra-microporosity to mesoporosity with different morphologies, and forms.

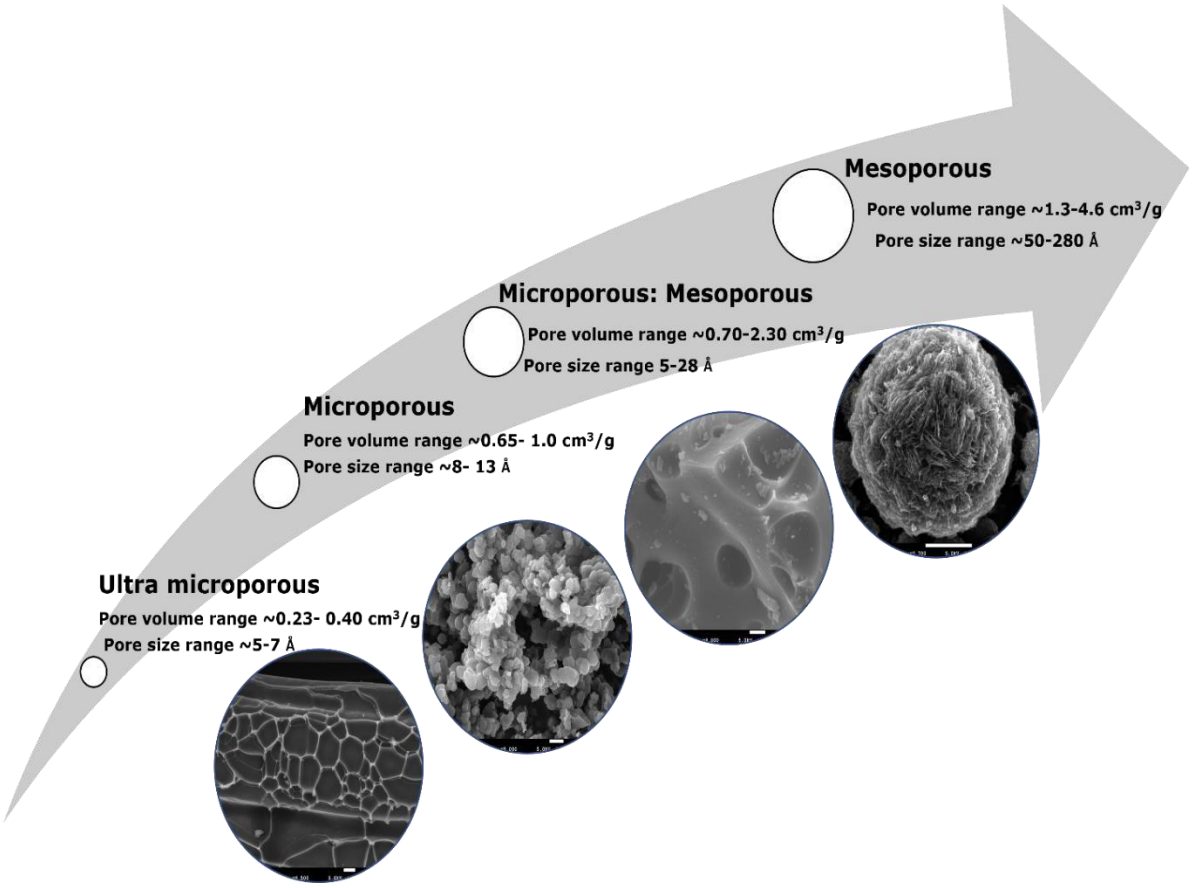


Figure 1. Demonstrates the range of porosity and morphology for the activated carbons produced in this work.

The activation of porous organic polymers using mild activation agents:

The chemical activation of porous organic polymers (PPY) with the less hazardous and mild activation agent potassium oxalate (PO) produced the desired porous structures for several gas applications: low pressure CO_2 capture (0.15 and 1 bar), high pressure CO_2 capture and storage (30 and 40 bar), and methane storage (35–100 bar). PPY-derived activated carbons prepared at KOH–carbon ratios of 2, 3, 4, and 5 exhibit moderate to ultra-high surface area and pore volume ranging from ~660–3000 m^2/g and ~0.27–1.77 cm^3/g, respectively.

Template-assisted carbonisation for ordered mesoporous carbons:

Template-assisted carbonisation via the carbon vapour deposition (CVD) and liquid impregnation (LI) techniques produced highly mesoporous carbons with unique, 3D hierarchical carbon nano-cages (hCNCs), which have a BET range SA 779 to 1711 m^2/g and medium to very large pore volume range of 1.5–4.6 cm^3/g. In addition, the chemical activation of hCNCs with KOH was enhanced by the BET SA by 29% and 37%.

Flash carbonization and chemical activation of biomass:

Flash carbonization at 350–600°C and the subsequent chemical activation with KOH processes can be used to remarkably develop the pore structure of biomass (prickly pear peels) so as to generate porosity ranging from narrowly distributed small micropore sizes to larger micropores and small mesopores. Prickly pear peels-derived activated carbons prepared at KOH–carbon ratios of 2, 3, and 4 exhibit moderate to ultra-high surface areas and pore volumes in the range of 1075–1512 m^2/g and 0.54–0.82 cm^3/g (AC-XY-350), 1167–3614 m^2/g and 0.68–2.19 cm^3/g (AC-XY-400), 1568–3720 m2/g and 1.10–2.37 cm^3/g (AC-XY-500), and 1391–2531 m^2/g and 0.69–1.74 cm^3/g (AC-XY-600).

Sustainable approaches for a flexible carbon cloth:

A mechanically stable and flexible ACC material was prepared via the following:

(i) chemical impregnation using an aqueous mixture of $ZnCl_2$ and NH_4Cl. The resulting ACCs demonstrate moderate to high surface areas of 516–1193 m^2/g and pore volumes between 0.3–0.5 cm^3/g.

(ii) Chemical stabilisation using an aqueous NH_4Cl, followed by chemical activation using the mild activating agent PO. The resulting ACCs have moderate to high surface areas of 923–1892 m^2/g and pore volumes between 0.4–0.8 cm^3/g.

(iii) Precursor carbonisation via pyrolysis at high temperatures of ~800°C, followed by PO chemical activation. The resulting ACCs have moderate to high surface areas of 654–2253 m^2/g and pore volumes between 0.3–1.2 cm^3/g.

Gas adsorption performance of porous activated carbon:

- CO_2 capture and storage

  Activated carbons that have ultra-microporosity and high N-content showed the highest CO2 uptake in very low pressures of ~0.15 bar and 25°C up to 1.4 mmol/g. In contrast, samples with high microporosity showed the highest uptake at atmospheric pressures up to ~4.2 mmol/g. Activated carbons with larger pore volumes show very high uptakes at high pressures ranging between 30–40 bar; up to 25 and 32 mmol/g respectively.

- Methane storage:

  Activated carbons with microporosity/mesoporosity structures showed very high gravimetric methane uptake at the pressure range 35–100 bar and at 25°C, up to 12.5– 16.6 mmol/g (excess) and up to (15.3 and 27.0 mmol/g (total). In addition. mesoporous hCNCs reported exceptional total methane storage, up to 13.4 and 29.9 at 35 and 100 bar, due to their large pore volume.

7.2. Future work

While it is acknowledged that it is difficult to design activated carbons with the exact needed pore size for specific gas adsorption applications, further investigations on synthesis conditions may result in a diverse array of materials. Some next steps could include post-synthesis incorporation of heteroatoms such as nitrogen (or other surface functional groups) to selectivity develop the carbons that can alter gas uptake properties for the materials prepared in this thesis. In addition, due to their textural properties and pore accessibility, the carbons presented in this thesis may be suitable for use as electrode materials.